Computational Exploration of 3d and 4f Metal Complexes Relevant to Magnetic Resonance Imaging and Molecular Magnetism

A Thesis Submitted to

Indian Institute of Technology Guwahati

for the Degree of

Doctor of Philosophy

By

Niharika Keot
Roll No.186122110

Under the Supervision of

Prof. Manabendra Sarma

Department of Chemistry
Indian Institute of Technology Guwahati
Guwahati-781039, India
August 2025

Dedicated to My Family

Department of Chemistry
Indian Institute of Technology Guwahati
Guwahati-781039, India

STATEMENT

The work contained in the thesis entitled "***Computational Exploration of 3d and 4f Metal Complexes Relevant to Magnetic Resonance Imaging and Molecular Magnetism***" has been carried out by me at the Indian Institute of Technology Guwahati, under the supervision of Prof. Manabendra Sarma, Department of Chemistry, Indian Institute of Technology Guwahati. This work has not been submitted elsewhere for the award of any degree.

Niharika Keot
Roll No. 186122110
Department of Chemistry
Indian Institute of Technology Guwahati
Guwahati-781039, India

Prof. Manabendra Sarma

Professor
Department of Chemistry
Indian Institute of Technology Guwahati
Guwahati-781039, India
Phone: +913612582318, Fax: +913612582349
Email: msarma@iitg.ac.in

CERTIFICATE

This is to certify that the work contained in the thesis entitled "***Computational Exploration of 3d and 4f Metal Complexes Relevant to Magnetic Resonance Imaging and Molecular Magnetism***" has been carried out by **Ms. Niharika Keot** (Roll No. 186122110) at the Indian Institute of Technology Guwahati, under my supervision. This work has not been submitted elsewhere for the award of any degree.

Prof. Manabendra Sarma

Thesis Supervisor

ACKNOWLEDGEMENT

First and foremost, I want to express my gratitude to my Ph.D. supervisor, Prof. Manabendra Sarma, for allowing me to work under his guidance. I am extremely grateful for your guidance, advice, and patience over my Ph.D. journey.

I want to thank the members of my Doctoral Committee, Professor Aditya Narayan Panda (Chairman**),** Professor Padmakumar Padmanabhan, and Professor Dipankar Srimani, for their valuable comments, suggestions, constructive criticism, and constant encouragement.

I extend my sincere thanks to the Department of Chemistry, Indian Institute of Technology Guwahati (IITG), and other faculty members and staff. I thank the supercomputing facilities, Param-Ishan IITG, and Parma-Kamrupa, IITG, for allowing me to conduct my research calculations. I especially want to thank Mr. Jeherul Islam and other staff members of the HPC support team for their help and cooperation throughout my Ph.D. journey.

I express my gratitude to the Council of Scientific and Industrial Research (CSIR), India, for its financial support.

I want to thank my labmates Dr. Haobam Kisan Singh (Alumni), Dr. Himangshu Pratim Bhattacharyya (Alumni), Dr. Juhi Dutta (Post-Doctoral Fellow), Bittu Lama, Upasana Nath, Monalisha Sarma, Biman Medhi, Rabu Ranjan Changmai, Shubam Kumar, Samsung Raja Daimari, Manash Pratim Sarmah, Anand Kumar Yadav, Rimi Chyrmang, Yugant P.M. Guddha, and Madhab Morang for their scientific suggestion, support, which played an important role in completing my work. I am thankful to my seniors and friends, Ritam Sarma, Dhrubajyoti Das, Manideepa Paul, Nandita Changmai, Priyanka Dowerah, Nilkamal Mahanta, Nitish Bharadwaj, Nilavjyoti Sharma, Hirakjyoti Basumatary, for always being there in my corner, during my research journey.

Finally, I would like to convey my deep gratitude to my family. Without their support, my studies would not be possible. Thank you to my mom, dad, and brother Pranjal Pratim Keot for their constant encouragement and unconditional support.

CONTENTS

SYNOPSIS

Lanthanides and transition metal-based complexes play a significant role in biomedicine and magnetism. Two prominent applications of these complexes are their use as contrast agents (CAs) in magnetic resonance imaging (MRI) and their use as single-molecule magnets (SMMs) in data storage devices. The selectivity and stability of specific ligands towards their metal center are a hot topic within coordination chemistry, influencing the efficacy of these MRI CAs. This thesis primarily focuses on the computational investigation of the atomistic behavior of Ln^{3+} (Ln=La^{3+}, Gd^{3+}, and Lu^{3+}) and Mn^{2+} complexes corresponding to their unique electronic and magnetic properties. The study involves various quantum chemical methods, including density functional theory (DFT) and post-Hartree Fock methods, along with molecular dynamics simulations to explore the magnetic characterization, stability, and structural determination of these complexes. The stability of these metal (Ln^{3+} and Mn^{2+}) ligand complexes in aqueous media plays a significant role in their application as MRI CAs. Taking into consideration, *ab initio* molecular dynamics (AIMD) simulations were carried out to investigate the structural dynamics of these complexes at varying temperatures. Additionally, the thermodynamic stability is analyzed through the Gibbs free energy of formation of the complexes. A key factor in MRI CAs is optimizing the water exchange rate (k_{ex}^{298}) of the coordinated water molecules with bulk water, as it directly influences relaxivity. The interaction between water molecules and metal ions has been evaluated using quantum chemical methods, providing insights into the water exchange kinetics. In the realm of molecular magnetism, the magnetic anisotropy of Mn^{2+} complexes is determined through the analysis of the axial zero-field splitting (ZFS) parameter (D). Variations in the ligand environment significantly impact both axial D and rhombic E components of ZFS parameters, thereby affecting the electronic relaxation of MRI CAs and the magnetic behavior of these complexes. We hope this new insight will pave the way for the development of novel diagnostic and therapeutic tools for biomedical use, as well as their applications in data storage devices.

Chapter 1

Introduction

The first chapter begins with a general introduction to the different aspects that this work considers. So, we begin with a brief introduction to MRI, the role of these Ln^{3+} ions as MRI CAs, and the importance of designing new alternatives of Gd^{3+} CAs and their applications. Moreover, the different parameters improve the ^{1}H relaxivity of MRI CAs, including water exchange kinetics, electronic relaxation, and the thermodynamic stability of these complexes. This chapter also includes a general introduction to using transition metal-based Mn^{2+} complexes in SMMs. The final section of this Chapter discusses the goals and limitations of this work.

Chapter 2

Methodology

Chapter 2 introduces fundamental concepts and numerical methods for investigating hydration properties, stability, and magnetic characterization of lanthanides and transition metal-based complexes. The computational analysis of heavy elements is difficult owing to the presence of many electrons. However, recent advances, particularly the use of effective core potentials (ECPs), have made these studies more feasible for computational chemists by incorporating relativistic effects and reducing computational expenses for large systems. This chapter includes the theoretical methods on which this work has been carried out. I have aimed to explain the basic electronic structure theory, and this covers DFT, the post-Hartree Fock methods (CASSCF/NEVPT2), and the various basis sets employed in this work. Moreover, the principles behind the effective core potential and the relativistic theory are discussed. The fundamentals of the Quantum Theory of Atoms in Molecules (QTAIM) and the electron localization function (ELF) are outlined. The basic concept of energy decomposition analysis (EDA), which partitions the interaction energy into physically significant components, including electrostatic, orbital interaction, Pauli repulsion, and dispersion interactions, is also explained in this chapter. Furthermore, to adequately describe the solvent phase dynamics of Ln^{3+} and Mn^{2+} complexes, classical molecular dynamics simulations were performed, followed by AIMD simulations

Chapter 3

Computational Insight into a Mechanistic Overview of Water Exchange Kinetics and Thermodynamic Stabilities of Bis and Tris-Aquated Complexes of Lanthanides

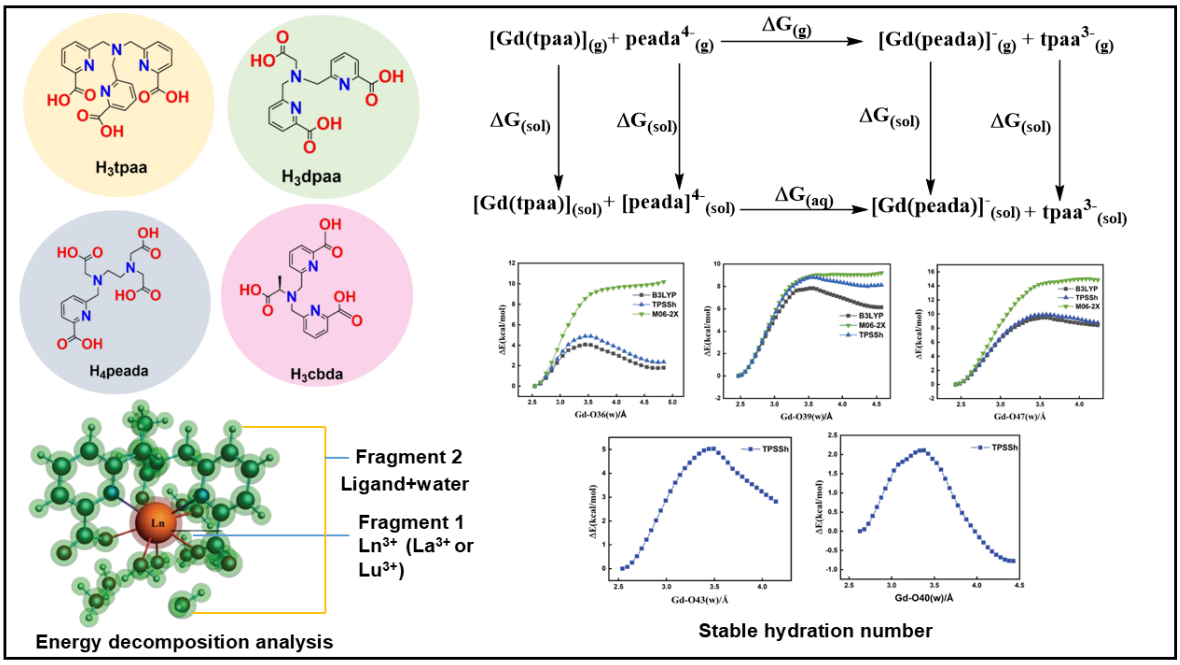

In this chapter, we investigated a series of Ln^{3+} complexes with more than one inner sphere water molecule, essential for designing high relaxivity MRI CAs. Among the studied ligands, hexadentate H_3cbda and heptadentate H_4peada showed high thermodynamic stability, with energy decomposition analysis showing higher binding affinity in H_4peada due to its higher charge density. Water exchange kinetics indicated that weaker metal-water bonds correlate with lower activation barriers and faster k_{ex}^{298}. Moreover, the ionic nature of the metal-ligand (M-L) bond was confirmed by the QTAIM, ELF, and EDA. The distinct ^{17}O and ^{1}H hyperfine coupling constants were computed using the second-order Douglas-Kroll-Hess (DKH2) method for all the coordinated water molecules. Overall, these findings provide valuable insights for designing next-generation Gd^{3+}-based MRI CAs with improved relaxivity and stability.

Chapter 4

Computational Investigation of Chiral DOTA-derivatives: Insights into Structure, Stability, and Relaxivity

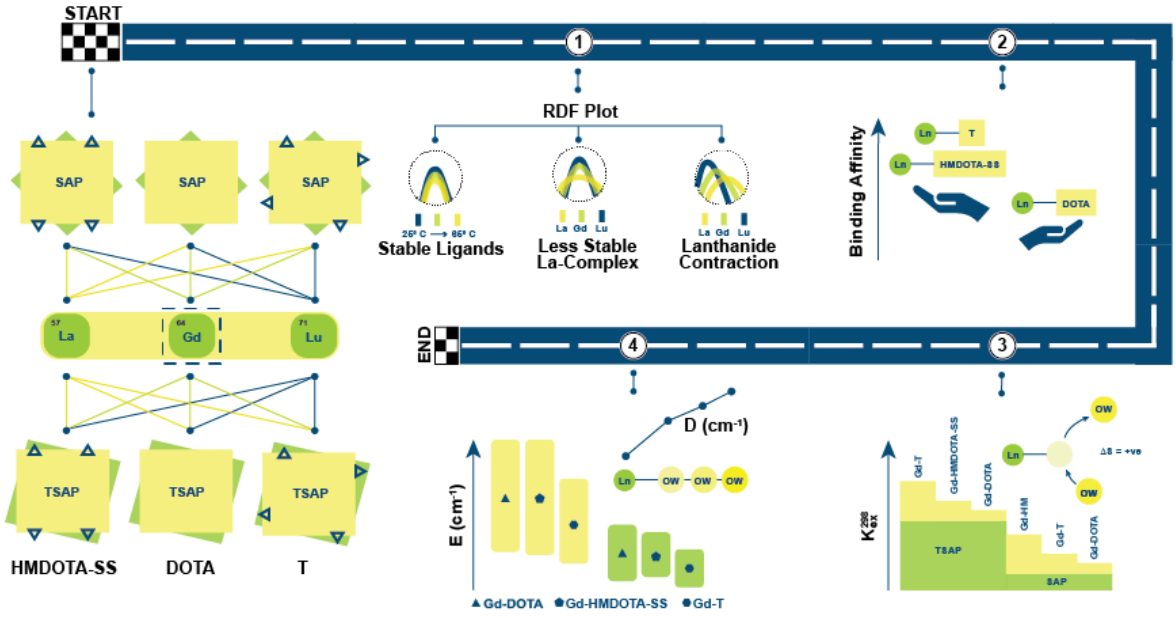

This chapter covers the atomic level analysis of chiral DOTA derivative $[Ln(HMDOTA\text{-}SS)]^-$ and $[Ln(T)]^-$ (Ln^{3+}= La^{3+}, Gd^{3+}, and Lu^{3+}), revealing their increased thermodynamic stability and faster k_{ex}^{298} compared to the clinically approved $[Gd(DOTA)]^-$ complex. These macrocyclic DOTA derivatives exhibited two different isomeric forms: square antiprism (SAP) and twisted square antiprism (TSAP). The $[Gd(DOTA)]^-$ and $[Gd(T)]^-$ complexes preferentially adopt SAP geometry, while $[Gd(HMDOTA\text{-}SS)]^-$ complex favors TSAP across the Ln^{3+}-series. Binding energy and Gibbs free energy analyses reveal that $[Gd(T)]^-$ and $[Gd(HMDOTA\text{-}SS)]^-$ complexes exhibit higher thermodynamic stability compared to their parent $[Gd(DOTA)]^-$ complex. The introduction of bulky hydrophilic groups into the ligand backbone enhances the k_{ex}^{298} of $[Gd(HMDOTA\text{-}SS)(H_2O)]^-$ and $[Gd(T)(H_2O)]^-$ complexes compared to their parent $[Gd(DOTA)(H_2O)]^-$ complex. Variation in coordination geometry leads to the energy splitting of the 4f orbitals of Gd^{3+} complexes, which ultimately affects the overall ZFS energy. Moreover, an increase in the Gd-O(w) bond length results in a higher D-value and a lower E/D ratio, reflecting a more symmetrical ligand field upon removal of the water molecule. This work offers valuable insights into metal-ligand stability, coordination behavior, and relaxation parameters, aiding the rational design of next-generation MRI CAs.

Chapter 5

Probing the Dynamic Behaviour and Magnetic Identification of Seven Coordinated Mn^{2+} Complexes: A Combined AIMD and Multi-reference Approach

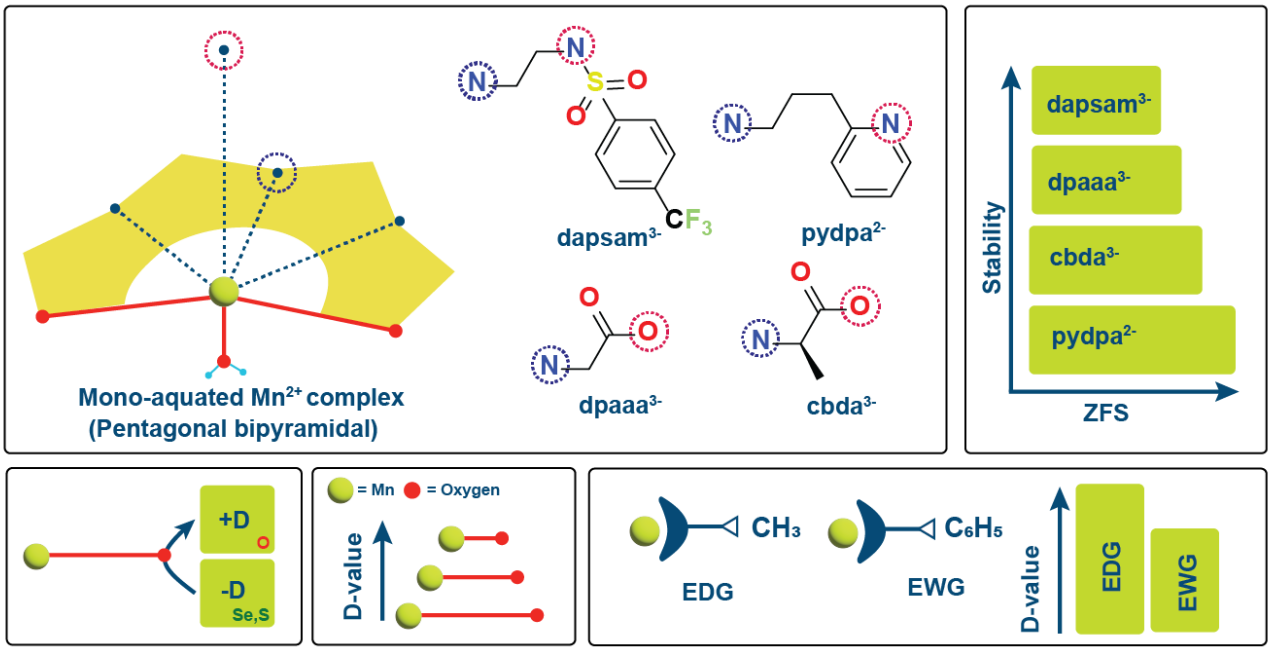

In this chapter, we present a comprehensive analysis of solution-phase dynamics of seven-coordinated pentagonal bipyramidal Mn^{2+} complexes, focusing on their stability and magnetic properties. It includes the assessment of their binding affinity, which is predicted using AIMD simulations combined with DFT. Additionally, simulations at two different temperatures (25˚C and 90˚C) provide insights into the rigidity and stability of the ligands in coordination with the Mn^{2+} ion. These complexes exhibit easy plane magnetic anisotropy characterized by a positive axial ZFS parameter (D), which increases with equatorial ligand symmetry. Substitution of the equatorial oxygen with sulfur and selenium reversed the sign of magnetic anisotropy. The D-value also correlates with the energy gap between the ground and excited state, and it increases by shortening the axial Mn-O(w) bond. In summary, this integrated investigation of solution-phase dynamics and magnetic properties of Mn^{2+} complexes opens new pathways in coordination chemistry, molecular magnetism, spin-crossover materials, and catalysis.

Chapter 6

Unraveling the Stability and Magnetic Properties of Bis-Hydrated Mn^{2+} Complexes via Tailored Ligand Design

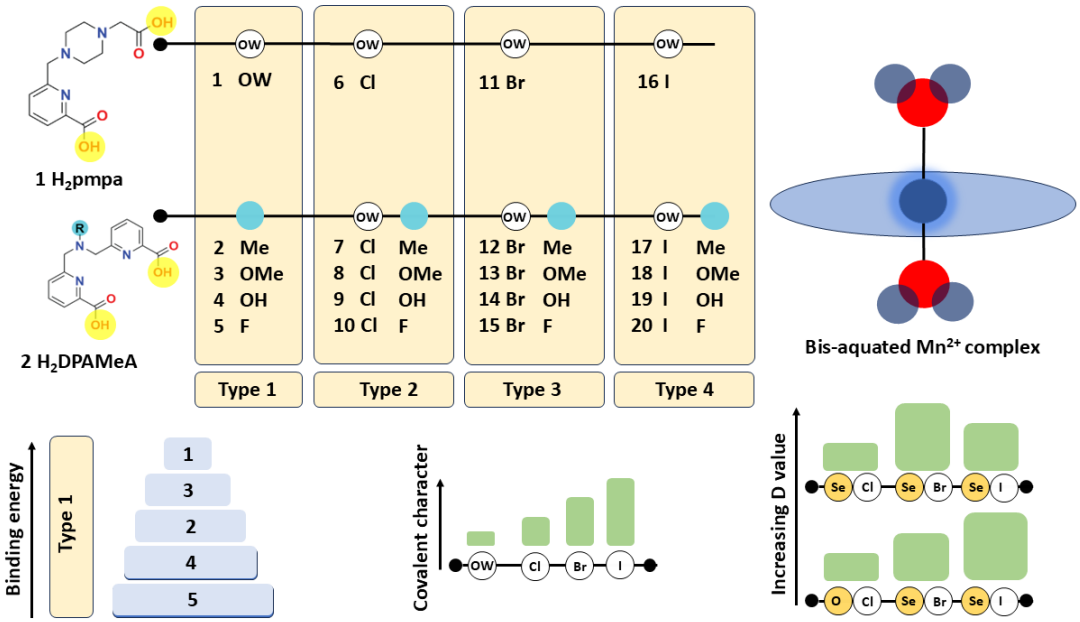

This chapter investigates the aqueous stability and magnetic anisotropy of five bis-hydrated, seven-coordinated Mn^{2+} complexes using AIMD and DFT methods. We simulate the Mn^{2+}-ligand complexes by incorporating explicit water molecules within a periodic box while subjecting the system to effectively varying temperatures. The heightened stability of the Mn^{2+}-ligand interaction is found to correspond with a decrease in structural variation as the temperature is raised. Magnetic characterization via CASSCF/NEVPT2 with active spaces CAS(5,5), CAS(9,7), and CAS(5,10) shows a consistent trend in ZFS values, increasing in the order D(I) > D(Br) > D(Cl), with negligible effect from the double d-shell. Additionally, an analysis of magnetostructural correlations shows that D-value and ZFS energy (△) increase with a decrease in axial Mn^{2+}-X (X=Cl, Br, and I) bond length. However, the D-value of halogen derivatives of Se-analogs follows the order of D(Cl) < D(I) < D(Br), which does not obey the normal spectrochemical series. This discrepancy is most likely a consequence of the interplay between the Se-M bond covalency and ligand field splitting. This study on the stability and the aqueous dynamics of bis-hydrated Mn^{2+} complexes, as well as the magnetic characterization of the complexes with heavy and soft donor atoms, provides novel insights into the development of MRI CAs and SMMs.

Chapter 7

Summary and Conclusions

The final chapter provides a comprehensive summary of our work and highlights potential directions for future research. It provides a wrap-up of what has been achieved and suggests potential areas to be further explored in the research domain. In the first chapter, we investigated the thermodynamic stability and water exchange kinetics of bis- and tris-hydrated Ln^{3+} complexes. Our study revealed the thermodynamic stability and comparative binding affinities of heptadentate (H_4peada, H_3tpaa) and hexadentate (H_3cbda, H_3dpaa) ligands with Ln^{3+} ions in aqueous solutions. The study rationalizes that the H_3cbda and H_4peada ligands form a moderately stable complex with the Ln^{3+} ion. The water exchange kinetics reveals that the inner-sphere water molecules have varying k_{ex}^{298} based on the ligand environment. Given the significance of Ln^{3+}-complexes, particularly those based on macrocyclic DOTA derivatives, the second chapter focused on the impact of bulky and hydrophilic substituents on the stability, water exchange kinetics, and coordination behavior of DOTA derivatives. Our in-depth investigation of the chiral hydrophilic HMDOTA-SS and T ligands will provide valuable insight for the design of DOTA-based chelators with improved thermodynamic stability and relaxivity parameters. The third chapter presented a detailed analysis of the solution-phase dynamics and magnetic characterization of seven-coordinated Mn^{2+} complexes. We designed Mn^{2+}-based complexes with varied ligand environments and demonstrated that the ZFS parameters (D and E) can be tuned by altering the symmetry around the Mn^{2+} ion. The effect of electron-withdrawing and donating groups on modulating the ZFS parameters was also explored. Finally, the last chapter highlights the influence of halogens on enhancing the magnetic anisotropy of seven-coordinated Mn^{2+} complexes with zero orbital contributions.

List of Publications

Thesis Work

1. **N. Keot** and M. Sarma, "Computational Insight into a Mechanistic Overview of Water Exchange Kinetics and Thermodynamic Stabilities of Bis and Tris-Aquated Complexes of Lanthanides", *RSC Adv.*, **2023**, 13, 1516-1529.
2. **N. Keot** and M. Sarma, "Probing the Dynamic Behaviour and Magnetic Identification of Seven Coordinated Mn^{2+} Complexes: a Combined AIMD and Multireference Approach", *Phys. Chem. Chem. Phys.* **2023**, 25, 31165-31177.
3. **N. Keot** and M. Sarma, "Unraveling the Stability and Magnetic Properties of Bis-Hydrated Mn(II) Complexes via Tailored Ligand Design", *J. Phys. Chem. A* **2024**, 39, 8346-8359.
4. **N. Keot** and M. Sarma, "Computational Investigation of Chiral DOTA-derivatives: Insights into Structure, Stability and Relaxivity", *J. Phys. Chem. A* **2025**, 129, 9243-9259.

Out of Thesis Work

1. **N. Keot**, B. Lama, H. K. Singh, H. P. Bhattacharyya, and M. Sarma, "Unveiling the Noncovalent Interaction of Thiazol-2-ylidene and its Derivatives as N-heterocyclic Carbene with Different Proton Donor Molecules", *ChemPhysChem.*, **2023**, 24, e202300413 (1-11).
2. H. K. Singh, U. Nath, **N. Keot,** M. Sarma, "Exploring π - π Interactions and Electron Transport in Complexes Involving a Hexacationic Host and PAH Guest: a Promising Avenue for Molecular Devices", *Phys. Chem. Chem. Phys.,* **2023**, 25, 26767-26778.
3. H. K. Singh, R. R. Changmai, **N. Keot,** H. P. Bhattacharyya, M. Sarma, "A Computational Insight on the Noncovalent Interactions of Aminothiazole-based Palladium (II)-Complexes with DNA as a Potent Anticancer Agent", *Polyhedron*, **2023**, 239, 116448 (1-12).

List of Conferences/Workshops Attended

1. **N. Keot** and M. Sarma*, "Computational Investigation on Water Exchange Rates of Different Stereo-isomers of Lanthanides complexes", Recent Trends in Chemical Sciences (RTCS-2020), Indian Chemical Society, Kolkata, December 26-29, 2020. (Poster)
2. **N. Keot** and M. Sarma*, "Computational Investigation on Water exchange Rates and Stability of Lanthanide-Based MRI Contrasting Agent", Theoretical Chemistry Symposium (TCS) 2021, IISER Kolkata, IACS Kolkata, Kalyani University and S. N Bose National Centre for Basic Sciences Kolkata, December 11-14, 2021. (Poster)
3. **N. Keot** and M. Sarma*, "Understanding the Structure and Water Exchange Rate of Two Bis and Tris-Aquated Complexes of Lanthanide: A Computational Study", North-East Research Conclave (NERC) 2022, IIT Guwahati, May 20-22, 2022. (Poster)
4. **N. Keot** and M. Sarma*, "A Mechanistic Overview of Water-Exchange Kinetics and Thermodynamic Stabilities of Bis and Tris-Aquated Complexes of Lanthanides: a Detailed Computational Insight", Spectroscopy, Dynamics of Molecular Clusters-2022 (SDMC-2022), Malpe, Mangalore, November 10-13, 2022. (Poster)
5. **N. Keot** and M. Sarma*, "Exploring the Role of Transition Metal Complexes in Magnetic Resonance Imaging (MRI) and Single Molecule Magnets(SMMs)", Chemistry Colloquium 2023, IIT Guwahati, November 04, 2023. (Talk)
6. **N. Keot** and M. Sarma*, "Dynamic Properties and Magnetic Characterization of Seven-Coordinate Mn(II) Complexes for their Application in Magnetic Resonance Imaging and Single Molecule Magnets", Theoretical Chemistry Symposium (TCS) 2023, IIT Madras, Chennai, December 07-10, 2023. (Poster)
7. **N. Keot** and M. Sarma*, "Solution Dynamics and Magnetic Properties of Seven-Coordinate Mn(II) Complexes: Implications for Magnetic Resonance Imaging and Single Molecule Magnets", Spectroscopy, Dynamics of Molecular Clusters (SDMC)-2024, Kaziranga, Assam, February 22-25, 2024. (Poster)
8. **N. Keot**, Introduction to Gaussian: Theory and Practice, Hyderabad, India, January 20-24, 2020. (Workshop)

LIST OF ABBREVIATIONS

Abbreviation	Description
MRI	Magnetic Resonance Imaging
CAs	Contrast agents
GBCA	Gadolinium-based contrast agent
SMMs	Single-molecule magnets
SBM	Solomon-Bloembergen-Morgan
TSAP	Twisted square antiprism
SAP	Square antiprism
TS	Transition state
HFCCs	Hyperfine coupling constants
NSF	Nephrogenic systemic fibrosis
FDA	Food and Drug Administration
ZFS	Zero field splitting
SOC	Spin-orbit coupling
SS	Spin-spin coupling
HF	Hartree-Fock
MCSCF	Multiconfigurational self-consistent field
CASSCF	Complete active Space, self-consistent field
NEVPT2	n-Electron valence state perturbation theory
MOs	Molecular orbitals
MP	Møller-Plesset perturbation theory
DFT	Density Functional Theory
LDA	Local density approximation
GGA	Generalized gradient approximation
ECPs	Effective core potentials

LCRECP	Large core relativistic effective core potential
SCRECP	Small core relativistic effective core potential
ZORA	Zeroth-order regular approximation
DKH	Douglas-Kroll-Hess
SARC	Segmented all-electron relativistically contracted
QTAIM	Quantum Theory of Atoms in Molecules
ELF	Electron localization function
BSSE	Basis set superposition error
CP	Counterpoise
MEP	Molecular electrostatic potential
EDA	Energy decomposition analysis
AILFT	Ab initio ligand field theory
MD	Molecular Dynamic
AIMD	Ab initio molecular dynamics
BE	Binding energy
CN	Coordination number
RDFs	Radial distribution functions
TM	Transition metal
PBP	Petangonal bipyramidal
SHPs	Spin Hamiltonian parameters
ROKS	Restricted open-shell Kohn-Sham

LIST OF FIGURES/SCHEMES

Figures/Schemes **Page No**

LIST OF TABLES

Tables **Page No**

Chapter 1

Introduction

The coordinating chemistry of lanthanides (Ln^{3+}) and transition metal (Mn^{2+}) complexes in aqueous solution is developed as a prominent research area owing to their vital role in diverse applications. Understanding the hydration properties and stability of lanthanides in aqueous solution is crucial for coordination chemistry and biomedical imaging. Similarly, insights into the coordination and magnetic properties of transition metal complexes in solution have significant applications in medicinal chemistry and quantum computing. This thesis focuses on the computational modeling of Ln^{3+} and Mn^{2+} ions to reveal their atomistic behavior when complexed with both acyclic and macrocyclic ligands, aiming to advance their potential applications in magnetic resonance imaging (MRI) and single-molecule magnets (SMMs). This introductory section aims to provide a detailed conceptual foundation of the research presented in this thesis, supported by a relevant literature review.

This chapter is organized into two main sections. Section 1.1 discusses the fundamental principles of MRI, highlighting the advantages and disadvantages of Gd^{3+}-based complexes as MRI contrast agents (CAs). Section 1.2 provides an overview of Mn^{2+}-based complexes as MRI CAs and explores their applications in SMMs.

1.1. Application of Lanthanides in Magnetic Resonance Imaging (MRI)

MRI is a diagnostic tool for monitoring and detecting abnormalities in various organs (especially muscles and veins) and soft tissues.[1,2] The advantage of using MRI is that, unlike other imaging modalities such as X-ray,[3] computed tomography (CT-scan),[4] positron emission tomography (PET),[5] and single photon emission computed tomography (SPECT),[6] it possesses minimal health risks, particularly safer for pregnant women.[7] However, a major limitation of MRI is its low sensitivity. So, to enhance this sensitivity, it is often necessary to add an agent called an MRI contrast agent (CA), as shown in Figure 1.1. The effectiveness or sensitivity of the CA is demonstrated in terms of its relaxivity.[8]

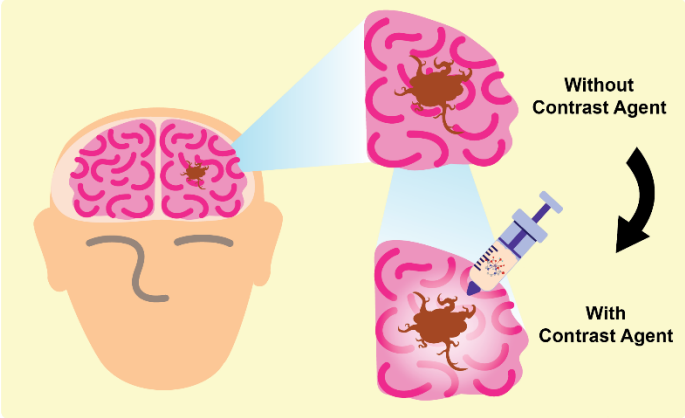

Figure 1.1. Illustration of brain imaging enhanced by a molecular MRI contrast agent (CA).

1.1.1. Principle of Magnetic Resonance Imaging (MRI)

In MRI, an image is generated from the behavior of hydrogen nuclei, which possess spin angular momentum. Without an external magnetic field, these nuclear spins are oriented randomly (Figure 1.2 (a)). However, upon the application of a magnetic field, the proton's spin aligns either with or against the direction of the field, with the majority of spins aligned parallel to the direction of the applied magnetic field, as shown in Figure 1.2 (b). The hydrogen nuclei precess around their own axis at a characteristic frequency known as the H-Larmor frequency ω_0 (MHz), which is proportional to the strength of the applied magnetic field.[9–11]

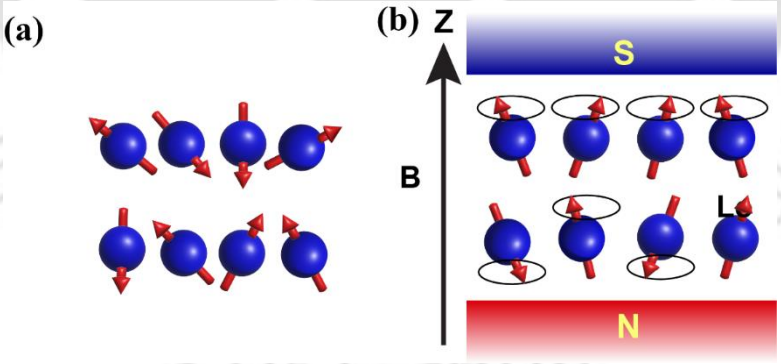

Figure 1.2. (a) In the absence of an external magnetic field, hydrogen proton spins exhibit random orientation. (b) Upon application of an external magnetic field (B), the spin aligns in the Z-direction, leading to longitudinal magnetization.[9]

Applying a radio frequency (RF) pulse with precise energy rotates the longitudinal magnetization by 90˚ to the transverse plane, which wobbles around the z-axis, generating the MRI signal. The magnetization in the transverse plane (M_{xy}) decays slowly in the longitudinal

direction (z) as the energy is transferred from the excited spin to the surrounding lattice. This is called longitudinal relaxation (r_1) or spin-lattice relaxation. Transverse relaxation (r_2) or spin-spin relaxation is the loss of phase coherence in the transverse plane, reducing MRI signal intensity.[9,11] These two relaxation mechanisms, as illustrated in Figure 1.3 (a, b), are characterized by the relaxation time parameters T_1 and T_2, respectively.

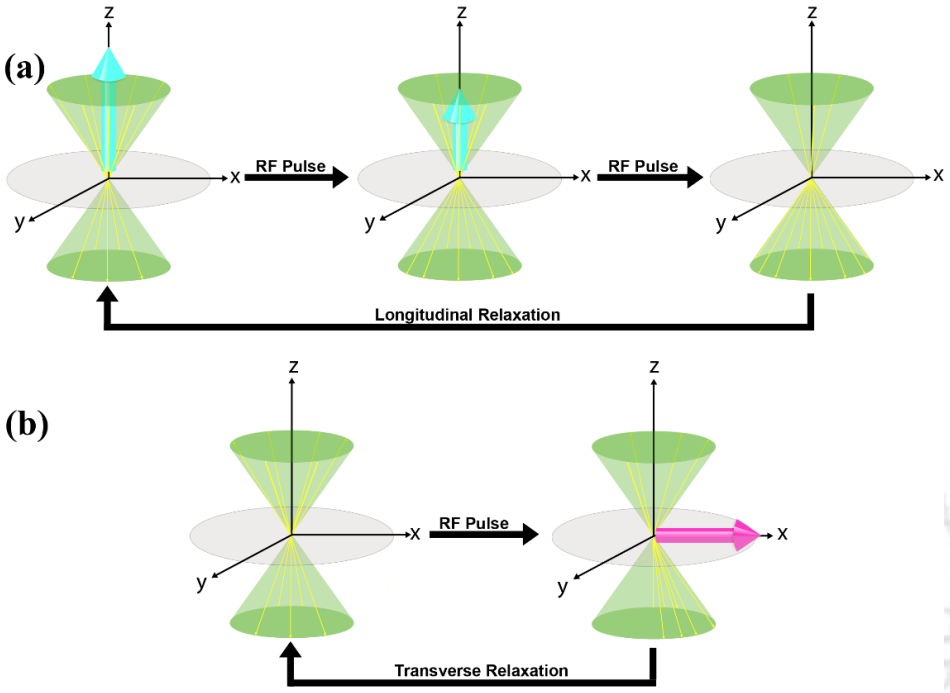

Figure 1.3. There are two ways by which magnetization in the M_{xy} plane to relax: (a) longitudinal relaxation and (b) transverse relaxation.[9]

1.1.2. Contrast agents (CAs) in Magnetic Resonance Imaging (MRI)

MRI can detect pathogenic tissue from normal tissue owing to the difference in proton relaxivity. However, sometimes it is difficult to differentiate this pathogenic tissue from normal tissue; at that time, a CA is necessary.[12–15] The CAs work by the dipole-dipole interactions between water protons and the free electrons of the paramagnetic metal ion. Gd^{3+}-based complexes are the most widely used MRI CAs. These Gd^{3+} ions possess seven unpaired electrons and exhibit a slow electron spin relaxation time (10^{-8}-10^{-9} s^{-1}).[16] This latter property (slow electron spin relaxation) allows sufficient interaction of the Gd^{3+} ion and the surrounding water protons.[17,18] The relaxivity r_1 or r_2 ($mM^{-1}S^{-1}$) defines the sensitivity of the CAs. Eqs. 1.1 and 1.2 show that the amount of the CAs used is directly related to the relaxivity.[18]

$$r_1 \times C = \frac{1}{T_1} \tag{1.1}$$

$$r_2 \times C = \frac{1}{T_2} \tag{1.2}$$

The relaxivity or effectiveness of the CA is influenced by the magnetic field strength and the electronic properties of the agents. Key parameters, as depicted in Figure 1.4 include the number of water molecules directly coordinated with the paramagnetic ion (q), this inner sphere contribution also depends on the water exchange rate (k_{ex}^{298}) between the inner sphere water and bulk solvent, the distance between the Gd^{3+} ion and the protons of the coordinated water molecule (r_{Gd-H}), the rotational correlation time (τ_R), and the electron spin relaxation times, both longitudinal (T_{1e}) and transverse (T_{2e}).[8,15,18,19] The optimization of these parameters is mainly governed by the Solomon-Bloembergen-Morgan (SBM) equations.[20] Apart from these parameters, outer sphere contributions, arising from the interaction between the metal center and nearby water molecules, also influence the overall relaxivity.[8]

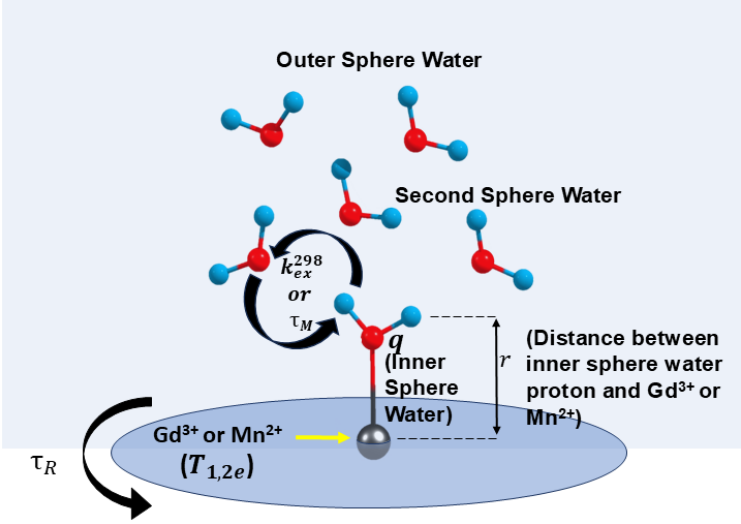

Figure 1.4. Key factors influencing relaxivity include the hydration number (q), water residence time (τ_M), water exchange rate (k_{ex}^{298}), and rotational correlation time (τ_R).[8,17]

The paramagnetic metal center is surrounded by three types of water molecules- inner sphere, second sphere, and outer sphere (Figure 1.4). These inner-sphere water molecules directly coordinated with the metal centre, have the greatest impact due to the close M-H distance and fast exchange with bulk water. Second sphere water molecules, hydrogen bonded to the ligand, contribute less due to a greater distance and short residence time. They reside in the inner sphere for a very short period of time before going to exchange. The outer sphere water molecules will not undergo any exchange; they diffuse surrounding the paramagnetic complex

(~ 4 Å). All three types of water molecules will influence the overall relaxivity (r_1) as shown in Eq. 1.3.[8]

$$r_1 = r_1(IS) + r_1(OS) + r_1(SS) \quad (1.3)$$

The paramagnetic metal ions, like Gd^{3+}, can accelerate the water protons' relaxation. Unfortunately, these free ions are very toxic to our bodies. Therefore, the strong and stable complexation with ligands is an essential criterion.[15,19,21–23] An effective MRI CA must combine high relaxivity with strong in vivo stability. In addition to the strong complexation of the ligand to the metal centre, the ligand should allow at least one water molecule to occupy the inner coordination sphere of the metal ion. Additionally, the relaxivity of the CAs is directly influenced by the number of water molecules coordinated to the metal center.[19] These inner-sphere water molecules rapidly exchange with the surrounding bulk solvent, facilitating the transfer of the paramagnetic effect and, thereby, enhancing the image contrast.[24] Relaxivity increases with an increase in the number of coordinated water molecules. However, this often results in a decrease in the thermodynamic stability and kinetic inertness of the complexes. Only a few thermodynamically and kinetically stable Gd^{3+} ions have been studied till now.[15,19,25]

1.1.3. Water Exchange Kinetics in Lanthanide-based MRI CAs: Mechanisms and Its Impact on Relaxivity

For optimal MRI applications, the k_{ex}^{298} of the coordinated water molecule must be fine-tuned. The CAs with the paramagnetic metal center have shortened the T_1 or T_2 relaxation times of water protons surrounding the metal complex. However, this rate of exchange should be in an optimal range.[8,24] As it is too slow, the k_{ex}^{298} does not properly propagate the paramagnetic effect to the solution. Conversely, if the exchange is too fast, the relaxivity may decrease as the coordinated water molecule does not remain bound long enough to interact with the electron spin of the paramagnetic center.[24,26] The significance of Ln^{3+} complexes as MRI CAs and the critical role of water exchange inspire many researchers to tailor ligand designs for optimal k_{ex}^{298}.[24,27–29]

Water exchange in aquated Ln^{3+} ions was studied across the Ln^{3+}-series by Merbach et al. during the late 1980s and early 1990s.[30,31] This generally involves the substitution of bound water molecules with free water molecules in the solution. This water exchange can occur via an associative, dissociative, or interchange mechanism, depending on the specific lanthanide complex and its ligand environment, as shown in Figure 1.5.

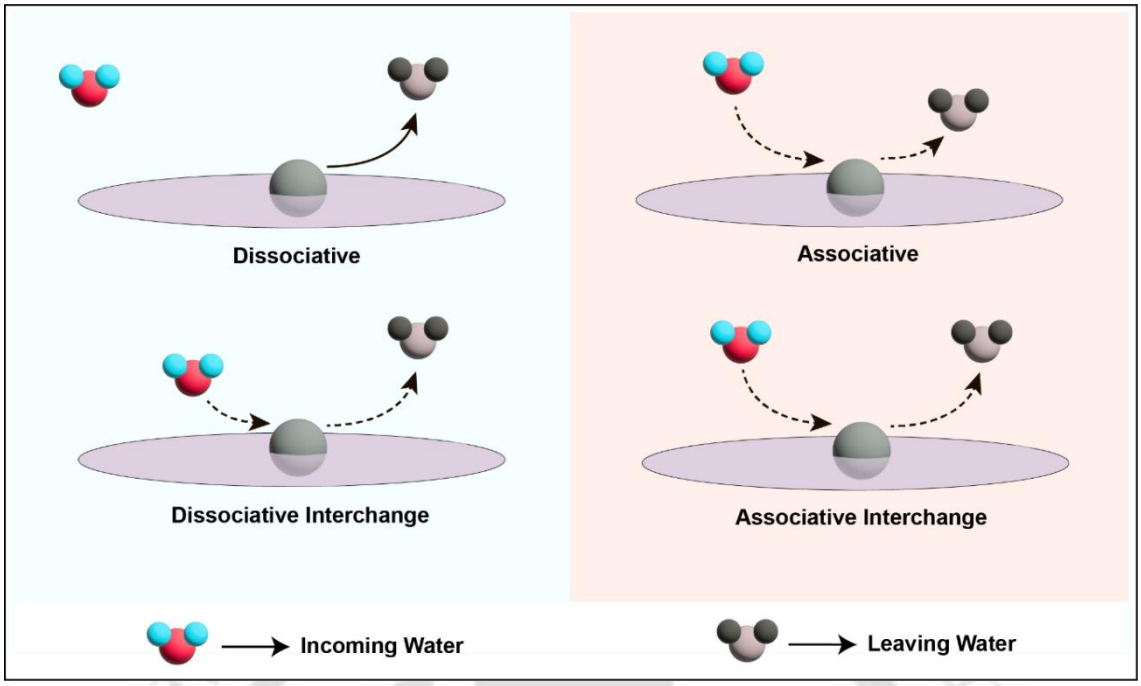

Figure 1.5. The transition states for water exchange processes involving Gd^{3+} via dissociative, associative, dissociative interchange, and associative interchange mechanisms are depicted.

Despite the importance of water exchange kinetics in obtaining more effective MRI CAs, this aspect has been largely unexplored in the literature, with only a few reviews addressing this issue.[29,32–35] Studies have shown that steric hindrance around the water binding site can hinder the close approach of the water to the metal ion, leading to an increase in k_{ex}^{298}. In macrocyclic DOTA-type ligands, the twisted square antiprism (TSAP) isomer exhibits k_{ex}^{298} up to 50 times faster than the square antiprism (SAP) isomer due to steric effects that favor a dissociative exchange mechanism.[24] Wood et al. observed nitrobenzyl-functionalized DOTMA derivative, the k_{ex}^{298} value for the TSAP isomer is an order of magnitude higher than the SAP-isomer. The modification effectively controls the isomeric population, favoring the TSAP configuration.[29,36] Ruloff et al. found that the k_{ex}^{298} value for $[Gd(DOTA)(H_2O)]^-$ (k_{ex}^{298} = 4.1×10^6 s^{-1}) is significantly lower compared to its analog with a thirteen-membered macrocyclic ring, $[Gd(TRITA)(H_2O)]^-$ (k_{ex}^{298}= 270×10^6 s^{-1}), demonstrating that increased steric bulk near the water binding site significantly accelerates k_{ex}^{298}.[37] The addition of an extra carbon atom to the macrocyclic chain causes steric compression, allowing it to leave the coordinated water molecule through a dissociative mechanism. In 2003, Laus et al. replaced the ethylenediamine unit in the DTPA framework with a propyl bridge, yielding $[Gd(EPTPA)(H_2O)]^{2-}$ complex, which shows k_{ex}^{298}, two orders of magnitude higher than that of the parent DTPA complex.[38] Similarly, Wang et al. reported an increase k_{ex}^{298} in the

[Gd(DTPA-cMA)(H_2O)]$^-$ complex, where a propylene linker substituted one of the ethylene spacers in the ligand.[39] Jaszberenyi et al. also found that extending one ligand arm by substituting an acetate with a propionate group (DTTA-Nprop, DTPA-N'prop, and DO3A-Nprop ligand) effectively accelerates k_{ex}^{298}.[40] The strategy of enhancing k_{ex}^{298} through steric compression has been effectively implemented by introducing bulky substituents such as phosphonates and phosphinates to replace one of the carboxylate arms in triazacyclononate derivatives with mixed carboxylate and picolinate arms (BPATCN and PBPATCN ligand).[41] In DOTAla and DOTAlaP derivatives of Gd^{3+} ion with phosphate-induced steric effects significantly increased k_{ex}^{298}.[42]

An important strategy to increase k_{ex}^{298} in lanthanide-based MRI CAs is to increase the number of inner-sphere water molecules (q). Bis- and tris-aquated complexes ($q = 2\ or\ 3$) exhibit higher k_{ex}^{298} compared to the classical mono-aquated [Gd(DOTA)(H_2O)]$^-$ and [Gd(DTPA)(H_2O)]$^-$ complexes, owing to the greater flexibility to obtain the eight-coordinated transition state (TS) in the dissociative mechanism.[43–45] Although the bis-hydrated complexes exhibit rapid k_{ex}^{298}, this behavior is not universal as some q =2 complexes still exhibit slow k_{ex}^{298}. This suggests that k_{ex}^{298} is governed not only by the hydration number but also by various structural and electronic factors.[46] In particular, the nature of ligand substituents also influences k_{ex}^{298}; electron donating group (e.g., OMe) tends to accelerate water exchange while electron-withdrawing growing groups (e.g., CN, CO_2, ^{t}Bu) generally slow it down. Sherry et al. proposed that introducing electron-donating groups at the para position of a phenyl amide moiety increases the electron density on the amide oxygen, thereby weakening its coordination with the metal center and facilitating faster water exchange.[47] In another study, an opposite trend was observed, as the introduction of Me-substituents slowed down k_{ex}^{298}, while the electron-withdrawing F-substituents leads to a faster k_{ex}^{298}.[48] This deviation highlights the importance of steric effects, as the presence of bulky groups like methyl near the water coordination site can hinder exchange and significantly slow down k_{ex}^{298}. Conversely, some ligand frameworks, such as hydroxypyridonate-based or AAZTA-type ligands developed by Aime and coworkers, support both fast k_{ex}^{298} and thermodynamic stability of the complexes, requisite characteristics for high relaxivity and efficient CA.[49]

Theoretical studies supported by experimental data have significantly advanced the understanding water exchange kinetics in bis-hydrated lanthanide complexes. A question that remains open for some time is whether the two coordinated water molecules in bis-hydrated

complexes exchange with identical or different rates. Computational investigations have demonstrated that the two water molecules occupy different coordination environments, leading to unequal Gd-O(w) bond lengths and distinct k_{ex}^{298}. Typically, the water molecule occupying the sterically hindered position is more labile and exchanges more rapidly. DFT investigation, including relativistic effects, has shown that inner-sphere water molecules can differ not only in their geometrical parameters but also in electronic properties with considerably different ^{17}O hyperfine coupling constants (HFCCs) values.[50] Recent studies have revealed that in [Ln(DO3A)(H_2O)$_2$] and [Ln(AAZTA)(H_2O)]$^-$ complexes, the two coordinated water molecules exhibit markedly different k_{ex}^{298}. They observed a decrease in inner-sphere water molecules from $q = 2$ to 1 in the later lanthanides, which indicates that the faster exchanging water occupies a sterically hindered capping position.[51,52] Ligand modification, such as the introduction of amide or glycine substituents, was expected to slow down the exchange due to the increased positive charge of the complex.[53] However, studies have revealed that an increase in positive charge does not necessarily hinder water exchange. The observed k_{ex}^{298} value remains high, indicating that steric and electronic effects, rather than the overall charge, play a more significant role. Leone et al. highlight the strength of the H-bond around the coordinated water molecule. The study shows that fast k_{ex}^{298} is associated with weaker H-bonding, whereas stronger H-bonding is associated with slower k_{ex}^{298}. TS analyses show that H-bonds between ligand substituents and the leaving water molecule can stabilize the eight coordinated TS, lowering the activation energy barrier and increasing the k_{ex}^{298}. This is typical of a dissociative mechanism with a positive value of activation entropy.[54] This highlights a promising area of research as coordination chemists now have a strategic framework for ligand design to tailor complexes with either slow or fast exchange kinetics.

An increase in the hydration number (q) is generally expected to enhance the inner-sphere relaxivity. However, this is often offset by a reduction of thermodynamic stability or kinetic inertness. Therefore, it is crucial to determine the hydration state of the complex in solution.[55,56] Theoretical calculations can offer valuable insights into the hydration number of these metal-based MRI CAs.[51]

1.1.4. Stability of MRI Contrast Agents (CAs)

About 450 million gadolinium-based contrast agent (GBCA) applications have been determined since their introduction, with usage increasing annually.[57] The development of safer CAs has focused on several key factors- enhancing the relaxivity of the CAs, improving

resistance to metal ion release, or exploring Gd^{3+}-free alternatives.[58–62,8] The stability of the CA is crucial, as it ensures that MRI CAs remain intact in the body long enough to achieve the desired relaxation phenomena without releasing potentially toxic ions into the body.[63,64] The release of Gd^{3+} ions from GBCAs is controlled by thermodynamic stability and kinetic inertness, which can be optimized through ligand design.[22,65,66] Thermodynamic stability, characterized by the Gibbs free energy of complexation, is often expressed as the stability constant $logK$ (also noted as $logK_{GdL}$, $logK_{therm}$, or $logK_{St}$).[65,67,68] To understand the hypothesis behind various ligand design strategies, it is useful to examine the solution behavior of Ln^{3+} complexes. High thermodynamic stability is vital for all metal-based MRI CAs, as the release of these free Gd^{3+} ions can lead to irreversible binding to skeletal tissue and may interfere with Ca^{2+} binding sites. During the 1990s and 2000s, it was very common to administer repeated doses of GBCAs within short intervals or even double or triple doses for angiography or perfusion-weighted scans.[69–71] At that time, these approved CAs (Figure 1.6) were regarded as safe without any adverse effects. In 2006, a strong association was established between Gd^{3+} CAs and a severe condition known as nephrogenic systemic fibrosis (NSF).[72,73] Although the exact mechanism underlying NSF remains unclear, Gd^{3+} exposure appears to be a strong contributing factor. Due to this adverse effect, regulatory bodies like the Food and Drug Administration (FDA) imposed strict guidelines on using GBCAs. In 2010, the FDA withdrew some approved agents- $[Gd(DTPA)(H_2O)]^-$, $[Gd(DTPA\text{-}BMA)(H_2O)]^-$, and $[Gd(DTPA\text{-}BMEA)(H_2O)]^-$ for use in patients with a glomerular filtration rate (GFR) below 30 mL/min/1.73 m² and recommended that GFR should be evaluated before administration.[15,74] The FDA further advised against using GBCA in patients with impaired renal function.[75] Thus, ensuring the safety of MRI CAs is the driving research area in chemistry to design and development of next-generation MRI CAs.

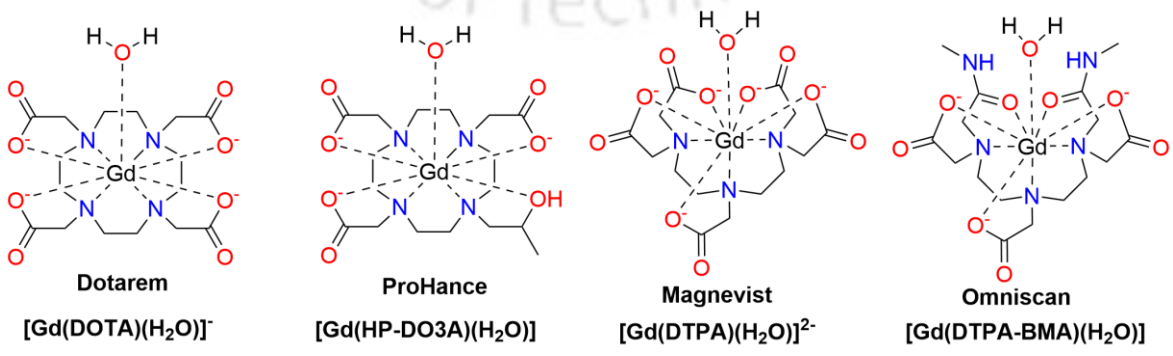

Figure 1.6. Clinically approved (or commercially available) MRI CAs.[15,62]

To increase the stability of lanthanide complexes, it requires the special arrangement of donor atoms in the ligand to optimally coordinate the Ln^{3+} ion. Garda et al. in 2020 reported that changes in ligand configuration, specifically cis (1,4-H3DO2APA) or trans (1,7- H3DO2APA) arrangement of pendant arms on a cyclen unit, can result in distinct stability trends across the Ln^{3+} series.[76] This demonstrates the critical role of ligand stereochemistry in influencing both the thermodynamic stability and dissociation kinetics of Ln^{3+} complexes. Moreover, the design of an efficient ligand requires a proper knowledge of the electronic and molecular structure of the complex. Quantum mechanical calculations and molecular dynamics simulations are useful for determining the structure of metal complexes and evaluating their stability in aqueous solvents. Most studies use DFT to determine the Gibbs free energy of formation to analyze the coordination properties of chelating ligands. In 2007, Pollet et al. presented an *ab initio* simulation study of a Gd^{3+} based CAs- [Gd(HP-DO3A)] in an aqueous solution, aiming to understand the molecular-level behavior of Gd^{3+}-based CAs, which are widely used in MRI to enhance contrast.[77] The *ab initio* approach, grounded in first-principles calculations, provides insight into these agents' structural, electronic, and dynamic properties in solution. Moreover, in another study, the coordination properties of EDTA-ligand with Ln^{3+}-series elements were evaluated by employing *ab initio* molecular dynamics simulations, emphasizing the solvent phase dynamics and stability of these complexes in aqueous solutions.[78] Kuta et al. in 2010 provided comprehensive trends in electronic structure and thermodynamic properties of lanthanides hydrates $[Ln(H_2O)_{8,9}]^{3+}$ and $[Ln(H_2O)_{8,9}]^{3+}$. $(H_2O)_{12,14,}$ (Ln = La-Lu) complexes. It assesses how the solvation structure and dynamic changes across the Ln^{3+}- series, providing insights into the coordination environment.[79] In 2014, Regueiro-Figueroa et al. developed a computational approach for rationally analyzing the stability trends of lanthanide complexes across the 4f period.[80] They carried out a DFT study to explore the underlying factors contributing to the varying stability trends of Ln^{3+} complexes in aqueous solutions.

All clinically approved MRI CAs are based on Gd^{3+} complexes due to the high relaxation efficiency of this paramagnetic ion, which enables strong image contrast. Because of the elevated toxicity of Gd^{3+}, Mn^{2+} ions are an obvious candidate to replace Gd^{3+}.

1.2. Transition Metal Complexes: The Role of Mn^{2+} ion

In recent years, non-lanthanide metals, particularly Mn^{2+}-based MRI CAs, have received growing attention and research interest. Notably, Mn^{2+} was the first paramagnetic ion to be considered for enhancing MRI contrast by Paul C. Lauterbur, the 'Father of MRI' himself, in 1978.[81] Lauterbur used $MnCl_2$ as a CA to differentiate between healthy and diseased tissue in

dogs. Like Gd^{3+}, Mn^{2+} has a high spin d^5 configuration (S=5/2) and a long electronic relaxation time. It typically forms 6 or 7 coordinated complexes in aqueous solution. While Mn^{2+} is a natural cellular component and less toxic than Gd^{3+} ion, due to its size similarity with Ca^{2+}, it easily crosses the blood-brain barrier, potentially causing Manganism (a disease similar to Parkinson's).[82] Although it exhibits high r_1 relaxivity (6.76 m M^{-1} S^{-1}), Mn^{2+} still requires chelation for safety. Only Mn^{2+}-based CA Teslascan or Mangafodipir, i.e., [Mn(DPDA)] as depicted in Figure 1.7, a liver-specific CA, is approved in part of North America, but not in Canada.[83]

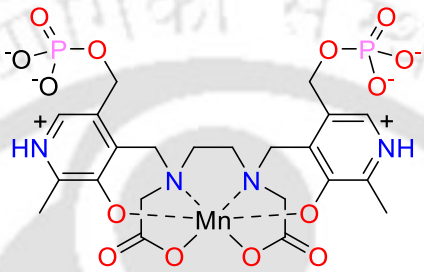

Figure 1.7. Molecular structure of Teslascan, a Mn^{2+}-based MRI contrast agent.[83]

In recent years, there has been a significant rise in Mn^{2+}-based MRI CAs, in parallel with studies discussing safety concerns of Gd^{3+}-based agents. Similar to Gd^{3+}, the development of a suitable low molecular weight ligand center for Mn^{2+} ion balance between two factors: ensure high thermodynamic stability and kinetic inertness to restrict the release of free Mn^{2+} ions, while also ensuring at least one water molecule remains coordinated directly to the metal center to enhance relaxivity.

1.2.1. Magnetic Properties of Mn^{2+} Complexes

Another key parameter influencing the relaxivity of MRI CAs is electronic relaxation, which plays a significant role in relaxivity at a low magnetic field (<~2 MHz). Although such low-field strengths are not commonly employed in clinical imaging, there is a growing interest in low-field imaging as a potential alternative to high-field MRI. This includes variable-field techniques (fast-field cycling MRI) and Mn^{2+} complexes for generating image contrast.[84] With the growing interest in low- and ultralow-field MRI in recent years, optimizing the relaxivities of CAs at low fields has become significantly important.[85] According to McLachlan's theory,[86] electron spin relaxation arises from the transient distortion of the metal coordination sphere, which influences the zero-field splitting (ZFS) energy. In transition metal (TM) ions with spin states, $S \geq 1$, electronic spin relaxation is primarily driven by thermal modulation of the ZFS tensors.[87] The ZFS of the electronic ground state in paramagnetic ions serves as a

sensitive probe of changes in both the electronic and molecular structure. In general, ZFS plays a significant role in high-spin Gd^{3+}/Mn^{2+}, where it has a profound effect on the paramagnetic relaxation enhancement and thereby affects the spin relaxation parameters.[88,89] For both Gd^{3+} and Mn^{2+} complexes, a symmetrical coordination environment and ligand rigidity are typically associated with slower electronic relaxation. Consequently, the accurate calculation of the ZFS is essential for understanding the magnetic behaviour of such complexes, especially in the field of molecular magnetism. Magnetic materials are of great interest due to their diverse applications in biomedicine, imaging, electronics, spintronics, and data storage.[90] Recent advances in material design and technology have been significantly evidenced by the tremendous increase in hard drive capacity from kilobytes to terabytes in recent decades. Scientists are focusing on controlling magnetic properties at the molecular level to design nanomaterials for next-generation devices. These materials exhibit unique field-induced transitions and switchable conductivity, influenced by changes in magnetic field, temperature, spin state, or magnetic ordering.[91,92]

Molecule-based magnetic materials are currently attracting significant interest due to their ability to reveal fundamental magnetic phenomena and their potential use in magnetic devices. However, major progress was obtained in the 1990s with the discovery of $Mn_{12}O_{12}$, the first molecule-based magnetic material to exhibit spontaneous magnetization.[93] Single-molecule magnets (SMMs) are discrete coordination complexes that can be magnetized by an external magnetic field and exhibit slow relaxation of magnetization below a certain temperature (the blocking temperature, TB). For a molecule to function as an SMM, it must possess a bistable electronic ground state, i.e., the lowest energy sublevel of either M_J (projection of total angular momentum) or M_S (projection of total spin angular momentum) must form a doublet, with the two orientations separated by an effective energy barrier (U_{eff}) due to magnetic anisotropy. For TM complexes, the effective energy barrier U_{eff} governing the magnetization reversal is given by Eqs. 1.3 or 1.4

$$U_{eff} = |D|S^2 \text{ ; for integer spin} \quad (1.3)$$

$$U_{eff} = |D|(S^2 - 1/4) \text{ ; for non-integer} \quad (1.4)$$

As the energy barrier (U_{eff}) shown in Figure 1.8 in TM-SMMs is determined by Eqs. 1.3 or 1.4, initial strategies focused to maximize the total spin (S) by assembling complexes with multiple metal centers. However, it was evident that optimizing the axial ZFS parameter (D) is

equally important. This was highlighted by the discovery of a complex with 19 manganese ions, which, despite its high spin, exhibited a very small effective energy barrier (U_{eff}), owing to its high symmetry.[94]

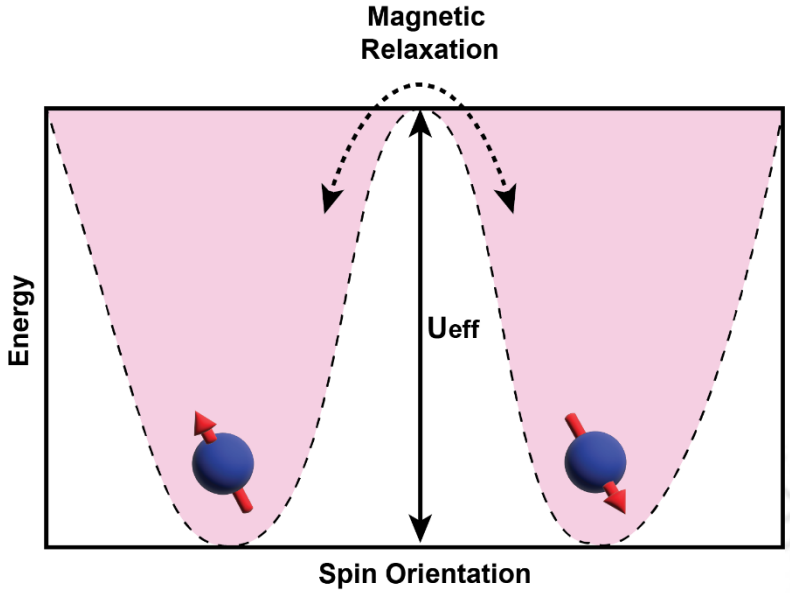

Figure 1.8. Illustrating an SMM energy barrier, where the spin transition between the $\pm M_S$ or $\pm M_J$ states require overcoming U_{eff}.

The advancements in the field have led to the development of SMMS, single-chain magnets (SCMs), and, more recently, single-ion magnets (SIMs). The discovery of the first SMM, $Mn_{12}OAc$, in 1993 changed the perspective of how information can be stored.[93] Since then, the field of SMMs or SIMs has evolved significantly, exploring various pathways towards designing high-performance magnetic systems. This ongoing journey has been crucial to deeply understanding the quantum dynamics that govern the behavior of these molecular magnets. Magnetic anisotropy in SMMS primarily arises from ZFS, which lifts the degeneracy of magnetic sublevels (M_S) in axially symmetric systems with S >1/2, due to spin-orbit coupling (SOC). ZFS is characterized by two components: axial (D) and rhombic (E) parameters. Monometallic SMMS offers promising platforms for investigating ZFS effects, where both the axial anisotropy (D) and spin ground state (S) determine their magnetic behavior owing to their potential applications in data storage, quantum computing, and molecular spintronics. Although Mn^{2+} complexes typically have an isotropic spin ground state, which limits their ability to exhibit slow magnetization relaxation, high-spin Mn^{2+} mononuclear complexes provide a unique opportunity to study how coordination environments influence magnetic anisotropy. This can also help in establishing some magneto-structural correlation.

In particular, the ZFS of seven coordinated Mn^{2+} complexes remains unexplored; only a few studies have been reported. Therefore, a more comprehensive analysis of their ZFS is essential to better understand their coordination geometries and magnetic properties.

The molecular magnetism of paramagnetic TM complexes has become a burgeoning field of interest.[95] SMMs bridge classical magnetic behavior at the macroscale to the quantum properties at the nanoscale, characterized by their ability to retain magnetization after the removal of the external magnetic field. However, high-spin Mn^{2+} complexes are generally considered unsuitable candidates for SMMs due to the lack of orbital angular momentum in their ^6S ground state. This leads to minimal spin-orbit coupling and, consequently, very weak magnetic anisotropy. As a result, the magnetic characterization of Mn^{2+}, particularly the magnetic anisotropy and magnetization blocking behaviour across various ligand environments, has been largely overlooked, unlike in Mn^{3+} and Mn^{4+} complexes, where the magnetic anisotropy has been more widely explored.[96] Thus far, few studies have explored the magnetic behavior of Mn^{2+} complexes. Most of the studies in this area have focused primarily on magnetic anisotropy arising from the SOC of the metal electrons.

In 2007, Duboc et al. carried out a DFT study on high-spin six-coordinated Mn^{2+} complexes $[Mn(tpa)(X_2)]$ (tpa=tris-2-picolylamine; X=I, Br, Cl), revealing that both the nature of the halide and the cis/trans configuration significantly influence the magnitude of the axial ZFS parameter (D).[97] Sabyasachi Roy Chowdhury et al. reported that magnetic anisotropy can be enhanced by using heavier halogens, based on *ab initio* calculations of a series of MnX_2 (X = Cl, Br, I) complexes.[98] These bi-coordinated complexes showed increasing ligand-induced spin-orbit splitting, while the contribution from the Mn^{2+} center remained negligible. Similarly, Hey et al. reported the tuning of magnetic anisotropy in high-spin trigonal bipyramidal Mn^{2+} monometallic complexes using various magnetostructural correlations.[99] The study focused on a series of mononuclear Mn^{2+} complexes and proposed a strategy to enhance the D-parameter using magnetostructural correlations developed from *ab initio* calculations. Quantum chemical calculations offer a cost-effective alternative to experimental hits and trials. High-level *ab initio* calculations have been extensively used for the interpretation and design of SMMS, especially through the development of a pseudospin Hamiltonian, which provides key parameters such as crystal field splitting and g-factors. These findings indicate that the D-parameter for this class of complexes could potentially increase by an order of magnitude, which would surpass the current record for high-spin mononuclear Mn^{2+} complexes.

1.3. Motivation

The study of Ln^{3+} and TM complexes is of significant importance due to their diverse applications in various fields such as medical imaging, catalysis, and materials science. This thesis aims to deepen the understanding of hydration behavior, relaxivity parameters, and magnetic properties of such complexes by exploring the influence of different ligand environments through quantum mechanical calculations and molecular dynamics simulations. One of the challenges associated with modeling these heavy elements is that comprehensive theoretical investigations remain limited- a gap this work aims to address. The motivation of this thesis lies in the necessity to improve our understanding of the aqueous stability, relaxivity parameters (including hydration number, water exchange kinetics, and electronic relaxation), and coordination behavior of Ln^{3+} complexes across various ligand environments. The k_{ex}^{298} in these molecules influence the relaxation time in MRI, directly affecting image contrast and resolution. On the other hand, the thermodynamic stability of these complexes in aqueous solution determines the safety and biocompatibility of these complexes in a physiological environment. Notably, properties such as metal-water distances, hydration number, and the coordination number of hydration shells remain central to theoretical and experimental investigations. Complexes featuring two or three inner-sphere water molecules can potentially exhibit higher relaxivity compared to those mono-aquated systems. Despite their significance, bis- and tris-aquated complexes remain unexplored due to the experimental challenges. This study aims to bridge that gap by providing a detailed electronic and geometric structure of such systems along with their associated relaxivity parameters. Additionally, a comprehensive computational investigation of commercially available DOTA and its chiral derivatives with Ln^{3+} ions has been carried out to assess their aqueous stability and relaxivity parameters. Moreover, this theoretical study offers valuable insights into the nature of the bonding in these systems. By investigating these properties computationally, we aim to provide insights that can lead to the rational design of more efficient and stable Ln^{3+}-based MRI CAs.

In addition, as an alternative to Gd^{3+} due to its toxicity, Mn^{2+} complexes, particularly those in a high spin state, are of interest due to their potential for applications in spintronics, quantum computing, and as CAs in MRI. Understanding the coordination geometry and hydration properties of these Mn^{2+} complexes is of utmost importance and relevance to environmental problems and medical applications. Moreover, very few studies have reported on the magnetic properties of Mn^{2+} based complexes. To date, most studies have primarily focused on magnetic anisotropy arising from the SOC of the metal electrons, which leaves other contributing factors

remain unexplored. On the other hand, the axial ZFS parameter D is a critical factor that influences the magnetic properties of these complexes. Modulating the ZFS parameter through ligand design can enhance the performance of Mn^{2+} complexes in various applications. By computationally exploring how different ligands affect the ZFS, we can identify strategies to tailor the magnetic properties of Mn^{2+} complexes for specific applications. Furthermore, the rational ligand design of hybrid molecule-based magnetic materials through ligand functionalization remains a central focus in the field of molecular materials and magnetism. Designing ligands that can effectively modulate the ZFS parameters in high-spin Mn^{2+} complexes involves understanding the interplay between electronic structure, coordination environment, and magnetic anisotropy. This aspect of the thesis aims to develop guidelines for ligand design that can be used to develop Mn^{2+} complexes with desired magnetic characteristics. The influence of halogens (Cl, Br, and I), along with the other soft donor atoms (S and Se), on the magnetic anisotropy of these complexes has been systematically explored via ligand modifications. Halogenated high spin Mn^{2+} complexes, largely unexplored until now, were investigated to understand how the nature and position of the halogen substituent influence the electronic structure and magnetic properties. We hope our study will help experimentalists with the strategy to design new ligands for their applications in medicinal chemistry and quantum computing.

1.4. Overview of Thesis

In this thesis, we studied the stability, relaxivity parameters, and magnetic characterization of Ln^{3+} and Mn^{2+} complexes via a combination of quantum chemical methods and molecular dynamics simulations. Chapter 2 presents an overview of the theoretical and computational methodologies used in our study. Chapter 3 provides a comprehensive analysis of Ln^{3+} complexes containing multiple inner-sphere water molecules, a key aspect in the design of high-relaxivity MRI contrast agents. Building upon the insights into Chapter 3, Chapter 4 explores the aqueous stability, coordination geometry, and electronic environments of commercially available $[Ln(DOTA)]^-$ and its chiral derivatives. Chapters 5 and 6 delve into the ligand design and impact of different substituents (electron-withdrawing and electron-donating) on the electronic relaxation of MRI CAs, a crucial parameter to modulate. The aqueous phase dynamics and magnetic properties of mono- and bis-aquated complexes of Mn^{2+} are also examined. The final chapter summarizes the major findings and conclusions of the thesis.

1.5. References

[1] R. W. Brown, Y. N. Cheng, E. M. Haacke, M. R. Thompson and R. Venkatesan, *Magnetic Resonance Imaging: Physical Principles and Sequence Design*, Wiley, 1st edn., 2014.

[2] V. P. B. Grover, J. M. Tognarelli, M. M. E. Crossey, I. J. Cox, S. D. Taylor-Robinson and M. J. W. McPhail, *J. Clin. Exp. Hepatol.*, 2015, **5**, 246-255.

[3] M. M. Rehani and D. Nacouzi, *Phys. Med.*, 2020, **79**, 80-86.

[4] N. J. Pelc, *Ann. Biomed. Eng.*, 2014, **42**, 260-268.

[5] J. Rong, A. Haider, T. E. Jeppesen, L. Josephson and S. H. Liang, *Nat. Commun.*, 2023, **14**, 3257-3279.

[6] R. Massari and G. S. P. Mok, *Front. Med.*, 2023, **10**, 1349877-1349879.

[7] E. Lazarus, C. DeBenedectis, D. North, P. K. Spencer and W. W. Mayo-Smith, *Radiology*, 2009, **251**, 517-524.

[8] P. Caravan, *Chem. Soc. Rev.*, 2006, **35**, 512-523.

[9] D. Weishaupt, V. D. Köchli and B. Marincek, *How does MRI work?*, Springer Berlin Heidelberg, Berlin, Heidelberg, 2003.

[10] R.-J. M. Van Geuns, P. A. Wielopolski, H. G. De Bruin, B. J. Rensing, P. M. A. Van Ooijen, M. Hulshoff, M. Oudkerk and P. J. De Feyter, *Prog. Cardiovasc. Dis.*, 1999, **42**, 149-156.

[11] J. K. M. Sanders and B. K. Hunter, *Modern NMR spectroscopy: a guide for chemists*, Oxford Univ. Press, Oxford, 2 ed., repr. (with corr.)., 2007.

[12] G.-P. Yan, L. Robinson and P. Hogg, *Radiography*, 2007, **13**, e5-e19.

[13] V. C. Pierre, M. J. Allen and P. Caravan, *JBIC J. Biol. Inorg. Chem.*, 2014, **19**, 127-131.

[14] V. C. Pierre and M. J. Allen, Eds., *Contrast Agents for MRI: Experimental Methods*, Royal Society of Chemistry, Cambridge, 2017.

[15] J. Wahsner, E. M. Gale, A. Rodríguez-Rodríguez and P. Caravan, *Chem. Rev.*, 2019, **119**, 957-1057.

[16] Z. Zhou and Z. Lu, *WIREs Nanomedicine Nanobiotechnology*, 2013, **5**, 1-18.

[17] P. Hermann, J. Kotek, V. Kubíček and I. Lukeš, *Dalton Trans.*, 2008, 3027-3047.

[18] G. J. Strijkers, W. J. M. Mulder, G. A. F. Van Tilborg and K. Nicolay, *Anticancer Agents Med. Chem.*, 2007, **7**, 291-305.

[19] P. Caravan, J. J. Ellison, T. J. McMurry and R. B. Lauffer, *Chem. Rev.*, 1999, **99**, 2293-2352.

[20] *Proc. R. Soc. Lond. Ser. Math. Phys. Sci.*, 1964, **280**, 271-288.

[21] J. Wang, T. Salzillo, Y. Jiang, Y. Mackeyev, C. David Fuller, C. Chung, S. Choi, N. Hughes, Y. Ding, J. Yang, S. Vedam and S. Krishnan, *Radiother. Oncol.*, 2021, **161**, 55-64.

[22] T. J. Clough, L. Jiang, K.-L. Wong and N. J. Long, *Nat. Commun.*, 2019, **10**, 1420-1433.

[23] J. Vymazal and A. M. Rulseh, *Insights Imaging*, 2024, **15**, 179-191.

[24] P. Caravan, D. Esteban-Gómez, A. Rodríguez-Rodríguez and C. Platas-Iglesias, *Dalton Trans.*, 2019, **48**, 11161-11180.

[25] W. P. Cacheris, S. K. Nickle and A. D. Sherry, *Inorg. Chem.*, 1987, **26**, 958-960.

[26] A. D. Sherry and Y. Wu, *Curr. Opin. Chem. Biol.*, 2013, **17**, 167-174.

[27] D. M. J. Doble, M. Botta, J. Wang, S. Aime, A. Barge and K. N. Raymond, *J. Am. Chem. Soc.*, 2001, **123**, 10758-10759.

[28] S. Laurent, F. Botteman, L. Vander Elst and R. N. Muller, *Magn. Reson. Mater. Phys. Biol. Med.*, 2004, **16**, 235-245.

[29] M. Woods, M. Botta, S. Avedano, J. Wang and A. D. Sherry, *Dalton Trans.*, 2005, 3829-3837.

[30] D. H. Powell and A. E. Merbach, *Magn. Reson. Chem.*, 1994, **32**, 739-745.

[31] C. Cossy, L. Helm and A. E. Merbach, *Inorg. Chem.*, 1989, **28**, 2699-2703.

[32] B. Siriwardena-Mahanama and M. Allen, *Molecules*, 2013, **18**, 9352-9381.

[33] R. Pujales-Paradela, F. Carniato, D. Esteban-Gómez, M. Botta and C. Platas-Iglesias, *Dalton Trans.*, 2019, **48**, 3962-3972.

[34] É. Tóth, D. Pubanz, S. Vauthey, L. Helm and A. E. Merbach, *Chem. – Eur. J.*, 1996, **2**, 1607-1615.

[35] S. Laurent, F. Botteman, L. Vander Elst and R. N. Muller, *Magn. Reson. Mater. Phys. Biol. Med.*, 2004, **16**, 235-245.

[36] M. Woods, K. M. Payne, E. J. Valente, B. E. Kucera and V. G. Young, *Chem. – Eur. J.*, 2019, **25**, 9997-10005.

[37] R. Ruloff, É. Tóth, R. Scopelliti, R. Tripier, H. Handel and A. E. Merbach, *Chem Commun*, 2002, 2630-2631.

[38] S. Laus, R. Ruloff, É. Tóth and A. E. Merbach, *Chem. – Eur. J.*, 2003, **9**, 3555-3566.

[39] Y.-M. Wang, C.-R. Li, Y.-C. Huang, M.-H. Ou and G.-C. Liu, *Inorg. Chem.*, 2005, **44**, 382-392.

[40] Z. Jászberényi, A. Sour, É. Tóth, M. Benmelouka and A. E. Merbach, *Dalton Trans.*, 2005, 2713-2719.

[41] A. Nonat, M. Giraud, C. Gateau, P. H. Fries, L. Helm and M. Mazzanti, *Dalton Trans.*, 2009, 8033-8046.

[42] M. F. Ferreira, A. F. Martins, J. A. Martins, P. M. Ferreira, É. Tóth and C. F. G. C. Geraldes, *Chem. Commun.*, 2009, 6475-6477.

[43] S. Aime, M. Botta, M. Fasano and E. Terreno, *Chem Soc Rev*, 1998, **27**, 19-29.

[44] E. M. Gale, N. Kenton and P. Caravan, *Chem. Commun.*, 2013, **49**, 8060-8062.

[45] E. Boros and P. Caravan, *Inorg. Chem.*, 2015, **54**, 2403-2410.

[46] Z. Baranyai, L. Tei, G. B. Giovenzana, F. K. Kálmán and M. Botta, *Inorg. Chem.*, 2012, **51**, 2597-2607.

[47] S. J. Ratnakar, M. Woods, A. J. M. Lubag, Z. Kovács and A. D. Sherry, *J. Am. Chem. Soc.*, 2008, **130**, 6-7.

[48] S. Viswanathan, S. J. Ratnakar, K. N. Green, Z. Kovacs, L. M. De León-Rodríguez and A. D. Sherry, *Angew. Chem. Int. Ed.*, 2009, **48**, 9330-9333.

[49] S. Aime, L. Calabi, C. Cavallotti, E. Gianolio, G. B. Giovenzana, P. Losi, A. Maiocchi, G. Palmisano and M. Sisti, *Inorg. Chem.*, 2004, **43**, 7588-7590.

[50] D. Esteban-Gómez, A. De Blas, T. Rodríguez-Blas, L. Helm and C. Platas-Iglesias, *ChemPhysChem*, 2012, **13**, 3640-3650.

[51] M. Regueiro-Figueroa and C. Platas-Iglesias, *J. Phys. Chem. A*, 2015, **119**, 6436-6445.

[52] D. Lalli, F. Carniato, L. Tei, C. Platas-Iglesias and M. Botta, *Inorg. Chem.*, 2022, **61**, 496-506.

[53] L. Tei, L. Leone, D. Lalli, M. Botta and C. Platas-Iglesias, *Eur. J. Inorg. Chem.*, 2024, **27**, e202300730 (1-11).

[54] L. Leone, D. Esteban-Gómez, C. Platas-Iglesias, M. Milanesio and L. Tei, *Chem. Commun.*, 2019, **55**, 513-516.

[55] A. M. Raitsimring, A. V. Astashkin, D. Baute, D. Goldfarb, O. G. Poluektov, M. P. Lowe, S. G. Zech and P. Caravan, *ChemPhysChem*, 2006, **7**, 1590-1597.

[56] A. Nucera, C. Platas-Iglesias, F. Carniato and M. Botta, *Dalton Trans.*, 2023, **52**, 17229-17241.

[57] R. J. McDonald, D. Levine, J. Weinreb, E. Kanal, M. S. Davenport, J. H. Ellis, P. M. Jacobs, R. E. Lenkinski, K. R. Maravilla, M. R. Prince, H. A. Rowley, M. F. Tweedle and H. Y. Kressel, *Radiology*, 2018, **289**, 517-534.

[58] M. Botta, F. Carniato, D. Esteban-Gómez, C. Platas-Iglesias and L. Tei, *Future Med. Chem.*, 2019, **11**, 1461-1483.

[59] B. Drahoš, I. Lukeš and É. Tóth, *Eur. J. Inorg. Chem.*, 2012, **2012**, 1975-1986.

[60] C. Henoumont, M. Devreux and S. Laurent, *Molecules*, 2023, **28**, 7275-7299.

[61] V. C. Pierre, M. J. Allen and P. Caravan, *JBIC J. Biol. Inorg. Chem.*, 2014, **19**, 127-131.

[62] A. Scarciglia, C. Papi, C. Romiti, A. Leone, E. Di Gregorio and G. Ferrauto, *Glob. Chall.*, 2025, **9**, 2400269-2400287.

[63] H. Schmitt-Willich, *Br. J. Radiol.*, 2007, **80**, 581-582.

[64] M. Port, J.-M. Idée, C. Medina, C. Robic, M. Sabatou and C. Corot, *BioMetals*, 2008, **21**, 469-490.

[65] Z. Garda, V. Nagy, A. Rodríguez-Rodríguez, R. Pujales-Paradela, V. Patinec, G. Angelovski, É. Tóth, F. K. Kálmán, D. Esteban-Gómez, R. Tripier, C. Platas-Iglesias and G. Tircsó, *Inorg. Chem.*, 2020, **59**, 8184-8195.

[66] W. P. Cacheris, S. C. Quay and S. M. Rocklage, *Magn. Reson. Imaging*, 1990, **8**, 467-481.

[67] M. Regueiro-Figueroa, D. Esteban-Gómez, A. de Blas, T. Rodríguez-Blas and C. Platas-Iglesias, *Chem. – Eur. J.*, 2014, **20**, 3974-3981.

[68] O. Porcar-Tost, A. Pallier, D. Esteban-Gómez, O. Illa, C. Platas-Iglesias, É. Tóth and R. M. Ortuño, *Dalton Trans.*, 2021, **50**, 1076-1085.

[69] A. F. Costa, C. B. Van Der Pol, P. J. Maralani, M. D. F. McInnes, J. R. Shewchuk, R. Verma, C. Hurrell and N. Schieda, *Can. Assoc. Radiol. J.*, 2018, **69**, 373-382.

[70] B. Tombach, T. Benner, P. Reimer, G. Schuierer, E.-M. Fallenberg, V. Geens, T. Wels and A. G. Sorensen, *Radiology*, 2003, **226**, 880-888.

[71] M. Filippi, *Brain*, 1998, **121**, 2011-2020.

[72] P. Marckmann, L. Skov, K. Rossen, A. Dupont, M. B. Damholt, J. G. Heaf and H. S. Thomsen, *J. Am. Soc. Nephrol.*, 2006, **17**, 2359-2362.

[73] S. K. Morcos, *Br. J. Radiol.*, 2007, **80**, 73-76.

[74] L. Yang, I. Krefting, A. Gorovets, L. Marzella, J. Kaiser, R. Boucher and D. Rieves, *Radiology*, 2012, **265**, 248-253.

[75] V. M. Runge, *Invest. Radiol.*, 2018, **53**, 571-578.

[76] Z. Garda, V. Nagy, A. Rodríguez-Rodríguez, R. Pujales-Paradela, V. Patinec, G. Angelovski, É. Tóth, F. K. Kálmán, D. Esteban-Gómez, R. Tripier, C. Platas-Iglesias and G. Tircsó, *Inorg. Chem.*, 2020, **59**, 8184-8195.

[77] R. Pollet and D. Marx, *J. Chem. Phys.*, 2007, **126**, 181102-181105.

[78] D. S. Kaliakin, J. A. Sobrinho, J. H. S. K. Monteiro, A. De Bettencourt-Dias and D. C. Cantu, *Phys. Chem. Chem. Phys.*, 2021, **23**, 4287-4299.

[79] J. Kuta and A. E. Clark, *Inorg. Chem.*, 2010, **49**, 7808-7817.

[80] M. Regueiro-Figueroa, D. Esteban-Gómez, A. de Blas, T. Rodríguez-Blas and C. Platas-Iglesias, *Chem. – Eur. J.*, 2014, **20**, 3974-3981.

[81] Lauterber,P.; Mendonca, M; Rudin, A. Frontiers of Biological Energetics, Academic Press, New York, 1978.

[82] J. Crossgrove and R. Yokel, *NeuroToxicology*, 2005, **26**, 297-307.

[83] P. K. Pal, A. Samii and D. B. Calne, *Neurotoxicology*, 1999, **20**, 227-238.

[84] D. J. Lurie, S. Aime, S. Baroni, N. A. Booth, L. M. Broche, C.-H. Choi, G. R. Davies, S. Ismail, D. Ó hÓgáin and K. J. Pine, *Comptes Rendus Phys.*, 2010, **11**, 136-148.

[85] A. M. Coffey, M. L. Truong and E. Y. Chekmenev, *J. Magn. Reson.*, 2013, **237**, 169-174.

[86] *Proc. R. Soc. Lond. Ser. Math. Phys. Sci.*, 1964, **280**, 271-288.

[87] S. Zein, C. Duboc, W. Lubitz and F. Neese, *Inorg. Chem.*, 2008, **47**, 134-142.

[88] S. Khan, A. Kubica-Misztal, D. Kruk, J. Kowalewski and M. Odelius, *J. Chem. Phys.*, 2015, **142**, 034304-034315.

[89] C. Duboc, M.-N. Collomb and F. Neese, *Appl. Magn. Reson.*, 2010, **37**, 229-245.

[90] N. A. Spaldin, *Magnetic materials: fundamentals and applications*, Cambridge university press, Cambridge (GB), 2nd ed., 2011.

[91] S. Nain, A. Mukhopadhyaya and Md. E. Ali, *Inorg. Chem.*, 2024, **63**, 7401–7411.

[92] E. Coronado, *Nat. Rev. Mater.*, 2019, **5**, 87–104.

[93] T. Lis, *Acta Crystallogr. B*, 1980, **36**, 2042–2046.

[94] A. M. Ako, I. J. Hewitt, V. Mereacre, R. Clérac, W. Wernsdorfer, C. E. Anson and A. K. Powell, *Angew. Chem. Int. Ed.*, 2006, **45**, 4926–4929.

[95] S. C. Coste, B. Vlaisavljevich and D. E. Freedman, *Inorg. Chem.*, 2017, **56**, 8195-8202.

[96] S. Roy Chowdhury, N. Nguyen and B. Vlaisavljevich, *J. Phys. Chem. A*, 2023, **127**, 3072-3081.

[97] C. Duboc, T. Phoeung, S. Zein, J. Pécaut, M.-N. Collomb and F. Neese, *Inorg. Chem.*, 2007, **46**, 4905-4916.

[98] S. R. Chowdhury and S. Mishra, *Phys. Chem. Chem. Phys.*, 2017, **19**, 16914-16922.

[99] M. A. Hay, A. Sarkar, K. E. R. Marriott, C. Wilson, G. Rajaraman and M. Murrie, *Dalton Trans.*, 2019, **48**, 15480-15486.

Chapter 2

Theoretical Background and Methodologies

Computational calculations are used to study the properties that are challenging to determine experimentally. This allows the exploration or examination of compounds that are difficult to synthesize, in which crystallographic data is rarely obtained, including several lanthanide and transition metal-based complexes. However, strong electron correlation, weak crystal field, and non-negligible relativistic effects of heavy metal-based complexes cause the computational investigations to be very challenging. This chapter includes a comprehensive overview of the fundamentals of quantum mechanics and the various theoretical methods employed in the studied projects. It begins by establishing the theoretical foundation for understanding and predicting the properties of chemical systems via electronic structure theory.

2.1. Electronic Structure Theory

One of the foundational principles underlying much of modern science is the time-independent Schrödinger Equation, first formulated in 1926, which describes quantum systems without considering relativistic effects.[1]

$$\hat{\mathrm{H}}\psi(r;R) = E\psi(r;R) \tag{2.1}$$

$\hat{\mathrm{H}}$ defines the Hamiltonian operator of the electron and nuclei of the system, E denotes the energy eigenvalue, and ψ represents the wave function of the system. The wavefunction ψ depends on the positions of electrons (r) and nuclei (R).

Because of the significant mass difference between nuclei and electrons, nuclei are considered as fixed relative to the electrons. This allows the Hamiltonian to be separated into an electronic and a nuclear component, resulting in an electronic wavefunction independent of the nuclear wavefunction. Consequently, nuclei can be treated classically, following Newton's equations of motion, while the electrons are addressed quantum mechanically. This method is known as the Born-Oppenheimer approximation.[1,2]

The general expression of the electronic Hamiltonian ($\hat{\mathrm{H}}_{el}$) of a system comprising n electrons and M nuclei is represented as

$$\hat{\mathrm{H}}_{el} = \hat{T}_e(r) + \hat{V}_{eN}(r,R) + \hat{V}_{ee}(r,r) \tag{2.2}$$

$$\hat{H}_{el} = -\sum_{i=1}^{n} \frac{1}{2}\nabla_i^2 - \sum_{i=1}^{n}\sum_{A=1}^{M} \frac{Z_A}{r_{iA}} + \sum_{i=1}^{n}\sum_{j>1}^{n} \frac{1}{r_{ij}} \quad (2.3)$$

In Eq. 2.3, ∇_i^2 is the Laplacian operator applied to the i^{th} electron. The mass of the nuclei A is denoted as M_A, while its atomic number is denoted as Z_A. The distance between i^{th} and j^{th} electron is denoted by r_{ij}, and the distance between i^{th} electron and nuclei A is represented by r_{iA}. The first terms correspond to the operators associated with the kinetic energy of the electrons. The second term represents the coulomb attraction between the electrons and nuclei, while the third term addresses the repulsive interactions between the electrons.

The electronic wave function, along with the Schrödinger equation involving this wave function, is expressed as follows

$$\psi_{el} = \psi_{el}(r; R) \quad (2.4)$$

$$\hat{H}_{el}\psi_{el} = E_{el}\psi_{el}(r; R) \quad (2.5)$$

In Eq. 2.5, E_{el} represents the electronic eigenvalue corresponding to the eigenfunction ψ_{el}. The total energy of the system, E_{tot}, for fixed nuclear positions, also includes the nucleus-nucleus repulsion energy term and is expressed as

$$E_{tot} = E_{el} + \hat{V}_{NN}(R) \quad (2.6)$$

2.2. Hartree-Fock Method

Hartree-Fock (HF) method[3,4] is a cornerstone of quantum physics and chemistry, providing an approximate solution to the many-electron systems through the independent particle model. Named after Douglas Hartree and Vladimir Fock, who independently developed this approach, the HF method plays a key role in understanding the electronic structure of atoms and molecules.

This approach employed a mean-field theory that models electrons in a many-electron system by accounting for their average electrostatic interactions while ignoring electron-electron correlation effects.

The many-electron wave functions, ψ_{el}, of a molecular system containing n electrons can be shown as the product of individual electron wave functions (ϕ_i), known as the Hartree product, as expressed in Eq. 2.7

$$\psi_{el}(r_1, r_2 \ldots\ldots r_n) = \phi_1(r_1)\phi_2(r_2)\,\phi_3(r_3)\ldots\ldots\phi_n(r_n) \quad (2.7)$$

The Hartree product (Eq. 2.7) fails to account for the antisymmetry principle and violates the Pauli exclusion principle. To address this issue, ψ_{el}, instead represented in the Slater determinant form as

$$\psi_{el}(r_1, r_2 \ldots\ldots r_n) = \frac{1}{\sqrt{n!}} \begin{vmatrix} \phi_1(x_1) & \phi_2(x_1) & \phi_3(x_1) & .. & \phi_n(x_n) \\ \phi_1(x_2) & \phi_2(x_2) & \phi_3(x_2) & .. & \phi_n(x_n) \\ . & . & . & .. & . \\ . & . & . & .. & . \\ \phi_1(x_n) & \phi_2(x_n) & \phi_3(x_n) & .. & \phi_n(x_n) \end{vmatrix} \quad (2.8)$$

The quantity $\frac{1}{\sqrt{n!}}$ is the normalization factor. In the Slater determinant expression of Eq. 2.8, the rows are represented using n electrons, and the columns are denoted with spin orbitals.

The primary goal is to find a set of orbitals $\{\phi_n\}$ that minimizes the electronic energy. This led to the Hartree-Fock equation:

$$f_i\, \phi_i(r) = \varepsilon_i\, \phi_i(r) \quad (2.9)$$

Where f_i denotes the Fock operator and ε_i represents the orbital energy.

$$f_i = -\frac{1}{2} \nabla_i^2 + V_{ext}(r_i) + \sum_{j=1}^{N} [< \phi_j | \hat{J} | \phi_i > - < \phi_j | \hat{K} | \phi_i >] \quad (2.10)$$

In Eq. 2.10, $\hat{J}$ and $\hat{K}$ denotes the coulomb and exchange operators, respectively.

Solving these equations required an iterative process called the Self-Consistent Field (SCF) approach, which is used to determine the spin orbitals $\phi_i(r)$.

2.3. Post-Hartree-Fock Methods

Post-Hartree-Fock (HF) methods[1,5] account for the correlation energy that HF method neglects. This correlation energy is determined by subtracting the limit HF energy (E_{HF}) from the exact non-relativistic energy (E_0).

$$E_{corr} = E_0 - E_{HF} \quad (2.11)$$

This includes dynamic electron correlation, providing a more precise way of accounting for electron repulsions compared to the Hartree–Fock approach, which only accounts for these interactions in an averaged manner. These methods involve Coupled Cluster (CC),[6,7] Møller–Plesset (MP) perturbation theory[8], and multiconfigurational self-consistent field (MCSCF),[9] N-electron valence state perturbation theory (NEVPT2).[10,11] However, CC and MP methods

are not used in this thesis; only the MCSCF and NEVPT2 methods employed in our work are discussed below.

2.4. Multireference Method

Most often, a single Slater determinant is insufficient to precisely determine the exact electronic wave function. Hence, a superposition of Slater determinants provides an improved approximation. The HF approach ignores the correlated motions of the electrons between opposite spins and fails to accurately reproduce the system's exact total energy. These post-Hartree-Fock methods incorporate the correlation energy to correct the HF energy. In the Hartree-Fock approach, the electronic wavefunction can be explained through a single Slater determinant for a given set of molecular orbitals (MOs). In contrast, the post-Hartree-Fock approach allows the formation of multiple additional determinants by substituting the occupied molecular orbitals in the Hartree-Fock Slater determinants with unoccupied molecular orbitals.[1] The resulting excited determinants are classified as single, double, triple, and quadruple excitations based on the number of occupied MOs replaced with unoccupied ones (Figure 2.1).

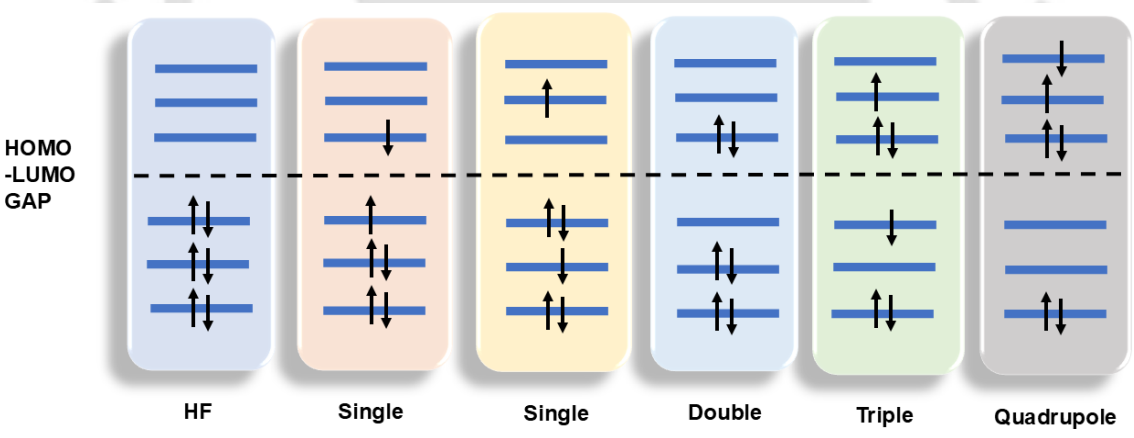

Figure 2.1. Excited Slater determinants and their corresponding Hartree-Fock reference determinants exhibit single, double, triple, and quadruple excitation.

The linear combinations of the ground state (Hartree-Fock), along with all the possible excited determinants, form the full Configuration Interaction (full CI) wavefunction.[12]

$$|\psi\rangle = C_0|\psi\rangle + C_i^a|\psi_i^a\rangle + c_{ij}^{ab}|\psi_{ij}^{ab}\rangle + c_{ijk}^{abc}|\psi_{ijk}^{abc}\rangle + \cdots \quad (2.12)$$

In Eq. 2.12, the first term corresponds to the Hartree-Fock determinant, while the determinants in the second, third, and subsequent terms are generated by incorporating all possible single, double, and higher excitations, respectively. Considering all possible configurations in the

calculations, it is called a full configuration interaction (full CI). This would give the exact solution to the non-relativistic time-independent Schrödinger equation, depending on the accuracy of the employed basis set. Further, due to inefficient scaling, full CI is computationally infeasible for large systems. To overcome this limitation, truncated forms of configuration interaction are employed, such as including only single excitations (CIS), single and double excitations (CISD), or up to triple excitations (CISDT), and so forth. However, for large systems, these methods also become computationally infeasible.

2.4.1. The Complete Active Space Self-Consistent Field Methods

The complete active space self-consistent field (CASSCF)[13] approach is typically employed to study strongly correlated systems. The CASSCF provides a method for executing full CI on a selected set of chemically essential orbitals, significantly reducing computational cost. The orbitals in this approach are categorized as active and inactive, with the active space containing the orbitals that are chemically important for the system under study.

According to Bjorn's rules,[14] the active space typically consists of sets of highest occupied and lowest unoccupied orbitals, along with the conjugated orbitals and bonding/antibonding orbitals associated with a particular bond under study. The determination of the active space is a challenging task. In general, the d-orbitals should be considered for transition metals (TMs). Moreover, metals with their high oxidation states typically require large active orbitals. Similarly, the 4f-orbitals of lanthanides should be included in the active region. We only carried out the full CI considering the active orbitals (Figure 2.2).

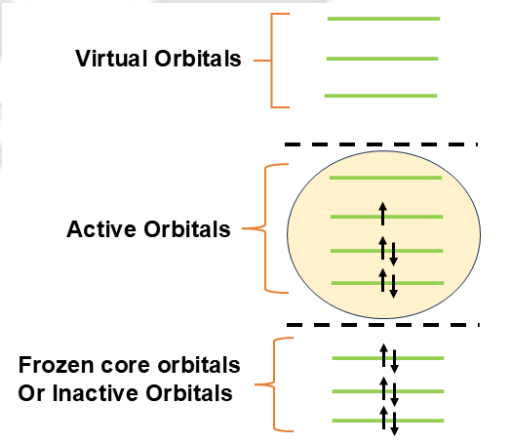

Figure 2.2. Schematic illustration of the active, inactive, and virtual regions of the orbital space.

CASSCF and RASSCF approaches confined calculations to only active orbitals. Likewise, they recover the total correlation energy but only the static correlation. Dynamic correlation can be recaptured perturbatively, using various methods like CASPT2 and RASPT2. Another approach we have considered in our work is the NEVPT2 method, which generalizes MP2 to CAS scenarios. Based on the corrections incorporated, these corrections are increased to many orders, such as MP2, MP3, etc.; MP1 is similar to the initial HF results.

2.4.2. n-Electron Valence State Perturbation Theory (NEVPT2) Method

NEVPT2 (n-Electron Valence State Perturbation Theory)[15–17] is a second-order perturbation theory applied to multi-reference wavefunctions, typically to the Complete Active Space Self-Consistent Field wavefunction. It accounts for the dynamic electron correlation that CASSCF fails to capture. The initial multiconfigurational wavefunction of the NEVPT2 method is generated from the CASSCF wavefunction (ψ_{CASSCF}). This wavefunction, ψ_{CASSCF}, contains static correlation and represents the strongly correlated part of the system (usually involving an active space of selected orbitals). The total Hamiltonian of the perturbed system can be expressed as

$$\hat{\mathrm{H}}_{total} = \hat{\mathrm{H}}_0 + \hat{V} \tag{2.13}$$

In Eq. 2.13, $\hat{\mathrm{H}}_0$ is the reference CASSCF Hamiltonian, which defines the zeroth-order wavefunction. $\hat{V}_0$ is the perturbation operator that accounts for the electron correlation neglected by the reference wavefunction.

NEVPT2 separated the total electronic space into three main regions- reference space, internal space, and external space. The reference space involves the CASSCF wavefunction ψ_{CASSCF}. The internal space considers the excitations within the active space. The external space explains the excitations beyond the active space. The interaction between these spaces through the perturbation operator $\hat{V}$ accounts for the electron correlation. The zeroth order wavefunction is expressed as

$$\hat{\mathrm{H}}_0|\psi_0\rangle = E_0|\psi_0\rangle \tag{2.14}$$

where $|\psi_0\rangle$ denotes the CASSCF reference wavefunction and E_0 is the corresponding energy eigenvalue. The first-order correction to the wavefunction accounts for the interaction between the active and virtual orbitals in the external space. The first-order wavefunction correction $\psi^{(1)}$ is expressed as

$$\psi^{(1)} = \sum_{\alpha} \frac{V_{\alpha 0}}{E_0 - E_\alpha} |\alpha\rangle \tag{2.15}$$

In Eq. 2.15, $V_{\alpha 0}$ represents the coupling between the reference state 0 and an excited state α, while E_α represent the energy of the excited state.

The NEVPT2 energy correction is derived by considering the second-order correction to the energy. This includes all possible excitations that interact with the reference space

$$E^{(2)} = \sum_{\alpha} \frac{|V_{\alpha 0}|^2}{E_0 - E_\alpha} \tag{2.16}$$

Eq. 2.16 represents the energy contribution from dynamic correlation, which involves the interaction between the electrons in the active space and those in the virtual region.

Thus, NEVPT2 initiates from a CASSCF reference wavefunction, provides a zeroth-order Hamiltonian, and uses second-order perturbation theory (MP2) to incorporate dynamic electron correlation, resulting in a corrected total energy for the system.

2.5. Density Functional Theory (DFT)

Density functional theory (DFT) offers an alternative method to determine the electronic wavefunction of a molecular system. Unlike wave function-based methods, DFT relies on the electron density $\rho(r)$ to describe the system. In 1965, Kohn and Sham,[18] accomplished the DFT energy of a molecular system using the functional of the electron density $\rho(r)$ as expressed in Eq. 2.17

$$E_{DFT}[\rho(r)] = T[\rho(r)] + V_{eN}[\rho(r)] + V_{ee}[\rho(r)] + E_{xc}[\rho(r)] \tag{2.17}$$

In this expression, $T[\rho(r)]$, $V_{eN}[\rho(r)]$, and $V_{ee}[\rho(r)]$ represent the kinetic energy of the non-interacting electrons, the electron-nuclei attraction energy, and the electron-electron repulsion energy, respectively. In the second and third terms, $V_{eN}[\rho(r)]$ and $V_{ee}[\rho(r)]$, are derived from classical expressions, as given in Eq. 2.18 and Eq. 2.19.

$$V_{eN}[\rho(r)] = -\sum_{A}^{N} \int \frac{Z_A \, \rho(r)}{|R_A - r|} \, dr \tag{2.18}$$

$$V_{ee}[\rho(r)] = \frac{1}{2} \iint \frac{\rho(r_1) \, \rho(r_2)}{|r_1 - r_2|} dr_1 dr_2 \tag{2.19}$$

The last term, $E_{xc}[\rho(r)]$, is the exchange-correlation functional, which describes all quantum mechanical effects not captured by V_{ee}. This includes non-classical corrections to electron-electron interactions, such as exchange and Coulomb corrections, and also to eliminate the

unphysical self-interaction errors. The most challenging aspect of DFT is explaining the $E_{xc}[\rho(r)]$ term. Additionally, it incorporates kinetic correlations to correct the kinetic energy, which reflects the interacting behavior of the electrons. Typically, this energy is categorised into two components: the pure exchange energy $E_x[\rho(r)]$, which accounts for the interactions between the electrons with the same spin state, and the correlation energy $E_c[\rho(r)]$, which addresses interactions between electrons of opposite spins.

$$E_{xc}[\rho(r)] = E_x[\rho(r)] + E_c[\rho(r)] = \int \rho(r)\varepsilon_x[\rho(r)]dr + \int \rho(r)\varepsilon_c[\rho(r)]dr \qquad (2.20)$$

ε_x and ε_c represent the exchange and correlation energies per particle. Like HF theory, DFT starts with an approximate set of molecules and employs an iterative self-consistent field (SCF) approach to solve the Kohn-Sham equations until convergence is achieved.

Over the last few decades, numerous exchange-correlation functionals, including the local density approximation (LDA),[19–21] generalized gradient approximation (GGA),[22–24] meta-GGA,[25] and hybrid functionals,[26,27] have been developed. Some of these functionals, along with their approximation, are displayed in Jacob's ladder[28] in Figure 2.3.

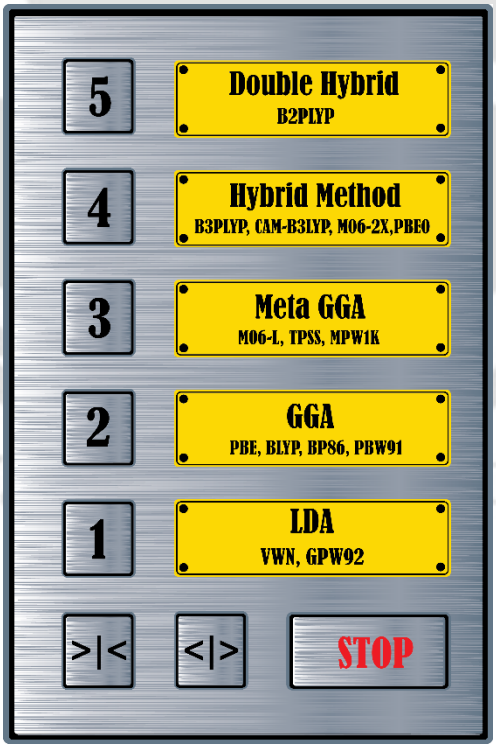

Figure 2.3. Jacob's ladder in quantum chemistry represents different levels of approximations of DFT functionals, highlighting their increasing accuracy level.

2.6. Basis Sets

Basis sets are applied in the HF or DFT methods to represent electronic wave functions that convert the partial differential equations into algebraic equations that can be efficiently solved on a computer. Basis sets in quantum mechanics are usually composed of atomic orbitals.[1,29]

$$\psi_i = \sum_b c_{ib}\, \chi_b \tag{2.21}$$

In addition to minimal basis sets, which assign one atomic orbital (AO) to each occupied AO in a molecule, split basis sets have two or three AOs for each minimal one. On the other hand, basis sets, including polarization and diffusion functions, offer greater adaptability for accurately modeling chemical bonding.

For heavy atoms, particularly those in the third row or below, pseudopotentials (PPs), also known as effective core potentials (ECPs), are generally employed to reduce computational cost and account for relativistic effects.[30–34] These PPs are designed to replace the inner (core) electrons in atomic and molecular systems, allowing only the explicit treatment of the valence electrons.

2.7. Relativistic Effects

Relativistic effects become significant for heavier elements and are often treated as perturbations or small corrections to the non-relativistic theory derived from the Schrödinger equation.[35–38] Based on the speed of electrons relative to the speed of light, these corrections impact the electrons differently. Relativistic effects can influence orbital sizes, shapes, interaction energies, and molecular properties. To combine the Schrödinger equation with the special theory of relativity, Paul Dirac's first attempt to consider the relativistic effect for a single electron. This leads to the time-independent Dirac equation[39]

$$\left[c\alpha.\hat{P} + c^2\beta + V\right] = E\psi \tag{2.22}$$

The Dirac Hamiltonian with α and β matrices are represented as

$$\hat{\mathrm{H}}_D = [\mathrm{c}\alpha.\hat{P} + c^2\beta + \mathrm{V}] \tag{2.23}$$

$$\alpha_{x,y,z} = \begin{pmatrix} 0 & \sigma_{x,y,z} \\ \sigma_{x,y,z} & 0 \end{pmatrix}, \quad \beta = \begin{pmatrix} I & 0 \\ 0 & I \end{pmatrix} \tag{2.24}$$

Where $\hat{P}$ denotes the momentum operator, c represents the speed of light, and V denotes the potential. The matrices $\sigma_{x,y,z}$ are the Pauli Spin matrices, I is identity matrix. Eq. 2.22 is the foundation of all molecular relativistic calculations. It explicitly explains an electron-positron

pair, while accounting for both spin states of each particle. Consequently, the four-component wavefunction is

$$\psi(x) = [\psi_1(x), \psi_2(x), \psi_3(x), \psi_4(x)] \tag{2.25}$$

Compared to the nonrelativistic Schrödinger equation, the Dirac equation is very computationally expensive, and it is only effective for a single electron system. To account for the multielectron system, the Dirac-Coulomb-Breit (DCB) Hamiltonian extends the Dirac Hamiltonian to an N-particle system.[40,41]

The Dirac-Coulomb-Breit (DCB) Hamiltonian, introduced in 1928, is the most accurate formulation for incorporating relativistic effects in quantum chemical calculations. It describes both scalar and spin-orbit relativistic effects.

$$\hat{H}_{DCB} = \sum_i \hat{h}_i + \sum_{i<j} \hat{h}_{ij} \tag{2.26}$$

Where $\hat{h}_i$ is the Dirac Hamiltonian, and $\hat{h}_{ij}$ represent the two-particle term

$$\hat{h}_{ij} = \frac{1}{r_{ij}} + \frac{1}{2r_{ij}}[\alpha_i.\alpha_j + \frac{(\alpha_i.r_{ij})(\alpha_j.r_{ij})}{r_{ij}^2}] \tag{2.27}$$

Using the Dirac-Coulomb-Breit Hamiltonian with a four-component wavefunction, similar to the Dirac equation, is considerably more computationally demanding compared to solving the nonrelativistic Schrödinger equation for the same system.

Separating scalar relativistic effects from the spin-orbit coupling reduces computational cost. One such approach is the zeroth-order regular approximation (ZORA)[42–44] based on the perturbational expansion of the Dirac equation.

$$\hat{H}_{ZORA} = V + \sigma.\hat{P}\frac{c^2}{2mc^2 - V}\sigma.\hat{P} \tag{2.28}$$

In Eq. 2.28, $\hat{P}$ denotes the momentum operator, V is a potential and σ represent the spin-orbit matrix.

The Douglas-Kroll-Hess (DKH) approximation is an alternative method derived by employing a series of unitary transformations to the Dirac equation.[45–47] This method effectively decouples the large and small components (i.e., positive and negative energy states), block-diagonalizing the Dirac Hamiltonian. This results into a simplified two-component Hamiltonian for the large components that include relativistic corrections, such as the mass-

velocity term, the Darwin term, and spin-orbit coupling. This decoupling of positive and negative energy terms produces an infinite series of operators (Eq. 2.29), with $\hat{\varepsilon}_k$ representing the expansion terms. In general, the lower-order terms from this series are utilized to efficiently and accurately incorporate relativistic effects in quantum calculations.

$$\hat{H}_{DKH\infty} = \sum_{k=0}^{\infty} \hat{\varepsilon}_k \tag{2.29}$$

Numerous quantum chemical calculations are achieved with sufficient accuracy with a second-order expansion. Therefore, the expansion is typically truncated at $k = 2$, resulting in the Hamiltonian referred to as $DKH2$.[38,48]

2.8. Quantum Theory of Atoms in Molecules (QTAIM)

Richard Bader introduced the Quantum Theory of Atoms in Molecules (QTAIM),[49–51] a powerful analytical framework that examines the topology of electron density ρ within a molecular system. QTAIM enables the quantitative analysis of various molecular properties by focusing on the distribution and behavior of electron density ρ, providing insights into bonding, molecular structure, and other key characteristics. In a molecule, electron density ρ is highest near the atomic nuclei and decreases in other regions, providing insight into the structure and interactions within the molecule. Since the electron density ρ depends on three spatial coordinates, it is feasible to analyze the gradient vector field correlated with it. The gradient of the electron density $[\nabla\rho(r_c)]$ can be determined and expressed as

$$\nabla\rho(r_c) = \hat{\imath}\frac{\delta\rho}{\delta x} + \hat{\jmath}\frac{\delta\rho}{\delta y} + \hat{k}\frac{\delta\rho}{\delta z} \tag{2.30}$$

In Eq. 2.30, $\hat{\imath}$, $\hat{\jmath}$ and $\hat{k}$ are the unit vectors. In a molecular system, the electron density exhibits maxima, minima, and saddle points in space, named critical points (CP).[52] At these critical points, the gradient of the electron density ($\nabla\rho(r_c)$) becomes zero [$\nabla\rho(r_c)$ =0]. The four types of critical points are (a) nuclear critical points (NCP), (b) bond critical points (BCP), (c) ring critical points (RCP), and (d) cage critical points (CCP), each related to distinct topological features of the electron density distribution. In the topological investigation of electron density $\rho(r)$, the Laplacian of the electron density $\nabla^2\rho(r_c)$, offers valuable insight into atomic interactions. When $\nabla^2\rho(r_c) < 0$, it indicates a concentration of electron density along the interaction line. This concentration causes $\rho(r_c)$ to contract perpendicularly to the interaction line, lowering the potential energy. Consequently, an attractive force and a shared interaction (or covalent bond) are observed. Conversely, when $\nabla^2\rho(r_c) > 0$, the interaction is dominated by the contraction of $\rho(r_c)$ towards the nucleus, indicating a more electrostatic or ionic

character. The classification and characteristics of critical points are determined by the number of non-zero eigenvalues of the Hessian matrix of ρ and the sum of their signs. The second derivative of ρ, also recognized as the Hessian of ρ, is written as

$$\nabla^2\rho(r_c) = \begin{vmatrix} \frac{\partial^2\rho}{\partial x^2} & \frac{\partial^2\rho}{\partial x\partial y} & \frac{\partial^2\rho}{\partial x\partial z} \\ \frac{\partial^2\rho}{\partial y\partial x} & \frac{\partial^2\rho}{\partial y^2} & \frac{\partial^2\rho}{\partial y\partial z} \\ \frac{\partial^2\rho}{\partial z\partial x} & \frac{\partial^2\rho}{\partial z\partial y} & \frac{\partial^2\rho}{\partial z^2} \end{vmatrix} \tag{2.31}$$

After diagonalization of Eq. 2.31, the off-diagonal elements are eliminated using a unitary transformation, leading to the Laplacian of ρ and yielding the eigenvalues λ_1, λ_2, and λ_3.

$$\nabla^2\rho(r_c) = \frac{\partial^2\rho}{\partial x^2} + \frac{\partial^2\rho}{\partial y^2} + \frac{\partial^2\rho}{\partial z^2} = \lambda_1 + \lambda_2 + \lambda_3 \tag{2.32}$$

The eigenvalues λ_1, λ_2, and λ_3 denotes the curvatures of the electron density and determines the types of critical points (CPs). In a (3, -3) nuclear CP, all three curvatures are negative, indicating a local maximum in the electron density. A (3, -1) bond CP has two negative curvatures, meaning ρ is maximized in the plane of these curvatures, while it is minimized along the third, perpendicular plane (the bond path). In a (3, +1) ring CP, two curvatures are positive, indicating a minimum of ρ in that plane and a maximum along the third, perpendicular axis. Finally, in a (3, +3) cage CP, all three curvatures are positive.

2.9. The Electron Localisation Function

The Electron Localization Function (ELF) is an important tool used in quantum mechanics to analyze the spatial distribution of electron density in molecules or solids.[53–55] It offers insights into a system's electronic structure and the nature of chemical bonding. ELF measures the probability of finding an electron in a localized region of space, quantifying how concentrated or expanded the electron density is around a specific point. ELF values range between 0 and 1, described by the scalar field $n(r)$.

$$n(r) = \frac{1}{1+\left(\frac{D\sigma}{D_\sigma^0}\right)^2} \tag{2.33}$$

D_σ and D_σ^0 denotes the curvatures of the electron pair density for electrons with identical spins in the real system and in a homogeneous electron gas with the same density, respectively. ELF ~ 1, which indicates high electron localization, such as in lone pairs or bonds. ELF ~ 0 represents the region with low electron density or where electrons are highly delocalized.[56]

2.10. Basis Set Superposition Error (BSSE)

When two atoms or fragments come into proximity, their respective basis sets borrowed from each atom begin to overlap. The dimer is stabilized when monomer A approaches monomer B, with monomer A using the additional basis functions of monomer B to explain its electron distribution more effectively and vice versa. This difference of the basis set for each monomer as the intermolecular distance changes is the origin of the basis set superposition error (BSSE). The magnitude of this effect increases as the interatomic distance decreases.[57]

The Counterpoise Correction (CP) method introduced by Boys and Bernardi[58] provides a way to eliminate BSSE. To understand this approach, let us consider two fragments A and B. The interaction between these two fragments (A and B) can be calculated as

$$\triangle E_{AB}^{int} = E_{AB}^{ab} - E_A^a - E_B^b \tag{2.34}$$

The superscripts ab, a, and b denotes the basis sets, while the subscripts AB, A, and B represent the molecular geometries. The E_{AB}^{ab} term corresponds to the energy of the dimer AB calculated using the dimer basis set ab. Similarly, E_A^a and E_B^b represent the energies of the isolated molecular fragments A and B calculated using their respective basis sets a and b. The additional stabilization energy acquired by the fragment A owing to the extra basis set extended from a fragment B (and vice versa) can be expressed as

$$E_A(BSSE) = E_A^{ab} - E_A^a \tag{2.35}$$

$$E_B(BSSE) = E_B^{ab} - E_B^b \tag{2.36}$$

The energy $[E_A^a]$ as shown in Eq. 2.35, representing the energy of the molecular fragment A in its own basis set. This energy is subtracted from $[E_A^{ab}]$ which is the energy of fragment A in the dimer basis sets ab. The same approach is applied to molecular fragment B. We have assumed that the geometries of molecular fragments A and B are in the dimeric forms. When evaluating the energy of a molecular fragment A in the dimer basis set, one considered all the basis functions of the fragment B's atomic center and neglecting the electrons and nuclear charges of fragment B. These functions on atoms of fragment B are referred to as ghost orbital. Similarly, the fragment B also estimated.

By subtracting Eq. 2.35 and Eq. 2.36 from the interaction energy expression (Eq. 2.34), the counter poise (CP) corrected interaction energy can be written as

$$\triangle E_{AB}^{int}(CP) = E_{AB}^{ab} - E_A^a - E_B^b - E_A^{ab} + E_A^a - E_B^{ab} + E_B^b \tag{2.37}$$

$$\triangle E_{AB}^{int}(CP) = E_{AB}^{ab} - E_{A}^{ab} - E_{B}^{ab} \quad (2.38)$$

2.11. Molecular Electrostatic Potential

The molecular electrostatic potential (MEP)[59,60] at a specific point, $P(x, y, z)$, on the vicinity of the molecule, represents the force applied on the positive test charge (a proton) placed at the point P. This force arises from the electrical charge distribution of the molecules, which includes contributions from both electrons and nuclei. The molecular electrostatic potential $V(r)$ at a specific point r is expressed as[61]

$$V(r) = \sum_A \frac{Z_A}{|R_A - r|} - \int \frac{\rho(r')dr'}{|r' - r|} \quad (2.39)$$

Here, Z_A denotes the charge of the nucleus A, located at R_A, while $\rho(r')$ denotes the electron density function at the point r'. The electrostatic potential $V(r)$ can be estimated computationally and analyzed experimentally using diffraction methods.

2.12. Energy Decomposition Analysis (EDA)

The supermolecular method, as expressed in Eq. 2.40 is the most commonly used approach to estimate the interaction strength between the two molecules or fragments.

$$\triangle E = E(XY) - E(X) - E(Y) \quad (2.40)$$

Where $E(XY)$, $E(X)$, and $E(Y)$ represent the energies of complex XY, fragment X, and fragment Y, respectively. The binding energy $\triangle E$ provides the single value for calculating the interaction between the two molecules, but cannot provide the different energy components.

The energy decomposition analysis partitions the total interaction energy into several physically meaningful components, including electrostatic, polarization, charge transfer, exchange, and correlation contributions. The energies of the individual fragments are separately determined, following an additional calculation to determine the interaction energy between them. The binding energy comprises two main components: the preparation energy (also referred to as strain energy, deformation energy) and the interaction energy.[62]

$$\triangle E = \triangle E_{prep} + \triangle E_{int} \quad (2.41)$$

This interaction energy, $\triangle E_{int}$, can be explained as the binding energy of the two fragments and is represented as the combination of the following energy components [63,64]

$$\triangle E_{int} = \triangle E_{elst} + \triangle E_{pauli} + \triangle E_{orb} \quad (2.42)$$

The term $\triangle E_{elst}$ represents the classical electrostatic forces acting between the unperturbed fragments as they are positioned together in their final positions. $\triangle E_{pauli}$ is the destabilizing repulsive interactions, including any steric interactions. The last term, $\triangle E_{orb}$ referred to the orbital interaction energy. This final term corresponds to the stabilizing effect arising from the mixing of fragment orbitals during complex formation. This term includes electron pair bonding, charge transfer, and polarisation effects.

2.13. The Spin Hamiltonian Concept

The spin Hamiltonian is a simplified method used to describe the part of the eigenvalues of the complete Hamiltonian. The spin Hamiltonian $\hat{\mathrm{H}}_{spin}$ expresses the total energy of a magnetic system that focuses on spin interactions.[65–67] Various effects contribute to the energy of states, including the electron Zeeman effect, hyperfine interaction, and zero-field splitting (ZFS).[68] Their contributions can be split into individual Hamiltonians. The general expression for the spin Hamiltonian is[69,70]

$$\hat{\mathrm{H}}_{spin} = u_B B.g.S + S.D.S + S.A.I \tag{2.43}$$

Here, u_B denotes the Bohr magneton, B is the magnetic field vector, S represent the spin operator, and g denotes the g-tensor, which relates the magnetic field vector to the spin vector, A is the hyperfine interaction tensor, and I denote the nuclear spin operator.

Only ZFS, which is relevant to this work, is explained here. To analyze the ZFS, the spin Hamiltonian formalism can be applied up to the second order, parameterized by the axial (D) and rhombic (E) ZFS parameters. In Eq. 2.43, the second term indicates the ZFS spin Hamiltonian ($\hat{\mathrm{H}}_{ZFS}$), which can be expressed as[71,72]

$$\hat{\mathrm{H}}_{ZFS} = D\left[\hat{\mathrm{S}}_z^2 - \frac{1}{2}S(S+1)\right] + E[\hat{\mathrm{S}}_x^2 - \hat{\mathrm{S}}_y^2] \tag{2.44}$$

The axial (D) and rhombic (E) components of the ZFS can be described using the formalism of effective Hamiltonian theory as

$$D = D_{zz} - \frac{1}{2}(D_{xx} + D_{yy}) \tag{2.45}$$

$$E = \frac{1}{2}(D_{xx} - D_{yy}) \tag{2.46}$$

In Eq. 2.45 and Eq. 2.46, D_{xx}, D_{yy}, and D_{zz} represent the principal components of the diagonalized D tensor. The ZFS energy ($\triangle$) can be determined from D and E using Eq. 2.47.

$$\triangle = \sqrt{\frac{2}{3}D^2 + 2E^2} \tag{2.47}$$

The ZFS determines the energy gap between Kramers doublets (Figure 2.4) and is crucial for analyzing the magnetic behavior, including spin relaxation and magnetic anisotropy, in Mn^{2+} and Gd^{3+} complexes.[73,74]

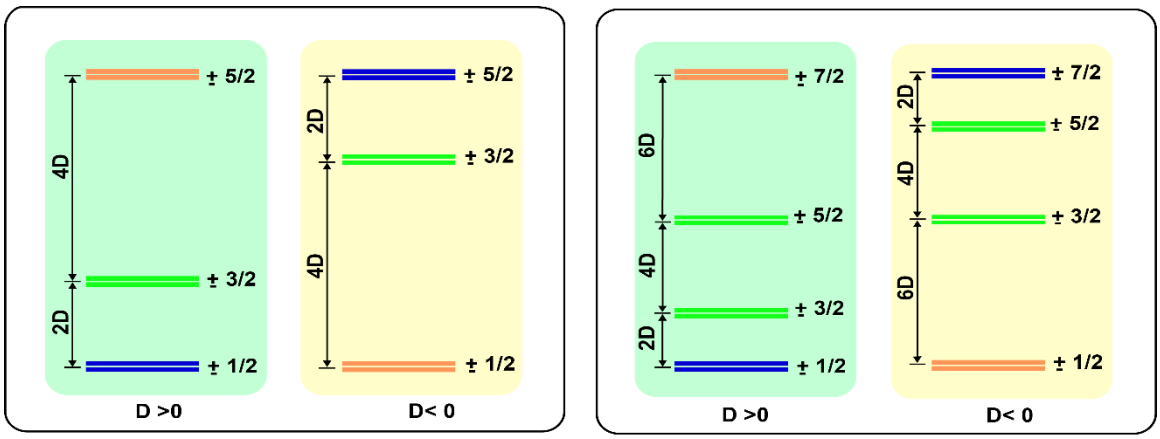

Figure 2.4. The ZFS of the Kramers doublets in symmetrical Mn^{2+} and Gd^{3+} complexes is represented in cylindrical *D* parameters.

2.14. *Ab Initio* Ligand Field theory

Ligand Field Theory (LFT)[75,76] examines how donor atoms affect the energy of d orbitals in the metal complexes. It is a model developed for coordination complexes of d-block and f-block in intermediate oxidation states, typically II and III. The AILFT builds upon LFT using a correlated multireference wavefunction approach that encapsulates the essential features of ligand field interactions.[77] Unlike the parametric formulation of LFT, AILFT does not depend on experimental data. It uses the CASSCF method to address static electron correlation, which is further augmented by an n-electron valence state perturbation theory (NEVPT2) to account for dynamic electron correlation. This approach allows unambiguous extraction of key ligand field parameters, including the ligand field one electron matrix V_{LFT}, the Racah parameters B and C, and the spin-orbit coupling parameter (ζ) through multi-reference *ab initio* calculations. This approach applies to mononuclear complexes having d^n or f^n configurations.

LFT is a projection operator scheme as presented in Eq. 2.48, the ligand field Hamiltonian, H_{LF}, consist of three components describing the d-d interelectron repulsion, $U(i,j)$, spin-orbit coupling ($l_i \cdot s_j$), and the ligand field potential, V_{LF}.

$$H_{LF} = \sum_{j<j}^{N} U(i,j) + \sum_{j}^{N} V_{LF}(r_i) + \zeta \sum_{i}^{N} l_i \cdot s_j \tag{2.48}$$

The terms in Eq. 2.48, operate on a set of states corresponding to a specific d configuration. The d symmetry label generally refers to spherical symmetry, where the initial two terms of Eq. 2.48, based on a central field (i.e., spherical) approximation. In this context, it is only V_{LF} that incorporate information regarding the true molecular symmetry.

The presence of d or f valence electrons in the crystal lattice of coordination complexes allows the ligand field (LF) or crystal field (CF) to significantly impact the observed magnetic properties of these materials. These effects can vary depending on the degree of covalency of the bonds formed between the magnetic metal centers and the ligands.

2.15. Molecular Dynamics Simulations

Molecular dynamics is a widely used computational simulation approach to investigate the time evolution of a system from specified initial boundary conditions. The equations of motion are solved numerically to determine the time evolution of the system. This allows the determination of the kinetic and thermodynamic properties of the system through simulations.[78]

2.15.1. Classical Molecular Dynamics

Classical molecular dynamics (MD) simulations are widely used computational methods in various fields of science to simulate the physical movements of atoms or molecules over time. It involves integrating Newton's equations of motion using a finite difference algorithm to simulate the system's behavior over time. Integrating the equation of motion provides velocity, a trajectory containing positions and accelerations of atoms over time. Newton's equation of motion is,

$$F_x = m_x a_x = m_x \frac{d^2 r_x}{dt^2} \tag{2.49}$$

Where F_x is the force applied on the particle x of mass m_x, and a_x is the acceleration of the particle x.

$$\frac{d^2 r_x}{dt^2} = \frac{F_x}{m_x} \tag{2.50}$$

$$\frac{d^2 r_x}{dt^2} = a_x \tag{2.51}$$

$$\frac{v_x}{dt} = \frac{F_x}{m_x} \tag{2.52}$$

Force is the derivative of potential with respect to position that can be calculated analytically. To determine the velocities and positions in the next time step, the forces must be integrated. Common algorithms used for integrating the equation of motion are Verlet,[79] Leapfrog,[80] and Velocity Verlet.[81]

2.15.2. Force Fields in Classical Molecular Dynamics

A force field is a mathematical model that describe the time evolution of bond lengths, bond angles, torsions, and non-bonding interactions such as van der Waals and electrostatic forces between atoms. It defines the system's energy as a function of the atomic coordinates and determines the forces exerted on each atom. These forces are then used to calculate atomic motion through Newton's equations of motion. The force field consists of interatomic potential energy and associated parameters. The parameters are usually derived through a combination of experimental data or *ab initio* or semi-empirical quantum mechanical calculations. The energy of the force field comprises bonded terms that involve the interactions between atoms connected via covalent bonds, as well as non-bonded terms which characterize the long-range electrostatic and van der Waals interactions.

The typical force field is expressed as[82]

$$U = \sum_{bonds} \frac{1}{2} k_b (r - r_0)^2 + \sum_{angles} \frac{1}{2} k_a (\theta - \theta_0)^2 + \sum_{torsions} \frac{V_n}{2} [1 + \cos(n\phi - \delta)] + \sum_{improper} V_{imp} + \sum_{LJ} 4\varepsilon_{ij} \left(\frac{\sigma_{ij}^{12}}{r_{ij}^{12}} - \frac{\sigma_{ij}^{6}}{r_{ij}^{6}}\right) + \sum_{elec} \frac{q_i q_j}{r_{ij}} \quad (2.53)$$

The initial four terms in Eq. 2.53 account for the bonded interactions, including bonds, angles, torsion angles, and improper torsions. The final two terms described the non-bonded interactions of repulsive and van der Waals interactions (computed with the Lennard-Jones potential) and the attractive Coulombic interactions. Different types of available force fields are UFF,[83] OPLS-AA,[84] AMBER,[85] GROMOS,[86] etc.

2.16. *Ab initio* Molecular Dynamics (AIMD) Simulations

The fundamental concept of the *ab initio* molecular dynamics (AIMD)[87] simulations is to resolve the electronic Schrödinger equation approximately to derive an effective potential for the nuclei. This obtained potential is applied to calculate the nuclear forces using Newton's equation of motion. This hybrid approach is the basis of the Ehrenfest MD, Born-Oppenheimer MD (BOMD), and Car-Parrinello MD (CPMD).[88] The DFT-based AIMD simulations in our work are Born-Oppenheimer simulations, wherein the electronic structure is computed using

DFT at each time step of the simulation. The Born-Oppenheimer approximation supposes that atomic nuclei remain fixed, allowing the electronic structure to be computed as a function of their nuclear positions. Molecular dynamics simulations using DFT are challenging because the Born-Oppenheimer approximation requires the Kohn-Sham wavefunction ψ, which depends parametrically on the nuclear positions. This leads to solving the electronic structure problem at every step. However, the forces can be efficiently determined using the Hellmann-Feynman theorem, as a converged Kohn-Sham wavefunction directly yields the gradients needed to propagate the system.

$$F_k = -\langle \psi_0 | \frac{\partial \hat{H}}{\partial R_k} | \psi_0 \rangle \tag{2.54}$$

This approach, in which the force F_k on nucleus k is derived from the ground state orbitals, is referred to as Born-Oppenheimer molecular dynamics (BOMD). AIMD simulations yield highly accurate descriptions of the systems; these are based on the electronic structure without any experimental or empirical parameters. However, the computational precision in these methods restricts the simulation time to the order of picoseconds only. AIMD is particularly valuable at this timescale for determining the structural properties and especially for studying the coordination geometry of lanthanide and transition metal complexes in solution. At this timescale, AIMD is particularly valuable for determining the formation of bonds and other structural properties, especially in the study of lanthanide coordination structures in solution. In AIMD simulation of water, the liquid is modeled using a simulation box that is periodically replicated in all directions (periodic boundary conditions) and typically contains between 50 and 500 independent water molecules. Throughout the simulation, the orbitals of all molecules are recalculated at every step of the trajectory. However, the classical MD simulations are suited for larger systems with longer time scales than AIMD, as they depend on the classical force field, which neglects the electronic structure calculations. One major drawback is the accuracy of the results of the calculations owing to the lack of precision in molecular mechanics. Moreover, classical MD cannot account for bond formation and breaking, making it unsuitable for simulating chemical reactions. Instead, it is employed for longer sampling times to study statistical mechanics, thermodynamics, and dynamic properties, such as water exchange in lanthanide (Ln)-ligand complexes.

2.17. References

[1] A. Szabo and N. S. Ostlund, *Modern Quantum Chemistry: Introduction to Advanced Electronic Structure Theory*, Dover Publications, Mineola, N.Y, 1996.

[2] J.-M. Combes, P. Duclos and R. Seiler, *The Born-Oppenheimer Approximation. In: Rigorous Atomic and Molecular Physics*, New York, Plenum, 1981.

[3] D. R. Hartree, *Math. Proc. Camb. Philos. Soc.*, 1928, **24**, 89-110.

[4] V. Fock, *Z. Phys.*, 1930, **61**, 126-148.

[5] T. Helgaker, P. Jørgensen and J. Olsen, *Molecular Electronic-Structure Theory*, Wiley, 1st edn., 2000.

[6] I. Shavitt and R. J. Bartlett, *Many-Body Methods in Chemistry and Physics: MBPT and Coupled-Cluster Theory*, Cambridge University Press, 1st edn., 2009.

[7] R. J. Bartlett and M. Musiał, *Rev. Mod. Phys.*, 2007, **79**, 291-352.

[8] Chr. Møller and M. S. Plesset, *Phys. Rev.*, 1934, **46**, 618-622.

[9] K. Hirao, *Recent Advances in Multireference Methods,* World Scientific, Singapore, 1999.

[10] C. Angeli, R. Cimiraglia and J.-P. Malrieu, *Chem. Phys. Lett.*, 2001, **350**, 297-305.

[11] B. O. Roos, R. Lindh, P. Å. Malmqvist, V. Veryazov and P.-O. Widmark, *Multiconfigurational quantum chemistry*, Wiley, Hoboken, New Jersey, 2016.

[12] B. O. Roos and P. E. M. Siegbahn, *Int. J. Quantum Chem.*, 1980, **17**, 485-500.

[13] B. O. Roos, P. R. Taylor and P. E. M. Sigbahn, *Chem. Phys.*, 1980, **48**, 157-173.

[14] V. Veryazov, P. Å. Malmqvist and B. O. Roos, *Int. J. Quantum Chem.*, 2011, **111**, 3329-3338.

[15] C. Angeli, R. Cimiraglia, S. Evangelisti, T. Leininger and J.-P. Malrieu, *J. Chem. Phys.*, 2001, **114**, 10252-10264.

[16] C. Angeli, R. Cimiraglia and J.-P. Malrieu, *J. Chem. Phys.*, 2002, **117**, 9138-9153.

[17] R. W. A. Havenith, P. R. Taylor, C. Angeli, R. Cimiraglia and K. Ruud, *J. Chem. Phys.*, 2004, **120**, 4619-4625.

[18] W. Kohn and L. J. Sham, *Phys. Rev.*, 1965, **140**, A1133-A1138.

[19] J. P. Perdew and A. Zunger, *Phys. Rev. B*, 1981, **23**, 5048-5079.

[20] J. P. Perdew and Y. Wang, *Phys. Rev. B*, 1992, **45**, 13244-13249.

[21] S. H. Vosko, L. Wilk and M. Nusair, *Can. J. Phys.*, 1980, **58**, 1200-1211.

[22] J. P. Perdew, K. Burke and Y. Wang, *Phys. Rev. B*, 1996, **54**, 16533-16539.

[23] J. P. Perdew, K. Burke and M. Ernzerhof, *Phys. Rev. Lett.*, 1996, **77**, 3865-3868.

[24] J. P. Perdew, K. Burke and M. Ernzerhof, *Phys. Rev. Lett.*, 1998, **80**, 891-891.

[25] J. Tao, J. P. Perdew, V. N. Staroverov and G. E. Scuseria, *Phys. Rev. Lett.*, 2003, **91**, 146401-146404.

[26] A. D. Becke, *J. Chem. Phys.*, 1993, **98**, 5648-5652.

[27] C. Lee, W. Yang and R. G. Parr, *Phys. Rev. B*, 1988, **37**, 785-789.

[28] J. P. Perdew, in *AIP Conference Proceedings*, AIP, Antwerp (Belgium), 2001, 577, 1-20.

[29] D. A. McQuarrie and J. D. Simon, *Physical chemistry: a molecular approach*, University Science Books, Sausalito, Calif, 1997.

[30] M. Dolg, H. Stoll, A. Savin and H. Preuss, *Theor. Chim. Acta*, 1989, **75**, 173-194.

[31] M. Dolg and H. Stoll, *Theor. Chim. Acta*, 1989, **75**, 369-387.

[32] X. Cao and M. Dolg, *J. Chem. Phys.*, 2001, **115**, 7348-7355.

[33] A. Höllwarth, M. Böhme, S. Dapprich, A. W. Ehlers, A. Gobbi, V. Jonas, K. F. Köhler, R. Stegmann, A. Veldkamp and G. Frenking, *Chem. Phys. Lett.*, 1993, **208**, 237-240.

[34] D. R. Beck, S. M. O'Malley and L. Pan, in *Computational Methods in Lanthanide and Actinide Chemistry*, ed. M. Dolg, Wiley, 1st edn., 2015, 1-21.

[35] R. D. Cowan and D. C. Griffin, *J. Opt. Soc. Am.*, 1976, **66**, 1010-1014.

[36] W. H. E. Schwarz, in *Relativistic Methods for Chemists*, eds. M. Barysz and Y. Ishikawa, Springer Netherlands, Dordrecht, 2010, 10, 1-62.

[37] N. Kaltsoyannis, *J. Chem. Soc. Dalton Trans.*, 1997, 1-12.

[38] K. G. Dyall and K. Faegri, *Introduction to Relativistic Quantum Chemistry*, Oxford University Press, 2007.

[39] P. A. M. Dirac *Proc. R. Soc. Lond. Ser. Contain. Pap. Math. Phys. Character*, 1929, **123**, 714-733.

[40] G. Breit, *Proc. Natl. Acad. Sci.*, 1928, **14**, 553-559.

[41] K. G. Dyall, *J. Chem. Phys.*, 1994, **100**, 2118-2127.

[42] E. V. Lenthe, E. J. Baerends and J. G. Snijders, *J. Chem. Phys.*, 1993, **99**, 4597-4610.

[43] C. Chang, M. Pelissier and P. Durand, *Phys. Scr.*, 1986, **34**, 394-404.

[44] J.-L. Heully, I. Lindgren, E. Lindroth and A.-M. Mrtensson-Pendrill, *Phys. Rev. A*, 1986, **33**, 4426-4429.

[45] M. Douglas and N. M. Kroll, *Ann. Phys.*, 1974, **82**, 89-155.

[46] B. A. Hess, *Phys. Rev. A*, 1985, **32**, 756-763.

[47] M. Reiher and A. Wolf, *J. Chem. Phys.*, 2004, **121**, 2037-2047.

[48] T. Saue and T. Helgaker, *J. Comput. Chem.*, 2002, **23**, 814-823.

[49] R. F. W. Bader, *Acc. Chem. Res.*, 1985, **18**, 9-15.

[50] R. F. W. Bader, *Chem. Rev.*, 1991, **91**, 893-928.

[51] R. F. W. Bader, *J. Phys. Chem. A*, 2009, **113**, 10391-10396.

[52] R. F. W. Bader, *Atoms in molecules: a quantum theory*, Clarendon press, Oxford, 1994.

[53] S. A. Kulkarni, *Phys. Rev. A*, 1994, **50**, 2202-2206.

[54] B. Silvi and A. Savin, *Nature*, 1994, **371**, 683-686.

[55] A. Savin, R. Nesper, S. Wengert and T. F. Fässler, *Angew. Chem. Int. Ed. Engl.*, 1997, **36**, 1808-1832.

[56] A. D. Becke and K. E. Edgecombe, *J. Chem. Phys.*, 1990, **92**, 5397-5403.

[57] D. B. Boyd and K. B. Lipkowitz, Eds., *Reviews in computational chemistry: Volume 13*, Wiley-VCH, New York, N.Y, 1999.

[58] S. F. Boys and F. Bernardi, *Mol. Phys.*, 1970, **19**, 553-566.

[59] C. A. Hunter, *Angew. Chem. Int. Ed.*, 2004, **43**, 5310-5324.

[60] G. Merino, A. Vela and T. Heine, *Chem. Rev.*, 2005, **105**, 3812-3841.

[61] S. R. Gadre, C. H. Suresh and N. Mohan, *Molecules*, 2021, **26**, 3289-3313.

[62] K. Morokuma and K. Kitaura, in *Chemical Applications of Atomic and Molecular Electrostatic Potentials*, eds. P. Politzer and D. G. Truhlar, Springer US, Boston, MA, 1981, 215-242.

[63] M. P. Mitoraj, A. Michalak and T. Ziegler, *J. Chem. Theory Comput.*, 2009, **5**, 962-975.

[64] F. M. Bickelhaupt and E. J. Baerends, in *Reviews in Computational Chemistry*, eds. K. B. Lipkowitz and D. B. Boyd, Wiley, 1st edn., 2000, 15, 1-86.

[65] A. Abragam and B. Bleaney, *Electron paramagnetic resonance of transition ions*, Oxford Univ. Press, Oxford, Repr., 2013.

[66] A. D. McLachlan, *Proc. R. Soc. Lond. Ser. Math. Phys. Sci.*, 1964, **280**, 271-288.

[67] M. M. Roessler and E. Salvadori, *Chem. Soc. Rev.*, 2018, **47**, 2534-2553.

[68] N. Schaefle and R. Sharp, *J. Chem. Phys.*, 2004, **121**, 5387-5394.

[69] L. Berliner and G. Hanson, Eds., *High Resolution EPR: Applications to Metalloenzymes and Metals in Medicine*, Springer New York, New York, NY, 2009.

[70] J. Lu, I. O. Ozel, C. A. Belvin, X. Li, G. Skorupskii, L. Sun, B. K. Ofori-Okai, M. Dincă, N. Gedik and K. A. Nelson, *Chem Sci*, 2017, **8**, 7312-7323.

[71] R. Boča, *Coord. Chem. Rev.*, 2004, **248**, 757-815.

[72] M. Retegan, N. Cox, D. A. Pantazis and F. Neese, *Inorg. Chem.*, 2014, **53**, 11785-11793.

[73] S. Khan, A. Kubica-Misztal, D. Kruk, J. Kowalewski and M. Odelius, *J. Chem. Phys.*, 2015, **142**, 034304-034315.

[74] R. Uzal-Varela, L. Valencia, D. Lalli, M. Maneiro, D. Esteban-Gómez, C. Platas-Iglesias, M. Botta and A. Rodríguez-Rodríguez, *Inorg. Chem.*, 2021, **60**, 15055-15068.

[75] J. S. Griffith and L. E. Orgel, *Q. Rev. Chem. Soc.*, 1957, **11**, 381-393.

[76] C. J. Ballhausen and M. A. Weiner, *J. Electrochem. Soc.*, 1963, **110**, 97Cb.

[77] S. K. Singh, J. Eng, M. Atanasov and F. Neese, *Coord. Chem. Rev.*, 2017, **344**, 2-25.

[78] M. E. Tuckerman, *Statistical mechanics: theory and molecular simulation*, Oxford university press, Oxford, 2nd ed., 2023.

[79] L. Verlet, *Phys. Rev.*, 1967, **159**, 98-103.

[80] M. A. Cuendet and W. F. Van Gunsteren, *J. Chem. Phys.*, 2007, **127**, 184102-184110.

[81] D. Frenkel and B. Smit, *Understanding molecular simulation: from algorithms to applications*, Academic press, San Diego, 2nd ed., 2002.

[82] M. A. González, *Collection SFN*, 2011, **12**, 169-200.

[83] A. K. Rappe, C. J. Casewit, K. S. Colwell, W. A. Goddard and W. M. Skiff, *J. Am. Chem. Soc.*, 1992, **114**, 10024-10035.

[84] W. L. Jorgensen, D. S. Maxwell and J. Tirado-Rives, *J. Am. Chem. Soc.*, 1996, **118**, 11225-11236.

[85] Y. Duan, C. Wu, S. Chowdhury, M. C. Lee, G. Xiong, W. Zhang, R. Yang, P. Cieplak, R. Luo, T. Lee, J. Caldwell, J. Wang and P. Kollman, *J. Comput. Chem.*, 2003, **24**, 1999-2012.

[86] N. Schmid, A. P. Eichenberger, A. Choutko, S. Riniker, M. Winger, A. E. Mark and W. F. Van Gunsteren, *Eur. Biophys. J.*, 2011, **40**, 843-856.

[87] D. Marx and J. Hutter, *Ab Initio Molecular Dynamics: Basic Theory and Advanced Methods*, Cambridge University Press, 1st edn., 2009.

[88] R. Car and M. Parrinello, *Phys. Rev. Lett.*, 1985, **55**, 2471-2474.

Chapter 3

Computational Insight into a Mechanistic Overview of Water Exchange Kinetics and Thermodynamic Stabilities of Bis and Tris-Aquated Complexes of Lanthanides

The work of this Chapter is published in *RSC Adv* **2023**, *13*, 1516-1529.

3.1. Introduction

The chemistry of lanthanide complexes in aqueous solution has been considered one of the prominent research areas due to their fruitful implementation in diagnostics and therapy.[1–3] This includes the luminescent lanthanide complexes (specifically Eu^{3+} and Tb^{3+}) used in bioanalytical and optical imaging,[4–6] and radioisotopes of lanthanides (^{177}Lu) used in radioimmunotherapy.[7] Indeed, Gd^{3+} complexes attract considerable interest since they are commonly used as contrast agents in magnetic resonance imaging (MRI).[8] Though MRI has tremendous medical applications, one of the major challenges is its relatively low sensitivity.[9,10] To increase the sensitivity, an additional agent called an MRI contrast agent (CA) is required, which alters the properties of nearby water protons after addition.[11] The capability or sensitivity of a CA is exhibited through its relaxivity (r). Relaxivity can be defined as the paramagnetic magnification of the relaxation rate of the water proton, which is directly proportional to the concentration of the CAs.[12,13] The most important MRI CAs are metal-based paramagnetic ions.[14] Discrete Gd^{3+} based complexes are widely used as clinical paramagnetic CAs due to their large number of unpaired electrons and slow electronic relaxation.[14,15] However, the toxicity profile of Gd^{3+} ion is very high. A large or repeated dose of them causes nephrogenic systemic fibrosis (NSF) in patients with renal disorder.[16-18] Current research focuses on developing safer MRI CAs with improved thermodynamic stability and kinetic inertness by using ligands that tightly bind $Gd^{3+,}$ preventing its release.[19,20] To reduce toxicity, many research groups focus on developing a CA with high relaxivity so that a lower dose can be administered.[21–23] Water exchange between the coordinated and the bulk water molecules is a key factor in optimizing CAs relaxivity. To enhance this, many groups[24–26] have explored CAs with multiple inner-sphere water

molecules. It is well established that, regardless of the field strength, relaxivity increases with the number of coordinated water molecules (q).[27] Merbach et al. first considered the whole lanthanide series to study the water exchange rate (k_{ex}^{298}).[28,29] Despite its significance, optimization of water exchange remains unexplored, with only limited studies reported.[30–33] The k_{ex}^{298} of the inner-sphere water molecules can be accelerated by factors such as increasing the overall compound negative charge and the steric hindrance surrounding the water molecules.[34] Clinically approved CAs contain only a single molecule of water in the inner coordination sphere.[30] The k_{ex}^{298} and structural elucidation of the most studied chelators 1,4,7,10-tetraaza-1,4,7,10-tetrakis(carboxymethyl) cyclododecane (DOTA)[35,36] and diethylenetriaminepentaacetic acid (DTPA)[37] have been well established. However, for $q > 1$ complexes, i.e. $[Ln(L)(H_2O)_{2\text{-}3}]^x$ [L= ligand, x= charge, Ln=La^{3+} to Lu^{3+}], no such systematic explanation of the water exchange and structural analysis has been done so far.[38,39] Indeed, with an increase in the number of inner-sphere water molecules, the ligand's denticity reduces, which may reduce the complexes' thermodynamic stability.

A few Gd^{3+} chelates with $q > 1$ have been reported. One such system is the Gd^{3+} complex of a pyridine-containing macrocyclic ligand with two acetic acids and one methylenephosphonic arm (PCP2A),[30,40] but further functionalization of this complex was found to be difficult. Another class of complexes with a higher hydration number ($q > 1$) is represented by tris-bidentate Gd^{3+}-hydroxypyridinone (HOPO) based derivatives, which are presently under strong scrutiny.[41] Previously, Bretonnière et al. synthesized a ligand α,α′,α″-nitrilotri(6-methyl-2-pyridinecarboxylic acid) (H_3tpaa) containing three picolinate groups with a longitudinal relaxivity value of 13.3 mM^{-1} s^{-1} at 1.4 T and 25˚C, and the stability was observed to be low.[42] In a subsequent study, they synthesized a Gd^{3+} complex with an octadentate N,N′-bis[(6-carboxy-2-pyridylmethyl]ethylenediamine-N,N′-diacetic acid (H_4bpeada) ligand, which has two picolinate groups with a longitudinal relaxivity of 5.0 mM^{-1} s^{-1} at a magnetic field of 20 MHz and 25˚C.[43] This relaxivity value is greater than for DOTA (r_1= 4.7 mM^{-1} s^{-1}) and DTPA (r_1 = 4.8 mM^{-1} s^{-1}).[44] The stability of this octadentate ligand (H_4bpeda) is less than that of the ethylenediaminetetraacetic acid (H_4EDTA) ligand, which is hexadentate in nature. Furthermore, the same group synthesized the ligand N, N′-bis[(6-carboxy-pyridin-2-yl)methyl] glycine (H_3dpaa),[45] replacing one of the picolinate groups with a carboxylate group. The ligand H_3dpaa exhibits a relaxivity value of 11.93 mM^{-1} s^{-1} at 4.7 T and 25˚C, with stability higher than the H_3tpaa ligand. Based on the above discussions, Phukan et al. synthesized a ligand H_4peada with one picolinate and three carboxylate groups to obtain higher relaxivity

and stability.[46] Later, they synthesized a hexadentate ligand (H_3cbda) with two picolinate and one carboxylate group to incorporate both the relaxivity and thermodynamic stability with a methyl group in the backbone of the ligand.[47]

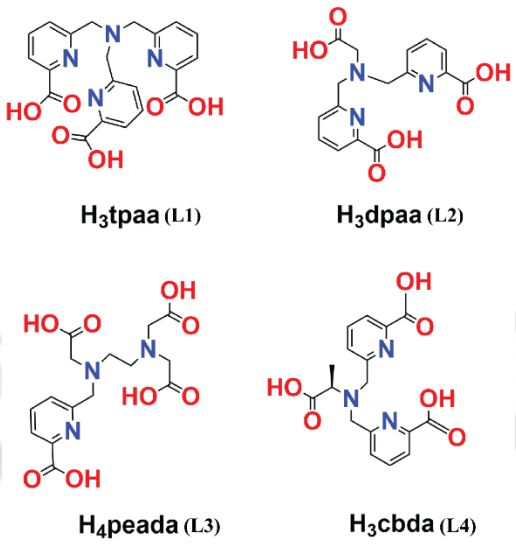

Figure 3.1. Ligands (L1[42]), (L2[45]), (L3[46]), and (L4[47]) considered in this study.

On account of the above perspectives, the present study uncovers the thermodynamic stability and comparative binding affinities of heptadentate ($peada^{4-}$ and $tpaa^{3-}$) and hexadentate ($cbda^{3-}$ and $dpaa^{3-}$) ligands (Figure 3.1) with Ln^{3+} ions in aqueous solution. Furthermore, the trend in the k_{ex}^{298} of the inner-sphere water with bulk water has been investigated, following the methodology proposed by Figueroa et al.[48] Moreover, this work computationally ascertained the k_{ex}^{298} mechanism based on the activation parameter values. The ligands chosen in this study are shown in Figure 3.1. In addition, the bonding interactions between the metal and ligand have been confirmed by the Quantum Theory of Atoms-In-Molecules (QTAIM) and energy decomposition analysis (EDA). This sheds light on the different binding affinity of the ligand with Ln^{3+} ions. Thus, we believe that the thermodynamic stability and mechanistic overview of the k_{ex}^{298} kinetics provided in this study will be helpful in future ligand design of stable lanthanide-based complexes.

3.2. Computational Details

All the geometries of the lanthanide complexes were optimized with relativistic density functional theory (DFT), using the hybrid meta-GGA TPSSh functional[48,49] as implemented in the Gaussian 16 program package.[50] The vibrational frequency analysis has been carried out to characterize the nature of the optimized geometries as energy minima or saddle points.

Additionally, we tested the performance of different density functionals (B3LYP, B3LYP-D3, and ωB97XD) for comparative purposes. The choice of the TPSSh functional is due to its better geometrical interpretation than the hybrid GGA (B3LYP) long-range corrected functional (ωB97XD) functional. [48,51] For the central metal atom (Ln^{3+}), we considered both large core relativistic effective core potential (LCRECP) with its related (7s6p5d)/[5s4p3d]-GTO valence basis set, and small core relativistic effective core potential (SCRECP)[52] with the ECP28MWB_GUESS[48] basis set for comparative purposes. The standard 6-31G(d,p) and 6-31+G(d,p) (for some specific calculations) basis sets were applied for the remaining elements (H, C, N, and O). The performance of different density functionals and basis sets is discussed in detail in the dedicated sections below. At the same level of theory, the transition state geometries were located, and the intrinsic reaction coordinate (IRC) paths were generated. Furthermore, to correct the activation energy barrier, we calculated the single point energy of the reactant and transition state by considering the wave function-based method, second order Møller-Plesset perturbation theory (MP2),[53] with the def2-TZVP basis set for the H, C, N, and O atoms.

The computational investigations of lanthanide complexes using relativistic effective core potential (ECP)[54,55] in conjugation with DFT, provide accurate results for most of the earlier reported complexes.[56,57] It has been mentioned earlier that large-core (LC) calculations provide a somewhat longer bond distance than that of the small-core (SC) calculations.[48] Despite its approximate nature, LCRECP is an efficient computational tool, which focuses mainly on the analysis of geometrical structures and estimation of relative energies of heavy metal-containing complexes at the DFT level.[48,58,59]

Moreover, to incorporate the solvent effect, the polarizable continuum model (PCM)[60,61] with the integral equation formalism, i.e. the IEFPCM[60] model, has been considered. To describe the accurate M-L bond and ^{17}O hyperfine coupling constant values, we have explicitly considered the second sphere of water along with the implicit solvent model (IEFPCM).[62,63] To describe the cavity of the solvent, universal force field radii[64] were applied and adjusted by a factor of 1.1. Optimization was carried out by imposing nosymm constraints. Furthermore, to evaluate the Gibbs free energy values, the solvation model based on density (SMD) has been applied to incorporate the non-electrostatic contributions.[65] Harmonic approximation was applied for the Gibbs free energy calculations at T = 298.15 K using four different density functionals (TPSSh, M06,[66] B3LYP-D3, and ωB97XD).

Wave function analysis was performed by applying Bader's Quantum Theory of Atoms-In-Molecules (QTAIM)[67,68] to obtain the electron density (ρ), electron localization function (ELF), and Laplacian of electron density (∇_ρ^2) at the bond critical points (BCPs) using the Multiwfn program (version 3.8).[69] Furthermore, for the extended transition state (ETS) energy decomposition analysis,[70] optimized structures of the $[Ln(cbda)(H_2O)_3].6H_2O$ and $[Ln(peada)(H_2O)_2]^-$. $4H_2O$ complexes were considered, having been obtained from the scalar relativistic[71] ZORA[72,73] method, along with the SARC-ZORA[74] basis set for the Ln^{3+} ion and the 6-31G(d,p) basis set for the rest of the elements. From these optimized structures, a single point energy decomposition analysis was performed in the ADF2021 package,[75] using SARC-ZORA approximation with the TZ2P[76] basis set for all the elements, and BP86 functional[77–79] with no frozen core approximation. This ETS analysis has been performed for the closed shell La^{3+} and Lu^{3+} metal centres. Due to their closed-shell character, spin-restricted formalism was applied.

The ORCA 4.0 program[80] package was used for the analysis of isotropic ^{17}O and ^{1}H hyperfine coupling constants, using TPSSh and the SARC2-DKH-QZVP[81] basis set for the Gd^{3+} ion and the DKH-def2-TZVPP[74] basis set for the remaining atoms. The molecular electrostatic potential (MEP) analysis was performed to evaluate the charge distribution of the complexes.[82,83] The MEP of the complexes was calculated using the Multiwfn program (version 3.8).[69]

The M-L binding energies (BEs) were evaluated from the optimized structures of the complexes (both LC and SC-optimized). The BEs were calculated by individually optimizing the geometries of the complexes, ligands (Figure 3.1), and inner-sphere water molecules. This includes basis set superposition error (BSSE) corrections using the counterpoise method[84] for the gas phase optimized structures of the complexes. The BEs of the ligands were also evaluated by doing single-point energy calculations using the TPSSh functional and LCRECP (for the Gd^{3+} ion) along with the def2-TZVP[85] basis set for the remaining elements (H, C, N, and O) to reduce the BSSE.

3.3. Results and Discussion

3.3.1. Stability Analysis of the Ln^{3+} Complexes

The stability of the Ln^{3+} complexes in aqueous solution is an important issue for the application of Ln^{3+} complexes, which can be decided mainly by two factors: (i) the binding energy of the

ligand to the metal ions and (ii) the solvation-free energy of the complexes and free metal ions. In the following two sections, these two factors are analyzed in detail.

3.3.1.1. Comparative Binding Energy (BE) Calculations of the Complexes

Initially, to ensure the strength of the ligands shown in Figure 3.1 with Gd^{3+} ions, the binding energies of the complexes were investigated. The optimized structures of the complexes considered for comparative binding energy calculations are shown in Figure 3.2.

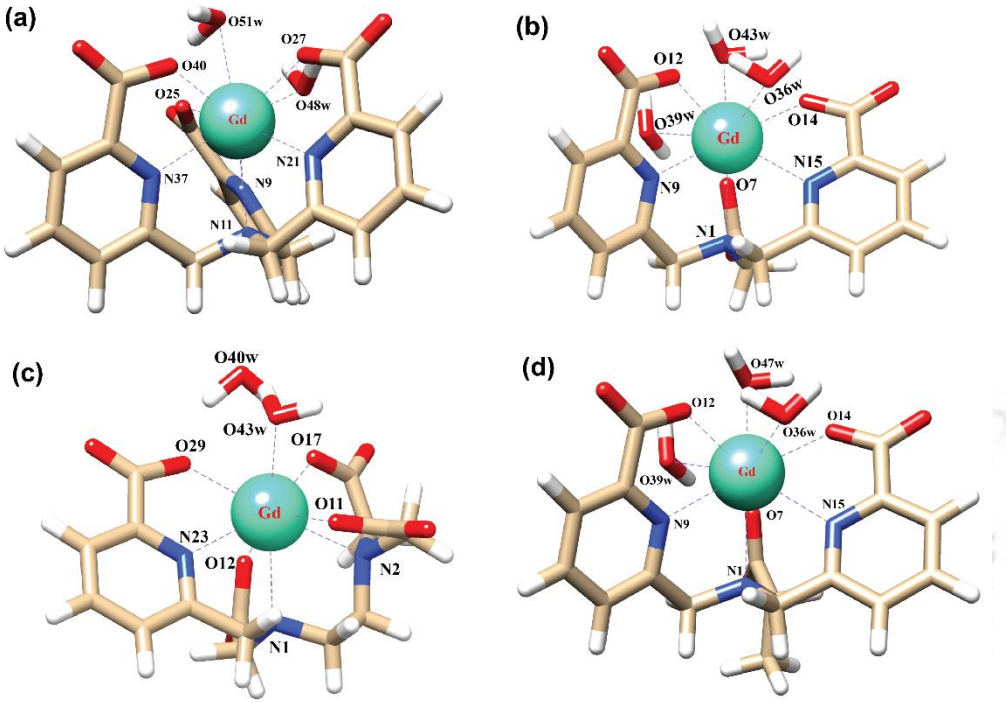

Figure 3.2. Optimized structures of (a) $[Gd(tpaa)(H_2O)_2]$, (b) $[Gd(dpaa)(H_2O)_3]$, (c) $[Gd(peada)(H_2O)_2]^-$, and (d) $[Gd(cbda)(H_2O)_3]$ complexes in aqueous solution using the TPSSh/SCRECP/6-31G(d,p) level of theory without the second sphere waters.

The results provided herein illustrate that the binding affinity of the ligand $peada^{4-}$ (-197.13 kcal mol^{-1}) with a Gd^{3+} ion is about +31.4 kcal mol^{-1} higher than that of the $tpaa^{3-}$ ligand (-165.73 kcal mol^{-1}), which agrees with the experimental results.[46] This is due to the presence of the three carboxylate groups, which bind more strongly to Gd^{3+} due to the oxyphilic nature of the Gd^{3+} ion.[46] Also, the binding affinity of the ligand $cbda^{3-}$ (-166.42 kcal mol^{-1}) is about +1.36 kcal mol^{-1} greater than that of the $dpaa^{3-}$ ligand (-165.06 kcal mol^{-1}). This may be due to the chirality induced by the methyl group in the ligand (H_3cbda) in line with the experimental results.[47] Evaluation of BE values using both core LC and SC pseudopotentials (Table A1-A2 of Appendix-A) regarding both sets of complexes (hexa and heptadentate) provided a similar trend in BE values. To validate our method, we re-evaluated the BE values of the respective

ligands with the Gd^{3+} using the LC optimized structure with def2-TZVP basis set and methods (B3LYP-D3, and ωB97XD).

3.3.1.2. Estimation of Thermodynamic Stabilities

To gain further insights into the reasons behind the relative thermodynamic stabilities of the ligands (Figure 3.1) with the Gd^{3+} ion, the free energy of formation of the complexes was estimated by using the methodology developed by Figueroa et al.[20,86] The thermodynamic cycle to determine the free energy of formation of the ligands $dpaa^{3-}$ and $cbda^{3-}$ with a Gd^{3+} ion is presented in Scheme 3.1.

As expected[47], the $\triangle G_{(g)}$ and $\triangle G_{(aq)}$ values tend to be negative on replacing the hexadentate $dpaa^{3-}$ ligand with the $cbda^{3-}$ ligand. The negative $\triangle G_{(g)}$ and $\triangle G_{(aq)}$ indicate the stronger binding affinity of the $cbda^{3-}$ ligand with the Gd^{3+} ion than the $dpaa^{3-}$ ligand, both in the gas phase and solution phase. This confirms the influence of the methyl group in the ligand backbone for increased stability of the [Gd(cbda)] complex compared to the [Gd(dpaa)] complex. Different density functionals (B3LYP, TPSSh, M06, B3LYP-D3, and ωB97XD) and core definitions (LC and SC) provide a similar trend in the $\triangle G_{(g)}$ and $\triangle G_{(aq)}$ values and ligand selectivity, as shown in Table A3 of Appendix-A.

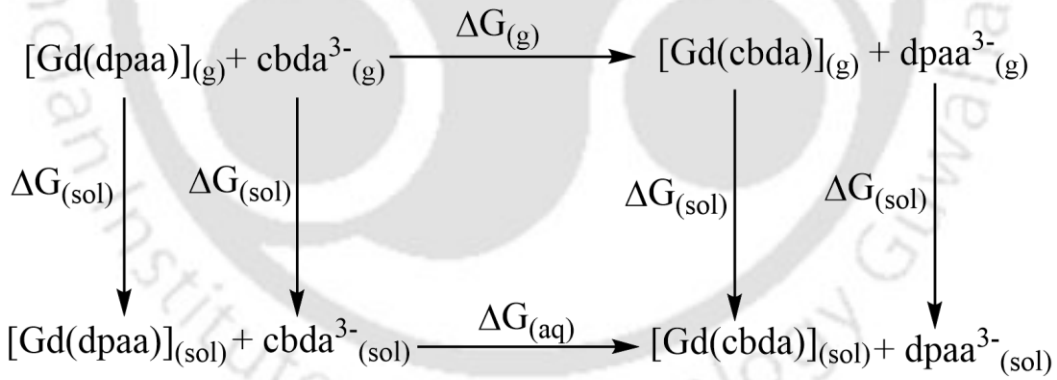

Scheme 3.1. Thermodynamic cycle for explaining the comparative stabilities of [Gd(cbda)] and [Gd(dpaa)] complexes.

Similarly, for the heptadentate ligand bearing $[Gd(peada)]^-$ and [Gd(tpaa)] complexes, the thermodynamic stabilities of the ligands $peada^{4-}$ and $tpaa^{3-}$ with the Gd^{3+} ion were analyzed. In this case, it was found that the $[Gd(peada)]^-$ complex formation is more stable than the [Gd(tpaa)] complex, with higher negative $\triangle G_{(g)}$ and $\triangle G_{(aq)}$ values (Table A4 in Appendix-A) owing to the presence of four negative carboxylate groups compared to the $tpaa^{3-}$ ligand.

These stability trends follow the experimental analysis of the thermodynamic stability of the complexes.[46,47] The experimental $\triangle G^{exp}_{(aq)}$ values, as shown in Tables A3 and A4, were estimated from the equilibrium constant values provided in the earlier literature.[46,47] Furthermore, different density functionals (TPSSh, M06, B3LYP-D3, and ωB97XD), and basis sets (6-31G(d,p) and 6-31+G(d,p)) impart similar trends in $\triangle G_{(g)}$ and $\triangle G_{(aq)}$ values and ligand selectivity (Tables A3 and A4 in Appendix-A).

In view of the above stability analysis, we will consider the more stable heptadentate (H_4peada) and hexadentate (H_3cbda) ligands for further investigation.

3.3.2. Structural Analysis

In order to explore the coordination polyhedra and bonding interactions of the ligands ($peada^{4-}$ and $cbda^{3-}$) with lanthanide series elements, we have considered the stable La^{3+} ($4f^0$), Gd^{3+} ($4f^7$) and Lu^{3+} ($4f^{14}$) ions. The optimized structures of the $[Ln(peada)(H_2O)_2]^-$ and $[Ln(cbda)(H_2O)_3]$ complexes [Ln = La, Gd, and Lu], obtained using the SC pseudopotential are shown in Figure 3.3 To limit the drawbacks of the continuum solvation model,[62,87,88] six explicit water molecules for the tris-aquated and four explicit water molecules for the bis-aquated complexes have been considered.

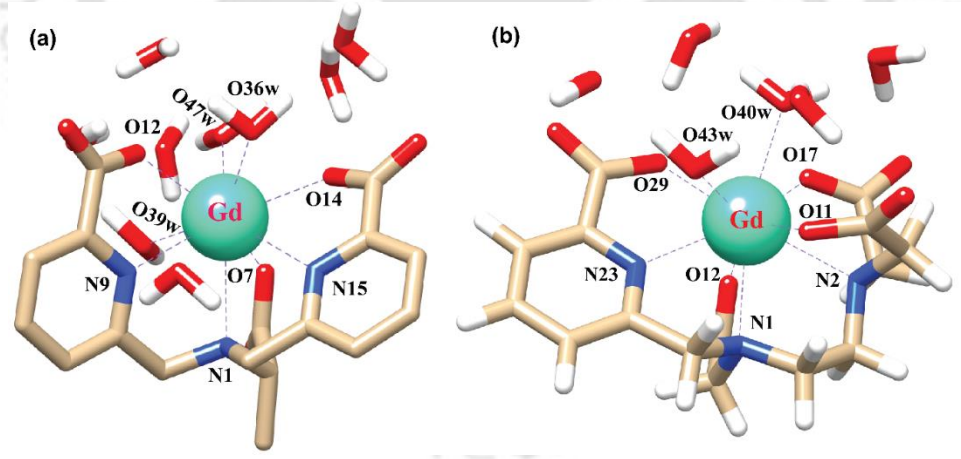

Figure 3.3. Optimized structures of the complexes (a) $[Gd(cbda)(H_2O)_3].6H_2O$, and (b) $[Gd(peada)(H_2O)_2]^-.4H_2O$ with second sphere waters obtained using the TPSSh/SCRECP/6-31G(d,p) level of theory.

The bond distances from SC and LC pseudopotentials (Tables A5-A6 in Appendix-A), are longer for LCRECP than SCRECP in line with previous investigations,[48] the bond length values are in good agreement with the previously synthesized $q > 1$ complex.[39,89] The labilities of the three water molecules in tris-aquated $[Gd(cbda)(H_2O)_3].6H_2O$ and the two water

molecules in the $[Gd(peada)(H_2O)_2]^-.4H_2O$ complex were found to be different based on the bond length analysis and the complexes are anticipated to exhibit different water exchange rates (k_{ex}^{298}). The bond length values decrease along the series as predicted as a consequence of the lanthanide contraction, as shown in Figure. 3.4 (a) and (b). The values calculated using SCRECP decreased from La^{3+} to Lu^{3+} with some fluctuation. At first, for the tris-aquated complex, the bond length values followed the trend Ln-O36 (w) > Ln-O39 (w) > Ln-O47 (w), and the fluctuations of the bond lengths were higher for Ln-O36 (w) and Ln-O39 (w) compared to Ln-O47 (w) due to the steric and pulling effects of water molecules, which reflects the weaker binding of the water molecules as shown in Figure 3.4 (a). In the bis-aquated complex, the bond length values follow the trend Ln-O40 (w) > Ln-O43 (w) (Figure. 3.4 (b)). Moreover, the average Ln-N bond length values for the tris-aquated and bis-aquated complexes decrease from 2.79 to 2.66 Å and 2.77 to 2.57Å, respectively. Whereas, the Ln-O (carboxylate) bond length only drops from 2.49 to 2.33 Å and 2.43 to 2.27 Å, respectively (Figure 3.4 (a-b)). In both bis and tris-aquated metal coordination polyhedra, the shortest distance is between the Ln^{3+} ion and the carboxylate oxygen because of the hard-hard interaction of oxygen and the Ln^{3+} ion according to Pearson's HSAB concept.[90]

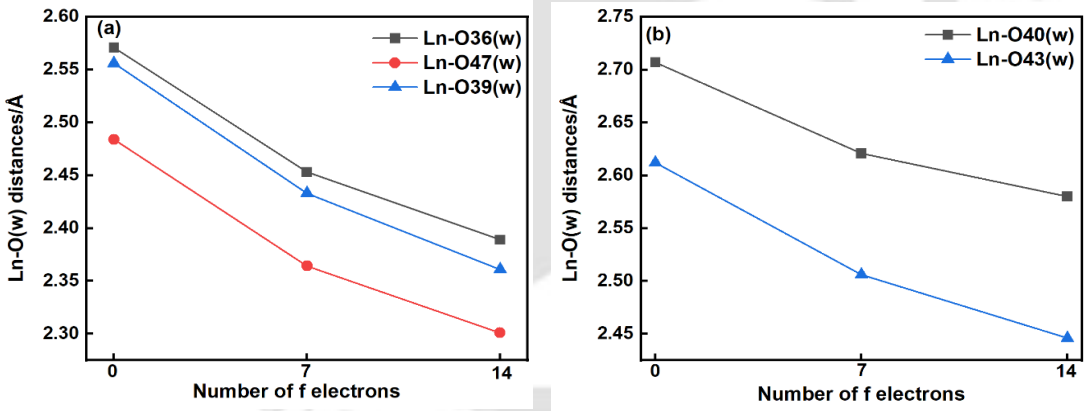

Figure 3.4. Variation of Ln-O(w) bond lengths along the lanthanide series (La, Gd, Lu) for (a) $[Ln(cbda)(H_2O)_3].6H_2O$ and (b) $[Ln(peada)(H_2O)_2]^-.4H_2O$ complexes obtained at the TPSSh/SCRECP/6-31G(d,p) level of theory.

The metal-(H_2O) bond strength was further confirmed by analysis of the electron density (ρ_{BCP}), the Laplacian of the electron density (∇_ρ^2), and the electron localization function (ELF) at the critical points of the respective bonds along the Ln^{3+}-series as presented in Tables A7-A8 in Appendix-A. Our investigations show that for the tris-aquated complex, the ρ_{BCP} values

follow the trend Ln-O47 (w) > Ln-O39 (w) > Ln-O36 (w), as shown in Figure 3.5 (a). Similarly, for the bis-aquated complex, the ρ_{BCP} value follows the trend Ln-O43 (w) > Ln-O40 (w) (Figure 3.5 (b)), opposite to that of bond length values. These ρ_{BCP} values tend to increase in the series' first half and then decrease. The decrease of the electron density indicates weaker binding of the inner-sphere water molecules.[48,91] Again, the ELF values decrease along the Ln^{3+}-series as ionic radii decrease. However, the bond length becomes shorter, indicating the weaker binding of water molecules at the end of the series as shown in Figure 3.5 (c) and (d). This agrees well with the labile capping bond phenomenon mentioned in previous literature.[91] The Ln-O (w) bond length values of the anionic $[Ln(peada)(H_2O)_2]^-.4H_2O$ complex are longer than those of the neutral $[Ln(cbda)(H_2O)_3].6H_2O$ complex, which indicates the faster k_{ex}^{298} in the anionic complex.[34] Furthermore, the calculation of ρ_{BCP}, ELF, and ∇_ρ^2, using the LC pseudopotential ensures the reliability of the SC pseudopotential for electron density calculations for $q > 1$ complexes.

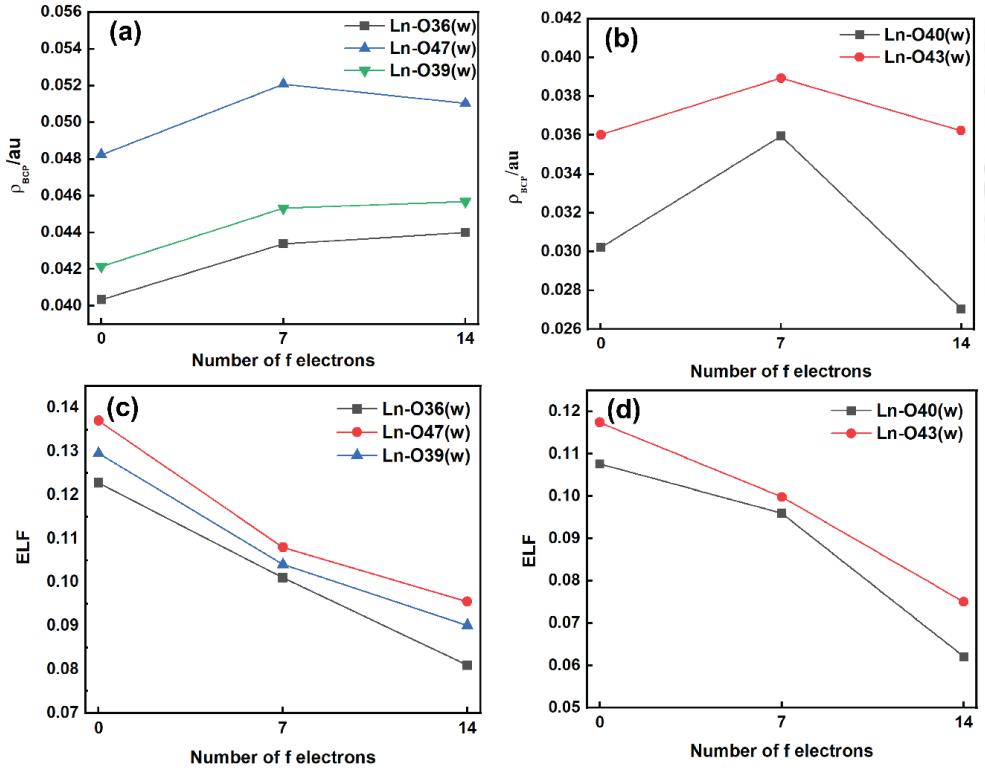

Figure 3.5. Electron density (ρ_{BCP}) and electron localization function (ELF) values along the Ln^{3+}-series for both $[Ln(cbda)(H_2O)_3].6H_2O$ (a and c) and $[Ln(peada)(H_2O)_2]^-.4H_2O$ (b and d) complexes at the TPSSh/SCRECP/6-31G(d,p) level of theory.

3.3.3. Evaluation of Water Exchange Kinetics

3.3.3.1. Stable Hydration Number (q) Calculations for Both Bis-Aquated and Tris-Aquated Complexes

The determination of the hydration state of Gd^{3+} complexes in aqueous solution is a challenging task. Yet, to understand the water exchange kinetics and relaxivity of Gd^{3+} complexes, understanding the hydration state of Gd^{3+} complexes is crucial. The relaxivity of Gd^{3+} complexes increases with an increase in q. Therefore, before determining the k_{ex}^{298}, we first analysed the stable hydration number of the complexes. We explore the stable hydration number of the tris-aquated $[Gd(cbda)(H_2O)_3].6H_2O$ and bis-aquated $[Gd(peada)(H_2O)_2]^-.4H_2O$ complexes using three different density functionals (B3LYP, TPSSh, and M06-2X). To determine the stable hydration number, a relaxed potential energy surface scan of the complexes was performed by changing the bond length values of each of the inner-sphere water molecules of the complexes, using a step size of 0.05Å as shown in Figure 3.6. These shows that the nine coordinated $[Gd(cbda)(H_2O)_3].6H_2O$ is more stable than the eight coordinated $[Gd(cbda)(H_2O)_2].7H_2O$ complex, in line with the experimental findings as shown in Figure 3.6 (a)-(c).[47] All three functionals (B3LYP, TPSSh, and M06-2X) provide similar trends in stable hydration numbers.

Based upon the above analysis, for the bis-aquated $[Gd(peada)(H_2O)_2]^-.4H_2O$ complex we considered only one functional (TPSSh). The scanning of the Gd-O40(w) bond stabilized the eight coordinated $[Gd(peada)(H_2O)]^-.5H_2O$ and the scanning of Gd-O43(w) stabilized the nine coordinated $[Gd(peada)(H_2O)_2]^-.4H_2O$ complex, in accordance with the experimental analysis[46] of the hydration equilibria, showing the co-existence of both eight and nine coordinated forms as shown in Figure. 3.6 (d)-(e). This co-existence is due to the flexible ligand environment due to the presence of four carboxylate groups. The relaxed PES scans for both complexes obtained using the SC pseudopotential are provided in Figure A1 in Appendix-A.

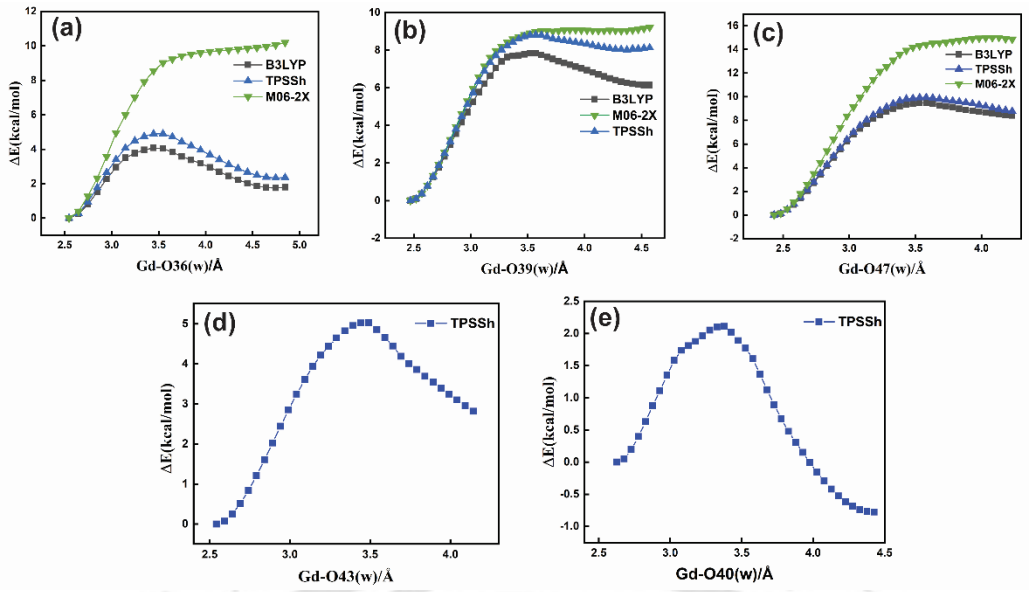

Figure 3.6. Relaxed potential energy surface scans for the $[Gd(cbda)(H_2O)_3].6H_2O$ complex (top) (a-c) and $[Gd(peada)(H_2O)_2]^-.4H_2O$ (bottom) (d-e) using LCRECP for Gd^{3+} and the 6-31G(d,p) basis set for other elements with different density functionals.

3.3.3.2. Hyperfine Coupling Constants (HFCCs) of the Inner Sphere Water Molecules

Computational investigations of the hyperfine interaction (HFI) of the coordinated water molecules with the metal centre (Gd^{3+}) have been carried out to deliver a brief illustration of the water exchange rate. During the last few decades, enormous improvements have been made in the study of HFI. Among them, DFT can be extensively used for systems containing a large number of atoms with experimental accuracy.[62,87,88] The ^{17}O and ^{1}H HFCC values are very sensitive to the change in bond length and the direction and position of the inner-sphere water molecule plane with the Gd-O vector. Therefore, applying the methodology proposed by Esteban Gómez et al.[62], we have calculated the HFCCs of the coordinated water molecules in both complexes as presented in Table 3.1. The three water molecules in the $[Gd(cbda)(H_2O)_3].6H_2O$ complex have different HFCC values in accordance with the different Gd-O (w) bond lengths. Similarly, in the bis-aquated $[Gd(peada)(H_2O)_2]^-.4H_2O$ complex, the two water molecules have significantly different ^{17}O HFCC values, with one having an extremely low value (0.2156 MHz) due to the existence of hydration equilibria for this complex.[46] Moreover, the isotropic (A_{iso}) HFCC values for the ^{1}H nucleus are minimal for these complexes.

Table 3.1. ^{17}O and ^{1}H hyperfine coupling constant values for $[Gd(cbda)(H_2O)_3].6H_2O$ and $[Gd(peada)(H_2O)_2]^{-}.4H_2O$ complexes using the TPSSh/DKH2/SARC2-DKH-QZVP (Gd)/DKH-def2-TZVPP (other atoms)/SMD method.

Ligand	Gd-O(w) (Å)	^{17}O (A_{iso}) (MHz)	^{1}H (MHz)
$cbda^{3-}$	Gd-O36(w) = 2.45	0.5491	0.0227/0.0390
	Gd-O39(w) = 2.43	0.6052	0.0633/0.0696
	Gd-O47(w) = 2.36	0.9661	0.0220/0.0350
$peada^{4-}$	Gd-O40(w) = 2.62	0.2156	0.0536/0.0517
	Gd-O43(w) = 2.50	0.4724	0.0746/0.0102

3.3.3.3. Water Exchange Rate (k_{ex}^{298}) for the Bis-Aquated and Tris-Aquated Complexes

To analyze the trend in the k_{ex}^{298} of all the coordinated water molecules with the bulk, we considered the Gd-O(w) bond length values. A longer Gd-O(w) bond means a shorter residence time related to the coordinated water molecule, as confirmed by the *ab initio* molecular dynamics study of [Gd(HP-DO3A)].[92] With an increase in the bond length, the residence time of the water molecule decreases.[32,48] Thus, a longer bond length value implies a faster k_{ex}^{298} value following a dissociative type of mechanism. Therefore, we will apply the model proposed by Figueroa et al.[48] to elucidate the k_{ex}^{298} by calculating ρ_{BCP} and ELF at the bond critical point of the respective bond. As a result, the three water molecules in $[Gd(cbda)(H_2O)_3].6H_2O$ and two water molecules in $[Gd(peada)(H_2O)_2]^{-}.4H_2O$ have significantly different k_{ex}^{298} values (Table 3.2). We employ Eq. 3.1 and Eq. 3.2 for LCRECP, and Eq. 3.3 and Eq. 3.4 for SCRECP to evaluate k_{ex}^{298} values computationally. The k_{ex}^{298} values obtained using LC optimized geometries with different density functionals (TPSSh, B3LYP-D3, and ωB97XD) are listed in Tables A9 and A10 in Appendix-A. The k_{ex}^{298} follows a similar trend for all the density functionals.

For LCRECP,

$$\rho_{BCP} = 0.05941 - 0.00316\, log k_{ex}^{298} \quad (3.1)$$

$$ELF = 0.13532 - 0.00503\, log k_{ex}^{298} \quad (3.2)$$

For SCRECP,

$$\rho_{BCP} = 0.06440 - 0.00325\, log k_{ex}^{298} \quad (3.3)$$

$$ELF = 0.12275 - 0.00296\, log k_{ex}^{298} \quad (3.4)$$

Table 3.2. Calculated Gd-O(w) bond length (r, au), ρ_{BCP}, ELF, and k_{ex}^{298} values of $[Gd(cbda)(H_2O)_3].6H_2O$ and $[Gd(peada)(H_2O)_2]^-.4H_2O$ complexes obtained using the TPSSh/SCRECP/6-31G(d,p) method.

Ln-O(w) bond length	ρ_{BCP}	ELF	k_{ex}^{298} /10^6 s^{-1}
$[Gd(cbda)(H_2O)_3].6H_2O$			
Gd-O36(w) = 2.453	0.04338	0.101	22.16
Gd-O39(w) = 2.433	0.04532	0.104	1.4
Gd-O47(w) = 2.364	0.05207	0.108	0.10
$[Gd(peada)(H_2O)_2]^-.4H_2O$			
Gd-O40(w) = 2.621	0.0359	0.0959	750.5
Gd-O43(w) = 2.506	0.0389	0.0998	56.6

From this analysis, we can conclude that the k_{ex}^{298} in bis and tris-aquated complexes is mainly related to the strength of the Gd-O(w) bond to reach the eight coordinated transition states (TS). The relatively high k_{ex}^{298} of the $[Gd(peada)(H_2O)_2]^-.4H_2O$ complex is due to the overall negative charge of the complex, as anionic complexes exhibit a faster k_{ex}^{298} than neutral complexes.[34] Among the two water molecules, Gd-O40(w) with a bond length of 2.62 Å shows a very high k_{ex}^{298}, which may be related to the hydration equilibrium between the mono and bis-aquated forms and the flexible coordination sphere surrounding the Gd^{3+} ion.

3.3.3.4. Mechanism of Water Exchange

DFT-based methods have been applied widely for the investigation of the k_{ex}^{298} and mechanism of metal-containing complexes. To elucidate whether factors other than the bond strength can also affect the k_{ex}^{298}, a mechanistic study has been conducted and the corresponding activation

parameter values of the complexes were calculated (Table 3.3). Generally, water exchange of the inner-sphere water molecules with bulk water for nine coordinated complexes mostly follows a dissociative mechanism.[44] To locate the TS, we optimized the structure that connects the nine and eight-coordinated forms of the complexes. The optimized TSs of the complexes are shown in Figure A2 and A3 in Appendix-A. An elongated Gd-O(w) bond facilitates faster exchange for a dissociative type of mechanism.[48] Thus, the Gd-O(w) bond length values at the transition states (TSs) indicate a dissociative mechanism. The Gd-O(w) bond length values of both tris-aquated $[Gd(cbda)(H_2O)_3].6H_2O$ and bis-aquated $[Gd(peada)(H_2O)_2]^-.4H_2O$ complexes increase in the transition state (TS) compared with their elementary states as shown in Table 3.3. In the case of the tris-aquated complex, the values increase from 2.53 Å, 2.46 Å, and 2.42 Å to 3.48 Å, 3.37 Å, and 3.55 Å, for Gd-O36(w), Gd-O39(w) and Gd-O47(w), respectively. Similar results are obtained in the case of the bis-aquated complex (Table 3.3). Thus, this confirms that a water molecule in the inner coordination sphere leaves the metal coordination environment, following a dissociative mechanism.

Moreover, we observe that the activation free energy ($\triangle G^{\ddagger}$) values increase with a decrease in the bond length for both complexes (Table 3.3). The analysis of the activation enthalpies ($\triangle H^{\ddagger}$) provides a shred of additional evidence for faster water exchange in Gd-O36(w) followed by Gd-O39(w) and Gd-O47(w) in the tris-aquated complex (Table 3.3). Further, for the bis-aquated complex, the $\triangle H^{\ddagger}$ value increases drastically from Gd-O40(w) to Gd-O43(w). In addition, the positive activation entropies ($\triangle S^{\ddagger}$) (Table 3.3) indicate a dissociative type of mechanism. Further, to confirm the nature of the mechanism, we have performed intrinsic reaction coordinate (IRC) calculations (Figure A4 in Appendix-A), ensuring the dissociative nature of the mechanism.

We tested both large core (4f, in core) and small core pseudopotentials and found that activation parameter values are sensitive to the core definitions. But both SCRECP and LCRECP show similar trends, except in Gd-O40 (w) (Table A11 in Appendix-A). The unexpectedly high k_{ex}^{298} in Gd-O40(w) is due to the very low $\triangle H^{\ddagger}$ values, is due to the weaker metal-water interaction. Moreover, the DFT (TPSSh) and MP2 methods exhibit quite similar values of activation energies (Table 3.3).

Table 3.3. Activation parameter values for $[Gd(cbda)(H_2O)_3]$. $6H_2O$ and $[Gd(peada)(H_2O)_2]^-$.$4H_2O$ complexes obtained using TPSSh/LCRECP/6-31G(d,p) and activation energy values calculated using the MP2/LCRECP/def2-TZVP level of theory.

		$[Gd(cbda)(H_2O)_3]$. $6H_2O$			$[Gd(peada)(H_2O)_2]^-.4H_2O$	
Methods	Parameters	Gd-O36(w)	Gd-O39(w)	Gd-O47(w)	Gd-O40(w)	Gd-O43(w)
TPSSh	$\triangle E^{\ddagger}$(kcal mol^{-1})	4.93	8.90	9.95	2.10	5.02
	$r_{Gd\text{-}O}$/Å	2.53	2.46	2.42	2.63	2.54
	$r_{Gd\text{-}O}$(TS)/Å	3.48	3.37	3.55	3.35	3.45
	$\triangle H^{\ddagger}$ (kcal mol^{-1})	4.26	8.31	9.25	1.34	4.32
	$\triangle G^{\ddagger}$ (kcal mol^{-1})	3.95	7.70	8.40	1.25	3.57
	$\triangle S^{\ddagger}$ (Jmol^{-1} K^{-1})	4.35	9.20	11.84	1.37	10.46
MP2	$\triangle E^{\ddagger}$(kcal mol^{-1})	4.24	8.67	8.80	1.43	4.54

3.3.4. Bonding Nature of the Complexes

3.3.4.1. Quantum Theory of Atoms-in-Molecules (QTAIM) Analysis

The bonding nature between the Ln^{3+} ion and the ligand was characterized with the help of Bader's Quantum Theory of Atoms-In-Molecules (QTAIM) and electron localization function (ELF) analysis. The primary application of QTAIM is the topological analysis of the electron density to characterize the important bonding nature of the M-L bonds. The locations of the respective BCPs in the $[Gd(cbda)(H_2O)_3].6H_2O$ and $[Gd(peada)(H_2O)_2]^-.4H_2O$ complexes are presented in Figure 3.7 (a) and (b) respectively. The orange dots indicate the BCPs in M-O/ N bonds. The value of ρ_{BCP} and its Laplacian (∇_ρ^2) at the BCPs suggest the type of bonding. The value $\rho_{BCP} < 0.10$ au and the positive ∇_ρ^2 value signifies ionic bonding (Tables A7 and A8 in Appendix-A). Thus, the electrostatic nature of the bonding is reflected.

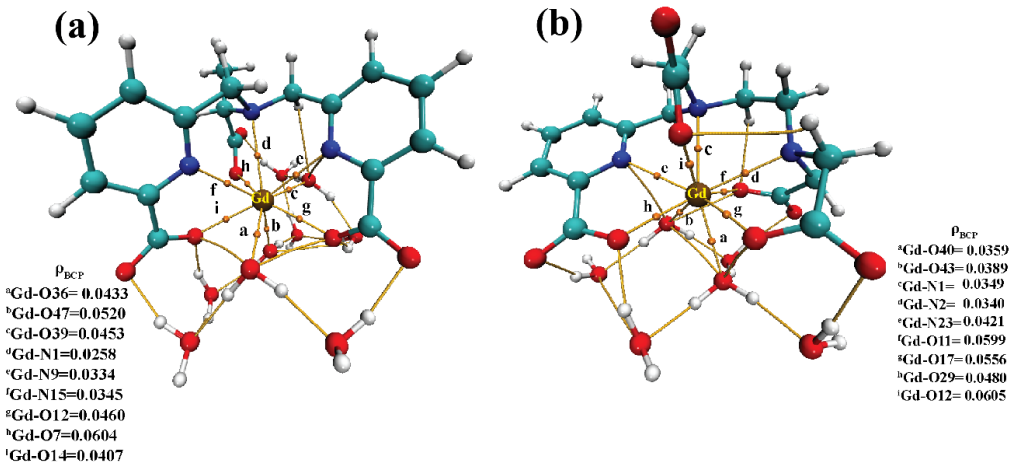

Figure 3.7. ρ_{BCP} values of (a) [Gd(cbda)(H_2O)$_3$].6H_2O and (b) [Gd(peada)(H_2O)$_2$]$^-$.4H_2O complexes.

To further evaluate the metal-ligand bonding interaction, the electron localization function (ELF) was employed (Figure 3.8). ELF is a simple and useful descriptor of the topological analysis of chemical bonds based on Pauli's repulsion effect.

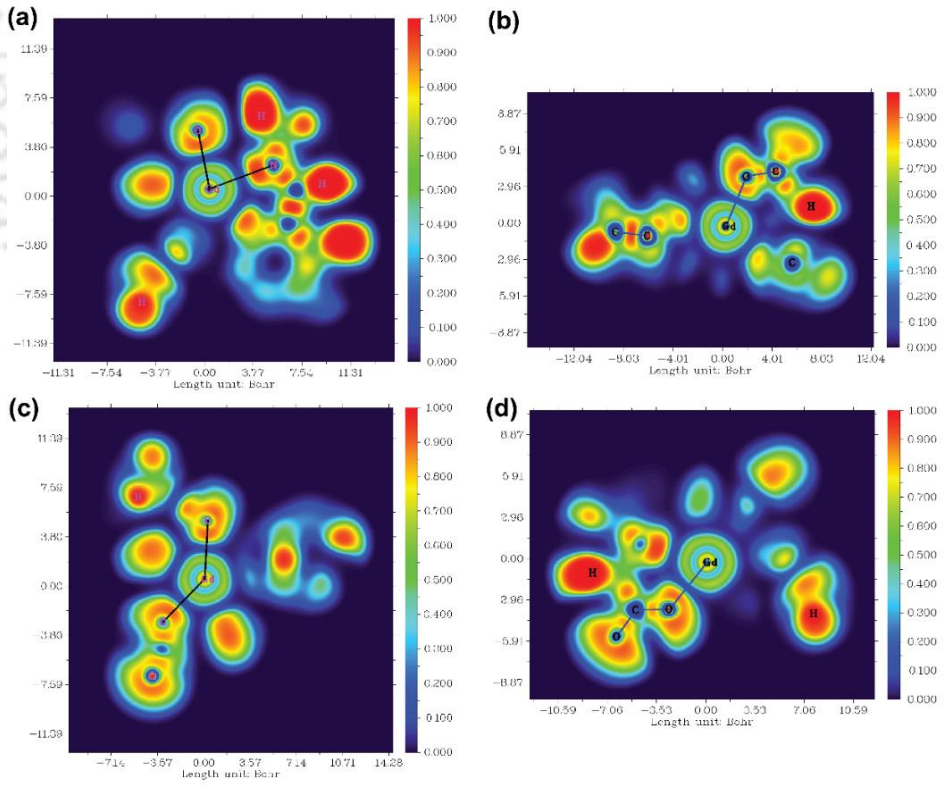

Figure 3.8. (a) and (b) ELF plots in the XZ and YZ planes for the [Gd(cbda)(H_2O)$_3$].6H_2O complex, and (c) and (d) ELF plots in the XZ and YZ planes for the [Gd(peada)(H_2O)$_2$]$^-$.4H_2O complex.

In the ELF color-filled map surface (Figure 3.8), the region between the metal (Gd^{3+}) and the oxygen or nitrogen atoms of the ligands is considered. The color scale is from 0 (blue) to 1 (red), as shown in Figure 3.8. According to Becke and Edgecombe,[93] an ELF value close to 1 (colored red in Figure 3.8) indicates the highest Pauli's repulsion zone. While a value close to 0 indicates the minimum Pauli's repulsion zone which is colored blue in the ELF color-filled map (Figure 3.8). The highest Pauli's repulsion zone corresponds to the localization of electrons, indicating covalent bonding, but electrons are delocalized in the lowest Pauli's repulsion area. Subsequently, in our analysis the ELF values are close to 0 (Tables A7-A8 in Appendix-A), exhibiting clearly the ionic nature of the M-L bond.

3.3.4.2. Energy Decomposition Analysis (EDA)

An in-depth analysis of the metal-ligand interaction was further carried out by the extended transition state method (ETS). For this, we have conducted an EDA analysis by considering the closed-shell La^{3+} and Lu^{3+} complexes of hexadentate ($cbda^{3-}$) and heptadentate ($peada^{4-}$) ligands. The different fragmentation model is shown in Figure 3.9. The total interaction energy ($\triangle E_{int}$) between the considered fragments [fragment 1 = Ln^{3+} and fragment 2 = ligand + H_2O] can be represented by the Morokuma-Ziegler energy partitioning model[94] as

$$\triangle E_{int} = \triangle V_{elst} + \triangle E_{pauli} + \triangle E_{oi} \qquad (3.5)$$

where $\triangle V_{elst}$ represents the classical electrostatic interactions between the different fragments when they are brought together, forming the complex, $\triangle E_{pauli}$ is the Pauli repulsion, especially the repulsion due to steric interactions, and $\triangle E_{oi}$ represents the orbital interactions.

The detailed physical significance of the above terms has been described by Bickelhaupt and Baerends.[95] The data for the EDA analysis are presented in Table A12 in Appendix-A. We observed that the attractive interaction within the M-L complex is derived from the $\triangle E_{oi}$ and $\triangle E_{elst}$ terms. Moreover, in ionic bonding, $\triangle E_{oi}$ is less than $\triangle E_{elst}$ but the opposite is true for covalent bonds. This analysis assesses the interaction of the ligand ($cbda^{3-}$ and $peada^{4-}$) with La^{3+} and Lu^{3+} to understand the strength and the changes in the M-L bonding in the series.

In particular, the data presented in Table A12 in Appendix A reflects the following salient features:

(I) A relationship can be derived between the metal complex stability in terms of interaction energy ($\triangle E_{int}$) and the f-electrons. The $\triangle E_{int}$ value of the Lu-ligand

(a fully occupied f-shell) complex is higher than that of the La-ligand complex (an empty f-shell).

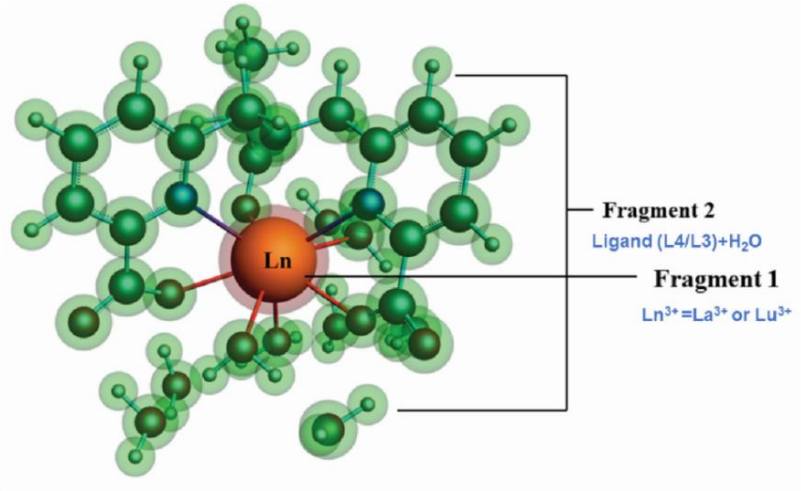

Figure 3.9. Schematic representation of different fragmentation modes of the $[Ln(cbda)(H_2O)_3].6H_2O$ and $[Ln(peada)(H_2O)_2]^-.4H_2O$ complexes (Ln = La^{3+} and Lu^{3+}).

(II) The electrostatic contribution is about two to three times larger in magnitude than the covalent contribution in f^0 and f^{14} systems, implying that M-L bonding is predominantly electrostatic in nature than covalent.

(III) Again, as the charge character of the ligand increases from $cbda^{3-}$ to $peada^{4-}$, the electrostatic contribution of the $[Ln(peada)]^-$ complex is larger compared to the [Ln(cbda)] complex, with higher percentage of electrostatic contribution in the $[Ln(peada)]^-$ complex.

(IV) The percentage of electrostatic contribution decreases from La (f^0) to the Lu (f^{14}) system, i.e., the covalent contribution is somewhat larger in the Lu (f^{14}) system.

(V) The Pauli ($\triangle E_{pauli}$) and orbital $\triangle E_{oi}$ contributions do not change markedly upon changing the ligand charges, as they fluctuate only within a few hundred $kJmol^{-1}$.

3.3.5. Analysis of Molecular Electrostatic Potential (MEP)

Molecular electrostatic potential analysis was performed to understand the charge distribution within the respective molecules based on their ligand's denticity (hexadentate or heptadentate). This helps evaluate the different interactive behaviour, reactivity, and structure of the molecules.[96] As noted earlier,[86] different colors of the molecular surface indicate different interactive areas. On account of this, we have investigated the MEP of the $[Gd(cbda)(H_2O)_3]$ and $[Gd(pada)(H_2O)_2]^-$ complexes, as shown in Figures 3.10 (a-b). The molecular surface shows two distinct regions: hydrophilic (blue) and hydrophobic (red). The blue color of the

$[Gd(peada)(H_2O)_2]^-$ complex indicates a hydrophilic area and a more negative electrostatic potential. This is due to the four carboxylic groups pointing in the same direction and the overall negative charge of the anionic complex. In the neutral $[Gd(cbda)(H_2O)_3]$ complex, carboxylate groups (three) are present and attached at different sides of the complex.

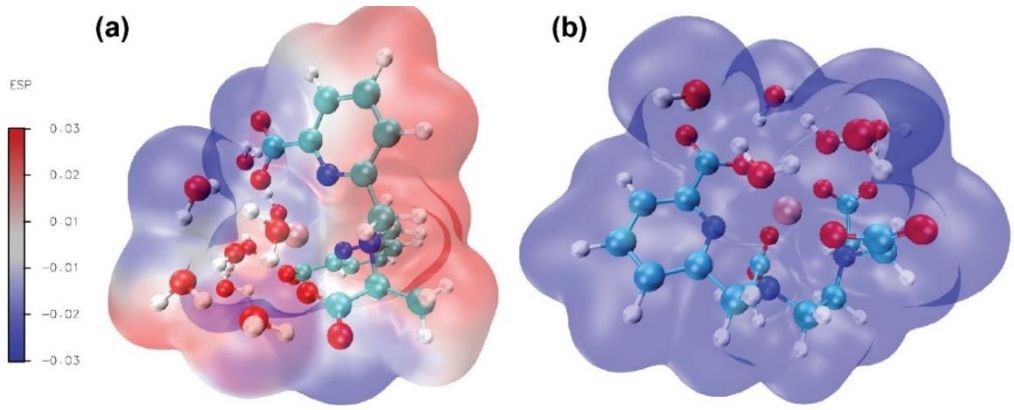

Figure 3.10. Computed molecular electrostatic potentials for: (a) $[Gd(cbda)(H_2O)_3].6H_2O$ and (b) $[Gd(peada)(H_2O)_2]^-.4H_2O$ complexes at the TPSSh/SCRECP/6-31G(d,p) level. Blue represents the highest electron density.

3.4. Conclusions

In summary, the stability of lanthanide complexes varies with the nature and environment of the ligand. First, a comparison of the coordination properties and the thermodynamic stability of hexadentate ($cbda^{3-}$ and $dpaa^{3-}$) and heptadentate ($peada^{4-}$ and $tpaa^{3-}$) ligands with the Gd^{3+} ion was carried out in aqueous solution. The stability analysis indicates that the hexadentate $cbda^{3-}$ ligand forms a reasonably stable complex with the Gd^{3+} ion than $dpaa^{3-}$ ligand. The methyl group in the $cbda^{3-}$ backbone enhances its selectivity. Likewise, the four carboxylate groups in $peada^{4-}$ increase its selectivity towards Gd^{3+} ion. A detailed structural analysis reveals that $[Gd(cbda)(H_2O)_3].6H_2O$ has a stable hydration number of three, while $[Gd(peada)(H_2O)_2]^-.4H_2O$ exists in equilibrium between mono- and bis-aquated forms. Kinetic analysis of k_{ex}^{298} shows that inner-sphere water molecules has varying exchange rate depending on the ligand environment. The increased k_{ex}^{298} is related to the weaker Ln-O(w) bond length, low electron density, and low ELF value. Mechanistically, a dissociative water exchange pathway is observed. However, we have established that for the bis-aquated complex, one coordinated water exhibits an unexpectedly fast k_{ex}^{298} rate (k_{ex}^{298}= 750 × 10^6 s^{-1}). This is due to the existence of hydration equilibria and a flexible ligand environment. Additionally, this study confirms that

the M-L bonding interaction is purely ionic. The percentage of electrostatic contribution increases with the increased charge of the ligand and decreases from La (f^0) to Lu (f^{14}) systems. The interaction energy between the metal and ligand was found to increase in the order $[La(cbda)(H_2O)_3]$ < $[Lu(cbda)(H_2O)_3]$ < $[La(peada)(H_2O)_2]^-$ < $[Lu(peada)(H_2O)_2]^-$. Thus, we believe that these findings will be helpful for designing lanthanide-based complexes with higher hydration numbers and stability. This lights the way for less toxic MRI contrast agents with higher relaxivity.

3.5. References

[1] D. Parker and J. A. G. Williams, *J. Chem. Soc. Dalton Trans.*, 1996, 3613-3628.

[2] E. Aluicio-Sarduy, N. A. Thiele, K. E. Martin, B. A. Vaughn, J. Devaraj, A. P. Olson, T. E. Barnhart, J. J. Wilson, E. Boros and J. W. Engle, *Chem. – Eur. J.*, 2020, **26**, 1238-1242.

[3] R. D. Teo, J. Termini and H. B. Gray, *J. Med. Chem.*, 2016, **59**, 6012-6024.

[4] J.-C. G. Bünzli, *Chem. Rev.*, 2010, **110**, 2729-2755.

[5] J. P. Leonard and T. Gunnlaugsson, *J. Fluoresc.*, 2005, **15**, 585-595.

[6] A. M. Nonat and L. J. Charbonnière, *Coord. Chem. Rev.*, 2020, **409**, 213192-213207.

[7] D. Carpanese, G. Ferro-Flores, B. Ocampo-Garcia, C. Santos-Cuevas, N. Salvarese, M. Figini, G. Fracasso, L. De Nardo, C. Bolzati, A. Rosato and L. Meléndez-Alafort, *Sci. Rep.*, 2020, **10**, 9313.

[8] Y.-D. Xiao, R. Paudel, J. Liu, C. Ma, Z.-S. Zhang and S.-K. Zhou, *Int. J. Mol. Med.*, 2016, **38**, 1319-1326.

[9] A. Webb, *Anal. Chem.*, 2012, **84**, 9-16.

[10] R. D. A. Alvares, D. A. Szulc and H.-L. M. Cheng, *Sci. Rep.*, 2017, **7**, 15493.

[11] P. Caravan, *Chem. Soc. Rev.*, 2006, **35**, 512-523.

[12] P. Marzola, F. Osculati and A. Sbarbati, *Eur. J. Radiol.*, 2003, **48**, 165-170.

[13] P. Caravan, C. T. Farrar, L. Frullano and R. Uppal, *Contrast Media Mol. Imaging*, 2009, **4**, 89-100.

[14] J. Wahsner, E. M. Gale, A. Rodríguez-Rodríguez and P. Caravan, *Chem. Rev.*, 2019, **119**, 957-1057.

[15] S. Aime, M. Botta, M. Fasano and E. Terreno, *Chem Soc Rev*, 1998, **27**, 19-29.

[16] S. A. Woolen, P. R. Shankar, J. J. Gagnier, M. P. MacEachern, L. Singer and M. S. Davenport, *JAMA Intern. Med.*, 2020, **180**, 223-230.

[17] D. Levine, R. J. McDonald and H. Y. Kressel, *JAMA*, 2018, **320**, 1853-1854.

[18] J. S. McDonald and R. J. McDonald, *Magn. Reson. Imaging Clin. N. Am.*, 2020, **28**, 497-507.

[19] M. Port, J.-M. Idée, C. Medina, C. Robic, M. Sabatou and C. Corot, *BioMetals*, 2008, **21**, 469-490.

[20] A. Rodríguez-Rodríguez, M. Regueiro-Figueroa, D. Esteban-Gómez, R. Tripier, G. Tircsó, F. K. Kálmán, A. C. Bényei, I. Tóth, A. D. Blas, T. Rodríguez-Blas and C. Platas-Iglesias, *Inorg. Chem.*, 2016, **55**, 2227-2239.

[21] B. Zhang, L. Cheng, B. Duan, W. Tang, Y. Yuan, Y. Ding and A. Hu, *Dalton Trans.*, 2019, **48**, 1693-1699.

[22] H. U. Rashid, M. A. U. Martines, J. Jorge, P. M. De Moraes, M. N. Umar, K. Khan and H. U. Rehman, *Bioorg. Med. Chem.*, 2016, **24**, 5663-5684.

[23] P. D. Garimella, A. Datta, D. W. Romanini, K. N. Raymond and M. B. Francis, *J. Am. Chem. Soc.*, 2011, **133**, 14704-14709.

[24] S. Aime, L. Calabi, C. Cavallotti, E. Gianolio, G. B. Giovenzana, P. Losi, A. Maiocchi, G. Palmisano and M. Sisti, *Inorg. Chem.*, 2004, **43**, 7588-7590.

[25] R. Negri, F. Carniato, M. Botta, G. B. Giovenzana and L. Tei, *ChemPlusChem*, 2016, **81**, 235-241.

[26] E. M. Gale, N. Kenton and P. Caravan, *Chem. Commun.*, 2013, **49**, 8060-8062.

[27] A. Varga-Szemes, P. Kiss, A. Rab, P. Suranyi, Z. Lenkey, T. Simor, R. G. Bryant and G. A. Elgavish, *PLOS ONE*, 2016, **11**, e0149260.

[28] C. Cossy, L. Helm and A. E. Merbach, *Inorg. Chem.*, 1988, **27**, 1973-1979.

[29] C. Cossy, L. Helm and A. E. Merbach, *Inorg. Chem.*, 1989, **28**, 2699-2703.

[30] S. Karimi and L. Helm, *Inorg. Chem.*, 2016, **55**, 4555-4563.

[31] Z. Baranyai, D. Delli Castelli, C. Platas-Iglesias, D. Esteban-Gomez, A. Bényei, L. Tei and M. Botta, *Inorg. Chem. Front.*, 2020, **7**, 795-803.

[32] L. Leone, D. Esteban-Gómez, C. Platas-Iglesias, M. Milanesio and L. Tei, *Chem. Commun.*, 2019, **55**, 513-516.

[33] B. Phukan, K. P. Malikidogo, C. S. Bonnet, É. Tóth, S. Mondal and C. Mukherjee, *ChemistrySelect*, 2018, **3**, 7668-7673.

[34] P. Caravan, D. Esteban-Gómez, A. Rodríguez-Rodríguez and C. Platas-Iglesias, *Dalton Trans.*, 2019, **48**, 11161-11180.

[35] P. Hermann, J. Kotek, V. Kubíček and I. Lukeš, *Dalton Trans.*, 2008, 3027-3047.

[36] S. Aime, M. Botta, M. Fasano, M. P. M. Marques, C. F. G. C. Geraldes, D. Pubanz and A. E. Merbach, *Inorg. Chem.*, 1997, **36**, 2059-2068.

[37] S. Laurent, L. V. Elst and R. N. Muller, *Contrast Media Mol. Imaging*, 2006, **1**, 128-137.

[38] M. K. Thompson, M. Botta, G. Nicolle, L. Helm, S. Aime, A. E. Merbach and K. N. Raymond, *J. Am. Chem. Soc.*, 2003, **125**, 14274-14275.

[39] Z. Baranyai, M. Botta, M. Fekete, G. B. Giovenzana, R. Negri, L. Tei and C. Platas-Iglesias, *Chem. – Eur. J.*, 2012, **18**, 7680-7685.

[40] S. Aime, M. Botta, L. Frullano, S. Geninatti Crich, G. Giovenzana, R. Pagliarin, G. Palmisano, F. R. Sirtori and M. Sisti, *J. Med. Chem.*, 2000, **43**, 4017-4024.

[41] A. Datta and K. N. Raymond, *Acc. Chem. Res.*, 2009, **42**, 938-947.

[42] Y. Bretonnière, M. Mazzanti, J. Pécaut, F. A. Dunand and A. E. Merbach, *Chem. Commun.*, 2001, 621-622.

[43] N. Chatterton, C. Gateau, M. Mazzanti, J. Pécaut, A. Borel, L. Helm and A. Merbach, *Dalton Trans*, 2005, 1129-1135.

[44] L. Helm, A. E. Merbach and É. Tóth, Eds., *The chemistry of contrast agents in medical magnetic resonance imaging*, John Wiley & Sons Inc, Hoboken, NJ, Second edition., 2013.

[45] A. Nonat, P. H. Fries, J. Pécaut and M. Mazzanti, *Chem. – Eur. J.*, 2007, **13**, 8489-8506.

[46] B. Phukan, C. Mukherjee and R. Varshney, *Dalton Trans.*, 2018, **47**, 135-142.

[47] M. Khannam, S. K. Sahoo and C. Mukherjee, *Eur. J. Inorg. Chem.*, 2019, **2019**, 2518-2523.

[48] M. Regueiro-Figueroa and C. Platas-Iglesias, *J. Phys. Chem. A*, 2015, **119**, 6436-6445.

[49] J. Tao, J. P. Perdew, V. N. Staroverov and G. E. Scuseria, *Phys. Rev. Lett.*, 2003, **91**, 146401.

[50] M. J. Frisch, G. W. Trucks, H. B. Schlegel, G. E. Scuseria, M. A. Robb, J. R. Cheeseman, G. Scalmani, V. Barone, G. A. Petersson, H. Nakatsuji, X. Li, M. Caricato, A. V. Marenich, J. Bloino, B. G. Janesko, R. Gomperts, B. Mennucci, H. P. Hratchian, J. V. Ortiz, A. F. Izmaylov, J. L. Sonnenberg, D. Williams-Young, F. Ding, F. Lipparini, F. Egidi, J. Goings, B. Peng, A. Petrone, T. Henderson, D. Ranasinghe, V. G. Zakrzewski, J. Gao, N. Rega, G. Zheng, W. Liang, M. Hada, M. Ehara, K. Toyota, R. Fukuda, J. Hasegawa, M. Ishida, T. Nakajima, Y. Honda, O. Kitao, H. Nakai, T. Vreven, K. Throssell, J. A. Montgomery, J. E. Peralta, F. Ogliaro, M. J. Bearpark, J. J. Heyd, E. N. Brothers, K. N. Kudin, V. N. Staroverov, T. A. Keith, R. Kobayashi, J. Normand, K. Raghavachari, A. P. Rendell, J. C. Burant, S. S. Iyengar, J. Tomasi, M. Cossi, J. M. Millam, M. Klene, C. Adamo, R. Cammi, J. W. Ochterski, R. L. Martin, K. Morokuma, O. Farkas, J. B. Foresman and D. J. Fox, Gaussian 16 Revision C.01, Gaussian Inc., Wallingford CT, 2016.

[51] A. Roca-Sabio, M. Mato-Iglesias, D. Esteban-Gómez, É. Tóth, A. D. Blas, C. Platas-Iglesias and T. Rodríguez-Blas, *J. Am. Chem. Soc.*, 2009, **131**, 3331-3341.

[52] M. Dolg, H. Stoll and H. Preuss, *J. Chem. Phys.*, 1989, **90**, 1730-1734.

[53] A. Grüneis, M. Marsman and G. Kresse, *J. Chem. Phys.*, 2010, **133**, 074107-11.

[54] M. Dolg and X. Cao, *Chem. Rev.*, 2012, **112**, 403-480.

[55] A. Weigand, X. Cao, J. Yang and M. Dolg, *Theor. Chem. Acc.*, 2010, **126**, 117-127.

[56] U. Cosentino, A. Villa, D. Pitea, G. Moro, V. Barone and A. Maiocchi, *J. Am. Chem. Soc.*, 2002, **124**, 4901-4909.

[57] R. O. Freire, G. B. Rocha and A. M. Simas, *J. Mol. Model.*, 2006, **12**, 373-389.

[58] L. Maron and O. Eisenstein, *J. Phys. Chem. A*, 2000, **104**, 7140-7143.

[59] D. Guillaumont, *J. Phys. Chem. A*, 2004, **108**, 6893-6900.

[60] J. Tomasi, B. Mennucci and R. Cammi, *Chem. Rev.*, 2005, **105**, 2999-3094.

[61] M. Cossi, V. Barone, R. Cammi and J. Tomasi, *Chem. Phys. Lett.*, 1996, **255**, 327-335.

[62] D. Esteban-Gómez, A. De Blas, T. Rodríguez-Blas, L. Helm and C. Platas-Iglesias, *ChemPhysChem*, 2012, **13**, 3640-3650.

[63] A. Zawada, R. W. Góra, M. M. Mikołajczyk and W. Bartkowiak, *J. Phys. Chem. A*, 2012, **116**, 4409-4416.

[64] A. K. Rappe, C. J. Casewit, K. S. Colwell, W. A. Goddard and W. M. Skiff, *J. Am. Chem. Soc.*, 1992, **114**, 10024-10035.

[65] A. V. Marenich, C. J. Cramer and D. G. Truhlar, *J. Phys. Chem. B*, 2009, **113**, 6378-6396.

[66] Y. Zhao and D. G. Truhlar, *Theor. Chem. Acc.*, 2008, **120**, 215-241.

[67] R. F. W. Bader, *Acc. Chem. Res.*, 1985, **18**, 9-15.

[68] R. F. W. Bader, *Atoms in molecules: a quantum theory*, Clarendon press, Oxford, 1994.

[69] T. Lu and F. Chen, *J. Comput. Chem.*, 2012, **33**, 580-592.

[70] M. P. Mitoraj, A. Michalak and T. Ziegler, *J. Chem. Theory Comput.*, 2009, **5**, 962-975.

[71] C. Van Wüllen, *J. Comput. Chem.*, 1999, **20**, 51-62.

[72] E. V. Lenthe, E. J. Baerends and J. G. Snijders, *J. Chem. Phys.*, 1993, **99**, 4597-4610.

[73] E. Van Lenthe, E. J. Baerends and J. G. Snijders, *J. Chem. Phys.*, 1994, **101**, 9783-9792.

[74] D. A. Pantazis and F. Neese, *J. Chem. Theory Comput.*, 2009, **5**, 2229-2238.

[75] G. Te Velde, F. M. Bickelhaupt, E. J. Baerends, C. Fonseca Guerra, S. J. A. Van Gisbergen, J. G. Snijders and T. Ziegler, *J. Comput. Chem.*, 2001, **22**, 931-967.

[76] E. Van Lenthe and E. J. Baerends, *J. Comput. Chem.*, 2003, **24**, 1142-1156.

[77] A. D. Becke, *Phys. Rev. A*, 1988, **38**, 3098-3100.

[78] J. P. Perdew, *Phys. Rev. B*, 1986, **33**, 882-8824.

[79] X. Yang, C. P. Burns, M. Nippe and M. B. Hall, *Inorg. Chem.*, 2021, **60**, 9394-9401.

[80] F. Neese, *WIREs Comput. Mol. Sci.*, 2012, **2**, 73-78.

[81] D. Aravena, F. Neese and D. A. Pantazis, *J. Chem. Theory Comput.*, 2016, **12**, 1148-1156.

[82] P. V. Bijina and C. H. Suresh, *J. Chem. Sci.*, 2016, **128**, 1677-1686.

[83] P. Politzer, P. R. Laurence and K. Jayasuriya, *Environ. Health Perspect.*, 1985, **61**, 191-202.

[84] S. F. Boys and F. Bernardi, *Mol. Phys.*, 1970, **19**, 553-566.

[85] R. Gulde, P. Pollak and F. Weigend, *J. Chem. Theory Comput.*, 2012, **8**, 4062-4068.

[86] M. Regueiro-Figueroa, D. Esteban-Gómez, A. de Blas, T. Rodríguez-Blas and C. Platas-Iglesias, *Chem. – Eur. J.*, 2014, **20**, 3974-3981.

[87] D. Esteban-Gómez, C. Cassino, M. Botta and C. Platas-Iglesias, *RSC Adv.*, 2014, **4**, 7094-7103.

[88] V. Patinec, G. A. Rolla, M. Botta, R. Tripier, D. Esteban-Gómez and C. Platas-Iglesias, *Inorg. Chem.*, 2013, **52**, 11173-11184.

[89] A. M. Nonat, C. Gateau, P. H. Fries, L. Helm and M. Mazzanti, *Eur. J. Inorg. Chem.*, 2012, **2012**, 2049-2061.

[90] P. W. Ayers, R. G. Parr and R. G. Pearson, *J. Chem. Phys.*, 2006, **124**, 194107-8.

[91] J. Zhang and M. Dolg, *J. Phys. Chem. A*, 2015, **119**, 774-780.

[92] R. Pollet, N. N. Nair and D. Marx, *Inorg. Chem.*, 2011, **50**, 4791-4797.

[93] A. D. Becke and K. E. Edgecombe, *J. Chem. Phys.*, 1990, **92**, 5397-5403.

[94] M. P. Mitoraj, A. Michalak and T. Ziegler, *J. Chem. Theory Comput.*, 2009, **5**, 962-975.

[95] F. M. Bickelhaupt and E. J. Baerends, in *Reviews in Computational Chemistry*, eds. K. B. Lipkowitz and D. B. Boyd, Wiley, 1st edn., 2000, 15, 1-86.

[96] E. M. López-Vidal, M. Regueiro-Figueroa, M. D. García, C. Platas-Iglesias, C. Peinador and J. M. Quintela, *Inorg. Chem.*, 2012, **51**, 4429-4431.

Chapter 4

Computational Investigation of Chiral DOTA-derivatives: Insights into Structure, Stability, and Relaxivity

The work is currently under consideration.

4.1. Introduction

The lanthanide chemistry of DOTA and its derivatives is of great significance owing to their broad application in biology and medicine, especially in various molecular imaging techniques.[1–3] Understanding the hydration properties of lanthanide (Ln^{3+}) complexes in aqueous solution are crucial, as they offer valuable insights into the metal-ligand selectivity and the relative strength of the metal-ligand interactions.[4] This stability analysis of Ln^{3+} complexes is crucial for the rational design of effective therapeutic and diagnostic agents.[5,6] Ln^{3+} ions play a significant role in medical imaging,[7] including X-ray computed tomography (CT),[8] magnetic resonance imaging (MRI),[9,10] single-photon emission computed tomography (SPECT),[11] optical imaging (OI),[12,13] and positron emission tomography (PET),[14] offer unique advantages for visualizing and diagnosing different pathological conditions. For instance, $^{153}Sm^{3+}$ is used in SPECT,[15] while Yb^{3+} and Eu^{3+} are used in optical imaging, [12,13] and Gd^{3+} is widely used as an MRI contrast agent (CA). Although Gd^{3+}-based CAs have been effective for decades,[16,17] reports of Gd^{3+}-deposition in the skeletal and central nervous systems of patients years after administering the CAs have led to safety concerns.[6,16] To address this, many groups are focusing on the design of new ligands that are more resistant to Gd^{3+} decomplexation.[18–21] Thus, the researchers are currently focusing on improving the safety of MRI CAs by developing new agents with higher sensitivity and high thermodynamic and kinetic stability.

One of the clinically approved CAs is the $[Gd(DOTA)(H_2O)]^-$ complex, which exhibits the highest thermodynamic and kinetic stability, effectively preventing the dissociation of the complex and release of toxic Gd^{3+} ions.[1,20] In aqueous solution, macrocyclic $[Ln(DOTA)]^-$ complexes exist as a mixture of two enantiomeric pairs of diastereomers, each featuring distinct ligand conformations: square antiprism (SAP) and twisted square antiprism (TSAP)

geometries.[22] The DOTA ligand, consisting of four nitrogen and four oxygen donor atoms, effectively wraps around the Ln^{3+} ion and forms complexes with exceptionally high thermodynamic and kinetic stability.[2,3,23] However, despite its stability, various animal studies have reported the deposition of Gd^{3+} ions in the brain after $[Gd(DOTA)(H_2O)]^-$ administration.[24–26] These agents have successfully passed initial clinical trials,[27,28] and the field continues to be an active area of research focused on further advancements. Despite their significant clinical use nowadays, it is a growing area of research for designing safer and more inert MRI CAs.[29] Chiral DOTA chelators are promising candidates for developing stable, high relaxivity CAs, with potential application in diagnostic imaging and therapy. [24,30] But what makes chiral DOTA chelators form stable complexes with Ln^{3+} ions compared to parent $[Ln(DOTA)]^-$? Typically, in the formation of the $[Ln(DOTA)]^-$ complex, four different diastereomers are formed. Two pairs of enantiomers lead to four stereoisomers that are interconvertible in solution, either by ring flipping or rotation of the acetate pendant arms, resulting in SAP and TSAP geometry. The chiral DOTA derivatives restrict the ring flipping and rotation of the acetate pendant arm, limiting the interconversion of the isomeric forms.[24,30–33] Moreover, the bulkiness of the chiral group creates steric hindrance, which restricts the susceptibility to transmetallation and acid-catalyzed decomplexation.[34–36] Thus, the selection of an appropriate ligand framework is crucial for designing Ln^{3+}-based MRI CAs for their in vivo application.

Another approach to reduce the toxicity of these Gd^{3+}-based CAs involve increasing their relaxivity, a key parameter for efficient MRI CAs.[37–41] One of the main factors influencing relaxivity is the mean residence time of water molecules in the first coordination sphere. This is represented as mean residence time (τ_m), which is inversely proportional to water exchange rate ($k_{ex}^{298}= \frac{1}{\tau_m}$).[19,42–44] Since relaxivity is governed by various physicochemical parameters, including k_{ex}^{298}, and electron relaxation dynamics,[37,41] it is important to evaluate each of these relaxivity parameters independently. Thus, an ideal chelator should not only exhibit high stability but also promote an optimal k_{ex}^{298} (10^8-10^9 S^{-1}). Notably, the conformation of the macrocyclic lanthanide complexes also significantly influences the k_{ex}^{298}. It has been established that k_{ex}^{298} in complexes with TSAP geometry is 10-100 times faster than those with SAP geometry.[32,43,45–48] The use of chiral DOTA derivatives significantly enhances the k_{ex}^{298} by favoring the formation of the TSAP isomer.[24,33] Consequently, TSAP-geometry complexes are commonly used as MRI CAs because they effectively reduce the longitudinal relaxation time (T_1) of the water nuclei in the vicinity of the targeted tissues.[32,45] In contrast,

SAP complexes are better suited for use as paramagnetic chemical exchange saturation transfer (PARACEST) agents.[47,49]

Electronic relaxation of the paramagnetic center is another important parameter influencing the relaxivity of MRI CAs.[37–41] The longitudinal (T_{1e}) and transverse (T_{2e}) electronic relaxation times of Gd^{3+} ions have often been overlooked. Electronic relaxation is generally associated with the fluctuation of zero-field splitting (ZFS),[50–54] which results from transient distortions in the metal coordination environment resulting from molecular vibrations and interactions with solvent molecules.[55–57] Since ZFS significantly influences the electron spin relaxation of Gd^{3+} ions, the structure and electronic dynamics of the chelating ligand surrounding the metal ion primarily govern the ZFS and, consequently, the electron spin relaxation rates in solution.[51–55] In particular, the ZFS in Gd^{3+} complexes significantly affects the paramagnetic relaxation enhancement, which in turn influences the spin relaxation parameter.

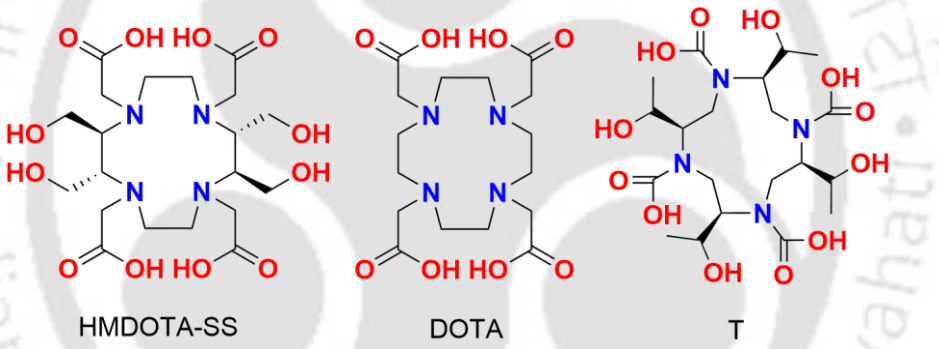

Figure 4.1. Ligand considered in this study. [29,58–60]

Although DOTA-based ligands have been extensively studied, the structure-activity relationship of their chiral derivatives remains underexplored. Deeper computational insights could help optimize CA performance. While experimental work on Ln^{3+} complexes is growing, theoretical studies are limited due to challenges in modeling Ln^{3+} ions. The most promising methods are those based on density functional theory (DFT), and when combined with molecular dynamics simulations,[61–65] they offer the potential to unveil their dynamic behavior to an atomic level that is beyond the reach of experimental techniques.

This study provides an in-depth analysis of the structural properties and stability of $[Ln(DOTA)]^-$[58,59] and its chiral analogs $[Ln(HMDOTA\text{-}SS)]^-$[60] and $[Ln(T)]^-$[29] complexes (Figure 4.1) in aqueous solution. We explore the coordination geometry of the solvated Ln^{3+} ions [Ln^{3+}= La^{3+}, Gd^{3+}, and Lu^{3+}] when chelated by DOTA and its derivatives. To simulate

these complexes in solution, both classical and *ab initio* molecular dynamics (MD) simulations were carried out. The findings of this work provide atomic-level details regarding the dynamic behavior of the $[Ln(DOTA)]^-$ derivatives and comprehensively analyze their structural dynamics in an aqueous solution. Additionally, we investigate the factors influencing the relaxivity properties of these complexes, focusing on the k_{ex}^{298} and electronic relaxation parameter, particularly the ZFS. By comparing their stability, structure, and relaxivity parameters, this work advances the understanding of these Ln^{3+} complexes for developing next-generation lanthanide-based systems for medical applications.

4.2. Computational Details

4.2.1. *Ab Initio* Molecular Dynamics (AIMD) Simulations

In this study, the *ab initio* molecular dynamics (AIMD) simulations were performed within the canonical (NVT) ensemble at 25°C, using a time step of 1.0 fs.[56,57,62] A cubic periodic simulation box of length 21 Å with explicit water molecules was used to investigate the solution structures of the $[Ln(DOTA)]^-$, $[Ln(HMDOTA\text{-}SS)]^-$, and $[Ln(T)]^-$ complexes. In line with our previous protocol,[57] the initial configuration for the AIMD simulations was generated by equilibrating the system through classical molecular dynamics (MD) simulations using GROMACS.[66,67] The ligand atoms were modeled using the Generalized AMBER Force Field (GAFF),[68] while the Universal Force Field (UFF)[69] was applied to the Ln^{3+} ion. The TIP3P model was used to represent the water molecules.[70,71] The topology files for the Ln^{3+} complex were generated with the Sobtop software package.[72] The solvated systems were minimized using these classical force field parameters via the steepest descent algorithm.[7] Following this, a 10 ns canonical ensemble (NVT) simulation was carried out, and subsequently, a 20 ns isothermal-isobaric (NPT) simulation, both with a 1.0 fs time step. In these simulations, the Parrinello-Rahman barostat[73] and V-rescale[74] thermostats were used. The NVT and NPT simulations were carried out at 298.15 K and a pressure of 1 bar. The energy minimization and the time-dependent variations of temperature, pressure, and density plots of $[Gd(DOTA)]^-$, $[Gd(HMDOTA\text{-}SS)]^-$, and $[Gd(T)]^-$ complexes are illustrated in Figures B1-B3 of Appendix-B. The final coordinates and box dimensions from the equilibrated classical MD frames were used to initiate the AIMD simulations in the canonical (NVT) ensemble. The AIMD simulations were performed with a timestep of 1.0 fs and continued until an equilibrated trajectory was obtained. The PBE[75,76] functional, as implemented in the CP2K v5.1 package, was used for AIMD simulations.[77] The core electrons were represented using GTH pseudopotential,[78,79] while the valence electrons were described using the double-ζ valence

polarized basis set.[80] A Nose-Hoover thermostat was used to maintain a constant temperature throughout the simulations. Long-range electrostatic interactions were treated using an auxiliary plane wave basis set, with an energy cutoff of 500 Ry for La^{3+} and Gd^{3+}, and 1000 Ry for Lu^{3+}. We have considered van der Waals interactions by applying Grimme's dispersion correction (DFT-D3) with a cutoff radius of 6 Å. To determine the spin multiplicity of the Ln^{3+} ions, Hund's rule was applied, resulting in singlet multiplicities for La^{3+} and Lu^{3+} ions and octet multiplicity for the Gd^{3+} ion. For each complex, AIMD simulations were performed for ~30-40 ps. The initial 10-20 ps of each trajectory were eliminated, and the subsequent 20 ps were used for further analysis. The AIMD simulations at elevated temperatures (45˚C and 65˚C) were carried out following the protocol described in our previous study by starting with an equilibrated frame at 25˚C until at least 20 ps of equilibrated trajectories were obtained.

4.2.2. Electronic Structure Methods

Binding energies (BEs) for the Ln^{3+}-ligand systems were determined from their solution structures obtained via DFT AIMD simulations and were computed using electronic structure methods with relativistic effects. The coordinates of the Ln^{3+}-ligand complex, used for BE calculations, were optimized in the solution phase within a fully explicit solvent simulation box using the following protocol: Starting with an equilibrated AIMD trajectory (the final 20 ps of the trajectory), a single-point energy calculation was performed on the optimized solution structure of the complexes using the Gaussian 16 package.[81] The extracted atomic coordinates of the Ln^{3+}-ligand complexes include the water molecules that are directly coordinated with the Ln^{3+} ion. All energy calculations were carried out using the TPSSh functional,[41,82] in combination with relativistic second-order Douglas-Kroll-Hess (DKH2) Hamiltonian.[83] The segmented all-electron relativistically contracted (SARC) basis set was employed for the Ln^{3+} ion, while the 6-311G(d,p) basis set was used for other atoms.[62,84,85] An implicit water solvent model, specifically the integral equation formalism (IEFPCM),[86] was applied for the single-point energy calculations. The Ln^{3+}-ligand binding energies (BEs) were computed using Eq. 4.1

$$\text{BE}=E\left(Ln^{3+}(ligand)(H_2O)_n\right)^{c} - E(Ln^{3+}) - E(ligand)^{c-2} - n.E(H_2O) \qquad (4.1)$$

Density functional theory (DFT) calculations were carried out with the Gaussian 16 suite of programs. Geometry optimization of the complexes used the TPSSh functional[41,82,87] with a large core relativistic effective core potential (LCRECP) and its associated (7s6p5d)/[5s4p3d]-GTO valence basis set for the metal center.[88] The 6-311G(d,p) basis set was applied to all

other atoms. Furthermore, additional DFT calculations were performed using the ωB97XD97[89] functional and the def2-TZVPP basis set[90] for the ligand atoms. Gibbs free energy calculations were performed under the harmonic approximation at a temperature of 298.15 K. To account for the non-electrostatic contributions to the Gibbs free energy, the solvation model based on density (SMD) was applied.[91] The investigated systems included a few second-sphere water molecules, essential for correctly describing the Ln-O(w) distances and spin-density distributions. The polarizable continuum model (PCM), in general, the integral equation formalism, i.e., the IEFPCM model, was considered to assess bulk solvent effects. A single negative frequency characterizes these TSs and generates the intrinsic reaction coordinate (IRC) paths. Wave function analysis was performed using the Quantum Theory of Atoms in Molecules (QTAIM) of Bader[92] to determine the electron density (ρ_{BCP}), electron localization function (ELF) at the bond critical points (BCPs) with the Multiwfn program (version 3.8).[93] Isotropic ^{17}O hyperfine coupling constants and the ZFS tensor were calculated using the ORCA program package (version 5.0.3).[94] Relativistic effects were treated using the Douglas-Kroll-Hess (DKH2) approximation. The SARC2-DKH-QZVP[95] basis sets were used for the Gd^{3+} ion, while the DKH-def2-SVP basis sets[90] were applied to the ligand atoms. The resolution of identity and chain of spheres (RIJCOSX) approach[96] was used along with the SARC2-DKH-QZVP/JK auxiliary basis set[95] for Gd^{3+} and auxiliary basis sets with the Autoaux method for ligand atoms. The quasi-restricted orbitals obtained from these calculations were initial guess orbitals for the complete active space self-consistent field (CASSCF) calculations. Dynamic electron correlation was subsequently included using the quasi-degenerate strongly contracted variant of N-electron valence state perturbation theory (SC-NEVPT2).[97] Quasi-degenerate perturbation theory (QDPT)[98] was used to incorporate the spin-orbit coupling (SOC) effect. The active space of the state-averaged CASSCF calculations comprise seven electrons distributed over the seven Gd^{3+}-based 4f molecular orbitals CAS(7,7), with 1 octet and 48 sextet roots. The SMD solvation model included bulk solvent effects in all ORCA calculations.

4.3. Results and Discussion

4.3.1. The Prediction and Analysis of Inner Coordination Sphere of Ln^{3+}-Ligand Complexes using AIMD

Characterizing the aqueous chemistry of Ln^{3+} complexes with high coordination numbers (CNs) remains challenging. Resolving the Ln^{3+}-solution structure at atomic resolution is relevant for the rational design of MRI CAs. AIMD simulations, which combine the advantages

of electronic structure and molecular dynamics simulations, is a powerful method for probing the structural and dynamic behaviour of the CAs. To determine the relative binding energies of a ligand to Ln^{3+} ions, it is necessary to resolve the molecular structures of Ln^{3+}-ligand complexes. In our previous study, we successfully elucidated the solution structure of seven coordinated Mn^{2+} complexes using AIMD simulations.[56,57] This work extended the same DFT AIMD approach to investigate the solution structures of La^{3+}, Gd^{3+}, and Lu^{3+} ions with DOTA, HMDOTA-SS, and T ligands at 25˚C. The coordination geometry of the $[Ln(HMDOTA-SS)]^-$ and $[Ln(T)]^-$ complexes closely resembles that of $[Ln(DOTA)]^-$ complex, such that the four nitrogen atoms of the cyclen ring (N1, N2, N3, N4) and four oxygen atoms of the pendant arms (O1, O2, O3, O4) are involved in metal ion coordination. However, the cyclen backbone of $[Ln(HMDOTA-SS)]^-$ and $[Ln(T)]^-$ complexes features rigid hydroxy-methylene and hydroxy-ethylene groups, further stabilizing the coordination environment (Figure 4.1). The coordinating N and O atoms are defined as two distinct planes, referred to as the N-plane and O-plane. In the studied Ln^{3+}-complexes, the metal ion is typically wedged between these two planes with a water molecule (O_W) occupying the 9th coordination site, as shown in Figure 4.2. The relative torsion of these two planes yields two distinct coordination geometries (TSAP and SAP). As these complexes exhibit two different conformations, TSAP and SAP geometries were considered in our study to assess their stability in an aqueous solution. The average coordination number (CN) of $[Gd(DOTA)]^-$, $[Gd(HMDOTA)]^-$ and $[Gd(T)]^-$ is 9, arising from Gd-O (CN=5) and Gd-N (CN=4) coordination. The optimized solution structure of Gd^{3+} ion with DOTA, HMDOTA-SS, and T ligands at the TSAP and SAP geometry without the explicit water molecules are shown in Figure 4.2 and Figure B4 of Appendix-B at 25˚C.

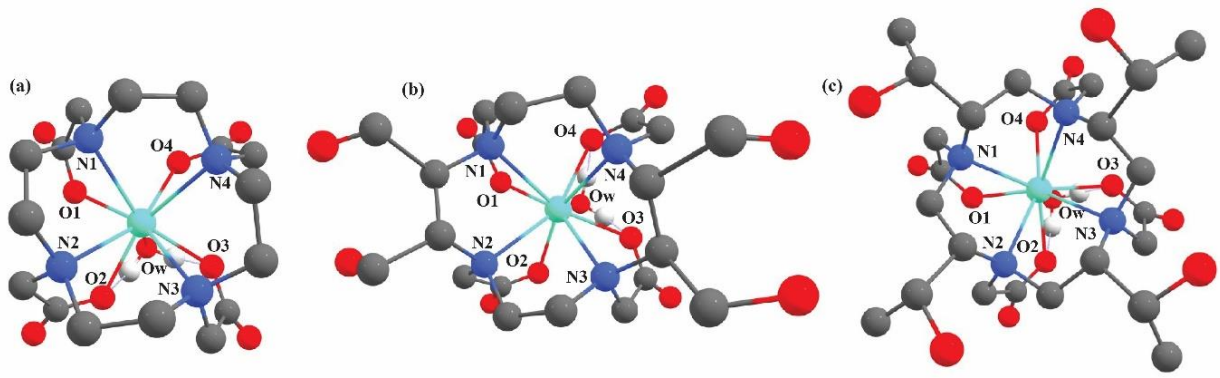

Figure 4.2. The optimized structures of the TSAP geometry of the (a) $[Gd(DOTA)(H_2O)]^-$, (b) $[Gd(HMDOTA-SS)(H_2O)]^-$, and (c) $[Gd(T)(H_2O)]^-$ complexes using PBE/DZVP method with GTH pseudopotentials.

The radial distribution functions (RDFs) calculated for the TSAP geometry of $[Gd(DOTA)(H_2O)]^-$ complexes at 25˚C (Figure 4.3) show an average maxima of 2.45 Å for Gd-O, 2.75 Å for Gd-N, and 3.45 Å for Gd-C atoms, respectively (Table 4.1). In contrast, the SAP geometry of $[Gd(DOTA)(H_2O)]^-$ complexes at 25˚C (Figure 4.3) exhibits an average maxima of 2.45 Å for Gd-O, 2.65 Å for Gd-N, and 3.45 Å for Gd-C atoms, respectively. A smaller peak was observed in the Gd-O RDFs at 4.45 Å (TSAP) and 4.55 Å (SAP) (Figure 4.2) corresponds to the second coordination sphere of the solvent (water) shell around the Gd^{3+} complexes. Comparatively, the sharpness of the RDF peaks at SAP geometry is higher than the TSAP geometry for all Gd-O, Gd-N, and Gd-C atoms (although the differences are not significant). This subtle increase in peak sharpness may suggest relatively higher structural stability of the SAP geometry in $[Gd(DOTA)]^-$ complexes compared to the TSAP geometry in an aqueous solution. This is in line with the classical molecular dynamic simulations of Gd^{3+} ion with DOTA ligand. All simulated Gd-O bond length values are in close agreement with the experimental observation in the literature.[58] This result highlights the reliability of the GTH AIMD simulations in accurately reproducing the solution structure of Ln^{3+} complexes. The potential energy plot from the AIMD trajectory is presented in Figures B5-B10 of Appendix-B. At the same time, the variations in Ln-N and Ln-O bond length along the AIMD simulations are shown in Figures B11-B22 in Appendix-B. Interestingly, for the $[Gd(HMDOTA\text{-}SS)]^-$ complex, the RDF peaks corresponding to the TSAP geometry are sharper than those of the SAP geometry. In contrast, in the $[Gd(T)]^-$ complex, the SAP geometry exhibits sharper RDF peaks compared to the TSAP form. This analysis aligns well with the experimental observation of higher thermodynamic stability of the TSAP isomer of $[Gd(HMDOTA\text{-}SS)]^-$ and SAP isomer of $[Gd(T)]^-$ complex in aqueous solution.[29,60] The RDFs calculated at 25˚C for the TSAP geometry of both $[Gd(HMDOTASS)]^-$ and $[Gd(T)]^-$ complexes exhibit an average maxima of 2.35 Å for Gd-O, 2.65 Å for Gd-N, and 3.45 Å for Gd-C atoms. A smaller peak at 4.45 Å in the Gd-O RDF for both $[Gd(HMDOTA\text{-}SS)]^-$ and $[Gd(T)]^-$ complexes indicated the presence of a second hydration sphere (Figure 4.3). Furthermore, the Gd-C RDFs of both $[Gd(HMDOTA\text{-}SS)]^-$ and $[Gd(T)]^-$ complexes show one or two minor peaks in the 4.95-5.05 Å range due to the presence of bulky hydrophilic hydroxymethylene and hydroxyethylene groups (Figure 4.3). Moreover, for both $[Gd(HMDOTA\text{-}SS)]^-$ and $[Gd(T)]^-$ complexes, the shorter Gd-O and Gd-N distances suggest a stronger binding affinity of the HMDOTA-SS and T ligands to the Gd^{3+} ion compared to the DOTA ligands, as shown in Table 4.1. Comparison of the solution structures of $[Gd(DOTA)]^-$, $[Gd(HMDOTA)]^-$, and $[Gd(T)]^-$ complexes, along with the RDFs shown in Figure 4.3, reveals that decreased complex stability is associated with

increased ligand/solvent disorder within the Ln^{3+}-Ligand complex. Despite this correlation, the peak sharpness does not significantly vary, likely due to the inherent stability of the DOTA-based complexes in aqueous solution.

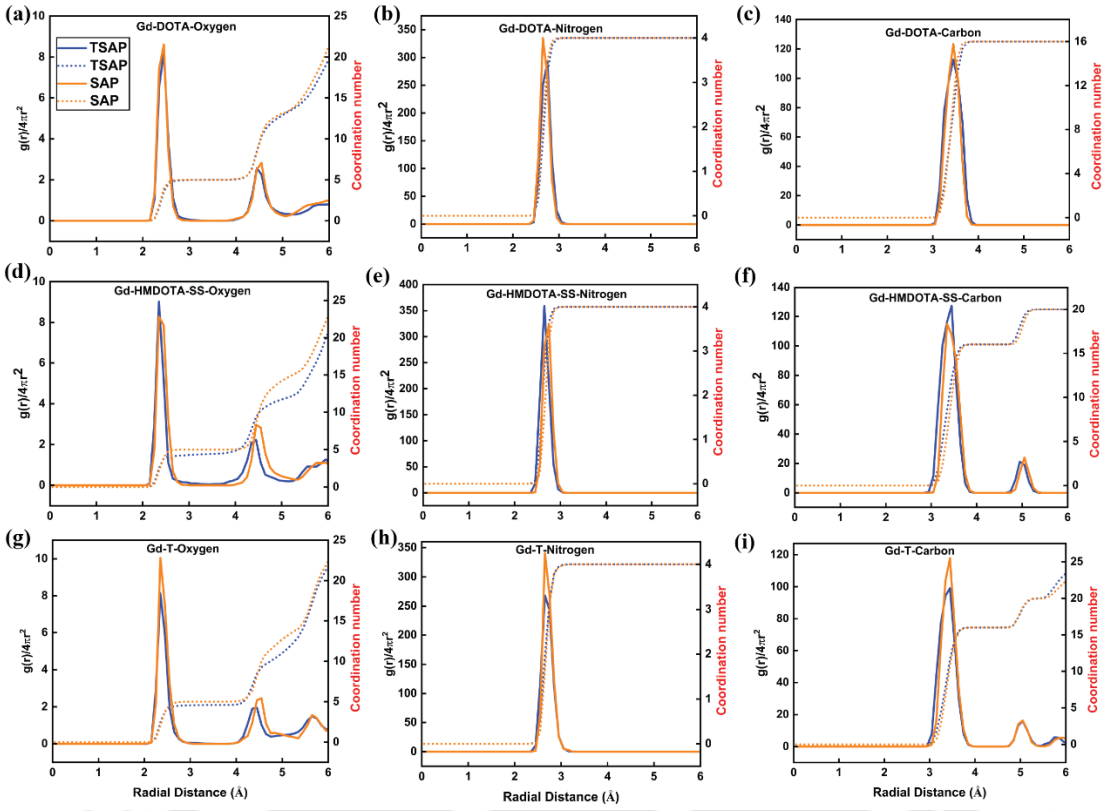

Figure 4.3. Radial distribution functions for the $[Gd(DOTA)]^-$ (a, b, c), $[Gd(HMDOTASS)]^-$ (d, e, f), and $[Gd(T)]^-$ (g, h, i) complexes at 25˚C for both TSAP (blue) and SAP (orange) geometry. The left, center, and right panels illustrate Gd-O, Gd-N, and Gd-C pair distribution functions, respectively.

Table 4.1. The peak distances (Å) of the RDFs obtained from AIMD simulations of $[Ln(DOTA)]^-$, $[Ln(HMDOTA)]^-$, and $[Ln(T)]^-$ complexes for both TSAP and SAP geometry at 25˚C. The symbol "-" indicates the absence of RDF peaks.

		$[Ln(DOTA)]^-$			$[Ln(HMDOTA-SS)]^-$			$[Ln(T)]^-$		
TSAP		1st	2nd	3rd	1st	2nd	3rd	1st	2nd	3rd
	La-O	2.55	4.55	-	2.55	4.65	-	2.55	4.55	5.85
	La-N	2.85	-	-	2.85	-	-	2.85	-	-

	La-C	3.55	-	-	3.65	5.15	-	3.55	5.15	-
	Gd-O	2.45	4.45	-	2.35	4.45	-	2.35	4.45	5.65
	Gd-N	2.75	-	-	2.65	-	-	2.65	-	-
	Gd-C	3.45	-	-	3.45	4.95	-	3.45	5.05	-
	Lu-O	2.25	4.35	-	2.25	4.35	-	2.25	4.35	5.65
	Lu-N	2.65	-	-	2.55	-	-	2.65	-	-
	Lu-C	3.25	-	-	3.25	4.75	-	3.25	5.05	-
SAP	La-O	2.45	4.65	-	2.45	4.55	-	2.45	4.65	5.75
	La-N	2.85	-	-	2.85	-	-	2.85	-	-
	La-C	3.45	-	-	3.55	5.15	-	3.55	5.15	-
	Gd-O	2.45	4.55	-	2.35	4.45	-	2.35	4.55	5.65
	Gd-N	2.65	-	-	2.75	-	-	2.65	-	-
	Gd-C	3.45	-	-	3.35	5.05	-	3.45	5.05	-
	Lu-O	2.25	4.45	-	2.25	4.35	-	2.25	4.35	5.45
	Lu-N	2.55	-	-	2.65	-	-	2.55	-	-
	Lu-C	3.35		-	3.35	4.95	-	3.35	4.85	-

The RDF peaks for the $[La(DOTA)]^-$, $[La(HMDOTA)]^-$ and $[La(T)]^-$ complexes and $[Lu(DOTA)]^-$, $[Lu(HMDOTA)]^-$, and $[Lu(T)]^-$ complexes of SAP and TSAP geometry of the complexes at 25˚C are shown in Table 4.1 and Figures B23-B24 of Appendix-B. The Lu^{3+} complexes have a similar ligand conformation to that of Gd^{3+} complexes. However, the coordinated water molecule moves towards the second or outer coordination sphere, as evidenced by the time evolution plot of the Lu-O(w) bond (Figures B11-B16). As a result, $[Lu(DOTA)]^-$ complex obtains a total CN of 8, arising from Lu-O (CN=4) and Lu-N (CN=4) coordination, as shown in Figure 4.4. Similarly, in the [Lu(HMDOTA)] complex, the average CN is also 8, arising from Lu-O (CN = 4) and Lu-N (CN = 4) bonds. In contrast, the $[Lu(T)]^-$

complex exhibits an average CN of 8.15, comprising Lu-O (CN = 4.15) and Lu-N (CN = 4) coordination.

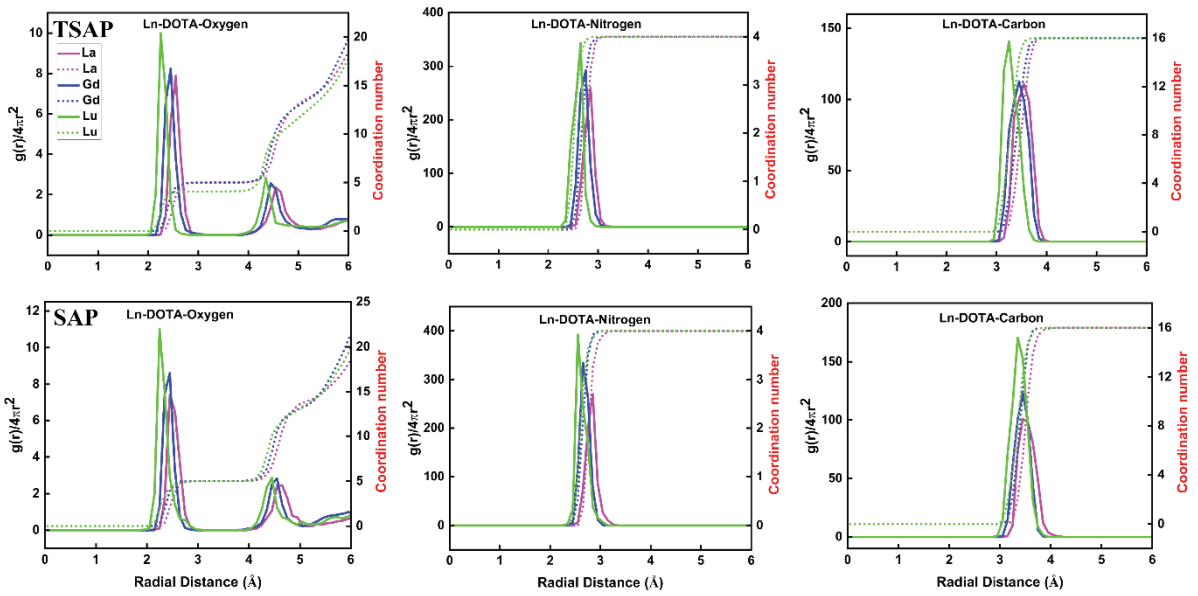

Figure 4.4. Radial distribution functions of the $[Ln(DOTA)]^-$, complexes along the Ln^{3+}-series (Ln^{3+}=La^{3+}, Gd^{3+}, and Lu^{3+}), at 25˚C in the TSAP (top) and SAP (bottom) geometries. The left, center, and right panels represent Ln-O, Ln-N, and Ln-C pair distribution functions, respectively.

The Ln-O, Ln-N, and Ln-C RDFs for the $[Ln(DOTA)]^-$ complex at 25˚C is shown in Figure 4.4. The Ln-O, Ln-N, and Ln-C RDFs of $[Ln(DOTA)]^-$, $[Ln(HMDOTA-SS)]^-$, and $[Ln(T)]^-$ complexes at 25˚C are illustrated in Figure 4.4 and Figures B25-B26 of Appendix-B. These RDFs provide insight into the first coordination sphere and compare the variation of bond length across the Ln^{3+} series. Specifically, these illustrate the probability of finding oxygen, nitrogen, and carbon atoms relative to the Ln^{3+} ion. As expected, the bond length values decrease progressively with increasing atomic number of the Ln^{3+} ion in all three complexes and both TSAP and SAP geometry, as shown in Table 4.1.

The RDFs calculated for the Ln-O and Ln-N bond pairs show a consistent decrease in bond distances across the Ln^{3+}-series at 25˚C, reflecting the effect of lanthanide contraction. For the TSAP geometry, the Ln-O bond lengths decrease from 2.55 Å (La^{3+}) to 2.25 Å (Lu^{3+}), while the Ln-N distances decrease from ~ 2.85 Å to 2.55-2.65 Å. The Ln-C RDFs decrease from 3.55 to 3.25 Å. Similarly, in SAP geometry, the Ln-O distances range from 2.45 Å (La^{3+}) to 2.25 Å (Lu^{3+}), Ln-N distances again decrease from around 2.85 Å to 2.55-2.65 Å, and the Ln-C distances decrease from 3.45-3.55 Å to 3.35 Å. These trends are consistent across the

$[Ln(DOTA)]^-$, $[Ln(HMDOTA\text{-}SS)]^-$, and $[Ln(T)]^-$ complexes and are shown in Table 4.1 and illustrated in Figure 4.4 and Figure B25-B26 of Appendix-B. The Ln-O, Ln-N, and Ln-C RDFs imply that O and N atoms are directly coordinated to the Ln^{3+} ion while the ligand carbon atom is positioned slightly further away.

4.3.2. Influence of Temperature on the Solution Behaviour of Ln^{3+} Complexes

Temperature influences the Ln^{3+}-ligand structure in different ways that depend on the complex interaction between ligands, anions, and solvent molecules. This study focused on the solution structure of the $[Ln(DOTA)]^-$, $Ln(HMDOTA\text{-}SS)]^-$, and $[Ln(T)]^-$ complexes across the Ln^{3+}-series at different temperatures to resolve its coordination geometry at two different geometries (TSAP and SAP). Simulations were performed in three different temperatures (25˚C, 45˚C, and 65˚C), for both TSAP and SAP geometry of $[Ln(DOTA)]^-$, $[Ln(HMDOTA\text{-}SS)]^-$, and $[Ln(T)]^-$ complexes. This will determine how temperature variations affect the solution-phase coordination structure of the complexes with distinct ligand environments. The sharpness of the RDF peak of the $[La(DOTA)]^-$, $[La(HMDOTA\text{-}SS)]^-$, and $[La(T)]^-$ complexes changes significantly at 65˚C compared to their corresponding Gd and Lu derivatives (Figure 4.5). The Ln-O, Ln-N, and Ln-C RDFs at 25˚C, 45˚C, and 65˚C for each complex are shown in Figure 4.5 and Figures B27-B31 of Appendix-B illustrate the influence of temperature on the structural dynamics of these studied complexes in an aqueous solution. It was established that complexes with relatively high thermodynamic stability constants exhibited only minor changes in RDF peaks and their intensities with increasing temperature, whereas those with lower stability constants showed more significant variation and sharpness of the peak decreases. In our study, we observed that Gd^{3+} and Lu^{3+} derivatives of all three studied ligands (DOTA, HMDOTA-SS, and T) show negligible changes in their RDF peaks with increasing temperature, maintaining a sharp peak at high temperature (45˚C, 65˚C) similar to the RDF peak at 25˚C. This may be due to the strong metal-ligand binding affinity of this DOTA and its derivatives (HMDOTA and T) with Ln^{3+} ions, which minimizes the temperature-induced disorder in the first coordination sphere. This indicates the stability of these complexes in an aqueous solution. Notably, the Gd-O and Gd-N RDFs of the TSAP isomer of the $[Gd(HMDOTA\text{-}SS)]^-$ complex maintains a sharp peak both at 45˚C and 65˚C, compared to its SAP isomer (broad peak at 65˚C), as shown in Figures B28-B29 of Appendix-B. In contrast, for the $[Gd(T)]^-$ complex, the SAP geometry showed greater rigidity as the RDF peaks remain sharp at elevated temperatures (Figures B30-B31). This indicates the geometry-dependent stabilization of these complexes in an aqueous solution. Furthermore, it was observed that

across the Ln^{3+}-series, the effect of temperature-induced structural disorder decreases as the stability of the complexes increases.

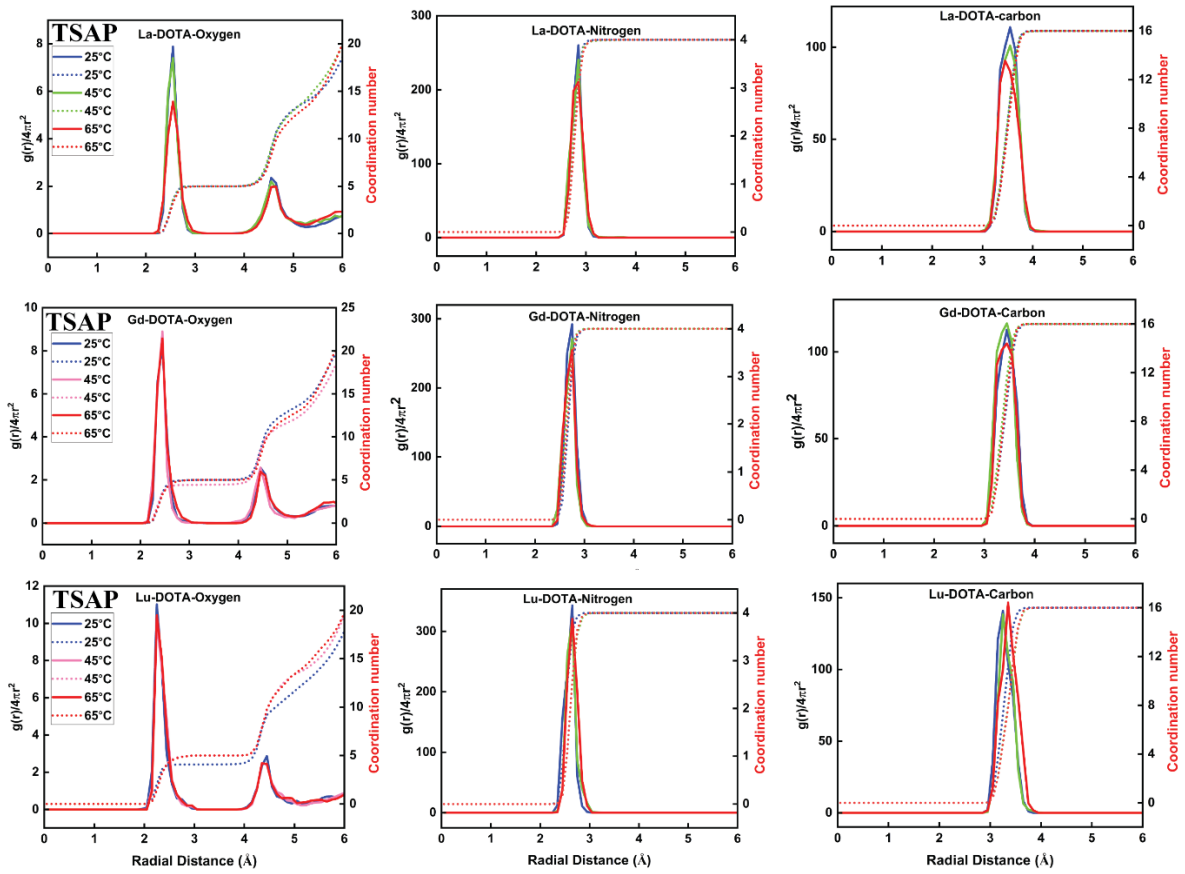

Figure 4.5. Radial distribution functions of the $[Ln(DOTA)]^-$, complexes, shown in three different temperatures (25˚C, 45˚C, and 65˚C). The left, center, and right panels represent Ln-O, Ln-N, and Ln-C pair distribution functions, respectively.

4.3.3. Electronic Structure Analysis

4.3.3.1. Relative Binding Energies (BEs) of $[Ln(DOTA)]^-$ and their Chiral Derivatives

To determine the relative binding affinity of the studied ligand to Ln^{3+} ions (La^{3+}, Gd^{3+}, and Lu^{3+}), the molecular structure of the Ln^{3+}-ligand complexes was resolved using DFT AIMD simulations. To determine the strength of the ligands (Figure 4.1) with Ln^{3+} ion, the BE of the complexes was determined using the Eq. 4.1. The binding affinity of the ligand to the Ln^{3+} ion increases in the order- DOTA < HMDOTA-SS < T, as shown in Table B1 of Appendix-B. Using the BE of the $[Gd(T)]^-$ as a reference point, the BE of the $[Gd(T)]^-$, $[Gd(HMDOTASS)]^-$, and $[Gd(DOTA)]^-$ are 1.00, 0.99, and 0.78, respectively, at both TSAP and SAP geometry. This indicates that the presence of a bulky hydroxy group increases the BE of the HMDOTA-SS and T ligand to Ln^{3+} centre compared to its parent DOTA-ligand. This is in line with the

experimental stability constant value. Moreover, for a given ligand, Table B1 of Appendix-B demonstrates that Ln^{3+}-ligand binding affinity increases down the Ln^{3+}-series (La^{3+}< Gd^{3+}< Lu^{3+}) as the ionic radius of the metal center decreases.

4.3.3.2. Structural Analysis of $[Ln(DOTA)(H_2O)]^-$ Complexes and their Chiral Derivatives

Understanding the structure-property relationships of Ln^{3+}-based complexes are inevitable for the design of new MRI CAs. The conformational properties of $[Ln(DOTA)]^-$ complexes have been widely investigated in the literature.[2,3,22,23] These studies revealed that the complexes from Pr^{3+} to Lu^{3+} (except for Tm^{3+}) crystallize in the SAP geometry, while the complexes with the larger lanthanides La^{3+} and Ce^{3+} crystallize in the TSAP geometry. Although theoretical studies on $[Ln(DOTA)(H_2O)]^-$ complexes using Hartree-Fock (HF) and DFT methods have been previously reported,[3,99–102] we revisit $[Ln(DOTA)(H_2O)]^-$ complex to validate our computational methodology. To investigate the thermodynamic stability and isomeric population trends of $[Ln(DOTA)(H_2O)]^-$, $[Ln(HMDOTA\text{-}SS)(H_2O)]^-$, and $[Ln(T)(H_2O)]^-$ complexes, DFT calculations were performed using TPSSh/6-311G(d,p)/LCRECP and ωB97XD/def2-TZVPP/LCRECP methods. The relative free energy difference ($\Delta G_{(TSAP\text{-}SAP)}$) of the SAP and TSAP isomers calculated using DFT across the Ln^{3+}-series for the studied complexes is shown in Figure 4.6.

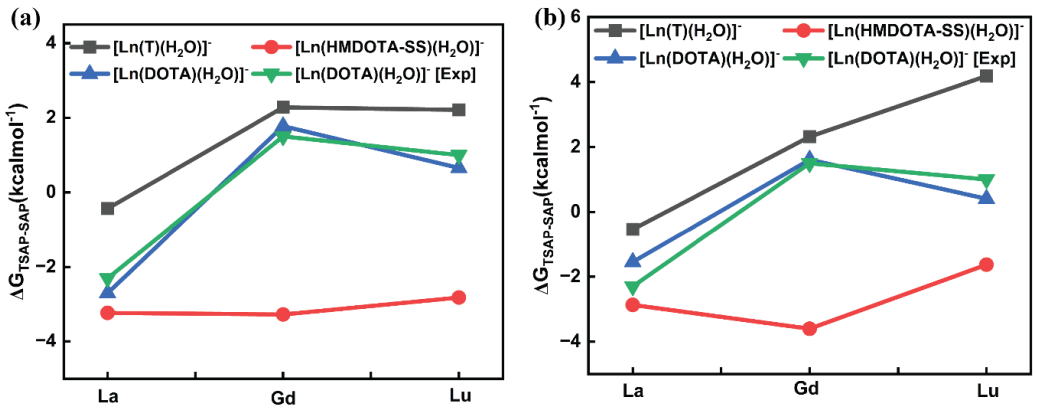

Figure 4.6. Experimental (∇) and DFT-calculated free energy differences between the TSAP and SAP isomers ($\Delta G_{(TSAP\text{-}SAP)}$) of $[Ln(DOTA)(H_2O)]^-$, $[Ln(HMDOTA\text{-}SS)(H_2O)]^-$, and $[Ln(T)(H_2O)]^-$ complexes in aqueous solution. Negative $\Delta G_{(TSAP\text{-}SAP)}$ indicates that the TSAP isomer is thermodynamically more stable compared to the SAP isomer. Results are shown for a) TPSSh and b) ωB97XD with 6-311G(d,p)/LCRECP level of theory.

The gradual shift in the population of coordination isomers across the $[Ln(DOTA)(H_2O)]^-$ series from predominantly TSAP at the beginning of the series to predominantly SAP towards the end is attributed to the gradual decrease in ionic radii of Ln^{3+} ions. In contrast, for the $[Ln(HMDOTA\text{-}SS)(H_2O)]^-$ complex, the TSAP isomer remains the dominant form across the Ln^{3+} series, although a slight shift towards the SAP isomer is observed near the middle of the Ln^{3+} series, as illustrated in Figure 4.6. This behavior is likely due to the presence of hydrophilic groups in the cyclen backbone, which increases the rigidity of the macrocyclic tetraaza ring and constrains it to adopt a single isomeric form. This indicates that other factors, in addition to ion size, contribute to this structural switch. This is in line with experimental analysis, with TSAP being the major isomer.[60] Interestingly, for the $[Ln(T)(H_2O)]^-$ complexes, the SAP geometry is favored over TSAP. The stability of SAP geometry increases across the series as Ln^{3+} ion size decreases with maximum stability in the middle of the series.

Furthermore, the variation in Ln-donor bond lengths provides additional support for the relative stabilities of SAP and TSAP isomers throughout the Ln^{3+}-series, as shown in Figure B32 and Table B2 of Appendix-B. The Ln-O(w) and Ln-N, Ln O(carboxylate) bonds change gradually down the Ln^{3+} series with a decrease in ionic radius. This decrease in bond length is owing to the lanthanide contraction. To explore the effect of metal nuclear charge and bonding interaction of the ligands (DOTA, HMDOTA-SS, and T) with the Ln^{3+} series, we have considered the stable La^{3+} ($4f^0$), Gd^{3+} ($4f^7$), and Lu^{3+} ($4f^{14}$) ions. The Ln-O(w) and Ln-N, Ln-O(carboxylate) bond distances are consistently shorter in the SAP isomer compared to the TSAP isomer across all three studied complexes (Figures B32 and Table B2 of Appendix-B). This trend indicates that moving across the lanthanide series from left to right, the increasing bond strength of Ln-O(w), Ln-N, and Ln-O(carboxylate) interactions indicates the greater stability of the SAP isomer. The calculated bond distances without explicit water and with two explicit water molecules (with different density functionals) are shown in Table B2 Appendix-B. The calculated bond length values of $[Ln(DOTA\ (H_2O)]^-$ complexes are in close agreement with both experimental data and previous computational studies.[58,59,99] Thus, a detailed examination of the bond length of the Ln^{3+}-ligand system across the Ln^{3+} series provides some insights into the coordination geometries and stability trends obtained for these three series of complexes.

The average Ln-N bond length for the TSAP geometry of $[Ln(DOTA)(H_2O)]^-.2H_2O$, $[Ln(HMDOTA\text{-}SS)(H_2O)]^-.2H_2O$, and $[Ln(T)(H_2O)]^-.2H_2O$ complexes decreases across the Ln^{3+} series from La^{3+} to Lu^{3+} ranging from 2.795 Å to 2.672 Å, 2.795 Å to 2.688 Å, and 2.825

Å to 2.705 Å, respectively. For the SAP geometry, the bond length decreases from 2.792 Å to 2.656 Å, 2.789 Å to 2.671 Å, and 2.805 Å to 2.684 Å, respectively, as shown in Figure B32 and Table B2 of Appendix-B. The Ln-O(carboxylate) bond length also shows a systematic contraction from 2.528 Å to 2.317 Å, 2.513 Å to 2.302 Å, and 2.503 Å to 2.294 Å for the TSAP isomer of $[Ln(DOTA)(H_2O)]^-.2H_2O$, $[Ln(HMDOTA\text{-}SS)(H_2O)]^-.2H_2O$, and $[Ln(T)(H_2O)]^-.2H_2O$ complexes, respectively. In the SAP geometry, the bond length decreases from 2.512 Å to 2.301 Å, 2.510 Å to 2.294 Å, and 2.511 Å to 2.292 Å, respectively. Likewise, the Ln-O(w) bond length for the TSAP geometry of $[Ln(DOTA)(H_2O)]^-.2H_2O$, $[Ln(HMDOTA\text{-}SS)(H_2O)]^-.2H_2O$, and $[Ln(T)(H_2O)]^-.2H_2O$ complexes decreases across the Ln^{3+}-series from 2.610 Å to 2.477 Å, 2.634 Å to 2.502 Å, and 2.641 Å to 2.522 Å respectively. In SAP geometry, the value decreased from 2.601 Å to 2.455 Å, 2.630 Å to 2.450 Å, and 2.623 Å to 2.491 Å, respectively. Among all the studied complexes, the shortest bond distance is observed between the Ln^{3+} ion and the carboxylate oxygen atoms. This is attributed to the strong hard-hard interaction between the oxygen donor and the Ln^{3+} ion, according to the Pearson HSAB concept.[87] The average Ln-N and Ln-O(carboxylate) bonds are notably longer in the $[Ln(DOTA)(H_2O)]^-.2H_2O$ complex compared to those in the $[Ln(HMDOTASS)(H_2O)]^-.2H_2O$, and $[Ln(T)(H_2O)]^-.2H_2O$ complexes. This observation supports the higher stability and binding affinity of HMDOTA-SS and the T ligand towards the Ln^{3+} center. These geometrical parameters indicate that the binding affinity of the ligand and the small Ln^{3+} ion follows the trend T> HMDOTA-SS> DOTA. The metal-ligand bond strength was further confirmed by the analysis of electron density (ρ_{BCP}) and electron localization function (ELF) values at the corresponding bond critical points along the Ln^{3+} series, as shown in Figure 4.7 and Figure B33 of Appendix-B. Thus, the trend obtained for the ρ_{BCP} and ELF values in the Ln-O and Ln-N bond values indicates stronger bonding interaction across the Ln^{3+} series, which accounts for the increased complex stability as well as increasing kinetic inertness with respect to complex dissociation. The ρ_{BCP} values of the Ln-O(w) bond tend to increase in the first half of the series and then decrease, indicating weaker binding of inner-sphere water molecules. Similarly, the ELF values decrease along the Ln^{3+}-series as ionic radii decrease.

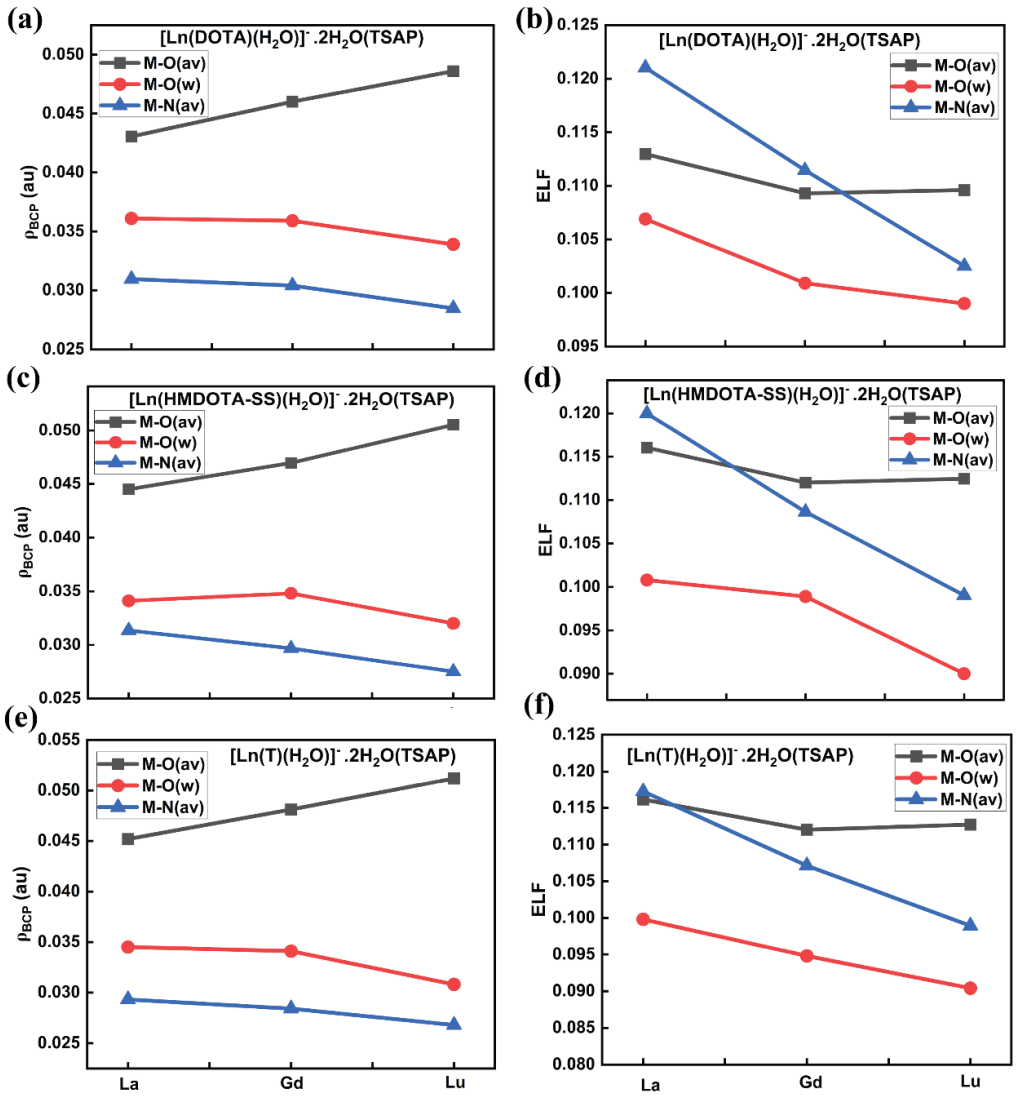

Figure 4.7. Electron density (ρ_{BCP}) and electron localization function (ELF) values along the lanthanide series for $[Ln(DOTA)(H_2O)]^-.2H_2O$ (a, b) and $[Ln(HMDOTA\text{-}SS)(H_2O)]^-.2H_2O$. (c, d) and $[Ln(T)(H_2O)]^-.2H_2O$ (e, f) complexes using TPSSh/6-311G(d,p)/LCRECP level of theory (Ln^{3+}=La^{3+}, Gd^{3+}, and Lu^{3+}) for TSAP isomer.

4.3.4. Thermodynamic Stability Assessment through Gibbs Free Energy Analysis

As free Ln^{3+} ions are toxic for in vivo application, the use of strong chelating agents is essential for biomedical applications to prevent the release of free Ln^{3+} ions into the body.[6,20] The thermodynamic stability of $[Gd(DOTA)]^-$, $[Gd(HMDOTA\text{-}SS)]^-$ and $[Gd(T)]^-$ complexes were further assessed by evaluating their free energy of formation using Scheme 4.1 and Scheme B1. Upon replacing the DOTA ligand with HMDOTA-SS, both the $\triangle G_{(g)}$ and $\triangle G_{(aq)}$ values become negative (Table B3 of Appendix-B), indicating a stronger binding affinity of the HMDOTA-SS ligand towards the Gd^{3+} ion in both gas and aqueous phases.

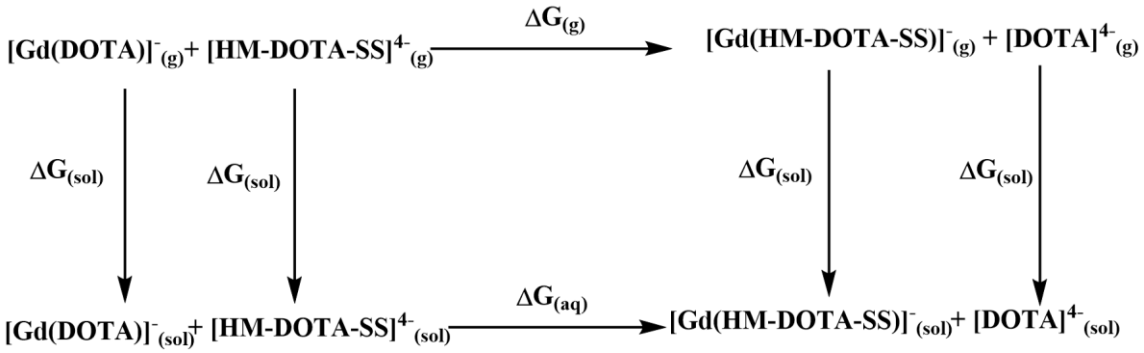

Scheme 4.1. Thermodynamic cycle illustrating the relative stabilities of $[Gd(DOTA)]^-$ and $[Gd(HMDOTA\text{-}SS)]^-$ complexes.

Similarly, the thermodynamic stability of the ligands DOTA and T was evaluated by the free energy of formation of the corresponding reaction, as shown in Scheme B1 of Appendix-B. In this case, the $[Gd(T)]^-$ complex exhibited greater stability than the $[Gd(DOTA)]^-$ complex, as confirmed by its more negative $\triangle G_{(g)}$ and $\triangle G_{(aq)}$ values (Table B4 of Appendix-B). This high thermodynamic stability of the $[Gd(HMDOTA\text{-}SS)]^-$ and $[Gd(T)]^-$ complexes can be attributed to the presence of rigid hydrophilic hydroxymethylene and hydroxyethylene groups within the macrocyclic ring. The observed stability trends are consistent with the experimental stability constant of the complexes.[29] The corresponding experimental $\triangle G_{aq}^{exp}$ values, presented in Table B4 of Appendix-B, were evaluated from the equilibrium constant reported in previous literature.[29]

4.3.5. Influence of Ligand Modification on Water Exchange Rate (k_{ex}^{298}) of DOTA Derivatives

Various strategies have been developed to modulate k_{ex}^{298} by altering the structural and electronic characteristics of Gd^{3+} complexes.[43,44,103] It is well known that the $[Gd(DOTA)]^-$ complex and its analogs may exist as two distinct diastereomers (SAP and TSAP). The TSAP isomer typically exhibits a higher k_{ex}^{298} than the SAP isomer, primarily due to increased steric hindrance around the coordinated water molecule.[32,43,45–47] Additionally, increasing steric compression through ligand modification was also proved to be an effective strategy to accelerate k_{ex}^{298}. In nine coordinated Gd^{3+} complexes, water exchange generally follows a dissociative mechanism and most strategies to increase k_{ex}^{298} rely on destabilizing the nine coordinated q=1 complex w.r.t. the eight coordinated transition state (TS).[103,104]

Table 4.2. Calculated Gd-O (w) bond length, (ρ, au), ELF, and k_{ex}^{298} values of [Gd(DOTA)(H_2O)]$^-$.2H_2O and [Gd(HMDOTA-SS)(H_2O)]$^-$.2H_2O and [Gd(T)(H_2O)]$^-$.2H_2O complexes using TPSSh/LCRECP/6-311G(d,p) method.

Complexes	Gd-O(w) bond length Å	ρ_{BCP}	ELF	k_{ex}^{298}(s^{-1}) $\times 10^6$
[Gd(DOTA)(H_2O)]$^-$.2H_2O (TSAP)	2.521	0.0359	0.1009	17.24
[Gd(DOTA)(H_2O)]$^-$.2H_2O (SAP)	2.492	0.0389	0.1050	2.00
[Gd(HMDOTA-SS)(H_2O)]$^-$.2H_2O (TSAP)	2.547	0.0348	0.0989	39.38
[Gd(HMDOTA-SS)(H_2O)]$^-$.2H_2O (SAP)	2.542	0.0351	0.1000	29.92
[Gd(T)(H_2O)]$^-$.2H_2O (TSAP)	2.551	0.0341	0.0948	106.10
[Gd(T)(H_2O)]$^-$.2H_2O (SAP)	2.510	0.0356	0.1030	18.43

Moreover, understanding the Gd-O(w) bond strength is essential for evaluating the k_{ex}^{298} and relaxivity of Gd^{3+} complexes. The Ln-O(w) bond calculated for [Ln(DOTA)(H_2O)]$^-$.2H_2O, [Ln(HMDOTASS)(H_2O)]$^-$.2H_2O and [Ln(T)(H_2O)]$^-$.2H_2O systems across the lanthanide series offer valuable insights into the varying lability of coordinated water molecules, as shown in Table B2 of Appendix-B. These Ln-O(w) bond length diverges with the decrease in the ionic radius of the Ln^{3+} ion across the Ln^{3+}-series. To analyze the trend in the k_{ex}^{298} between the coordinated water molecule and the bulk waters in the three studied complexes, we focused only on the Gd-O(w) bond. It was observed that the Gd-O(w) bond is significantly longer in the TSAP isomer compared to the SAP isomer for all complexes, consistent with the higher lability and faster k_{ex}^{298} typically associated with the TSAP geometry, as shown in Table B2 of Appendix-B. For a dissociatively activated mechanism, where the Ln-O(w) bond breaks to form an eight-coordinated TS, the residence time of the coordinated water molecule is expected to increase as the Ln-O(w) bond becomes shorter. It was found that, among the studied complexes, the Gd-O(w) bond is the shortest in the [Ln(DOTA)(H_2O)]$^-$.2H_2O complex, suggesting a more tightly bound water molecule and, consequently, a longer residence time. To probe the strength of the coordinated water molecule, we further investigated the ρ_{BCP} and ELF at the corresponding bond critical point of the Ln-O(w) bond. Our results reveal that both

ρ_{BCP} and ELF values follow the trend [Ln(DOTA)(H_2O)]$^-$.2H_2O > [Ln(HMDOTA-SS)(H_2O)]$^-$.2H_2O > [Ln(T)(H_2O)]$^-$.2H_2O, as shown in Table 4.2 and Figure 4.7. The k_{ex}^{298} values observed for both TSAP and SAP isomer of [Ln(DOTA)(H_2O)]$^-$.2H_2O, [Ln(HMDOTA-SS)(H_2O)]$^-$.2H_2O, and [Ln(T)(H_2O)]$^-$.2H_2O complexes show an increase in the middle of the Ln^{3+}-series followed by a decrease toward the end. The ELF value decreases gradually along the series (Figure 4.7), indicating the weak interaction between the inner-sphere water molecule and the metal ion as we move toward the end of the Ln^{3+}-series. Although the Ln-O(w) bond length becomes shorter, the decreasing ELF values suggest a reduction in covalent character. This is called the labile capping bond phenomenon.[105] This is also in line with the observed k_{ex}^{298}, as weaker Ln-O(w) bonds facilitate faster k_{ex}^{298} in dissociatively activated mechanisms. Furthermore, the ρ_{BCP} value > 0.10 au indicates the ionic nature of bonding. As a result, the coordinated water molecule in all three complexes exhibits significantly different k_{ex}^{298}, which correlates with variations in Ln-O(w) bond strength, as shown in Table 4.2. Additionally, the SAP and TSAP isomers exhibit distinct k_{ex}^{298}. Therefore, we have applied the model proposed by Carlos et al.,[41] which determines the ρ_{BCP} and ELF at the bond critical point of the respective bond, to evaluate k_{ex}^{298}, as shown in Eqs. 4.2 and 4.3. The [Ln(HMDOTA SS)(H_2O)]$^-$.2H_2O, [Ln(T)(H_2O)]$^-$.2H_2O complexes exhibit higher k_{ex}^{298} compared to the [Ln(DOTA)(H_2O)]$^-$.2H_2O complex. These findings suggest that the k_{ex}^{298} in these macrocyclic DOTA derivatives is primarily governed by the strength of the Gd-O(w) bond, which influences the ability of the system to reach the eight-coordinated TS.

$$\rho_{BCP} = 0.05941 - 0.00316\, log k_{ex}^{298} \quad (4.2)$$

$$ELF = 0.13532 - 0.00503\, log k_{ex}^{298} \quad (4.3)$$

To understand whether factors beyond the bond strength influence the k_{ex}^{298}, we performed a mechanistic investigation and calculated the activation parameter values of the complexes, as shown in Table B5 of Appendix-B. Typically, the exchange of inner-sphere water molecules in nine-coordinated complexes primarily proceeds via a dissociative mechanism. This was confirmed by determining the TS connecting the nine-coordinated complex and the eight-coordinated intermediate. The Gd-O(w) distances in the TSs differ significantly from those in the ground state (GS), as shown in Figure 4.8 and Figure B34 of Appendix-B. For the TSAP isomer of [Gd(DOTA)(H_2O)]$^-$.2H_2O, [Gd(HMDOTA-SS)(H_2O)]$^-$.2H_2O, and [Gd(T)(H_2O)]$^-$.2H_2O complexes, the Gd-O(w) distances are 3.44 Å, 3.42 Å, and 3.46 Å, while for the SAP isomer, Gd-O(w) bond lengths are 3.33 Å, 3.41 Å, and 3.42 Å, respectively. The optimized

TSs for both TSAP and SAP isomers of $[Gd(DOTA)(H_2O)]^-.2H_2O$, $[Gd(HMDOTA\text{-}SS)(H_2O)]^-.2H_2O$, and $[Gd(T)(H_2O)]^-.2H_2O$ complexes are shown in Figure 4.8 and Figure B34 of Appendix-B. The increasing Gd-O(w) bond length in these TSs facilitates a dissociative water exchange mechanism, with a positive value of activation entropy ($\triangle S^{\ddagger}$). To further confirm the mechanistic pathway, intrinsic reaction coordinate (IRC) calculations were performed (Figure B35 of Appendix-B), which support the dissociative nature of k_{ex}^{298} .

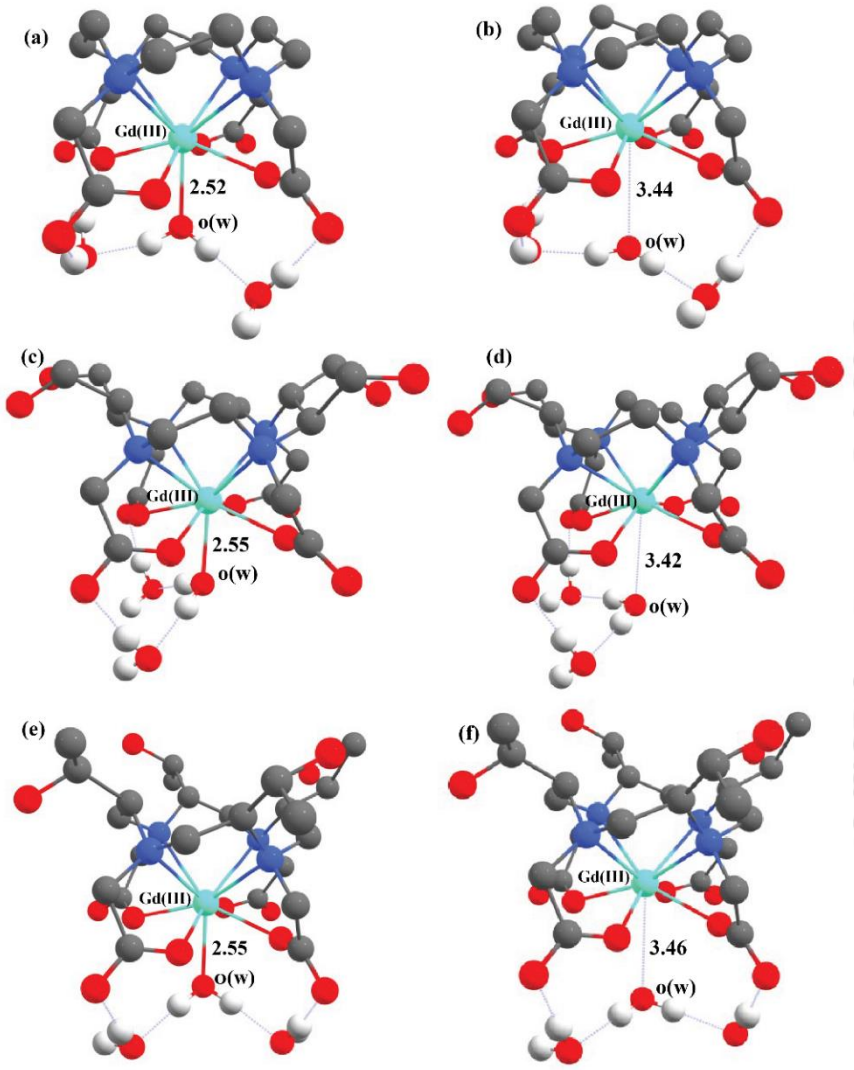

Figure 4.8. Optimized structures of the ground states (left panel) and transition states (right panel) obtained from DFT calculations for the $[Gd(DOTA)(H_2O)]$-$.2H_2O$ (a and b), $[Gd(HMDOTA\text{-}SS)(H_2O)]^-.2H_2O$ (c and d) and $[Gd(T)(H_2O)]^-.2H_2O$ (e and f) systems for TSAP isomer.

The activation free energy ($\triangle G^{\ddagger}$) values obtained from DFT calculations were 4.34, 2.25, and 2.87 kcal mol^{-1}, respectively, for the TSAP isomer of $[Gd(DOTA)(H_2O)]^-.2H_2O$,

$[Gd(HMDOTA\text{-}SS)(H_2O)]^{-}.2H_2O$, and $[Gd(T)(H_2O)]^{-}.2H_2O$ complexes. For the corresponding SAP isomers, the $\triangle G^{\ddagger}$ values were slightly higher at 4.72, 2.83, and 4.12 kcal mol^{-1}, respectively. These results further confirmed the stabilization of the TSs. Notably, we observe that the $\triangle G^{\ddagger}$ values increase as the Gd-O(w) bond strength of the complexes decreases (Table B5 of Appendix-B). The analysis of activation enthalpies ($\triangle H^{\ddagger}$) further supports the fast k_{ex}^{298} in the TSAP isomers compared to their SAP. The k_{ex}^{298} for $[Gd(HMDOTA\text{-}SS)(H_2O)]^{-}.2H_2O$, and $[Gd(T)(H_2O)]^{-}.2H_2O$ complexes are higher than that of the parent $[Gd(DOTA)(H_2O)]^{-}.2H_2O$ complex as shown in Table B5 of Appendix-B, due to steric effect from hydrophilic substituents weakeing the Gd-O(w) bond. To support the observed difference in k_{ex}^{298} among the studied complexes, we carried out a computational analysis of the hyperfine interaction (HFI) between the coordinated water molecule and the Gd^{3+} center. As ^{17}O HFCC values are highly sensitive to the change in bond length, orientation, and position of the inner sphere water molecules relative to the Gd-O vector. A high ^{17}O HFCCs value indicates stronger Gd-O(w) bond strength.

4.3.6. Impact of Coordination Geometry on Zero-Field Splitting (ZFS)

ZFS in Gd^{3+} complexes is key to their electronic relaxation and magnetic properties. The ^{8}S ground state (S=7/2) split into eight M_S sublevels (=±7/2, ±5/2, ±3/2 and ±1/2) without an external magnetic field, due to ZFS, mainly arises from spin-orbit coupling (SOC) and, to a lesser extent, spin-spin coupling (SSC).[51,52] ZFS is highly responsive to the interplay of the ligand field, SOC, and interelectronic repulsion, offering valuable insights into the ground-state electronic and magnetic properties. In our study, the TSAP and SAP isomers exhibit distinct coordination geometries, leading to varied 4f orbital splitting. While the D value remains relatively unchanged with the change in coordination geometry, the overall ZFS energy ($\triangle$) varies notably. A comprehensive understanding of the relationship between electronic relaxation and the coordination environment will require further in-depth investigation.[106] It is well established that for Mn^{2+} and Gd^{3+} complexes, when E/D values are >0.2, predicting the sign of D becomes challenging.[51,56,57] Since electronic relaxation is related to the fluctuation in the mean square ZFS energy ($\triangle^2$), only the absolute value of $\triangle$ is significant. The $|D|$ value for the $[Gd(DOTA)(H_2O)]^{-}.2H_2O$, $[Gd(HMDOTA\text{-}SS)(H_2O)]^{-}.2H_2O$, and $[Gd(T)(H_2O)]^{-}.2H_2O$ complexes are similar and closely align with those reported for other Gd^{3+} complexes using a multireference approach, as shown in Table B6 of Appendix-B. DFT-based methods overestimated the ZFS parameters by an order of magnitude, highlighting the higher accuracy of *ab initio* CASSCF/NEVPT2 method (Table B6 of Appendix-B) for Gd^{3+}

complexes. Additionally, for the pair of isomers TSAP and SAP, the SAP show slightly higher D-value and lower E/D ratio, due to its more symmetrical coordination environment. This explains the smaller ZFS energy observed in the TSAP isomer (Table B6, Appendix-B). The trend observed in the calculated $|D|$ values for this series of complexes is related to the splitting of the Kramers doublets originating from the ^8S configuration of the Gd^{3+} ion. In systems with axial symmetry, the Krammer doublets are separated by energy intervals of 2D, 4D, and 6D w.r.t. the lowest energy level if $D > 0$ and a reverse pattern if $D < 0$. The separation of Kramers doublet in SAP increases with an increase in ZFS energy, with a corresponding increase in D-value compared to the TSAP isomer, as shown in Figure 4.9.

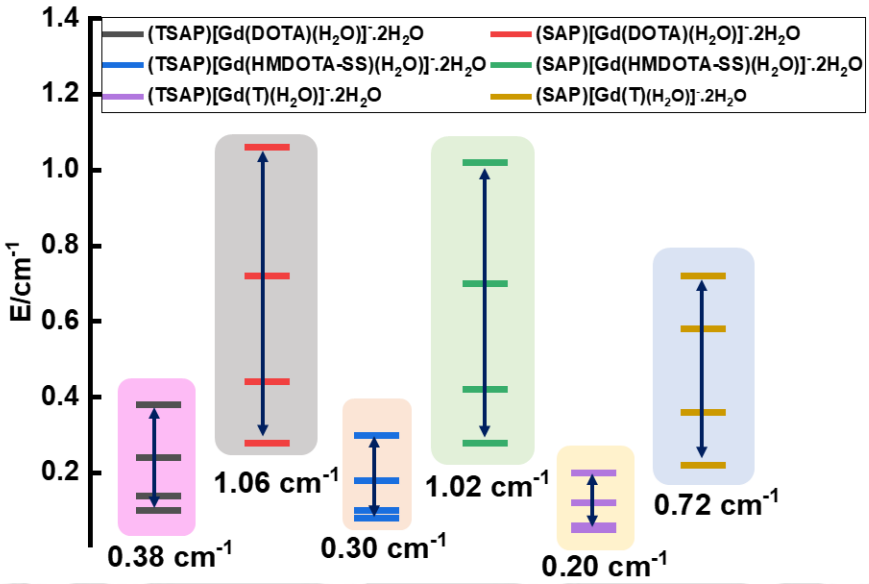

Figure 4.9. Splitting of the Kramers doublets as determined by CASSCF/ NEVPT2 calculations.

This suggests that a more symmetrical ligand environment enhances ZFS energy as seen in both TSAP and SAP geometries. This aligns well with previous magnetostructural correlation studies on $[Gd(DOTA)(H_2O)]^-$ complex.[51] These findings confirm that the distance between the Gd^{3+} and water molecules plays a significant role in fluctuating ZFS parameters, with the D-value showing an almost linear increase with the Gd-O(w) bond length. However, the sign of the D parameter remains unaffected by changes in the Gd-O(w) distance. To better explore the influence of structural parameters on the ZFS parameters (D and E/D) for $[Gd(HMDOTA\text{-}SS)(H_2O)]^-.2H_2O$, and $[Gd(T)(H_2O)]^-.2H_2O$ complexes, we carried out a detailed analysis of the dynamic effects by systematically varying the distance of the water molecule and the Gd^{3+} center.

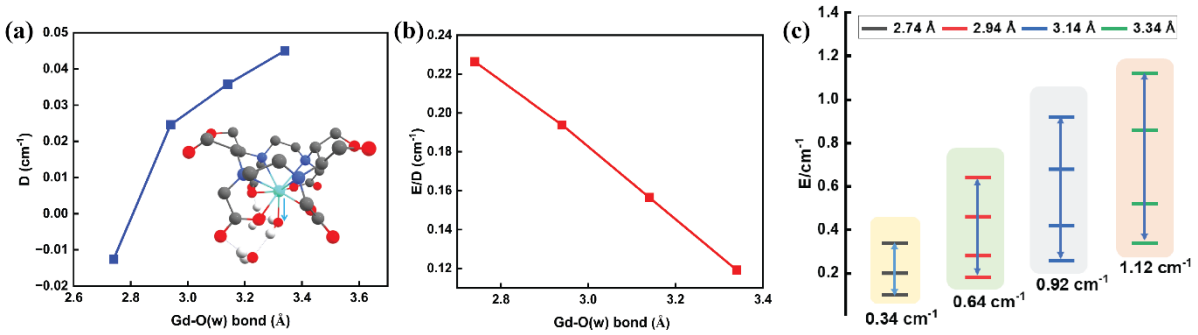

Figure 4.10. Graphical representation of *ab initio* CASSCF/NEVPT2 results for the TSAP isomer of $[Gd(HMDOTA\text{-}SS)(H_2O)]^-.2H_2O$ complex with the variation of Gd-O(w) bond length from 2.74 to 3.34 Å (a) variation in D-parameter, (b) variation in E/D ratio, and (c) corresponding variation of Kramers doublet energy levels with bond length.

We studied the effects of the distortion of the water molecule by increasing the bond length from 2.74 to 3.34 Å and 2.75 to 3.35 Å, respectively. The elongation of the Gd-O(w) bond gradually increases the D-value while the E/D ratio decreases, as shown in Figure 4.10 and Figures B36-B38 of Appendix-B. Thus, an effective strategy for developing efficient MRI CAS involves the structural modification of the pendant arms of DOTA.

4.4. Conclusions

This study explores the aqueous phase dynamics of two distinct isomeric forms of $[Ln(DOTA)]^-$ and its derivatives $[Ln(HMDOTA\text{-}SS)]^-$ and $[Ln(T)]^-$ complexes using DFT-based AIMD simulations. The findings highlight the reliability of the DFT-AIMD simulations in accurately predicting the solution structure of Ln^{3+}-ligand complexes and reveal the high aqueous stability of DOTA and its derivatives with minimal changes in RDF sharpness from 25˚C to 65˚C. La^{3+} complexes show relatively broad RDF peaks, reflecting their lower stability compared to the corresponding Gd^{3+} and Lu^{3+} derivatives. Moreover, the RDF peak shift from La^{3+} to Lu^{3+} reflects the expected lanthanide contraction. The increased binding affinity and thermodynamic stability of the $[Ln(HMDOTA\text{-}SS)]^-$ and $[Ln(T)]^-$ complexes are attributed to the presence of hydrophilic substituents in the cyclen backbone, strengthening the metal-ligand interactions.

Beyond aqueous stability, the water dynamics at the 9th coordination site significantly impact the efficiency of MRI CAs. Our finding shows that the k_{ex}^{298} is consistently higher for the TSAP geometry across all three complexes as compared to SAP geometry, likely due to increased steric compression around the coordinated water. Notably, $[Gd(HMDOTA\text{-}SS)(H_2O)]^-.2H_2O$

and $[Gd(T)(H_2O)]^-.2H_2O$ complexes exhibit faster k_{ex}^{298} than $[Gd(DOTA)(H_2O)]^-.2H_2O$, attributed to the presence of bulky, hydrophilic groups in their ligand backbones, which leads to an elongation of the Gd-O(w) bond, i.e., dissociative water exchange mechanism. These results support the higher relaxivity, essential for reducing toxic metal ion dosages in clinical MRI. Although the SAP isomer exhibits a higher D value than the TSAP, leading to smaller Kramers doublet splitting in the TSAP isomer. However, the limited data available in this study prevents the establishment of a clear correlation between the ligand field and electron spin relaxation. Overall, this study provides insights for designing safer, more efficient Gd^{3+}-based MRI agents.

4.5. References

[1] A. S. Merbach, *The Chemistry of Contrast Agents in Medical Magnetic Resonance Imaging*, John Wiley & Sons, Incorporated, New York, 2nd ed., 2013.

[2] E. Caillet, L. Nunes, S. V. Eliseeva, M. Ndiaye, M. Isaac, A. Pallier, J.-F. Morfin, H. Meudal, S. Petoud, S. Routier, C. Platas-Iglesias, F. Buron and C. S. Bonnet, *Dalton Trans.*, 2024, **53**, 9028-9041.

[3] C. Platas-Iglesias, *Eur. J. Inorg. Chem.*, 2012, **2012**, 2023-2033.

[4] J. Ciupka, X. Cao-Dolg, J. Wiebke and M. Dolg, *Phys. Chem. Chem. Phys.*, 2010, **12**, 13215-13223.

[5] Z. Garda, V. Nagy, A. Rodríguez-Rodríguez, R. Pujales-Paradela, V. Patinec, G. Angelovski, É. Tóth, F. K. Kálmán, D. Esteban-Gómez, R. Tripier, C. Platas-Iglesias and G. Tircsó, *Inorg. Chem.*, 2020, **59**, 8184-8195.

[6] T. Grobner, *Nephrol. Dial. Transplant.*, 2006, **21**, 1104-1108.

[7] A. C. Oliveira, H. A. L. Filipe, J. P. P. Ramalho, A. Salvador, C. F. G. C. Geraldes, M. J. Moreno and L. M. S. Loura, *Inorg. Chem.*, 2022, **61**, 11837-11858.

[8] N. O. Nuñez, F. Cussó, E. Cantelar, B. Martin-Gracia, J. M. De La Fuente, A. Corral, M. Balcerzyk and M. Ocaña, *Nanomaterials*, 2020, **10**, 149-161.

[9] S. Aime, M. Botta, S. G. Crich, G. B. Giovenzana, G. Jommi, R. Pagliarin and M. Sisti, *J. Chem. Soc. Chem. Commun.*, 1995, 1885-1886.

[10] S. Lacerda and É. Tóth, *ChemMedChem*, 2017, **12**, 883-894.

[11] Y. Wu, Y. Sun, X. Zhu, Q. Liu, T. Cao, J. Peng, Y. Yang, W. Feng and F. Li, *Biomaterials*, 2014, **35**, 4699-4705.

[12] M. C. Heffern, L. M. Matosziuk and T. J. Meade, *Chem. Rev.*, 2014, **114**, 4496-4539.

[13] Y. Ning, J. Tang, Y.-W. Liu, J. Jing, Y. Sun and J.-L. Zhang, *Chem. Sci.*, 2018, **9**, 3742-3753.

[14] C. Müller, C. Vermeulen, K. Johnston, U. Köster, R. Schmid, A. Türler and N. P. Van Der Meulen, *EJNMMI Res.*, 2016, **6**, 1-10.

[15] M. Van De Voorde, C. Duchemin, R. Heinke, L. Lambert, E. Chevallay, T. Schneider, M. Van Stenis, T. E. Cocolios, T. Cardinaels, B. Ponsard, M. Ooms, T. Stora and A. R. Burgoyne, *Front. Med.*, 2021, **8**, 675221-675229.

[16] A. Scarciglia, C. Papi, C. Romiti, A. Leone, E. Di Gregorio and G. Ferrauto, *Glob. Chall.*, 2025, **9**, 2400269.

[17] E. Lancelot, J.-S. Raynaud and P. Desché, *Invest. Radiol.*, 2020, **55**, 578-588.

[18] H. Li and T. J. Meade, *J. Am. Chem. Soc.*, 2019, **141**, 17025-17041.

[19] J. Wahsner, E. M. Gale, A. Rodríguez-Rodríguez and P. Caravan, *Chem. Rev.*, 2019, **119**, 957-1057.

[20] A. D. Sherry, P. Caravan and R. E. Lenkinski, *J. Magn. Reson. Imaging*, 2009, **30**, 1240-1248.

[21] P. Caravan, *Chem. Soc. Rev.*, 2006, **35**, 512-523.

[22] S. Aime, M. Botta, M. Fasano, M. P. M. Marques, C. F. G. C. Geraldes, D. Pubanz and A. E. Merbach, *Inorg. Chem.*, 1997, **36**, 2059-2068.

[23] S. Aime, M. Botta and G. Ermondi, *Inorg. Chem.*, 1992, **31**, 4291-4299.

[24] L. Dai, C. M. Jones, W. T. K. Chan, T. A. Pham, X. Ling, E. M. Gale, N. J. Rotile, W. C.-S. Tai, C. J. Anderson, P. Caravan and G.-L. Law, *Nat. Commun.*, 2018, **9**, 857-866.

[25] P. Robert, S. Lehericy, S. Grand, X. Violas, N. Fretellier, J.-M. Idée, S. Ballet and C. Corot, *Invest. Radiol.*, 2015, **50**, 473-480.

[26] S. Bussi, A. Coppo, C. Botteron, V. Fraimbault, A. Fanizzi, E. De Laurentiis, S. Colombo Serra, M. A. Kirchin, F. Tedoldi and F. Maisano, *J. Magn. Reson. Imaging*, 2018, **47**, 746-752.

[27] M. Port, J.-M. Idée, C. Medina, C. Robic, M. Sabatou and C. Corot, *BioMetals*, 2008, **21**, 469-490.

[28] S. Laurent, L. V. Elst and R. N. Muller, *Contrast Media Mol. Imaging*, 2006, **1**, 128-137.

[29] J. Zhang, L. Dai, L. He, A. Bhattarai, C.-M. Chan, W. C.-S. Tai, V. Vardhanabhuti and G.-L. Law, *Commun. Chem.*, 2023, **6**, 251-260.

[30] M. Chan, J. Lux, T. Nishimura, K. Akiyoshi and A. Almutairi, *Biomacromolecules*, 2015, **16**, 2964-2971.

[31] R. S. Ranganathan, N. Raju, H. Fan, X. Zhang, M. F. Tweedle, J. F. Desreux and V. Jacques, *Inorg. Chem.*, 2002, **41**, 6856-6866.

[32] M. Woods, Z. Kovacs, S. Zhang and A. D. Sherry, *Angew. Chem. Int. Ed.*, 2003, **42**, 5889-5892.

[33] K. B. Maier, L. N. Rust, F. Carniato, M. Botta and M. Woods, *Chem. Commun.*, 2024, **60**, 2898-2901.

[34] K. M. Payne and M. Woods, *Bioconjug. Chem.*, 2015, **26**, 338-344.

[35] V. Comblin, D. Gilsoul, M. Hermann, V. Humblet, V. Jacques, M. Mesbahi, C. Sauvage and J. F. Desreux, *Coord. Chem. Rev.*, 1999, **185**, 451-470.

[36] M. D. Lee, C.-T. Loh, J. Shin, S. Chhabra, M. L. Dennis, G. Otting, J. D. Swarbrick and B. Graham, *Chem. Sci.*, 2015, **6**, 2614-2624.

[37] I. Solomon, *Phys. Rev.*, 1955, **99**, 559-565.

[38] I. Solomon and N. Bloembergen, *J. Chem. Phys.*, 1956, **25**, 261-266.

[39] N. Bloembergen, *J. Chem. Phys.*, 1957, **27**, 572-573.

[40] N. Bloembergen and L. O. Morgan, *J. Chem. Phys.*, 1961, **34**, 842-850.

[41] M. Regueiro-Figueroa and C. Platas-Iglesias, *J. Phys. Chem. A*, 2015, **119**, 6436-6445.

[42] H. U. Rashid, M. A. U. Martines, J. Jorge, P. M. De Moraes, M. N. Umar, K. Khan and H. U. Rehman, *Bioorg. Med. Chem.*, 2016, **24**, 5663-5684.

[43] S. J. Ratnakar, M. Woods, A. J. M. Lubag, Z. Kovács and A. D. Sherry, *J. Am. Chem. Soc.*, 2008, **130**, 6-7.

[44] E. Boros, S. Karimi, N. Kenton, L. Helm and P. Caravan, *Inorg. Chem.*, 2014, **53**, 6985-6994.

[45] M. Woods, S. Aime, M. Botta, J. A. K. Howard, J. M. Moloney, M. Navet, D. Parker, M. Port and O. Rousseaux, *J. Am. Chem. Soc.*, 2000, **122**, 9781-9792.

[46] G. Tircso, B. C. Webber, B. E. Kucera, V. G. Young and M. Woods, *Inorg. Chem.*, 2011, **50**, 7966-7979.

[47] S. Zhang, Z. Kovacs, S. Burgess, S. Aime, E. Terreno and A. D. Sherry, *Chemistry*, 2001, **7**, 288-296.

[48] R. J. Dimelow, N. A. Burton and I. H. Hillier, *Phys. Chem. Chem. Phys.*, 2007, **9**, 1318-1328.

[49] C. Kumas, W. S. Fernando, P. Zhao, M. Regueiro-Figueroa, G. E. Kiefer, A. F. Martins, C. Platas-Iglesias and A. D. Sherry, *Inorg. Chem.*, 2016, **55**, 9297-9305.

[50] F. Senn, L. Helm, A. Borel and C. A. Daul, *Comptes Rendus Chim.*, 2011, **15**, 250-254.

[51] S. Khan, A. Kubica-Misztal, D. Kruk, J. Kowalewski and M. Odelius, *J. Chem. Phys.*, 2015, **142**, 034304-034314.

[52] S. Khan, R. Pollet, R. Vuilleumier, J. Kowalewski and M. Odelius, *J. Chem. Phys.*, 2017, **147**, 244306-244314.

[53] M. Benmelouka, J. Van Tol, A. Borel, M. Port, L. Helm, L. C. Brunel and A. E. Merbach, *J. Am. Chem. Soc.*, 2006, **128**, 7807-7816.

[54] M. Benmelouka, A. Borel, L. Moriggi, L. Helm and A. E. Merbach, *J. Phys. Chem. B*, 2007, **111**, 832-840.

[55] R. B. Clarkson, A. I. Smirnov, T. I. Smirnova, H. Kang, R. L. Belford, K. Earle and J. H. Freed, *Mol. Phys.*, 1998, **95**, 1325-1332.

[56] N. Keot and M. Sarma, *Phys. Chem. Chem. Phys.*, 2023, **25**, 31165-31177.

[57] N. Keot and M. Sarma, *J. Phys. Chem. A*, 2024, **128**, 8346-8359.

[58] C. A. Chang, L. C. Francesconi, M. F. Malley, K. Kumar, J. Z. Gougoutas, M. F. Tweedle, D. W. Lee and L. J. Wilson, *Inorg. Chem.*, 1993, **32**, 3501-3508.

[59] F. Benetollo, G. Bombieri, L. Calabi, S. Aime and M. Botta, *Inorg. Chem.*, 2003, **42**, 148-157.

[60] Q. Miao, R. Dekkers, K. B. S. S. Gupta, M. Overhand, R. Dasgupta and M. Ubbink, *Inorg. Chem.*, 2023, **62**, 3776-3787.

[61] R. Pollet, C. S. Bonnet, P. Retailleau, P. Durand and É. Tóth, *Inorg. Chem.*, 2017, **56**, 4317-4323.

[62] D. S. Kaliakin, J. A. Sobrinho, J. H. S. K. Monteiro, A. De Bettencourt-Dias and D. C. Cantu, *Phys. Chem. Chem. Phys.*, 2021, **23**, 4287-4299.

[63] R. D. O'Brien, T. J. Summers, D. S. Kaliakin and D. C. Cantu, *Phys. Chem. Chem. Phys.*, 2022, **24**, 10263-10271.

[64] A. Ramírez-Solís, J. I. Amaro-Estrada, J. Hernández-Cobos and L. Maron, *J. Phys. Chem. A*, 2017, **121**, 2293-2297.

[65] R. C. Shiery, J. L. Fulton, M. Balasubramanian, M.-T. Nguyen, J.-B. Lu, J. Li, R. Rousseau, V.-A. Glezakou and D. C. Cantu, *Inorg. Chem.*, 2021, **60**, 3117-3130.

[66] D. Van Der Spoel, E. Lindahl, B. Hess, G. Groenhof, A. E. Mark and H. J. C. Berendsen, *J. Comput. Chem.*, 2005, **26**, 1701-1718.

[67] M. J. Abraham, T. Murtola, R. Schulz, S. Páll, J. C. Smith, B. Hess and E. Lindahl, *SoftwareX*, 2015, **1**, 19-25.

[68] J. Wang, R. M. Wolf, J. W. Caldwell, P. A. Kollman and D. A. Case, *J. Comput. Chem.*, 2004, **25**, 1157-1174.

[69] A. K. Rappe, C. J. Casewit, K. S. Colwell, W. A. Goddard and W. M. Skiff, *J. Am. Chem. Soc.*, 1992, **114**, 10024-10035.

[70] W. L. Jorgensen, J. Chandrasekhar, J. D. Madura, R. W. Impey and M. L. Klein, *J. Chem. Phys.*, 1983, **79**, 926-935.

[71] P. Mark and L. Nilsson, *J. Phys. Chem. A*, 2001, **105**, 9954-9960.

[72] T. Lu and V. Sobtop, 1.0 (dev3. 1), 2022.

[73] M. Parrinello and A. Rahman, *J. Appl. Phys.*, 1981, **52**, 7182-7190.

[74] H. J. C. Berendsen, J. P. M. Postma, W. F. Van Gunsteren, A. DiNola and J. R. Haak, *J. Chem. Phys.*, 1984, **81**, 3684-3690.

[75] J. P. Perdew, K. Burke and M. Ernzerhof, *Phys. Rev. Lett.*, 1996, **77**, 3865-3868.

[76] I.-C. Lin, A. P. Seitsonen, I. Tavernelli and U. Rothlisberger, *J. Chem. Theory Comput.*, 2012, **8**, 3902-3910.

[77] J. Hutter, M. Iannuzzi, F. Schiffmann and J. VandeVondele, *WIREs Comput. Mol. Sci.*, 2014, **4**, 15-25.

[78] S. Goedecker, M. Teter and J. Hutter, *Phys. Rev. B*, 1996, **54**, 1703-1710.

[79] C. Hartwigsen, S. Goedecker and J. Hutter, *Phys. Rev. B*, 1998, **58**, 3641-3662.

[80] J. VandeVondele and J. Hutter, *J. Chem. Phys.*, 2007, **127**, 114105-114114.

[81] M. J. Frisch, G. W. Trucks, H. B. Schlegel, G. E. Scuseria, M. A. Robb, J. R. Cheeseman, G. Scalmani, V. Barone, G. A. Petersson, H. Nakatsuji, X. Li, M. Caricato, A. V. Marenich, J. Bloino, B. G. Janesko, R. Gomperts, B. Mennucci, H. P. Hratchian, J. V. Ortiz, A. F. Izmaylov, J. L. Sonnenberg, D. Williams-Young, F. Ding, F. Lipparini, F. Egidi, J. Goings, B. Peng, A. Petrone, T. Henderson, D. Ranasinghe, V. G. Zakrzewski, J. Gao, N. Rega, G. Zheng, W. Liang, M. Hada, M. Ehara, K. Toyota, R. Fukuda, J. Hasegawa, M. Ishida, T. Nakajima, Y. Honda, O. Kitao, H. Nakai, T. Vreven, K. Throssell, J. A. Montgomery, J. E. Peralta, F. Ogliaro, M. J. Bearpark, J. J. Heyd, E. N. Brothers, K. N. Kudin, V. N. Staroverov, T. A. Keith, R. Kobayashi, J. Normand, K. Raghavachari, A. P. Rendell, J. C. Burant, S. S. Iyengar, J. Tomasi, M. Cossi, J. M. Millam, M. Klene, C. Adamo, R. Cammi, J. W. Ochterski, R. L. Martin, K. Morokuma, O. Farkas, J. B. Foresman and D. J. Fox, Gaussian 16 Revision C.01, Gaussian Inc., Wallingford CT, 2016.

[82] J. Tao, J. P. Perdew, V. N. Staroverov and G. E. Scuseria, *Phys. Rev. Lett.*, 2003, **91**, 146401-146404.

[83] M. Douglas and N. M. Kroll, *Ann. Phys.*, 1974, **82**, 89-155.

[84] F. E. Jorge, L. S. C. Martins and M. L. Franco, *Chem. Phys. Lett.*, 2016, **643**, 84-88.

[85] A. Z. De Oliveira, I. B. Ferreira, C. T. Campos, F. E. Jorge and P. A. Fantin, *J. Mol. Model.*, 2019, **25**, 1-9.

[86] J. Tomasi, B. Mennucci and R. Cammi, *Chem. Rev.*, 2005, **105**, 2999-3094.

[87] N. Keot and M. Sarma, *RSC Adv.*, 2023, **13**, 1516-1529.

[88] M. Dolg, H. Stoll, A. Savin and H. Preuss, *Theor. Chim. Acta*, 1989, **75**, 173-194.

[89] J.-D. Chai and M. Head-Gordon, *Phys. Chem. Chem. Phys.*, 2008, **10**, 6615-6620.

[90] F. Weigend, *Phys. Chem. Chem. Phys.*, 2006, **8**, 1057-1065.

[91] A. V. Marenich, C. J. Cramer and D. G. Truhlar, *J. Phys. Chem. B*, 2009, **113**, 6378-6396.

[92] C. F. Matta, *The Quantum Theory of Atoms in Molecules: From Solid State to DNA and Drug Design*, John Wiley & Sons, Incorporated, Hoboken, 1st ed., 2007.

[93] T. Lu and F. Chen, *J. Comput. Chem.*, 2012, **33**, 580-592.

[94] F. Neese, *WIREs Comput. Mol. Sci.*, 2012, **2**, 73-78.

[95] D. Aravena, F. Neese and D. A. Pantazis, *J. Chem. Theory Comput.*, 2016, **12**, 1148-1156.

[96] F. Neese, F. Wennmohs, A. Hansen and U. Becker, *Chem. Phys.*, 2009, **356**, 98-109.

[97] J. W. Park, *J. Chem. Theory Comput.*, 2019, **15**, 5417-5425.

[98] F. Neese, *J. Chem. Phys.*, 2005, **122**, 034107-034119.

[99] U. Cosentino, A. Villa, D. Pitea, G. Moro, V. Barone and A. Maiocchi, *J. Am. Chem. Soc.*, 2002, **124**, 4901-4909.

[100] B. A. Hess, A. Kędziorski, L. Smentek and D. J. Bornhop, *J. Phys. Chem. A*, 2008, **112**, 2397-2407.

[101] L. Smentek, B. Andes Hess, J. P. Cross, H. Charles Manning and D. J. Bornhop, *J. Chem. Phys.*, 2005, **123**, 244302-244311.

[102] O. V. Yazyev, L. Helm, V. G. Malkin and O. L. Malkina, *J. Phys. Chem. A*, 2005, **109**, 10997-11005.

[103] L. Leone, D. Esteban-Gómez, C. Platas-Iglesias, M. Milanesio and L. Tei, *Chem. Commun.*, 2019, **55**, 513-516.

[104] L. Leone, S. Camorali, A. Freire-García, C. Platas-Iglesias, D. Esteban Gomez and L. Tei, *Dalton Trans.*, 2021, **50**, 5506-5518.

[105] J. Zhang and M. Dolg, *J. Phys. Chem. A*, 2015, **119**, 774-780.

[106] A. Borel, J. F. Bean, R. B. Clarkson, L. Helm, L. Moriggi, A. D. Sherry and M. Woods, *Chem. – Eur. J.*, 2008, **14**, 2658-2667.

Chapter 5

Probing the Dynamic Behaviour and Magnetic Identification of Seven Coordinated Mn^{2+} Complexes: a Combined AIMD and Multi-reference Approach

The work of this Chapter is published in *Phys. Chem. Chem. Phys.* **2023**, *25*, 31165-31177.

5.1. Introduction

In biological systems, the coordination chemistry of the Mn^{2+} ion is of utmost significance.[1,2] Mn^{2+} ions are also extensively utilized as probes in various biological systems, replacing Zn^{2+}, Mg^{2+}, or Ca^{2+} ions.[3,4] Due to the possible use of high-spin complexes of this metal ion as contrast-enhancing agents in MRI, the stable complexation of Mn^{2+} ions in an aqueous solution has recently drawn significant interest.[5,6] During 1980s to 1990s, research largely focused on developing Gd^{3+} based contrast agents (CAs).[7] However, concerns over nephrogenic systemic fibrosis (NSF), and Gd^{3+} aggregations in the brain and bones have resulted in severe limitations in the clinical usage of this agent.[8,9] These concerns prompted the development of biocompatible paramagnetic ions with high relaxivity and stable complex formation. Mn^{2+} is a suitable alternative for Gd^{3+} with d^5 electronic configuration, offering slower electron spin relaxation times[6,10] having a superior toxicity profile to that of Gd^{3+}.[11,12] However, excess Mn^{2+} ions can lead to neurological abnormalities in humans, a condition known as manganism.[5,13] Therefore, in order to prevent the release of harmful Mn^{2+} ions, the complex should be thermodynamically and kinetically stable.[14–16] The coordination sphere, which includes the ligand and the solvent molecules, substantially influences the solution structure and stability of the Mn^{2+} complexes. However, owing to the dynamic nature of the Mn^{2+} complexes, it might be challenging to resolve their solution structure.[17] Although Mn^{2+} complexes are important in many technological and biological sites, their theoretical investigations in aqueous medium have been scarce. To accomplish this, DFT and *ab initio* molecular dynamics (AIMD) simulations are applied to simulate the bond dynamics, considering ligand flexibility and solvent rearrangements at the same time. The AIMD

simulations have proven effective in investigating the hydration structure of different ions.[18–20] Additionally, when modeling the solution structure, explicit solvent molecules must also be included along with periodic boundary conditions for a realistic solution structure.[21,22] In MRI, various factors influence the ^{1}H relaxivity of MRI CAs.[23,24] The rotational correlation time (τ_r), the mean residence time of the inner-sphere water molecule (τ_m), the exchange rate of the inner-sphere water molecules (k_{ex}^{298}), and the electronic relaxation time (T_{ie}) are commonly used parameters that influence the ^{1}H relaxivity of MRI CAs in aqueous solution. The latter element, electronic relaxation, significantly contributes to relaxivity at low magnetic fields (2 MHz), which are typically not used for clinical imaging.[25,26] However, low-field imaging is now employed as an alternative to high-field scanners by varying fields (fast field cycling MRI) and Mn^{2+} ions to generate contrast.[27] Given the recent surge in low and ultralow field MRI, optimizing CAS relaxivity at low fields has inspired researchers to investigate this parameter in depth. McLachlan's theory describes electron spin relaxation as a transient distortion of the metal coordination sphere, which regulates the zero-field splitting (ZFS) energy.[28] The thermal energy modulation of the ZFS tensors causes electron spin relaxation of transition metal (TM) ions with spin $S \geq 1.35$.[29] In Gd^{3+} and Mn^{2+} complexes, a symmetrical environment around the metal center and ligand rigidity was found to prefer slower electronic relaxation.[30,31] Along with this line, the calculation of the ZFS of TM complexes is crucial to obtain the magnetic properties of these complexes in the area of molecular magnetism.[32] Magnetic anisotropy is caused by ZFS, which lift the degeneracy of magnetic sublevel (M_S) in system with $S > 1/2$ via spin-orbit coupling (SOC). ZFS, defined by axial (D) and rhombic (E) parameters, is key to understanding the magnetic behaviour of Monometallic single-molecule magnets (SMMs),[33–36] which have potential in data storage, quantum computing, and molecular spintronics.[37,38] Because of their essentially isotropic spin ground state, Mn^{2+} complexes are not expected to exhibit slow magnetisation relaxation; however, high-spin Mn^{2+} monometallic complexes impart an additional possibility to analyse the nature of magnetic anisotropy in certain coordination environments, and some magneto-structural correlation can be drawn out.[35,39–41] Furthermore, only a few studies on the ZFS of seven coordinated Mn^{2+} complexes have been reported to date.[42–44] Hence, a deeper analysis of the ZFS of seven coordinated Mn^{2+} complexes is required to explore their coordination geometries and magnetic characterization. As per the author's knowledge, there is no report available for the analysis of ZFS parameters of pentagonal bipyramidal (PBP) Mn^{2+} complexes using the first principles approach.

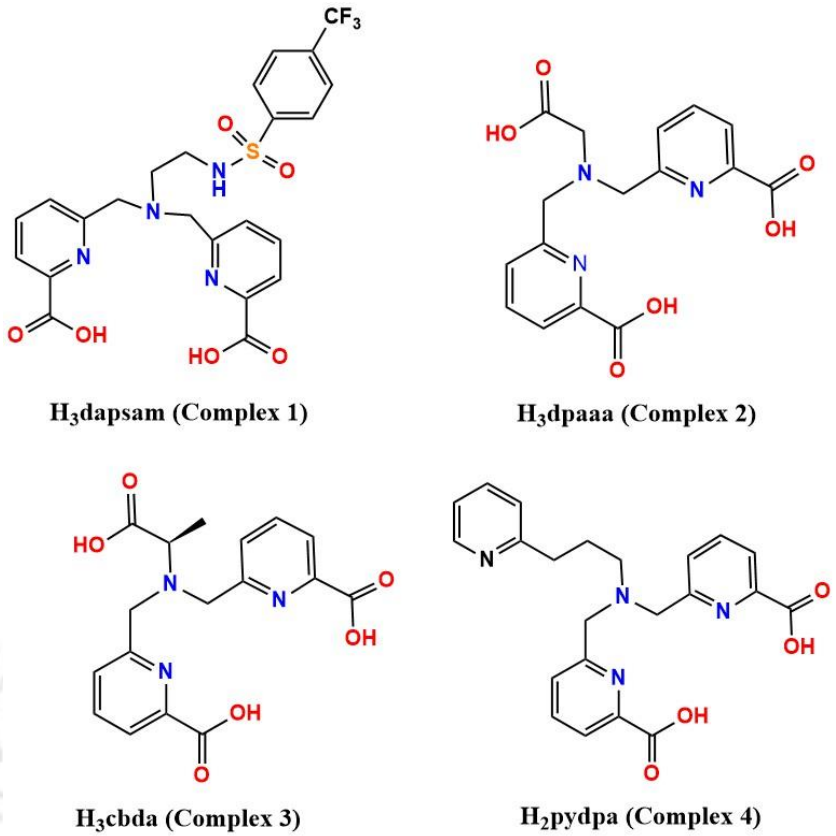

Figure 5.1. Ligands discussed in this study.[44-47]

This work has two objectives: (a) it provides an overview of the molecular and electronic structure of the four Mn^{2+} complexes in aqueous medium based on AIMD simulation. In addition, we have conducted a study to examine the effect of temperature on the coordination sphere and their comparative binding affinities of the ligands H_3dpasam,[45] H_3dpaaa,[44] H_3cbda,[46] and H_2pydpa[47] with Mn^{2+} ions in aqueous media, and (b) to explore the factors and parameters that influence the magnetic anisotropy and ZFS in high-spin PBP Mn^{2+} complexes, specifically the effect of ligand coordination environment and substituent at the ligand backbone. Also, we envisaged the factors that affect the sign of the magnetic anisotropy parameter (D) in a mixed ligand environment. Furthermore, herein, we propose a method that enhances the ZFS parameter (D) for Mn^{2+} ions in PBP geometry by reducing the Mn-O(w) distance in the axial position.[35] Finally, we retrieved the *ab initio* ligand field theory (AILFT) parameters to assess the metal-ligand covalency in comparison to the free metal ions. We expect that our study will provide valuable insights into the development of stable Mn^{2+} complexes with optimized magnetic anisotropy and electronic relaxation. This work considers four experimentally synthesized[44–47] Mn^{2+} complexes classified as Class I complexes (Figure 5.1). The other fifteen complexes we have modeled based on the ligand donor atoms and the

substituents on the ligand backbone are classified as Class II and Class III complexes, respectively.

5.2. Computational Details

5.2.1. *Ab Initio* Molecular Dynamics (AIMD) Simulations

All the geometry optimizations and AIMD simulations were performed in a cubic periodic box of 17.5 Å length with implemented PBE functional[48,49] and GTH-DZVP basis set[50] for all the atoms in the CP2K package.[51] An additional plane wave basis set was used to determine long-range electrostatic terms with a cutoff of 300 Ry. To account for van der Waals interactions, Grimme's D3 corrections[48] were applied to all simulations within a 6.0 Å radius. All AIMD simulations were run in the NVT ensemble at 298 K in 17.5 Å cubic boxes with a 1.0 fs time step.[21] The complex structure was solvated with 180 water molecules and placed in the center of a 17.5 Å cubic box. Prior to the production run, we followed the following procedures: (i) initial geometry optimization, (ii) 5 ps of NVT simulation at 298 K with 1 fs time step to ensure appropriate mixing and to evaluate the stability of each of the Mn^{2+} complexes, and (iii) simulated temperature annealing to 0 K (2 ps), followed by final geometry optimization. After the geometry optimization, a production run of > 20 ps has been performed. The radial distribution function (RDF) and coordination number (CN) of the complexes were calculated using the equilibrium structure reconstructed from the trajectories. Furthermore, we ran the AIMD simulations at 90˚C by starting with an equilibrium frame at 25˚C and running an NVT simulation until at least 20 ps of equilibrated trajectory were recorded.[22] In addition, one Na^+ ion is added for the anionic complexes to ensure overall charge neutrality of the periodic unit cell. This Na^+ ion functions as a non-coordinating cation positioned at a sufficient distance (7-9 Å) from the ligand to avoid any interactions or bonding. The geometry of the Mn^{2+}-ligand complexes is unaffected by this Na^+ ion. We also estimated the root mean square deviations (RMSDs) between each AIMD frame (at 2 ps interval) with the X-ray crystallographic structure, as shown in Figure 5.2 and Tables A1 in Appendix-C, and averaged these across the entire AIMD trajectory to identify the reference molecular geometry for further investigations. Our model unit cell for the [Mn(pydpa)(H_2O)] complex (Figure 5.3) had 588 atoms, including 48 atoms representing the [Mn(pydpa)] complex and 180 explicit water molecules. An additional 10 ps AIMD simulation at 25˚C has been performed to ensure that the complexes persisted in the binding mode (Figure C1 in Appendix-C). The time evolution plots of bond length was drawn by using VMD[52] displayed in Figure C2-C5 in Appendix-C.

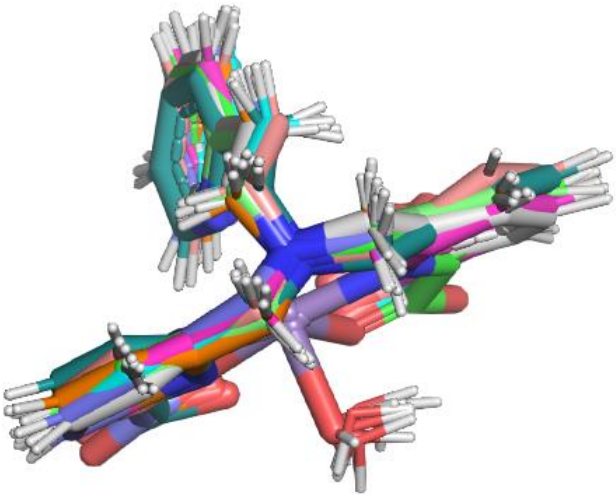

Figure 5.2. Superimposed crystallographic and AIMD simulated structures of the [Mn(pydpa)(H_2O)] complex at 25˚C.

5.2.2. Electronic Structure Methods

We explored the electronic structure of the complexes in greater depth from the extracted Cartesian coordinates of the Mn^{2+} complexes, including the inner-sphere water molecule. From the optimized (annealing plus geometry optimization) solution structures of the Mn^{2+} complexes with explicit water molecules, we extracted the atomic coordinates of the Mn^{2+} complexes, including water molecules that are directly coordinated with the Mn^{2+} ion. A single-point energy calculation has been performed on the optimized solution structure of the complexes applying the M06-2X and M06 functional and def2-TZVP basis set in the Gaussian 16 program package.[53] We considered sextet multiplicity for Mn^{2+} ions throughout the calculations. Furthermore, the molecular geometries of the complexes were optimized within the framework of DFT to estimate the magnetic property, utilizing the M06-2X functional[54,55] and def2 TZVP[56] basis set as implemented in the Gaussian 16 program package. Vibrational frequency analysis has been carried out to characterize the nature of the optimized geometries as energy minima. The solvent effect was incorporated using the polarizable continuum model (PCM)[57] in general, with the integral equation formalism, i.e., the IEFPCM[57] model implemented in the Gaussian 16 program. No symmetry constraints have been imposed during the optimizations. The highest spin state (sextet, $3d^5$) was designated the ground state. All computations used the default grid and the quadratic convergence criteria. Initially, the ZFS parameters were calculated at the TPSS[58] and M06-2X theoretical level with the def2- TZVP basis set by using the coupled perturbed method to estimate the SOC contribution[59] and the

spin unrestricted natural orbital (UNO) determinant to obtain the spin-spin contribution.[60] Spin-orbit effects were included by using the mean-field approach SOMF (1X).[61]

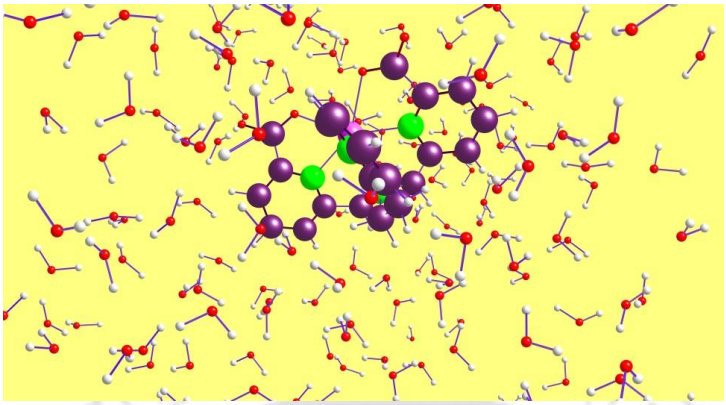

Figure 5.3. Unit cells used in periodic simulations of the [Mn(pydpa)(H_2O)] complex. Distinct colors represent different atoms. manganese (pink), carbon (purple), nitrogen (green), oxygen (red), and hydrogen (white).

The DFT-optimized structures were used for the state-averaged complete active space self-consistent field (SA-CASSCF)[62–64] calculations and carried out with the help of the ORCA 5.0.2 program package.[65] The active space comprises five 3d electrons from the Mn^{2+} ion, distributed over five metal d-orbitals [CAS(5,5)] using 1 sextet, 24 quartet, and 75 doublet roots.[26,66] All-electron Douglas-Kroll Hess (DKH) approximation accounts for the scalar relativistic effect.[67] Here, we have employed the DKH-adapted version of the def2-TZVP basis sets[68,69] for all atoms, which were sped up by combining the resolution of identity (RIJK) [70] approximation with the def2/JK auxiliary basis set.[71] The dynamic correlation was investigated using the strongly contracted variant of the N-valence state perturbation theory (SC-NEVPT2).[72] Spin-orbit coupling was developed in the quasi-degenerate perturbation theory (QDPT) framework.[73] Furthermore, the solvent effects in the ORCA program were integrated with Truhlar's universal solvation model, the density-based solvation model (SMD).[74] For a paramagnetic high-spin Mn^{2+} complex with S=5/2, the ZFS lifts the degeneration of the magnetic sublevels M_S= 5/2, 3/2, and 1/2, generating three Kramers' doublets. We have carried out Bader's quantum theory of atoms in molecules (QTAIM)[75] analysis to quantify the bonding nature of Mn-O, Mn-S, and Mn-Se bonds using the Multiwfn program (version 3.8).[76] Additionally, we derived atomic charges through natural population analysis (NPA)[77] and performed Mayer bond order analysis to determine the bond orders.[78]

5.3. Results and Discussion

5.3.1. Analysis of the Coordination Sphere of Mn^{2+} Complexes from AIMD Simulations

The structural parameters of the optimised geometries of [Mn(dpasam)(H_2O)], Mn(dpaaa)(H_2O)], [Mn(cbda)(H_2O)], and [Mn(pydpa)(H_2O)] complexes are in good agreement with the previously obtained X-ray crystallographic structures (Table C2 in Appendix-C).[44–47] These optimized Mn^{2+} geometries were hexacoordinated with an additional water molecule in the inner coordination sphere. In the [Mn(dpasam)(H_2O)] complex, two oxygen atoms were coordinated to the central Mn^{2+} ion, one oxygen atom from inner sphere water, two pyridinic nitrogen atoms, and two amine nitrogen atoms. However, in [Mn(dpaaa)(H_2O)] and [Mn(cbda)(H_2O)] complexes Mn^{2+} ion is coordinated with three oxygen atoms from the carboxylate group, one oxygen atom from the coordinated water, one nitrogen atom from the amine group, and two nitrogen atoms from the pyridine group. In the neutral [Mn(pydpa)(H_2O)] complex, two oxygen atoms from the carboxylate group, one oxygen atom from inner-sphere water, three nitrogen atoms from the pyridinic group, and one nitrogen atom from the amine group link to the core Mn^{2+} ion. This established that the applied GTH-pseudopotential and the AIMD protocol describe the solution structure of the Mn^{2+} complexes correctly. The observed similarity not only implies the accuracy of the theoretical methods in describing the solution phase structure but also suggests the potential stability of the studied Mn^{2+} complexes, either kinetically or thermodynamically, when dissolved in a solution and does not undergo any ligand exchange, retaining its solid-state geometry. Table C2 in Appendix-C displays the Mn-N and Mn-O bond length values, as well as experimental XRD data. At the outset, from the 20 ps (between 20-40 ps) of equilibrated AIMD simulations of all the complexes, we determine the RDFs and CNs of Mn-O, Mn-N, and Mn-C bond pairs to justify the solution phase dynamics of the complexes and their fluctuation throughout the simulation at 25˚C. The potential energy plots for the corresponding AIMD trajectories are reported for both 25˚C and 90˚C as shown in Figures C1 and C6 of Appendix-C. The RDFs computed for all the complexes at 25˚C (Figure 5.4) exhibit an average maxima of 2.35 Å for the Mn-O pair, 2.40 Å for the Mn-N pair, and 3.26 Å for the Mn-C pair, respectively. The oxygen and nitrogen atoms directly coordinated to the Mn^{2+} ion correspond to the first coordination sphere, with the ligand carbon atom slightly further away. In Mn-O RDFs, a smaller peak at 4.57 Å corresponds to the second coordination sphere of the solvent (water) shell around the Mn^{2+} complexes. Moreover, in Mn-C RDFs, we observed two smaller maxima between 4-5 Å. These two peaks may be indicative of the different (carboxylate,

amine, and pyridine) types of carbon atoms within the ligands. The bond length values (Mn-N, Mn-O) calculated from the RDFs of the equilibrated frame of AIMD simulations closely match the experimental crystallographic structure as shown in Tables C2 of Appendix-C. All the simulated Mn-O distances are within 0.04-0.07 Å of experimental measurements. This demonstrates the reliability of the AIMD method that we have followed to replicate the solution structure of the Mn^{2+} complex. The peak distances of the RDFs are shown in Table 5.1. The optimized geometries of all the complexes using PBE/DZVP with GTH pseudopotential are shown in Figure C7 of Appendix-C. The water molecule directly coordinated with the metal center is presented.

Table 5.1. Peak distances (Å) of the RDFs from AIMD simulations of complexes 1, 2, 3, and 4 at 25˚C. The absence of peaks in RDFs is denoted by the symbol ‘‘-’’.

	Complex 1			Complex 2			Complex 3			Complex 4		
	1st	2nd	3rd	1st	2nd	3rd	1st	2nd	3rd	1st	2nd	3rd
Mn-O	2.32	4.4	-	2.35	4.4	-	2.43	4.44	-	2.31	4.5	-
Mn-C	3.30	4.5	5.0	3.30	4.5	5.10	3.22	4.50	5.0	3.25	4.55	5.0
Mn-N	2.30	-	-	2.50	-	-	2.40	-	-	2.40	-	-

5.3.2. The Effect of Temperature on the Behavior of Mn^{2+} Complexes in Solution

All the simulations were carried out at 90˚C for the Mn^{2+} complexes to determine if the temperature induces changes in the solution phase with different ligand environments. The weakly bound complexes are more prone to changing shape in solution as the temperature rises. Most distinctly, in the neutral [Mn(pydpa)(H_2O)] complex, the binding strength of the coordinated solvent molecule is affected by the temperature-induced disorder, as shown in Figure 5.4. Figure 5.4 presents the Mn-O, Mn-N, and Mn-C RDFs at both 25˚C (blue) and 90˚C (red). The RDFs of the [Mn(dpasam)(H_2O)] complex with comparatively larger stability become rigid at higher temperatures (90˚C). However, the neutral [Mn(pydpa)(H_2O)] complex changes its structure at a higher temperature in line with its lower stability.

The peak becomes sharper at 90˚C for the stable [Mn(dpasam)(H_2O)] complex (Mn-N and Mn-O RDFs) and broader for the [Mn(pydpa)(H_2O)] complex. Notably, a smaller peak at 3.5 Å appears for the Mn-O RDF of the neutral [Mn(pydpa)(H_2O)] complex. This may be due to the

inner sphere water molecule moving away from the first coordination sphere at a higher temperature (90˚C), which is also reflected in the time evolution plot of the [Mn(pydpa)(H_2O)] complex at 90˚C (Figure C4, Appendix-C).

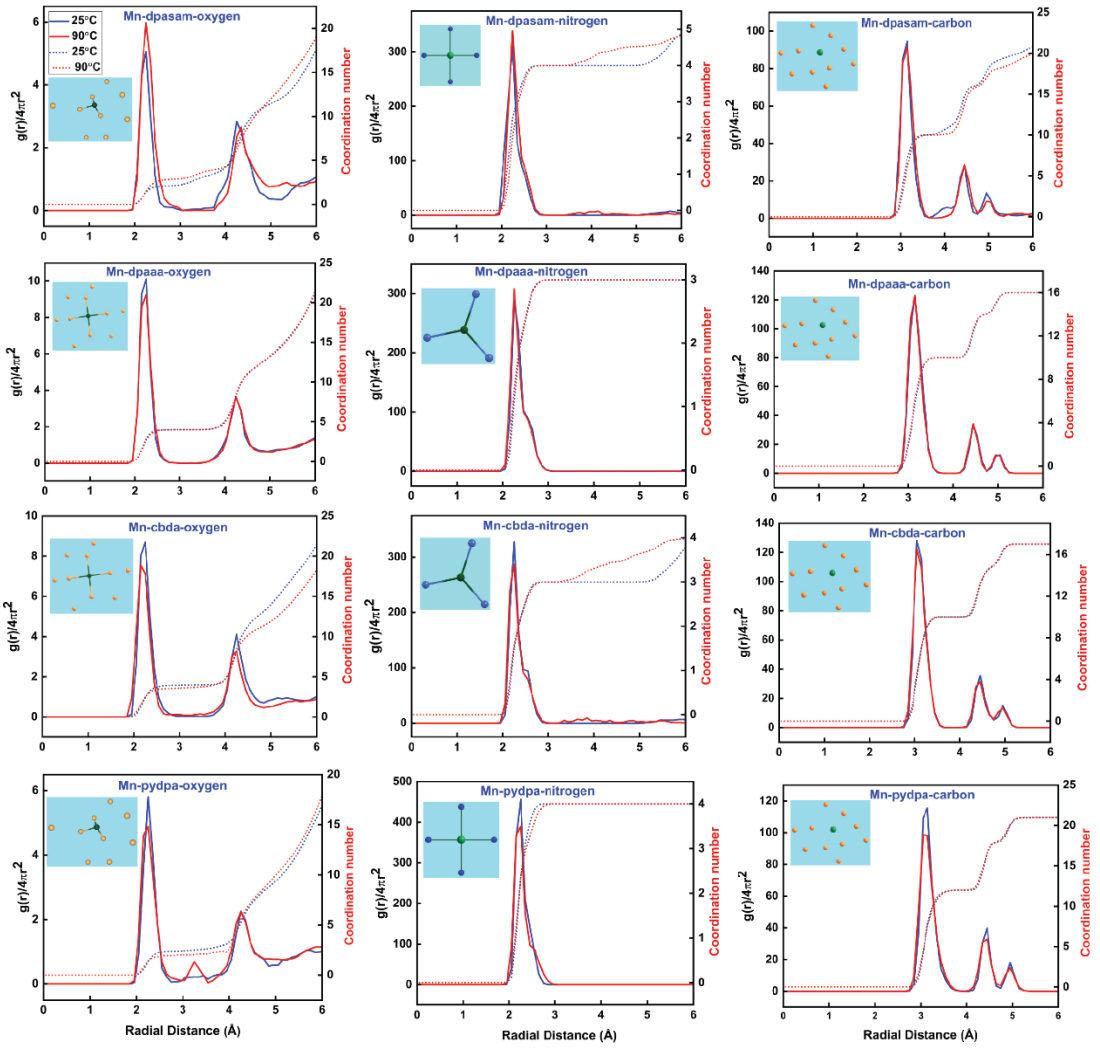

Figure 5.4. Radial distribution functions of the [Mn(dpasam)(H_2O)], [Mn(dpaaa)(H_2O)], [Mn(cbda)(H_2O)] and [Mn(pydpa)(H_2O)] complexes, shown in descending order of stability at 25˚C and 90˚C. The left, center, and right represent Mn-C, Mn-N, and Mn-O pair distribution functions respectively.

5.3.3. Binding Affinity of the Ligand to the Metal Mn^{2+}

To ensure the strength of the ligands as shown in Figure 5.1 with Mn^{2+} ion, the binding energies (BEs) of the complexes were investigated using Eq. 5.1. The binding affinity of the ligands to Mn^{2+} ion decreases in the order-$dpasam^{3-}$ (152.0 kcal mol^{-1}) > $dpaaa^{3-}$ (150.9 kcal mol^{-1}) > $cbda^{3-}$ (146.1 kcal mol^{-1}) > $pydpa^{2-}$ (130.8 kcal mol^{-1}) as depicted in Table C3 of the Appendix-C. The observed lower stability of the ligands $pydpa^{2-}$ may be attributed to the overall charge

neutrality of the [Mn(pydpa)(H_2O)] complex. Experimentally, it has already been established that the stability of the dpasam^{3-} ligand to Mn^{2+} ion is higher than the dpaaa^{3-} ligand.[45]

$$\text{BE}=E\left(Mn^{2+}(ligand)(H_2O)_n\right)^{c} - E(Mn^{2+}) - E(ligand)^{c-2} - n.E(H_2O) \quad (5.1)$$

where n denotes the number of inner-sphere water molecules coordinated to the metal ion in the Mn^{2+}-ligand complex and c denotes the charge of the Mn^{2+}-ligand complex (ligand = dpasam^{3-}, dpaaa^{3-}, cbda^{3-}, and pydpa^{2-} respectively).

5.3.4. Magnetic Anisotropy and Zero-Field Splitting (ZFS) Parameters

In the field of molecular magnetism, the term ZFS accounts for many interesting aspects related to the magnetic behavior of the studied complexes (Figure 5.5).[26,35,66] In this context, we determine the spin Hamiltonian parameters (SHPs) of the considered mononuclear Mn^{2+} complexes in various mixed coordination spheres. Based on the ligand/donor atoms used, the twenty complexes were categorized into three distinct classes. Class I complexes (1-4) were experimentally[44–47] synthesized using mixed oxygen/nitrogen (O/N) donor atoms with pentagonal bipyramidal (PBP) geometry. We have modeled the Class II complexes by replacing the equatorial O-atoms of Class I complexes with heavier S and Se-donor atoms, which result in complexes 5-12. Lastly, the Class III complexes were designed by replacing one -H atom of the -CH_2 group (in the equatorial position) with bulky methyl and phenyl groups (complexes 13-20), as shown in Figure 5.5. Our study involves the determination of ZFS parameters using both DFT and the ab initio CASSCF/NEVPT2 method. The computed ZFS parameters along with the ZFS energies of all twenty complexes are presented in Table 5.2.

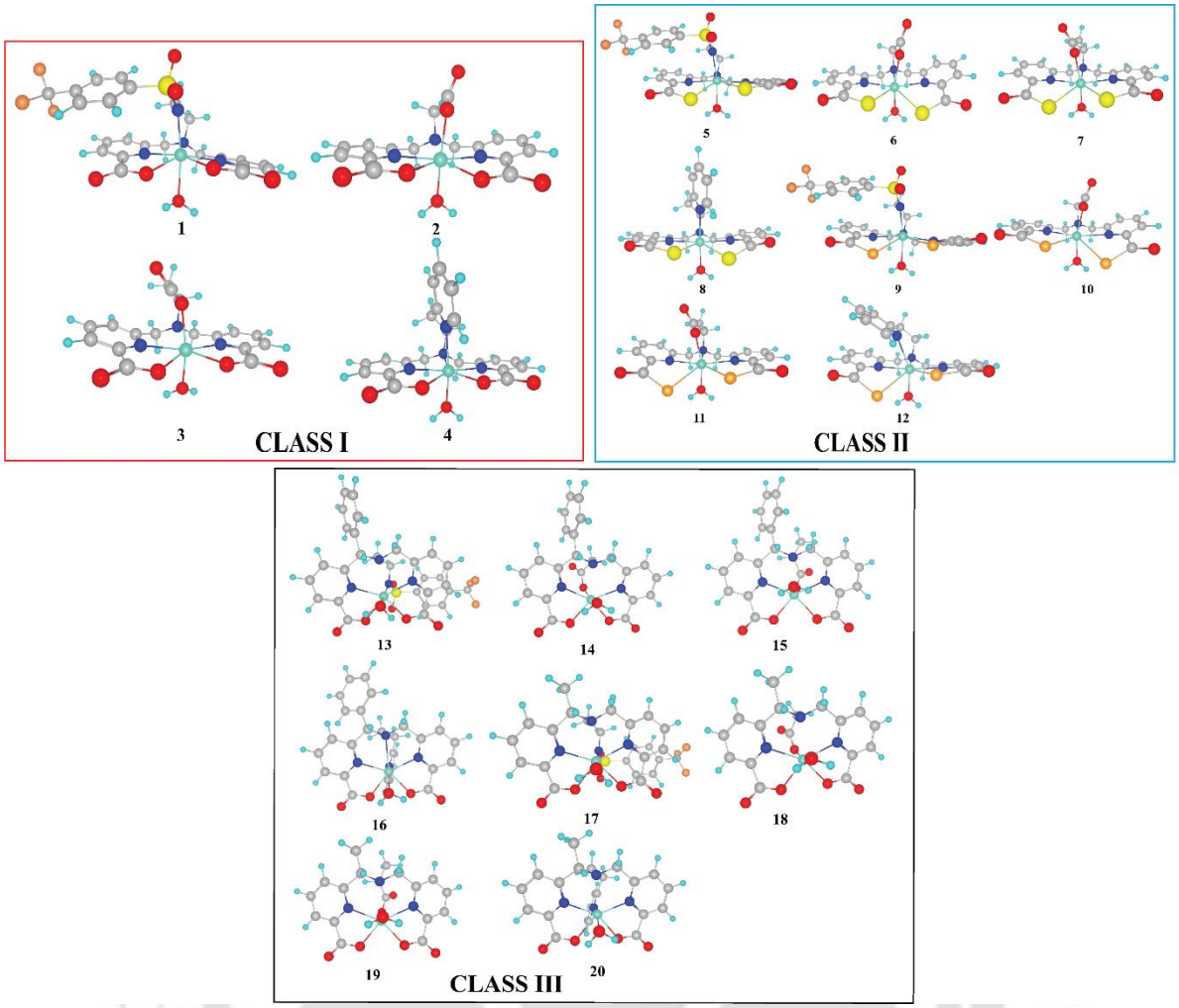

Figure 5.5. Two-dimensional structural representation of complexes 1-20. Structures 1-4 are based on the X-ray crystallographic structure.[44–47] Other complexes are designed in silico. The substitution group includes S and Se atoms in place of equatorial oxygen atoms (Class II) and phenyl and methyl in the ligand backbone (Class III) of the complexes.

Table 5.2. ZFS parameters of Mn^{2+} complexes were calculated using both DFT and *ab initio* multireference methods, along with their available experimental values in the brackets.

	Method	D (cm^{-1})	E/D	$\triangle$ (cm^{-1})	$\triangle^2(10^{20}S^{-2})$ Calculated (Experimental)
Complex 1	TPSS	-0.0896	0.2505	0.0797	2.2590
	CASSCF	0.0183	0.1707	0.0156	0.0862
	CASSCF/NEVPT2	0.0292	0.2067	0.0253	0.2270 (0.76)[45]
Complex 2	TPSS	-0.0341	0.2091	0.0296	0.3117
	CASSCF	0.0238	0.0891	0.0196	0.1360

	CASSCF/NEVPT2	0.0297	0.0712	0.0244	0.2112 (0.55)[44]
Complex 3	TPSS	-0.0309	0.2365	0.0273	0.2647
	CASSCF	0.0247	0.0819	0.0201	0.1422
	CASSCF/NEVPT2	0.0299	0.0429	0.0246	0.2140
Complex 4	TPSS	-0.0502	0.0859	0.0415	0.6105
	CASSCF	0.0223	0.0652	0.0183	0.1186
	CASSCF/NEVPT2	0.0339	0.0335	0.0277	0.2725
Complex 5	TPSS	-0.0541	0.1248	0.0452	0.7248
	CASSCF	-0.0195	0.0952	0.0159	0.0901
	CASSCF/NEVPT2	-0.0219	0.1802	0.0188	0.1247
Complex 6	TPSS	-0.0529	0.1873	0.0455	0.7345
	CASSCF	-0.0171	0.2416	0.0151	0.0808
	CASSCF/NEVPT2	-0.0266	0.1991	0.0229	0.1877
Complex 7	TPSS	-0.0519	0.2026	0.0425	0.6401
	CASSCF	-0.0270	0.1745	0.0231	0.1884
	CASSCF/NEVPT2	-0.0273	0.1502	0.0231	0.1884
Complex 8	TPSS	-0.0761	0.1313	0.0637	1.4404
	CASSCF	-0.0199	0.2459	0.0177	0.1115
	CASSCF/NEVPT2	-0.0313	0.1199	0.0261	0.2424
Complex 9	TPSS	0.1094	0.2997	0.1006	3.5948
	CASSCF	-0.0220	0.1929	0.0189	0.1277
	CASSCF/NEVPT2	-0.0282	0.3125	0.0262	0.2434
Complex 10	TPSS	-0.1033	0.2431	0.0915	2.9711
	CASSCF	-0.0295	0.3148	0.0275	0.2677
	CASSCF/NEVPT2	-0.0302	0.3274	0.0283	0.2851
Complex 11	TPSS	-0.1027	0.1981	0.0887	2.7915
	CASSCF	-0.0299	0.3073	0.0276	0.2708
	CASSCF/NEVPT2	-0.0310	0.2913	0.0284	0.2855
Complex 12	TPSS	-0.1361	0.2044	0.1179	4.9379
	CASSCF	-0.0244	0.1649	0.0207	0.1518
	CASSCF/NEVPT2	-0.0319	0.1223	0.0266	0.2512

Complex 13	TPSS	-0.0402	0.0625	0.0331	0.3876
	CASSCF	0.0189	0.1633	0.0157	0.0869
	CASSCF/NEVPT2	0.0209	0.1827	0.0179	0.1143
Complex 14	TPSS	-0.0529	0.1873	0.0455	0.7345
	CASSCF	0.0183	0.2227	0.0159	0.0951
	CASSCF/NEVPT2	0.0205	0.0655	0.0168	0.1003
Complex 15	TPSS	0.0293	0.2809	0.0239	0.2041
	CASSCF	0.0186	0.2441	0.0165	0.0967
	CASSCF/NEVPT2	0.0235	0.2963	0.0216	0.1654
Complex 16	TPSS	-0.0402	0.0732	0.0331	0.3828
	CASSCF	0.0166	0.1187	0.0138	0.0679
	CASSCF/NEVPT2	0.0241	0.1737	0.0205	0.1494
Complex 17	TPSS	-0.0449	0.0689	0.0369	0.4832
	CASSCF	0.0187	0.1568	0.0158	0.0885
	CASSCF/NEVPT2	0.0306	0.2169	0.0267	0.2531
Complex 18	TPSS	-0.0344	0.2806	0.0313	0.3471
	CASSCF	0.0245	0.0861	0.0202	0.1453
	CASSCF/NEVPT2	0.0309	0.0858	0.0255	0.2309
Complex 19	TPSS	-0.0325	0.2492	0.0289	0.2959
	CASSCF	0.0272	0.1118	0.0226	0.1811
	CASSCF/NEVPT2	0.0346	0.0241	0.0283	0.2840
Complex 20	TPSS	-0.0561	0.0263	0.0459	0.7471
	CASSCF	0.0243	0.1963	0.0209	0.1556
	CASSCF/NEVPT2	0.0346	0.2116	0.0432	0.6628

5.3.5. DFT-Based Methods for Calculating Spin Hamiltonian Parameters (SHPs)

DFT computations are beneficial for rationalizing the various contributions to the overall D-value (D_{SSC} and D_{SOC}). The spin-orbit coupling (SOC) of the excited state (ES) to the ground state (GS), as well as the direct electron-electron magnetic dipole spin-spin (SS) interaction involving unpaired electrons, results in ZFS.[79] D_{SOC} parameters are reliably determined by *ab initio* calculations, while D_{SSC} contributions are overestimated.[26,35,80] Using DFT calculations

on the examined systems, we discovered that the D_{SSC} part is one order of magnitude less than the D_{SOC} part. This shows that the SOC component of ZFS is generally dominating. However, it contradicts previous computational work that found that SS contributions played a dominant role in six-coordinated Mn^{2+} complexes, including neutral N/O donor ligands with positive D-values.[39]

The $\alpha \rightarrow \alpha$ and $\beta \rightarrow \beta$ excitations responsible for the spin multiplicity of the system contribute negatively to the total negative D-value in most of the complexes, as shown in Tables C4 and C5 of Appendix C. $\beta \rightarrow \alpha$ excitation, on the other hand, enhances the electronic spin by one unit and typically offers a small positive contribution to the total negative D value. The $\alpha \rightarrow \beta$ contribution is the most important among all variable contributions. Furthermore, complexes 9-12 of Class II exhibit a particularly large contribution of $\alpha \rightarrow \beta$ excitation, which may be due to the longer bond distance of the Mn-Se bond compared to the Mn-O and Mn-S bond distances, i.e., the weak contribution of the ligand. The SS and SOC parameters calculated using DFT are shown in Tables C4 and C5 of Appendix-C. However, it is already established that the analysis of SHPs using a single-determinant DFT-based method becomes problematic.[42,81] The results strongly depend on the functional used and the amount of HF exchange (Table 5.2 and Table C6, Appendix-C). In addition, the correct sign of D cannot predict for complexes with $E/D > 0.20$.[42,81,82] The DFT-estimated ZFS parameter values shown in Table 5.2 and Table C6 (Appendix-C) are significantly overestimated compared to the values obtained from *ab initio* calculations.

To address this limitation, we have employed multireference *ab initio* methods to calculate the D-matrix elements. This method involves the explicit evaluation of magnetic sublevels and is possibly the most significant approach for calculating the magnetic properties to date.[66,83] The possible advantages of this method are that it correctly treats the spin-flip within the metal d-orbitals and uses suitable spin eigenvalues.[26,84,85]

5.3.6. The Multi-Configurational *Ab Initio* Methods

To investigate the origin of the magnetic anisotropy of the complexes (1-20) resulting from spin-orbit interactions, we used ab initio CASSCF and CASSCF/NEVPT2 methods, which are known to produce reliable SHPs estimates for such systems. Table 5.2 presents the computed ZFS parameters of all twenty complexes along with the experimental values available only for complex 1 and complex 2. The high-spin Mn^{2+} ions are expected to have very small ZFS

energy, owing to their totally symmetrical $^6A_1$ ground state. The values of the ZFS parameters D and E were subsequently used to determine the ZFS energy using Eq. 2.47 (Chapter 2).

The addition of dynamic correlation effects utilizing CASSCF/NEVPT2 computations did not change the sign of D but raised their absolute values. Despite significant structural diversity, the D-value for structurally similar Class I complexes is roughly the same. These multi-reference *ab initio* calculations have shown that the Mn^{2+} complexes have a positive value of D in contrast with the DFT calculations.[41,82] In addition, an attempt has been made to establish the effect of the coordination environment on the easy plane magnetic anisotropy $(+D)$ of the complexes. Although the ZFS parameters remain in the same range (Table 5.2), a more symmetrical ligand environment around the metal center increases the amplitude of the easy plane magnetic anisotropy. This finding can be explained by examining the electronic states and their contribution to the overall D-values (Tables C7-C26 of Appendix-C). We observed that the gap between the d-orbital decreases in the case of complex 4, as shown in Figure 5.6. This could be due to the ligand's greater symmetry around the metal center. As for complexes 1, 2, and 3, the degeneracy of the d-orbitals decreases between (d_{xz}, d_{yz}) and (d_{xy} and $d_{x^2-y^2}$). Moreover, the E/D value of Class I complexes decreases from complex 1 to complex 4, as shown in Table 5.2, depicting the higher symmetry of complex 4.

In high-spin Mn^{2+} complexes, due to the totally symmetrical $^6A_1$ ground state, it does not contribute to the total ZFS. Hence, the ZFS essentially arises from the spin-flip excited quartet state which is more than 22000 cm^{-1} higher in energy compared to the ground state (Tables C7-C26 in Appendix-C). The studied complexes with GS electronic configuration of $d^1_{xz}d^1_{yz}d^1_{xy}d^1_{x^2-y^2}d^1_{z^2}$, reflects a PBP geometry. The D_{zz} axis points towards the axial Mn-N bond in complex 1, complexes 4-5, complexes 8-9, complexes 12-13, complexes 16-17, and complex 20. However, in complexes 2-3, complexes 6-7, complexes 10-11, complexes 14-15, and complexes 18-19 the D_{zz} axis points towards the axial Mn-O bond. From Tables C7-C26 in Appendix-C, it is observed that the first two excited states contribute significantly to the total D-value. The next significant contribution arises mostly from the quartet excited states and ψ_8(9^{th} ES), ψ_9 (10^{th} ES) along with ψ_{16} (17^{th} ES) for all the Class I and Class II complexes. In the case of Class III complexes, ψ_{10} (11^{th} ES), ψ_{11} (12^{th} ES) and ψ_{16} (17^{th} ES) contribute significantly to the phenyl analogs (complexes 13-16) and ψ_{10} (11^{th} ES), and ψ_{16} (17^{th} ES) contribute considerably for methyl analogs (complexes 17-20). Although the contribution of these ES mentioned above is very high in energy compared to the GS, its contribution to the

total D-value is significant compared to the GS. Other than these major contributions, other minor contributions are also present with very small magnitude. Because of the significant positive and negative contributions, all the seven studied coordinated Mn^{2+} complexes have a small overall D-value. Moreover, the computed g-anisotropy for high-spin Mn^{2+} ion is isotropic with an estimated value of 2.00, with a symmetrical $^6A_1$ GS.

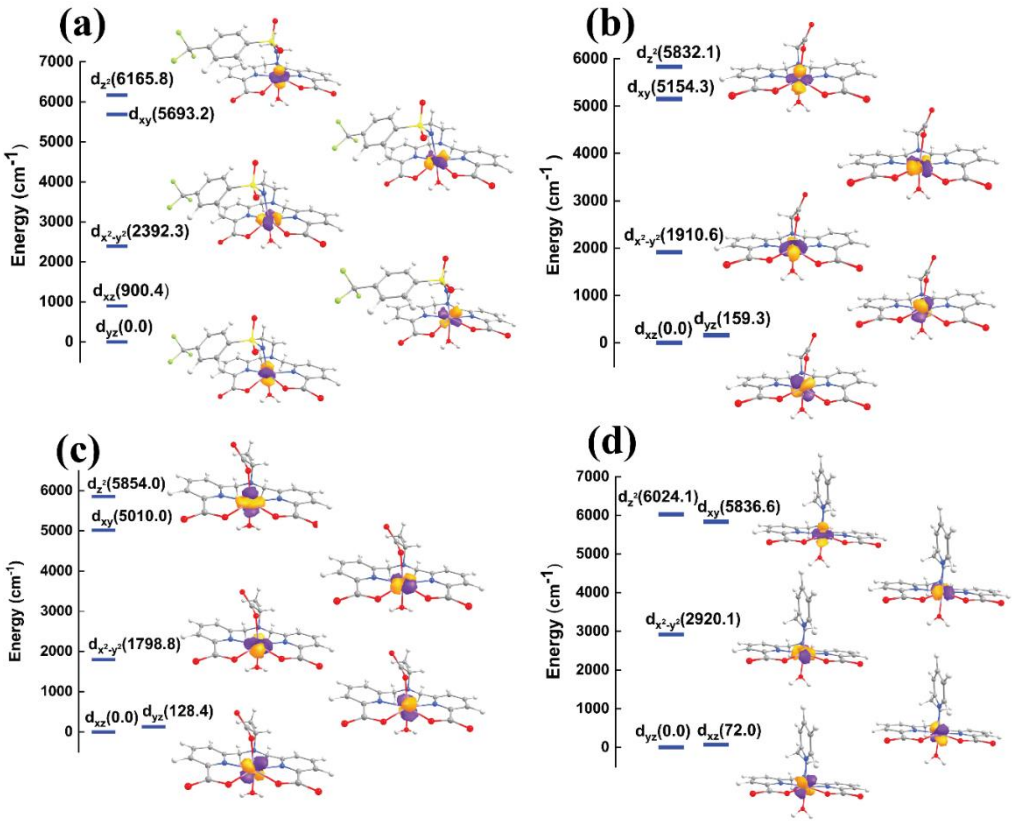

Figure 5.6. NEVPT2-LFT d-orbital splitting diagram of the complexes 1-4 together with their respective orbitals.

Likewise, for the rhombic E parameter, an analysis of the state-wise contribution to the total E value reveals a similar pattern of contribution for all the studied complexes, with the main contribution coming from the first and second ESs in addition to the third ES, as shown in Tables C7-C26 in Appendix-C. In addition, with the decrease in symmetry of the ligands, the E/D value increases, as shown in Table 5.2. This analysis established that in the case of PBP geometry of Mn^{2+} complexes, the fine-tuning of the symmetry around the metal center can change the rhombic ZFS parameter. This leads to the possibility of using these complexes in qubits, which equates to a larger rhombic ZFS parameter with stronger state coupling and a higher tunneling probability.[86,87]

Moreover, the magnitude of the D-value in the seven coordinated Mn^{2+} complexes (Class I, Class II, and Class III) is strongly correlated to the energy gap of the ground and first excited state ($\triangle E_{1st-GS}$) and is found to have a linear correlation with the D-value with a smaller gap yielding a larger D-value. The variations of D value with $\triangle E_{1st-GS}$ for Class I, Class II, and Class III complexes are shown in Figure 5.7 and Figure C8(a)-(d) (Appendix-C), respectively.

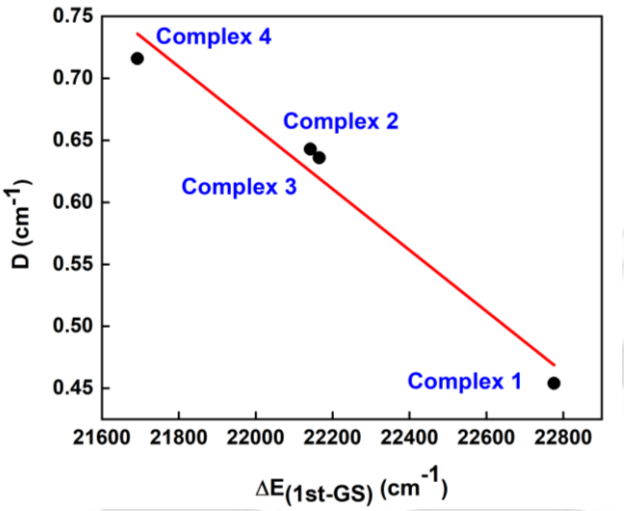

Figure 5.7. Variation of D values of all the complexes with the energy difference between the ground and first excited states. The solid red line serves only as a guide for the eye.

The sign of D is believed to be positive when two of the three Kramers doublets are lower in energy than the center of gravity[26] that holds for all the complexes. Moreover, the separation of Kramers doublets decreases with a decrease in the D-value, as shown in Figure 5.8, for Class I complexes.

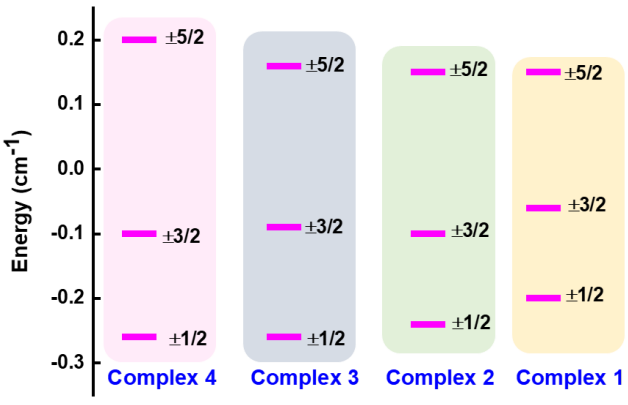

Figure 5.8. Energies of the Kramers doublets of Class I complexes investigated in this work at the CASSCF/NEVPT2 level of theory.

5.3.7. Magneto-Structural Correlation

To comprehend the relationship between the structural parameter along with computed SHP D, we have modeled a magneto-structural correlation by decreasing the axial Mn-O(w) bond length of the axial water molecule. This Magneto-structural correlation is a method of relating a specific molecular geometry to SHPs, D and E/D.[39] These magneto-structural correlations prove to be useful to the biochemical community. These studies focused on seven-coordinated PBP Mn^{2+} complexes, as a limited number of studies have been found for the magnetic characterization of seven-coordinated Mn^{2+} complexes. We selected the symmetrical [Mn(pydpa)(H_2O)] complex and reduced the Mn-O(w) bond length in the axial direction. This shortening of the bond will destabilize the d_{z^2} orbital in the axial direction and consequently decrease the sextet-quartet energy gap. Notably, this lowering of the sextet-quartet energy gap increased the value of D. Our analysis established that replacing the water molecule at the axial position with a stronger (e.g., OH) ligand may increase the value of ZFS parameter D. This is because deprotonation of a water molecule leads to an increase in D, consistent with the relative ligand-field strength of OH vs. H_2O ligand (Figure 5.9).

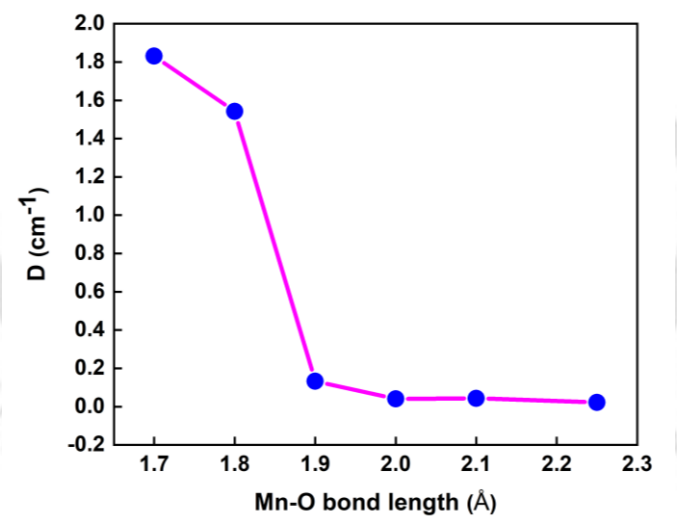

Figure 5.9. Magneto-structural correlation of Mn-O(w) bond length and D-value of [Mn(pydpa)(H_2O)] complex.

5.3.8. Switching the Sign of the ZFS Parameter using a Mixed Ligand

It is found that simple substitution of the equatorial oxygen atoms of Class I complexes by heavier S and Se donor atoms (Class II complexes) results in switching in the magnetic anisotropy parameter (D) from positive to negative. The positive D-values determined for these complexes are counterproductive toward the design of effective SMMs.[88,89] The average Mn-O bond length value of the complexes (Class I) is in the range of 2.12-2.30 Å. However, the

Mn-S and Mn-Se bond length values are 2.62-2.72 Å and 2.73-2.89 Å respectively. This switching in anisotropy from easy plane anisotropy ($+D$) to easy axis anisotropy (D) may be due to the structural changes observed. It was found that after replacing with heavier S and Se donor ligands, the splitting of the d-orbitals (d_{xy} and $d_{x^2-y^2}$) decreases which may cause the shifting of the D-parameter as shown in Figure C9 and C10 (Appendix-C). Although we did not find any shifting of the d-orbitals. This observed difference in the sign of the D-value may be due to the difference in the metal-ligand interaction and the hard/soft nature of the ligand, with the Mn-S/Mn-Se bond being more covalent than the Mn-O bond.[90] In addition, we have observed that in the case of Se, the D-value increases compared to the S-donor ligands, and this key difference we can predict from the energetic separation of the metal d-orbitals (d_{xy}, $d_{x^2-y^2}$) compared to the S analogs, as shown in Figure C9 and C10 of Appendix-C.

5.3.9. Ligand Substitution Beyond the First Coordination Sphere

The ZFS parameters are directly related to the spin density distribution in the molecule. To assess the effect of bulkier groups (Class III complexes) at the second coordination sphere, we have substituted one -H atom of the equatorial -CH_2 group with methyl (Complexes 17-20) and phenyl (Complexes 13-16) groups. However, the substituent effect on ZFS also depends on the position of the substituents.[91] In these seven coordinated Mn^{2+} complexes, we have noticed that the electron-donating methyl group increases the D-parameter compared to the electron-withdrawing phenyl group. Although further study in this regard is necessary. Efforts to extend this analysis of the electronic effect of substituents on seven coordinated Mn^{2+} complexes are ongoing and will be reported in due course.

5.3.10. *Ab Initio* Ligand Field Theory (AILFT) and Covalency

Ab initio ligand field theory extracts the ligand field parameters (the ligand field one electron matrix V_{LFT}, the Racah parameters B and C, and spin-orbit coupling constant (ζ)) using multireference *ab initio* calculations.[92] We have analysed the *ab initio* ligand field parameters and effective spin-orbit coupling parameter using all 24 quartet states. It is already established that the complexation of free metal ions with ligands causes a decrease in Racah parameter (B) and SOC constant (ζ) relative to the free metal ion, as shown in Table C27 in Appendix-C. The percentage reduction in B-parameter and SOC constant were introduced by calculating $[(1-\frac{B}{B_0})\times 100]$ and $[(1-\frac{\zeta}{\zeta_0})\times 100]$ as shown in Figure 5.9. It has been observed that among the Class I complexes, Complex 1 causes a large reduction in nephelauxetic parameters B, and ζ compared to the other three complexes. This indicates that a large sulphonamide group present

on the ligand backbone may cause a decrease in the value of the ZFS parameter. Hence, Complexes 2-4 (Class I) possess more ionic character. As we go from Class I to Class II complexes, a stronger reduction in B and ζ parameters is observed, hence a larger covalency compared to the Class I and Class III complexes. As, S and Se donor complexes are expected to have more diffuse orbitals and consequently offer strong metal-ligand covalency. The increase in covalency has been further confirmed by QTAIM analysis as illustrated in Table C28 in the Appendix-C, which justifies that electron density (ρ_{bcp}) decreases with an increase in covalency[24,93,94] in the order of Mn-O< Mn-S< Mn-Se. The Laplacian of electron density, $\nabla^2_{\rho(bcp)}$, describes the degree of electron density concentration ($\nabla^2_{\rho(bcp)}$< 0) or depletion $\nabla^2_{\rho(bcp)}$> 0) at the bond critical point (bcp). Consequently, the decrease in $\nabla^2_{\rho(bcp)}$ at the corresponding bcp, as we progress from Mn-O to Mn-Se bond (Table C28 in Appendix-C), suggests a strengthening of the covalent bond along this group.

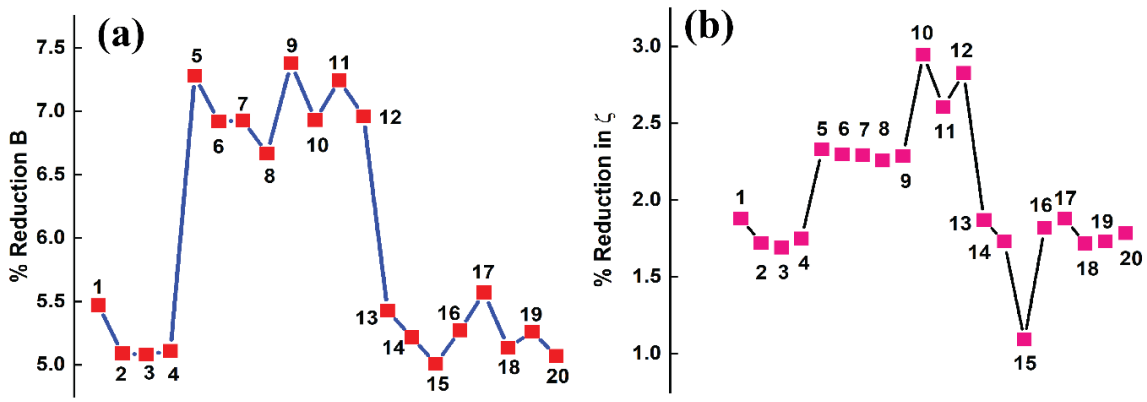

Figure 5.9. (a) Variation of nephelauxetic reduction of Racah parameter B and (b) effective spin-orbit coupling constant ζ among the twenty complexes.

In a similar way, a decrease in the kinetic electron energy density (G_{bcp}) at the corresponding bcp is related to a lower electron density at that point.[95] This is supported by NPA charge analysis,[96,97] which shows that the positive charge on the Mn^{2+} atom and negative charge on the O, S, and Se atoms decreases with increased covalency down the group. The NPA charge analysis, as shown in Table C29 in Appendix-C, reaffirms this trend of covalency.

Further, the increased covalent character of the Mn-S and Mn-Se bond compared to the Mn-O bond is also reflected in Mayer's bond order analysis (Table C30 in Appendix-C), where the bond order of Mn-O is smaller than Mn-S and Mn-Se bond in all the studied (Class I and Class II) complexes. While Class I and II complexes follow this trend, Class III does not show a clear

pattern. Overall, no direct correlation between covalency (B and ζ) and ZFS can be established. As ZFS also depends on other structural factors.

5.4. Conclusions

This work shows that AIMD simulations effectively predict the solution phase dynamics of Mn^{2+} complexes. Radial distribution functions reveal that as the stability decreases the sharpness of the peak decreases, as in the case of the neutral [Mn(pydpa)(H_2O)] complex, where an inner-sphere water migrate to the outer sphere at higher temperature. This is due to the lower stability of this complex with a neutral charge. In contrast, more stable complexes remain rigid with temperature. Binding energy analysis confirms the ligand stability trend- $dpasam^{3-}$> $dpaaa^{3-}$> $cbda^{3-}$> $pydpa^{2-}$, with [Mn(pydpa)(H_2O)] being the least stabledue to its neutral charge.

In the context of molecular magnetism, the ZFS parameter (D) values of the four complexes (Class I) increase in the order $[Mn(dpasam)(H_2O)]^-$ < $[Mn(dpaaa)(H_2O)]^-$ < $[Mn(cbda)(H_2O)]^-$ < [Mn(pydpa)(H_2O)]. The lower D and higher E/D values of the complex $[Mn(dpasam)(H_2O)]^-$ is due to the significant variation of the structure from the ideal PBP geometry. The energies of the Kramers doublets confirmed the positive value of D, with splitting decreasing as D decreases. Notably, the [Mn(pydpa)(H_2O)], the most symmetric complex, exhibits the smallest d-orbital splitting. An unexpected phenomenon was observed by decreasing the Mn-O(w) bond distance of the axial water molecule, i.e., the D-value increased with relative ligand field strength. Among the NEVPT2 transition energies, the first and second excited states provide the highest contribution toward the overall D-values along with some higher energy states. In addition, we have also observed a switch in the sign of the D-value after replacing the equatorial oxygen atom (Class I) with heavier S and Se-donor atoms (Class II). This shifting of the magnetic anisotropy from the easy plane ($+D$) to the easy axis ($-D$) is due to the structural difference in the metal-ligand bond and the hard/soft nature of the ligand. Moreover, these Mn-S and Mn-Se bonds become more covalent compared to the Mn-O bonds. Finally, we observed that the ligand coordination at the second coordination sphere for seven coordinated Mn^{2+} complexes with an electron-donating methyl group enhances the ZFS energy compared to the electron-withdrawing phenyl group. We hope that this work will be helpful in the determination of relative metal-ligand stability, designing transition metal-based MRI CAs, developing transition metal-based SMMs, and in any field where resolving the solution structure and its electronic and magnetic properties are necessary at an atomic scale.

5.5. References

[1] P. Cieslik, P. Comba, B. Dittmar, D. Ndiaye, É. Tóth, G. Velmurugan and H. Wadepohl, *Angew. Chem. Int. Ed.*, 2022, **61**, e202115580.

[2] Z. Rappoport, Ed., *PATAI'S Chemistry of Functional Groups*, Wiley, 1st edn., 2009.

[3] T. Dudev and C. Lim, *J. Phys. Chem. B*, 2001, **105**, 10709-10714.

[4] M. Kueny-Stotz, A. Garofalo and D. Felder-Flesch, *Eur. J. Inorg. Chem.*, 2012, **2012**, 1987-2005.

[5] B. Drahoš, I. Lukeš and É. Tóth, *Eur. J. Inorg. Chem.*, 2012, **2012**, 1975-1986.

[6] J. Wahsner, E. M. Gale, A. Rodríguez-Rodríguez and P. Caravan, *Chem. Rev.*, 2019, **119**, 957-1057.

[7] P. Caravan, J. J. Ellison, T. J. McMurry and R. B. Lauffer, *Chem. Rev.*, 1999, **99**, 2293-2352.

[8] T. Grobner, *Nephrol. Dial. Transplant.*, 2006, **21**, 1104-1108.

[9] T. Kanda, T. Fukusato, M. Matsuda, K. Toyoda, H. Oba, J. Kotoku, T. Haruyama, K. Kitajima and S. Furui, *Radiology*, 2015, **276**, 228-232.

[10] E. M. Gale, I. P. Atanasova, F. Blasi, I. Ay and P. Caravan, *J. Am. Chem. Soc.*, 2015, **137**, 15548-15557.

[11] D. Pan, A. H. Schmieder, S. A. Wickline and G. M. Lanza, *Tetrahedron*, 2011, **67**, 8431-8444.

[12] J. S. Troughton, M. T. Greenfield, J. M. Greenwood, S. Dumas, A. J. Wiethoff, J. Wang, M. Spiller, T. J. McMurry and P. Caravan, *Inorg. Chem.*, 2004, **43**, 6313-6323.

[13] E. Terreno, D. D. Castelli, A. Viale and S. Aime, *Chem. Rev.*, 2010, **110**, 3019-3042.

[14] D. P. Riley, S. L. Henke, P. J. Lennon, R. H. Weiss, W. L. Neumann, W. J. Rivers, K. W. Aston, K. R. Sample, H. Rahman, C.-S. Ling, J.-J. Shieh, D. H. Busch, and Witold Szulbinski, *Inorg. Chem.*, 1996, **35**, 5213-5231.

[15] R. Botár, E. Molnár, G. Trencsényi, J. Kiss, F. K. Kálmán and G. Tircsó, *J. Am. Chem. Soc.*, 2020, **142**, 1662-1666.

[16] R. Uzal-Varela, F. Pérez-Fernández, L. Valencia, A. Rodríguez-Rodríguez, C. Platas-Iglesias, P. Caravan and D. Esteban-Gómez, *Inorg. Chem.*, 2022, **61**, 14173-14186.

[17] K. Leung and C. J. Medforth, *J. Chem. Phys.*, 2007, **126**, 024501-8.

[18] L. M. Ramaniah, M. Bernasconi and M. Parrinello, *J. Chem. Phys.*, 1999, **111**, 1587-1591.

[19] I. Kuo and D. J. Tobias, *J. Phys. Chem. B*, 2001, **105**, 5827-5832.

[20] K. Leung and S. B. Rempe, *J. Am. Chem. Soc.*, 2004, **126**, 344-351.

[21] D. S. Kaliakin, J. A. Sobrinho, J. H. S. K. Monteiro, A. De Bettencourt-Dias and D. C. Cantu, *Phys. Chem. Chem. Phys.*, 2021, **23**, 4287-4299.

[22] R. D. O'Brien, T. J. Summers, D. S. Kaliakin and D. C. Cantu, *Phys. Chem. Chem. Phys.*, 2022, **24**, 10263-10271.

[23] P. Caravan, C. T. Farrar, L. Frullano and R. Uppal, *Contrast Media Mol. Imaging*, 2009, **4**, 89-100.

[24] N. Keot and M. Sarma, *RSC Adv.*, 2023, **13**, 1516-1529.

[25] S. Aime, M. Botta, D. Esteban-Gómez and C. Platas-Iglesias, *Mol. Phys.*, 2019, **117**, 898-909.

[26] R. Uzal-Varela, L. Valencia, D. Lalli, M. Maneiro, D. Esteban-Gómez, C. Platas-Iglesias, M. Botta and A. Rodríguez-Rodríguez, *Inorg. Chem.*, 2021, **60**, 15055-15068.

[27] A. E. Campbell-Washburn, R. Ramasawmy, M. C. Restivo, I. Bhattacharya, B. Basar, D. A. Herzka, M. S. Hansen, T. Rogers, W. P. Bandettini, D. R. McGuirt, C. Mancini, D. Grodzki, R. Schneider, W. Majeed, H. Bhat, H. Xue, J. Moss, A. A. Malayeri, E. C. Jones, A. P. Koretsky, P. Kellman, M. Y. Chen, R. J. Lederman and R. S. Balaban, *Radiology*, 2019, **293**, 384-393.

[28] A. McLachlan, Proc. R. Soc. A: Math. Phys. Eng. Sci., 1964, 280, 271–288.

[29] N. Schaefle and R. Sharp, *J. Chem. Phys.*, 2004, **121**, 5387-5394.

[30] A. Borel, H. Kang, C. Gateau, M. Mazzanti, R. B. Clarkson and R. L. Belford, *J. Phys. Chem. A*, 2006, **110**, 12434-12438.

[31] A. Borel, S. Laus, A. Ozarowski, C. Gateau, A. Nonat, M. Mazzanti and L. Helm, *J. Phys. Chem. A*, 2007, **111**, 5399-5407.

[32] D. Gatteschi, R. Sessoli and J. Villain, *Molecular nanomagnets*, Oxford University Press, Oxford; New York, 2006.

[33] R. Sessoli, H. L. Tsai, A. R. Schake, S. Wang, J. B. Vincent, K. Folting, D. Gatteschi, G. Christou and D. N. Hendrickson, *J. Am. Chem. Soc.*, 1993, **115**, 1804-1816.

[34] C. J. Milios, A. Vinslava, W. Wernsdorfer, S. Moggach, S. Parsons, S. P. Perlepes, G. Christou and E. K. Brechin, *J. Am. Chem. Soc.*, 2007, **129**, 2754-2755.

[35] M. A. Hay, A. Sarkar, K. E. R. Marriott, C. Wilson, G. Rajaraman and M. Murrie, *Dalton Trans.*, 2019, **48**, 15480-15486.

[36] A. F. R. Kilpatrick, F.-S. Guo, B. M. Day, A. Mansikkamäki, R. A. Layfield and F. G. N. Cloke, *Chem. Commun.*, 2018, **54**, 7085-7088.

[37] M. Affronte, F. Troiani, A. Ghirri, A. Candini, M. Evangelisti, V. Corradini, S. Carretta, P. Santini, G. Amoretti, F. Tuna, G. Timco and R. E. P. Winpenny, *J. Phys. Appl. Phys.*, 2007, **40**, 2999-3004.

[38] L. Bogani and W. Wernsdorfer, *Nat. Mater.*, 2008, **7**, 179-186.

[39] C. Duboc, M. Collomb, J. Pécaut, A. Deronzier and F. Neese, *Chem. – Eur. J.*, 2008, **14**, 6498-6509.

[40] C. Duboc, M.-N. Collomb and F. Neese, *Appl. Magn. Reson.*, 2010, **37**, 229-245.

[41] C. Rajnák, J. Titiš, J. Moncol, R. Mičová and R. Boča, *Inorg. Chem.*, 2019, **58**, 991-994.

[42] J. Rich, C. E. Castillo, I. Romero, M. Rodríguez, C. Duboc and M. Collomb, *Eur. J. Inorg. Chem.*, 2010, **2010**, 3658-3665.

[43] A. Forgács, M. Regueiro-Figueroa, J. L. Barriada, D. Esteban-Gómez, A. De Blas, T. Rodríguez-Blas, M. Botta and C. Platas-Iglesias, *Inorg. Chem.*, 2015, **54**, 9576-9587.

[44] A. Forgács, R. Pujales-Paradela, M. Regueiro-Figueroa, L. Valencia, D. Esteban-Gómez, M. Botta and C. Platas-Iglesias, *Dalton Trans.*, 2017, **46**, 1546-1558.

[45] R. Uzal-Varela, A. Rodríguez-Rodríguez, M. Martínez-Calvo, F. Carniato, D. Lalli, D. Esteban-Gómez, I. Brandariz, P. Pérez-Lourido, M. Botta and C. Platas-Iglesias, *Inorg. Chem.*, 2020, **59**, 14306-14317.

[46] M. Khannam, T. Weyhermüller, U. Goswami and C. Mukherjee, *Dalton Trans.*, 2017, **46**, 10426-10432.

[47] R. Mallik, M. Saha and C. Mukherjee, *ACS Appl. Bio Mater.*, 2021, **4**, 8356-8367.

[48] S. Grimme, J. Antony, S. Ehrlich and H. Krieg, *J. Chem. Phys.*, 2010, **132**, 154104-154123.

[49] I.-C. Lin, A. P. Seitsonen, I. Tavernelli and U. Rothlisberger, *J. Chem. Theory Comput.*, 2012, **8**, 3902-3910.

[50] J. VandeVondele and J. Hutter, *J. Chem. Phys.*, 2007, **127**, 114105-114114.

[51] J. Hutter, M. Iannuzzi, F. Schiffmann and J. VandeVondele, *WIREs Comput. Mol. Sci.*, 2014, **4**, 15-25.

[52] W. Humphrey, A. Dalke and K. Schulten, *J. Mol. Graph.*, 1996, **14**, 33-38.

[53] M. J. Frisch, G. W. Trucks, H. B. Schlegel, G. E. Scuseria, M. A. Robb, J. R. Cheeseman, G. Scalmani, V. Barone, G. A. Petersson, H. Nakatsuji, X. Li, M. Caricato, A. V. Marenich, J. Bloino, B. G. Janesko, R. Gomperts, B. Mennucci, H. P. Hratchian, J. V. Ortiz, A. F. Izmaylov, J. L. Sonnenberg, D. Williams-Young, F. Ding, F. Lipparini, F. Egidi, J. Goings, B. Peng, A. Petrone, T. Henderson, D. Ranasinghe, V. G. Zakrzewski, J. Gao, N. Rega, G. Zheng, W. Liang, M. Hada, M. Ehara, K. Toyota, R. Fukuda, J. Hasegawa, M. Ishida, T.

Nakajima, Y. Honda, O. Kitao, H. Nakai, T. Vreven, K. Throssell, J. A. Montgomery, J. E. Peralta, F. Ogliaro, M. J. Bearpark, J. J. Heyd, E. N. Brothers, K. N. Kudin, V. N. Staroverov, T. A. Keith, R. Kobayashi, J. Normand, K. Raghavachari, A. P. Rendell, J. C. Burant, S. S. Iyengar, J. Tomasi, M. Cossi, J. M. Millam, M. Klene, C. Adamo, R. Cammi, J. W. Ochterski, R. L. Martin, K. Morokuma, O. Farkas, J. B. Foresman and D. J. Fox, Gaussian 16 Revision C.01, Gaussian Inc., Wallingford CT, 2016.

[54] Y. Zhao and D. G. Truhlar, *J. Chem. Phys.*, 2008, **128**, 184109-8.

[55] Y. Wang, P. Verma, X. Jin, D. G. Truhlar and X. He, *Proc. Natl. Acad. Sci.*, 2018, **115**, 10257-10262.

[56] F. Weigend, *Phys. Chem. Chem. Phys.*, 2006, **8**, 1057-1065.

[57] J. Tomasi, B. Mennucci and R. Cammi, *Chem. Rev.*, 2005, **105**, 2999-3094.

[58] V. N. Staroverov, G. E. Scuseria, J. Tao and J. P. Perdew, *Phys. Rev. B*, 2004, **69**, 075102-11.

[59] F. Neese, *J. Chem. Phys.*, 2007, **127**, 164112-9.

[60] S. Sinnecker and F. Neese, *J. Phys. Chem. A*, 2006, **110**, 12267-12275.

[61] F. Neese, *J. Chem. Phys.*, 2005, **122**, 034107-13.

[62] B. O. Roos, P. R. Taylor and P. E. M. Sigbahn, *Chem. Phys.*, 1980, **48**, 157-173.

[63] P. Siegbahn, A. Heiberg, B. Roos and B. Levy, *Phys. Scr.*, 1980, **21**, 323-327.

[64] P. E. M. Siegbahn, J. Almlöf, A. Heiberg and B. O. Roos, *J. Chem. Phys.*, 1981, **74**, 2384-2396.

[65] F. Neese, *WIREs Comput. Mol. Sci.*, 2012, **2**, 73-78.

[66] C. Platas-Iglesias, D. Esteban-Gómez, L. Helm and M. Regueiro-Figueroa, *J. Phys. Chem. A*, 2016, **120**, 6467-6476.

[67] T. Nakajima and K. Hirao, *Chem. Rev.*, 2012, **112**, 385-402.

[68] S. K. Singh, M. Atanasov and F. Neese, *J. Chem. Theory Comput.*, 2018, **14**, 4662-4677.

[69] J. Acharya, A. Sarkar, P. Kumar, V. Kumar, J. Flores Gonzalez, O. Cador, F. Pointillart, G. Rajaraman and V. Chandrasekhar, *Dalton Trans.*, 2020, **49**, 4785-4796.

[70] F. Weigend, M. Kattannek and R. Ahlrichs, *J. Chem. Phys.*, 2009, **130**, 164106-8.

[71] F. Weigend, *J. Comput. Chem.*, 2008, **29**, 167-175.

[72] C. Angeli, R. Cimiraglia and J.-P. Malrieu, *Chem. Phys. Lett.*, 2001, **350**, 297-305.

[73] D. Ganyushin and F. Neese, *J. Chem. Phys.*, 2006, **125**, 024103-11.

[74] A. V. Marenich, C. J. Cramer and D. G. Truhlar, *J. Phys. Chem. B*, 2009, **113**, 6378-6396.

[75] C. F. Matta, *The Quantum Theory of Atoms in Molecules: From Solid State to DNA and Drug Design*, John Wiley & Sons, Incorporated, Hoboken, 1st ed., 2007.

[76] T. Lu and F. Chen, *J. Comput. Chem.*, 2012, **33**, 580-592.

[77] A. E. Reed, R. B. Weinstock and F. Weinhold, *J. Chem. Phys.*, 1985, **83**, 735-746.

[78] I. Mayer, *Chem. Phys. Lett.*, 1983, **97**, 270-274.

[79] F. Neese, *J. Am. Chem. Soc.*, 2006, **128**, 10213-10222.

[80] M. Retegan, N. Cox, D. A. Pantazis and F. Neese, *Inorg. Chem.*, 2014, **53**, 11785-11793.

[81] S. Zein, C. Duboc, W. Lubitz and F. Neese, *Inorg. Chem.*, 2008, **47**, 134-142.

[82] S. Zein and F. Neese, *J. Phys. Chem. A*, 2008, **112**, 7976-7983.

[83] A. Kubica, J. Kowalewski, D. Kruk and M. Odelius, *J. Chem. Phys.*, 2013, **138**, 064304-064313.

[84] D. G. Liakos, D. Ganyushin and F. Neese, *Inorg. Chem.*, 2009, **48**, 10572-10580.

[85] S. R. Chowdhury and S. Mishra, *Phys. Chem. Chem. Phys.*, 2017, **19**, 16914-16922.

[86] M. S. Fataftah, J. M. Zadrozny, S. C. Coste, M. J. Graham, D. M. Rogers and D. E. Freedman, *J. Am. Chem. Soc.*, 2016, **138**, 1344-1348.

[87] M. S. Fataftah, S. C. Coste, B. Vlaisavljevich, J. M. Zadrozny and D. E. Freedman, *Chem. Sci.*, 2016, **7**, 6160-6166.

[88] S. Gomez-Coca, E. Cremades, N. Aliaga-Alcalde and E. Ruiz, *J. Am. Chem. Soc.*, 2013, **135**, 7010-7018.

[89] R. Ruamps, L. J. Batchelor, R. Guillot, G. Zakhia, A.-L. Barra, W. Wernsdorfer, N. Guihéry and T. Mallah, *Chem. Sci.*, 2014, **5**, 3418-3424.

[90] S. Tripathi, S. Vaidya, N. Ahmed, E. Andreasen Klahn, H. Cao, L. Spillecke, C. Koo, S. Spachmann, R. Klingeler, G. Rajaraman, J. Overgaard and M. Shanmugam, *Cell Rep. Phys. Sci.*, 2021, **2**, 100404.

[91] A. Sarkar, S. Tewary, S. Sinkar and G. Rajaraman, *Chem. – Asian J.*, 2019, **14**, 4696-4704.

[92] S. K. Singh, J. Eng, M. Atanasov and F. Neese, *Coord. Chem. Rev.*, 2017, **344**, 2-25.

[93] P. S. V. Kumar, V. Raghavendra and V. Subramanian, *J. Chem. Sci.*, 2016, **128**, 1527-1536.

[94] L. J. Farrugia, C. Evans, D. Lentz and M. Roemer, *J. Am. Chem. Soc.*, 2009, **131**, 1251-1268.

[95] E. Espinosa, E. Molins and C. Lecomte, *Chem. Phys. Lett.*, 1998, **285**, 170-173.

[96] J. Jung, M. Atanasov and F. Neese, *Inorg. Chem.*, 2017, **56**, 8802-8816.

[97] V. E. J. Berryman, J. J. Shephard, T. Ochiai, A. N. Price, P. L. Arnold, S. Parsons and N. Kaltsoyannis, *Phys. Chem. Chem. Phys.*, 2020, **22**, 16804-16812.

Chapter 6

Unraveling the Stability and Magnetic Properties of Bis-Hydrated Mn^{2+} Complexes via Tailored Ligand Design

The work of this Chapter is published in *J. Phys. Chem. A* **2024**, *39*, 8346-8359.

6.1. Introduction

The growing interest in stable paramagnetic complexes is driving ongoing advancements in our understanding of coordination chemistry and crucial applications for these complexes.[1–3] Transition metal (TM) complexes play a vital role in catalysis, materials synthesis, photochemistry, and biological systems due to their remarkable optical, electronic, mechanical, and magnetic properties,[4,5] with their applications in magnetic resonance imaging (MRI)[6–9] and single-molecule magnets (SMMs).[10–12] In MRI, these TM complexes serve as contrast agents (CAs) to enhance diagnostic imaging.[13,14] Gd^{3+}-based complexes are the most widely used clinically approved CAs, owing to their ability to enhance water proton longitudinal relaxation.[15,16] However, administering Gd^{3+}-based complexes causes a risk of nephrogenic systemic fibrosis (NSF),[17–19] promoting to explore Gd^{3+}-free alternatives, including magnetic nanoparticles,[20,21] fluorine MRI,[22,23] non-metal nitroxide radical-based systems,[24,25] and Mn^{2+}-based CAs.[26–28] This work focuses on Mn^{2+}-based complexes, which exhibit slow electronic relaxation, a rapid water exchange rate (k_{ex}^{298}), and efficient positive contrast.[2,29] Nevertheless, prolonged exposure to Mn^{2+} in humans can result in a neurological disorder called manganism, characterized by symptoms similar to Parkinsonism.[27,30,31] Therefore, the effectiveness of paramagnetic complexes as efficient CAs is contingent upon various conditions.[32] Among these conditions, thermodynamic and kinetic stabilities of the complexes are essential for the safe in vivo use of the CAs.[33,34] Moreover, the presence of water molecules directly coordinated to the metal center, with an appropriate exchange rate with bulk water,[35–37] and electronic relaxation time (T_{ie})[38–40] influence the ^{1}H relaxivity of MRI CAs in aqueous solution. Therefore, it is essential to conduct a comprehensive investigation into the structural, dynamical, and magnetic properties of paramagnetic complexes. This is essential for the development of CAs, highlighting the importance of exploring stable paramagnetic complexes.

Electronic relaxation, though often overlooked in clinical MRI, plays a key role in relaxivity at low magnetic fields (~ 2 MHz). With growing interest in low and ultra-low field MRI, particularly fast-field cycling MRI, optimizing CA relaxivity at these fields has gained attention.[39–41] According to McLachlan's theory, electron spin relaxation arises from temporary distortion of the metal coordination sphere, influencing the zero-field splitting (ZFS) energy.[42] The calculation of the ZFS of transition metal complexes is vital for determining their magnetic properties in the field of molecular magnetism. Thus, recent works have focused on the precise determination of the ZFS of TM ion complexes with a total ground spin state S > 1/2.[43–45] Moreover, the ZFS plays a significant role in designing SMMs, with a large and negative axial ZFS (D parameter) being a key factor in achieving desirable magnetic properties. The variation of the ZFS parameter D with different ligands has been given significant attention.[40,46,47] It was demonstrated previously that the magnetic anisotropy can be effectively tuned by tailoring the electronic structure of the metal center by switching the ligand field strength (different donor atoms) and/or symmetry (different coordination numbers and geometries).[48–50] The ZFS of the Mn^{2+} ion is influenced by the nature of the coordinated halide ligands.[51,52] For instance, in hexa-coordinated dihalide Mn^{2+} complexes $[Mn(tpa)(X)_2]$ (tpa=tris-2-picolylamine; X=I, Br, Cl), the D-value increases with heavier halide D(I)> D(Br)> D(Cl).[51] Recently, Karunadasa et al.[53] demonstrated changes in magnetic anisotropy in a set of pseudo-octahedral first-row transition metal complexes by altering ligands. As in earlier studies, the octahedral (O_h) complexes $[Cr(dmpe)_2(CN)(X)]^+$ (dmpe= 1,2-bis-(dimethylphosphino) ethane, X=Cl, Br, I) and $[Cr(dmpe)_2(CN)(X)]$ (X=Cl, I) reveals a similar trend. The observed trend can likely be ascribed to alterations in d-orbital splitting due to halides and the impact of spin-orbit coupling (SOC). A simple computational model can be beneficial for a lucid analysis of the observed variations in the ZFS parameter (D) concerning the nature of the ligand. Bloembergen and Morgan were the first to elucidate the profound impact of electron spin relaxation on the diminution of paramagnetic relaxation enhancement (PRE) in nuclear relaxation.[54,55] The relaxation can be elucidated by solving the time evolution of the electron spin using a spin Hamiltonian. This Hamiltonian comprises a Zeeman term, characterizing the interaction with the external magnetic field, and a ZFS term, which describes the electronic structure and molecular arrangement around the paramagnetic center.[39,40,56]

This work is structured as follows: In the first segment of our study, we aim to explore the thermodynamic stability and coordination geometry of seven-coordinated bis-hydrated Mn^{2+} complexes (Figure 6.1). Additionally, we investigate the effect of temperature on the relative

stability of the complexes by varying temperatures (25˚C and 90˚C). This complements our earlier investigation of solvation dynamics and magnetic characterization of complexes involving mono-hydrated Mn^{2+} complexes. We compared the calculated relative binding energy (BE) of the resolved complex structure in solution to the experimental stability constant. This comparison helps to predict the selectivity of a ligand towards the metal center (Mn^{2+}).

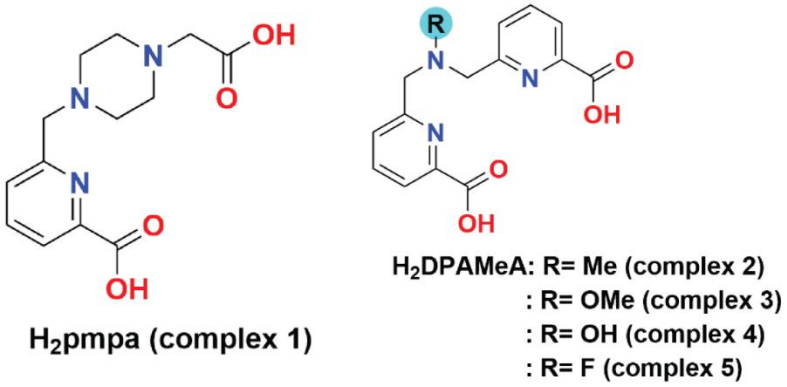

Figure 6.1. Structures of the ligands discussed in this study.

The subsequent section addresses the influence of ligands in fine-tuning the magnetic anisotropy of TM complexes. A systematic *ab initio* multireference and DFT analyses were conducted on the selected systems (Figure 6.2). The observed pattern in the D-values of the studied complexes enable us to determine the contribution of halides to the ZFS of the high-spin Mn^{2+} complexes. We explore the magnetic anisotropy from the incorporation of ligand orbitals, particularly emphasizing cases where the ligands significantly contribute to SOC. The ligand environment is systematically modified by replacing the equatorial O-atoms with heavier Se-atoms, followed by the subsequent replacement of axial water molecules with halogens (Cl, Br, and I). This study sheds new insights into the underlying physical origins of the ZFS parameters in bis-hydrated Mn^{2+} complexes and their halogen derivatives. It particularly highlights the heavier atom effects and their role in influencing the magnitude of the spin Hamiltonian parameter (D) and leads to the conclusion that substitution is a way forward to obtain a large D-value.

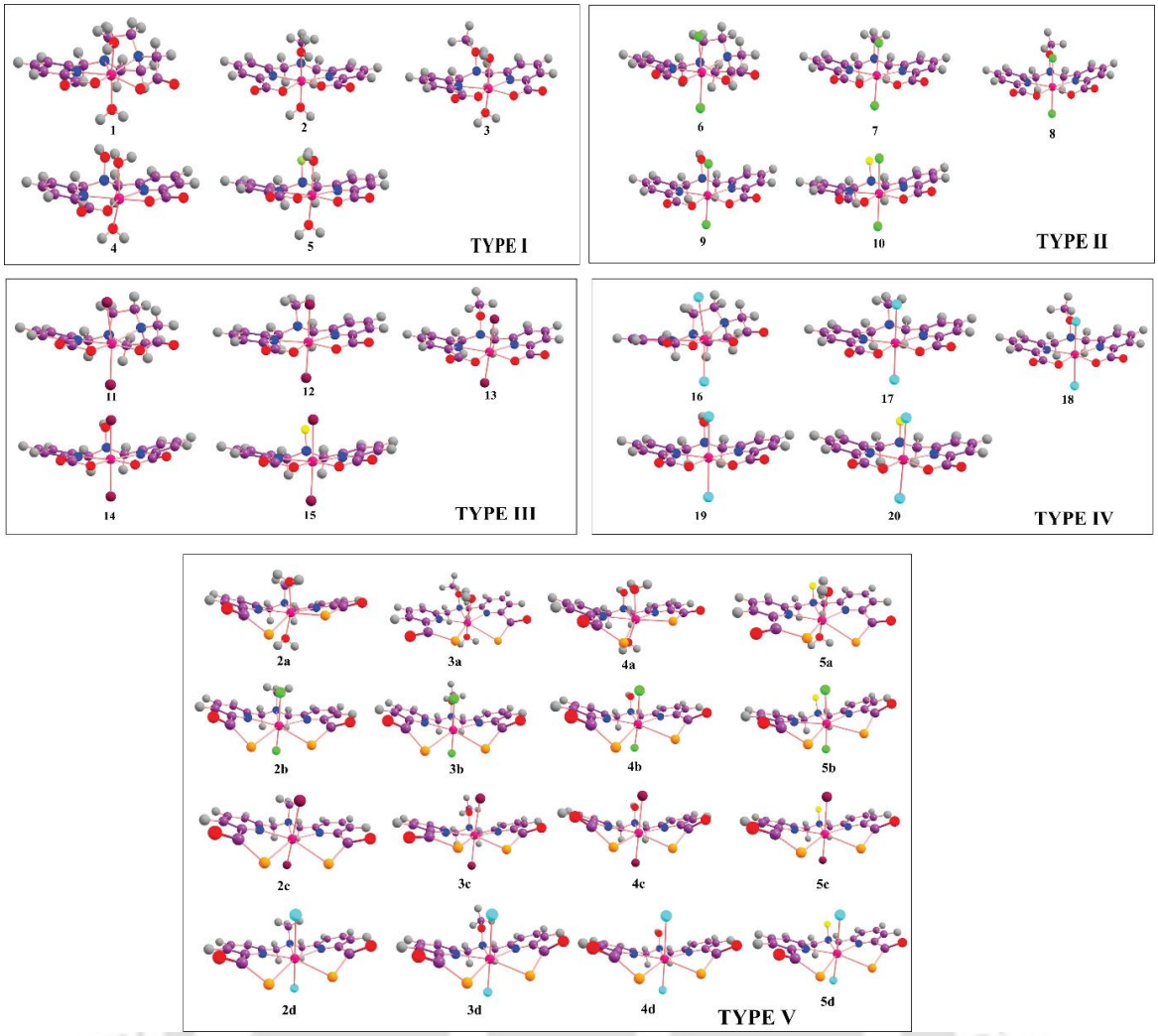

Figure 6.2. Two-dimensional structural representation of all the studied complexes. Type I complexes: Water molecules are in the axial position. Type II complexes: Water molecules in the axial position are replaced by chlorine atoms. Type III complexes: Bromine atom is in the axial position, Type IV complexes: Iodine atom is in the axial position, Type V complexes: Oxygen-donor atoms are replaced by selenium-donor atoms in the equatorial position. Distinct colors have been assigned to represent various atoms: manganese (pink), carbon (purple), nitrogen (blue), oxygen (red), hydrogen (gray), Fluorine (yellow), Chlorine (green), Bromine (maroon), iodine (cyan), selenium (orange).

6.2. Computational Details

In this study, the *ab initio* molecular dynamics (AIMD) simulations were conducted within the canonical (NVT) ensemble, utilizing a time step of 1.0 fs at a temperature of 25˚C.[40,57,58] The AIMD simulations at 90˚C were performed following the protocol outlined in our previous study by taking an equilibrated frame at 25˚C until at least 20 ps of equilibrated trajectories were sampled. The initial configuration for the AIMD simulations is obtained by equilibrating

the system using classical molecular dynamics (MD) simulations. The Generalized AMBER Force Field (GAFF)[59,60] was used for the ligand atoms, the Universal Force Field (UFF)[61,62] was applied for the Mn^{2+} ion, and the TIP3P model[63,64] was used to describe the water molecules. The topology files for the Mn^{2+} complex were generated using the Sobtop software package.[65] These classical MD simulations were performed using GROMACS.[66,67] With these classical force field parameters, the solvated system was minimized using the steepest descent algorithm.[68] This was followed by a canonical ensemble (NVT) simulation for 10 ns and, an isothermal-isobaric (NPT) simulation for 20 ns with a 1.0 fs time step. Parrinello-Rahman barrostat[69] and V-rescale[70] thermostats were used during these simulations. The NVT and NPT simulations were conducted at 298.15 K and a pressure of 1 bar. After equilibration, the system, with a cubic box size of 20 Å, contains 206 water molecules for complex 1 and 203 water molecules for complexes 2, 3, 4, and 5. The AIMD simulations in the canonical (NVT) ensemble were initiated using the final coordinates and box size from the equilibrated classical MD frames. A 1.0 fs timestep was used, and the simulations were run until the equilibrated trajectory was fully sampled. The energy minimization, temperature, pressure, and density plot over time using classical MD simulations are shown in Figures D1-D5 in Appendix-D. AIMD simulations were performed employing the PBE[71] functional with GTH-DZVP[72] basis set in the CP2K v5.1 package.[73] A Nose-Hoover thermostat was used to keep the temperature constant. The AIMD simulations corresponding to each complex were performed for ~ 40-45 ps. The first 20 ps of dynamics is discarded, and the following 20 ps is used for further analysis. The long-range electrostatic terms were computed using an additional plane wave basis set, with a cutoff of 300 Ry. Grimme's dispersion correction (DFT-D3) was applied to assess van der Waals interactions, employing a 6 Å radius. A sextet multiplicity was used consistently throughout the calculations. This protocol has previously demonstrated high accuracy in reproducing structural parameters for the seven-coordinated Mn^{2+} complexes, providing a good fit with experimental results.[40] The Mn-O distances exhibit a deviation within the range of 0.04-0.07 Å from experimental measurements, highlighting the robustness and reliability of the AIMD protocol.

The binding energy (BE) of the Mn^{2+}-ligand complexes was computed using the extracted Cartesian coordinates of the Mn^{2+} complexes, including the inner-sphere water molecules. The coordinates of the Mn^{2+}-ligand complex, used for BE calculations, were optimized in the solution phase by the following protocol in the full explicit solvent simulation box: starting from an AIMD equilibrated frame (last 20 ps) a single-point energy calculation

was performed on the optimized solution structure of the complexes using the M06-2X functional,[74] with def2-TZVP basis set[40] in the Gaussian 16 program package.[75] The BE of the ligand to the metal center was determined using Eq. 6.1

$$\text{BE}=E\left(Mn^{2+}(ligand)(H_2O)_n\right)^{c} - E(Mn^{2+}) - E(ligand)^{c-2} - n.E(H_2O) \quad (6.1)$$

Where c denotes the overall charge of the complex, and n represents the number of inner-sphere water molecules.

For the *ab initio* CASSCF/NEVPT2 computations, we considered the molecular geometries optimized at the M06-2X/def2-TZVP level of theory. Additionally, to account for the influence of the solvent, we employed the polarizable continuum model (PCM)[76] in general with the integral equation formalism, i.e., the IEFPCM model.[76] These *ab initio* state averaged complete active space self-consistent field (SA-CASSCF) computations were executed using the ORCA 4.0.1 program package.[77] The dynamic electron correlation was explored using the strongly contracted form of the N-valence state perturbation theory (SC-NEVPT2).[78] The zeroth-order regular approximation (ZORA) scalar relativistic Hamiltonian was considered.[79] In addition, the contracted ZORA basis set, specifically ZORA-def2-TZVP, was used for the Mn^{2+}, halogens (X=Cl, Br), and Se. The basis sets used for I and elements of the first coordination sphere (O, N) were SARC-ZORA-TZVP and ZORA-def2-TZVP(-f), respectively, while the ZORA-def2-SVP basis set was applied to the remaining elements (H, C, N, O). The restricted open-shell Kohn-Sham (ROKS) approach was used to generate the initial guess orbitals for the multiconfigurational self-consistent field method, using the BP86 functionals and ZORA-def2-SVP basis set.[47,80] These basis sets were retained for the *ab initio* CASSCF/NEVPT2 calculations. However, there was a modification in the auxiliary basis sets, transitioning from SARC/J to def2-TZVP/C for the metal center and halogens (Cl, Br, and I), while for the surrounding environment, def2-SVP/C basis sets were employed. To calculate the excited state energies in the high-spin d^5 Mn^{2+} system, the SACASSCF calculations primarily focused on five metal d-electrons in five metal 3d orbitals using CAS(5,5) active space. The CAS(5,5) active space does not explicitly incorporate the correlation of ligand electrons. To account for the SOC of heavy ligands and assess the impact of metal-ligand interactions on the magnetic anisotropy of the studied seven coordinated Mn^{2+} complexes, the CAS(5,5) active space was extended by introducing the ligand orbitals, particularly the p_z-orbitals in the axial direction, i.e., CAS(9,7) active space. To better capture electron correlation, the effect of the double d-shell (4d orbitals) was

incorporated by employing a CAS(5,10) active space. Thus, by employing various active spaces, we can compare the influence of different configurations in the context of SMMs for determining ZFS parameters. The metal-ligand bonding nature was validated using the quantum theory of atoms in molecules (QTAIM) analysis.[81] In addition, the bond order analysis was performed using Mayer bond order with the Multiwfn program package (version 3.8).[82]

6.3. Results and Discussion

6.3.1. The Structural Resolution of Bis-Hydrated Mn^{2+} Complexes using AIMD

The AIMD simulations of five bis-hydrated Mn^{2+} complexes have been carried out, and two of which are experimentally synthesized (complex 1 and complex 2), while the remaining three complexes were designed by altering the R-substituent of complex 2, as shown in Figure 6.1. The optimized structure of complex 1 with coordinate sites 1 and 5 connected to the carboxylate oxygen, coordinate site 2 corresponding to pyridine nitrogen, coordinate sites 3 and 4 for amine nitrogen, and coordinate sites 6 and 7 corresponding to axial water molecules, as depicted in Figure 6.3(a). In the case of complex 2, complex 3, complex 4, and complex 5, coordinate sites 1 and 5 correspond to the carboxylate oxygens, coordinate sites 2 and 4 correspond to pyridine nitrogen, and coordinate site 3 corresponds to amine nitrogen, coordinate sites 6 and 7 correspond to axial water molecules, as shown in Figure 6.3(b).

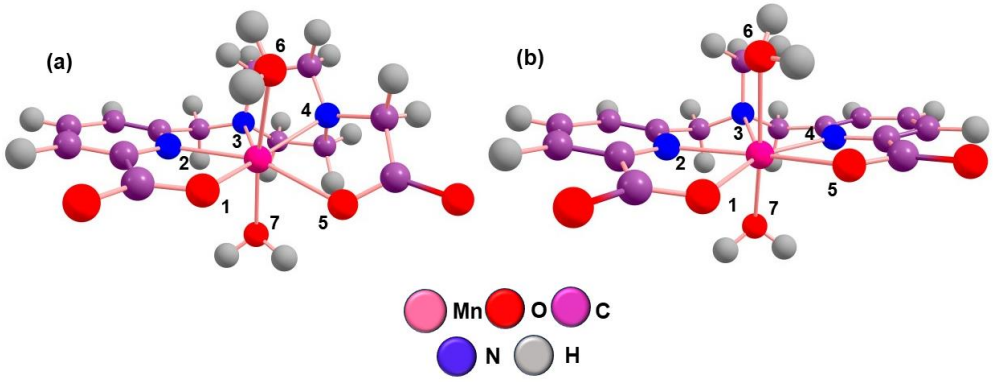

Figure 6.3. The optimized structures of (a) $[Mn(pmpa)(H_2O)_2]$ or complex 1 and (b) $[Mn(DPAMeA)(H_2O)_2]$ or complex 2 using PBE/DZVP method with GTH pseudopotentials.

We calculated the Mn-O, Mn-N, and Mn-C radial distribution functions (RDFs) and coordination numbers (CNs) for all the studied complexes (Figure 6.1), using the last 20 ps of equilibrated AIMD trajectory at two different temperatures (25˚C and 90˚C), as shown in

Figure 6.4 and Figure D6 in Appendix-D. We observed that the RDFs computed for all the complexes at 25˚C exhibit an average maxima of 2.25 Å for the Mn-O atoms, 2.29 Å for the Mn-N atoms, and 3.15 Å for the Mn-C atoms, respectively. The first coordination sphere of the complexes contains the oxygen and nitrogen atoms that are directly coordinated to the Mn^{2+} ion, with the ligand's carbon atoms positioned slightly further away. A smaller peak at ∼4.25-4.35 Å corresponds to the second coordination sphere, representing the solvent (water) shell surrounding the Mn^{2+} complexes in Mn-O RDFs. Additionally, we found two smaller peaks in Mn-C RDFs between ∼4-5 Å. These two peaks may indicate the presence of different types of carbon atoms (carboxylate, amine, and pyridine) within the ligands. These values indicate that our computational protocol replicated the solution structure of the studied Mn^{2+} complexes correctly. The potential energy (PE) plots obtained from the AIMD trajectory at 25˚C and 90˚C are shown in Figures D7-D8 in Appendix-D. Additionally, Table D1 in Appendix-D shows the peak distances extracted from the RDFs obtained through AIMD simulations at 25˚C. The variations in Mn-O and Mn-N bond lengths for the studied complexes throughout the AIMD simulations at 25˚C are illustrated in Figures D9-D10 in Appendix-D.

To investigate the effect of temperature (25˚C and 90˚C) on the solution phase structure of the Mn^{2+}-ligand complex, we compared the RDFs for Mn-O, Mn-N, and Mn-C atoms in complex 1 and complex 2 as shown in Figure 6.4. This analysis reaffirms our previous findings, indicating that the binding affinity of the Mn^{2+} ion to the ligand remains notably stable at high temperatures for rigid ligands.[40] Among the studied complexes, $[Mn(pmpa)(H_2O)_2]$ exhibits the highest stability, maintaining a sharp peak at high temperature (90˚C) similar to the RDF peak at 25˚C, as shown in Figure 6.4 (a-c). As stability decreases, the sharpness of the peak decreases with increasing temperature. This trend is evident in the less stable $[Mn(DPAMeA)(H_2O)_2]$ complex, as illustrated in Figure 6.4 (d-f), when compared to the $[Mn(pmpa)(H_2O)_2]$ complex. This indicates that complexes with high stability exhibit a minimal change in their RDFs between 25˚C and 90˚C, whereas the RDFs of the less stable complex undergoes more significant alteration with temperature.

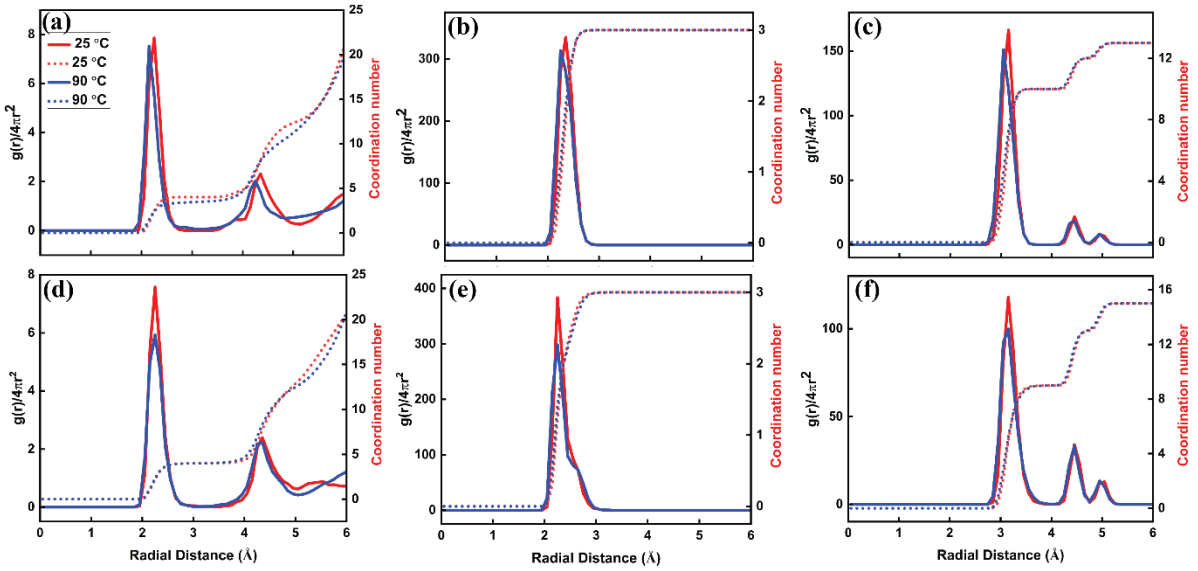

Figure 6.4. Radial distribution functions (RDFs) and coordination numbers (CNs) of the [Mn(pmpa)(H_2O)$_2$] (above) and [Mn(DPAMeA)(H_2O)$_2$] (below) complexes at 25˚C and 90˚C. (a, d) Mn-O, (b, e) Mn-N, and (c, f) Mn-C atoms.

6.3.2. Relative Binding Energy (BE) of Mn^{2+}-Ligand Complex

The calculation of binding energy (BE) between metal and ligand is essential for understanding the stability and reactivity of metal-ligand complexes. The relative binding affinity of the ligand to the metal center is determined using Eq. 6.1. The experimental stability constant value shows that the ligand H_2pmpa forms a stronger complex with the Mn^{2+} center compared to H_2DPAMeA.[29] This observation is in line with our findings. Table 6.1 displays the total BE and relative BE values of the studied Mn^{2+}-ligand complexes along with their experimental stability constant. A comparison of the BEs of the [Mn(pmpa)(H_2O)$_2$] and [Mn(DPAMeA)(H_2O)$_2$] complexes, as well as the RDFs in Figure 6.4, reveal that lower complex stability correlates with an increased disorder of ligand/solvent in the Mn^{2+}-ligand complex. The results indicate that the binding affinity of the ligand H_2pmpa for Mn^{2+} is 5.435 kcal mol^{-1} higher than that of the H_2DPAMeA ligand, which is consistent with the experimental stability constant values (Table 6.1)

Table 6.1. Total binding energy ($\triangle E_{tot}$) and relative binding energy ($\triangle E_{relative}$) values (in kcal mol^{-1}) of the selected complexes at 25˚C along with the experimental (Exp) stability constant.

Method	Complex	$\triangle E_{tot}$	$\triangle E_{relative}$	Experimental stability constant ($logK_{MnL}$)
M06-2X/def2-TZVP	Complex 1	-294.057	0.000	14.29[29]
	Complex 2	-288.623	5.435	10.13[29]
	Complex 3	-293.769	0.289	
	Complex 4	-285.234	8.823	
	Complex 5	-282.216	11.842	

6.3.3. Quantum Chemistry Calculations for Rationalizing Magnetic Properties of Bis-Hydrated Mn^{2+} Complexes

The primary objective of this study is to predict the magnetic anisotropy of Mn^{2+} complexes using quantum chemical methods, incorporating both DFT and *ab initio* multireference approaches.[48] Recently, we have highlighted that replacing an equatorial oxygen atom with a soft donor atom (S, Se) causes a shift in the magnetic anisotropy in pentagonal bipyramidal Mn^{2+} geometries. To investigate the influence of other ligating atoms, such as halides, alongside the soft-donor ligands, here we have considered thirty-six Mn^{2+} complexes. Figure 6. 2 illustrates the classification of thirty-six complexes into five distinct categories. Complexes of Type I (1-5) feature a core structure of (MnO_2N_3), having two water molecules in the axial positions. Complexes 1 and 2 are experimentally synthesized, while complexes 3, 4, and 5 are designed with variation in the R-substituent (R= -OMe, -OH, and -F), as shown in Figure 6.1. Type II, III, and IV complexes have the same core structure as Type I complexes, with the axial water molecules replaced by halogens (Cl, Br, and I, respectively). In Type V complexes, the equatorial O-atoms in Type II, III, and IV complexes are substituted with Se-atoms. Consequently, derivatives containing Se at the equatorial position and halogens at the axial positions were designed. The following sections address the origin of ZFS parameters as well as the effect of axial halogens (Cl, Br, and I) and equatorial hard/soft (O and Se) donor atoms on the magnetic anisotropy of seven coordinated Mn^{2+} complexes.

6.3.4. DFT Methods to Determine the Spin-Spin Coupling (SSC) and Spin-Orbit Coupling (SOC) Parameters to Overall *D*-Value

A systematic DFT study was performed to comprehend the impact of halogens and Se-donor atoms on the ZFS parameters. The DFT computations are useful for elucidating the various contributions to the overall D-values (D_{SSC} and D_{SOC}).[83] The DFT-optimized bond length values of the studied complexes are shown in Table D2 in Appendix-D. The structural features of high spin Mn^{2+} complexes, such as the nature of the coordinated ligand and coordination number, determine the relative contribution of SSC vs. SOC.[40,51,52,83] Our investigation demonstrates that SSC contributions to the D-tensor are non-negligible for lighter halides (Cl) but become insignificant for heavier halides (Br, I), as shown in Figure 6.5 and Table D3 in Appendix-D.

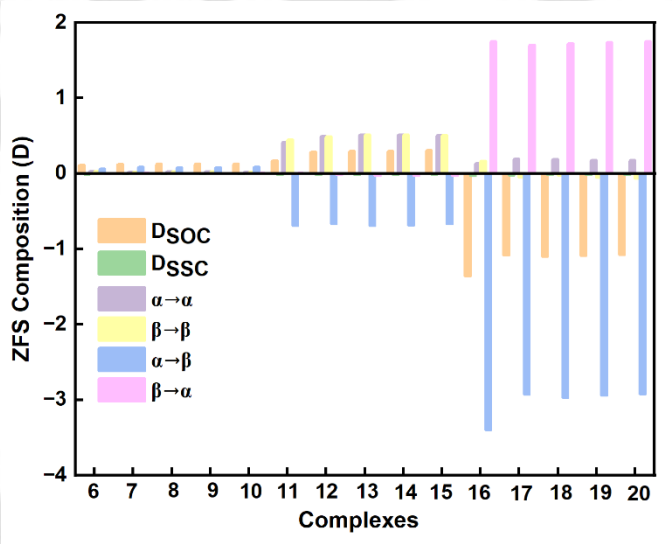

Figure 6.5. Individual contributions of D_{SSC} and D_{SOC} to the DFT-calculated ZFS parameter D with X= Cl, Br, I.

Moreover, the four different types of excitations within the SOC component of the D-tensor contributes with comparable magnitude and opposite signs. The observed usual trend for these halide Mn^{2+} systems (D(I) > D(Br) > D(Cl)) can be elucidated by the dominance of halide SOC in the total D-value. Table A4 in Appendix-D represent the ZFS parameter values obtained using M06-2X methods, with the def2-TZVP basis set.

This is primarily attributed to the significant contribution from the interference in the metal and halide SOC contributions. This interference is proportional to the product of the SOC constant of Mn^{2+} and X (halide). Furthermore, in the case of Type IV complexes (I-derivatives), the $\alpha \rightarrow \alpha$ and $\beta \rightarrow \beta$ contributions are more significant than other halogen derivatives (Type II and Type III complexes). This is because the Mn-I bond distance is longer

than that of the Mn-Cl and Mn-Br bond distances, indicating a weak ligand field. The decomposition of the calculated D-values for the halogen derivatives (Type II, Type III, and Type IV) is depicted in Figure 6.5. D_{SOC} contributions increase from Cl to I in almost all cases, as shown in Figure 6.5. This result is consistent with the fact that, due to the the heavy nucleus of I, the SOC introduced by this ligand is expected to be higher than that of Br, which, in turn, is greater than Cl. The trend in the SHPs from Cl to I derivatives is consistent with the results from previous investigations of Mn^{2+}-based complexes.[51,53] Additionally, for Type I and Type V complexes, this representation is depicted in Table D3 in Appendix-D, which illustrates that the D_{SOC} value of Se-analogs is higher than that of the O-analogs. To validate the accuracy of our single-determinant DFT-based method, we further proceed to the multireference approach.[47,49,52,84,85]

6.3.5. Multireference Approach for Evaluating Magnetic Anisotropy

The accurate prediction of the SHPs of Mn^{2+} complexes relies on the precise illustration of the multiplets originating from the appropriate d^N configurations. Thus, in a multiconfigurational approach, it is important to select a balanced active space that accurately provides the electronic description of both ground and excited states.[86] The DFT-optimized Mn^{2+} complexes were used for multiconfigurational electronic structure calculations. Initially, we considered *ab initio* CASSCF and CASSCF/NEVPT2 methods, which include the correlation of five electrons in five orbitals, i.e., CAS(5,5). The ZFS parameters of Type I, Type II, Type III, and Type IV complexes, as well as the experimental mean square ZFS energy ($\triangle^2$) of complex 2, are depicted in Table 6.2.

The energy levels of the scalar-relativistic states generated from the CAS(5,5) calculations reveal that the sextet state is the ground state, while the lowest quartet and doublet states are ~17000-18000 and 25000-30000 cm^{-1} above the ground state respectively, as shown in Tables D5-D24 in Appendix-D. To increase the radial correlation, a second d-shell (4d) was used in the calculation, i.e., CAS(5,10). We noted that D-parameter alter within a margin of ± 0.01-0.04 cm^{-1} and E/D value of ± 0.01-0.20 cm^{-1} compared to CAS (5,5), as shown in Figure 6.6 and Tables D25 in Appendix-D, which are almost negligible. Atomic Mn^{2+} has a ground state of $^6S_{5/2}$ with no orbital contribution. However, when Mn^{2+} forms complexes with heavy elements (Cl, Br, and I) where ligands contribute significantly to the overall large SOC, it is important to consider the mixing of metal and ligand orbitals for accurate electron contribution. To explore how heavier ligands affect the magnetic anisotropy of seven coordinated Mn^{2+} complexes, it is necessary to include the ligand orbitals (here, p_z-orbitals) in the active

space. To this end, we used extended active space CAS(9,7), i.e., 9 electrons in 7 orbitals. The additional two orbitals correspond to the bonding and antibonding orbitals arising from the valence p_z orbitals of the halogens.

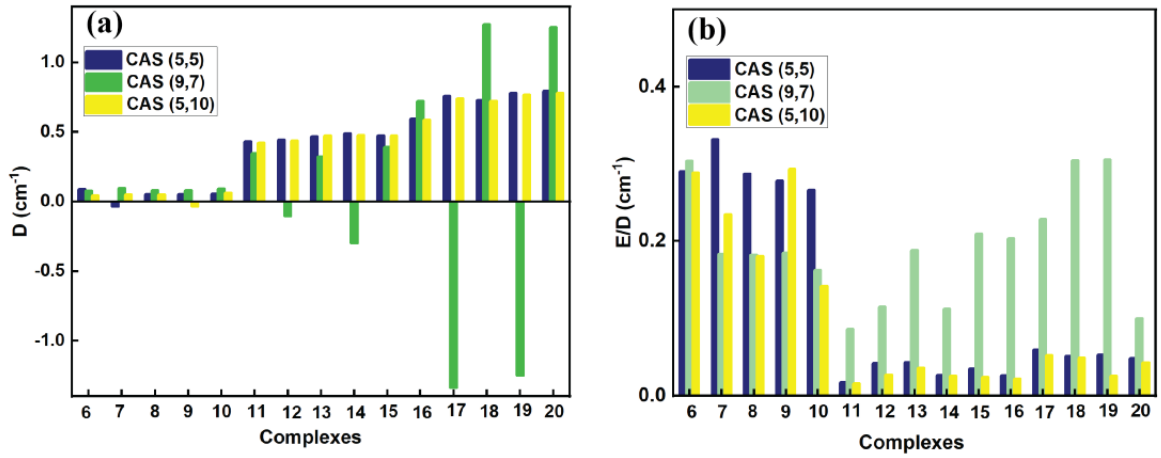

Figure 6.6. (a) Calculation of D-parameter of optimized Type II-IV complexes using *ab initio* CASSCF/NEVPT2 method, with CAS(5,5), CAS(9,7), and CAS(5,10) active spaces, and (b) E/D parameter using three different active spaces.

Table 6.2. ZFS parameters of Mn^{2+} complexes (Type I, Type II, Type III, and Type IV) calculated using *ab initio* multireference methods with their available experimental values.

Complex	Method	D (cm^{-1})	E/D	$\triangle$ (cm^{-1})	$\triangle^2$ (10^{20} S^{-2})
Complex 1	CAS(5,5)	0.039	0.069	0.033	0.383
	NEVPT2(5,5)	0.038	0.179	0.033	0.369
Complex 2	CAS(5,5)	0.068	0.226	0.059	1.258
	NEVPT2 (5,5)	0.069	0.192	0.059	1.249
	EXP	-	-	-	0.238[87]
Complex 3	CAS(5,5)	0.049	0.021	0.040	0.573
	NEVPT2(5,5)	0.049	0.187	0.043	0.642
Complex 4	CAS(5,5)	0.054	0.235	0.047	0.782
	NEVPT2(5,5)	0.054	0.185	0.049	0.746

Complex 5	CAS(5,5)	0.047	0.298	0.428	0.651
	NEVPT2(5,5)	0.047	0.234	0.041	0.596
Complex 6	CAS(5,5)	0.084	0.293	0.077	2.087
	NEVPT2(5,5)	0.089	0.291	0.082	2.346
Complex 7	CAS(5,5)	-0.033	0.307	0.031	0.329
	NEVPT2(5,5)	-0.037	0.332	0.035	0.421
Complex 8	CAS(5,5)	0.048	0.293	0.044	0.686
	NEVPT2(5,5)	0.053	0.288	0.048	0.812
Complex 9	CAS(5,5)	0.047	0.287	0.043	0.638
	NEVPT2(5,5)	0.051	0.279	0.047	0.762
Complex 10	CAS(5,5)	0.052	0.273	0.047	0.774
	NEVPT2(5,5)	0.057	0.267	0.055	1.071
Complex 11	CAS(5,5)	0.425	0.019	0.348	42.839
	NEVPT2(5,5)	0.431	0.018	0.352	43.959
Complex 12	CAS(5,5)	0.437	0.044	0.358	45.351
	NEVPT2(5,5)	0.442	0.042	0.366	47.442
Complex 13	CAS(5,5)	0.464	0.046	0.379	51.218
	NEVPT2(5,5)	0.469	0.044	0.384	52.268
Complex 14	CAS(5,5)	0.486	0.029	0.398	56.095
	NEVPT2(5,5)	0.491	0.027	0.402	57.201
Complex 15	CAS(5,5)	0.468	0.038	0.383	52.045
	NEVPT2(5,5)	0.473	0.036	0.387	53.131
Complex 16	CAS(5,5)	0.586	0.028	0.479	81.479
	NEVPT2(5,5)	0.596	0.026	0.487	84.123

Complex 17	CAS(5,5) NEVPT2(5,5)	0.751 0.759	0.062 0.059	0.617 0.624	135.049 138.023
Complex 18	CAS(5,5) NEVPT2(5,5)	0.719 0.729	0.054 0.052	0.590 0.597	123.679 126.603
Complex 19	CAS(5,5) NEVPT2(5,5)	0.773 0.781	0.055 0.053	0.634 0.641	142.733 145.738
Complex 20	CAS(5,5) NEVPT2(5,5)	0.786 0.794	0.051 0.049	0.644 0.651	147.301 150.329

The CAS orbitals generated after the state-averaged calculations were found to exhibit maximum metal-ligand overlap in chloride derivatives, followed by bromide and iodide derivatives. The active orbitals generated after the SA-CASSCF calculations of the complex 6, 11, and 16 are shown in Figures D11 in Appendix-D.

The contribution of *nroots* (number of excited states) to magnetic anisotropy is significant, as thoroughly elucidated by Llanos and Aravena,[88] that selecting the *nroots* of a specific multiplicity is pivotal for minimizing computational costs and focusing on the inclusion of only those low-lying excited states. Due to computational constraints, we included only the low-lying excited states for the CAS(9,7) active space. The effect of the inclusion of *nroots* and their contribution to magnetic anisotropy for CAS(9,7) active space for complexes 6, 11, and 16 are shown in Tables D26-D28 in Appendix D. We observed that the values of the SHPs using CAS (5,5) and CAS(9,7) active spaces are in similar trends, as shown in Figure 6.6. Hence, we focused on the more computationally affordable active space CAS(5,5) for further analysis.

For the Type I complexes, we analyze the electronic effect of ligands (electron-withdrawing and donating groups) at the second coordination sphere. Among Type I complexes, the D-value is highest for the methyl-analogs (complex 2). The d-orbital splitting pattern of these Type I complexes are shown in Figure D12 in Appendix-D. These reaffirmed that ZFS parameters are related directly to the electron density distribution in the molecule. In these seven coordinated Mn^{2+} complexes, we found that the *D*-value increases with the electron-donating methyl (-Me)

group compared to the electron-withdrawing methoxy, hydroxy, and fluoride (-OMe, -OH, -F) groups.[40] The ligand field analysis indicates the first three excited states (ESs) make notable contributions to the overall D-value for Type I complexes, as demonstrated in Tables D5-D9 in Appendix-D. The next significant contribution arises from the 12^{th} and 17^{th} excited states. While these Ess mentioned above have very high energies compared to the GS, their impact on the D-value is non-negligible. Besides these major contributions, several minor contributions are also observed. Likewise, the state-wise contribution to the total Rhombic E parameter reveals a similar contribution pattern for all the Type I complexes with the main contributions from 2^{nd}, 3^{rd}, and 16^{th} ESs, as illustrated in Tables D5-D9 in Appendix-D. In addition, for Type I complexes, we investigated the inclusion of explicit water molecules. We observed that explicit water molecules enhance the ZFS parameter (D), as indicated in Table D29 in Appendix-D. This could be attributed to a shortening of the Mn-O(w) bond distance following the insertion of explicit water molecules, which impacts the magnetic anisotropy parameters.

To explore the impact of halogens on the magnetic anisotropy of seven coordinated Mn^{2+} complexes, we modeled Type II, Type III, and Type IV complexes (Figure 6.2). The ligand field analysis indicates that the major contribution to D-value in Type II complexes originates from the first three excited quartet states and 12^{th} and 16^{th} ESs. The major contribution in Type III and Type IV complexes arises from the first two excited quartet states and 10^{th}, 11^{th}, 12^{th}, and 15^{th} or 16^{th} ESs. The NEVPT2 LFT computed d-orbitals splitting diagram for Type II, III, and IV complexes are shown in Figure 6.7. The splitting of d-orbitals between equatorial $d_{x^2-y^2}$ and d_{xy} orbitals decrease from Cl to I, and the D value increases with a decrease in E/D. Therefore, the one-electron ligand field d-orbital energies are important to rationalize the origin of magnetic anisotropy. As the axial ligands control the energy of the d_{z^2} orbital through strong axial coordination, the d_{z^2} orbital in all these complexes remains higher in energy than the $d_{x^2-y^2}/d_{xy}$ set of orbitals. Consequently, the d_{xz}/d_{yz} to d_{z^2} transition prevails at higher energy. Iodide and bromide have diffused valence orbitals and overlap poorly with the metal, leading to a weak ligand field. They are also π-donor in addition to σ-donor, which destabilizes the metal orbitals and further decreases the splitting, as shown in Figure 6.7.

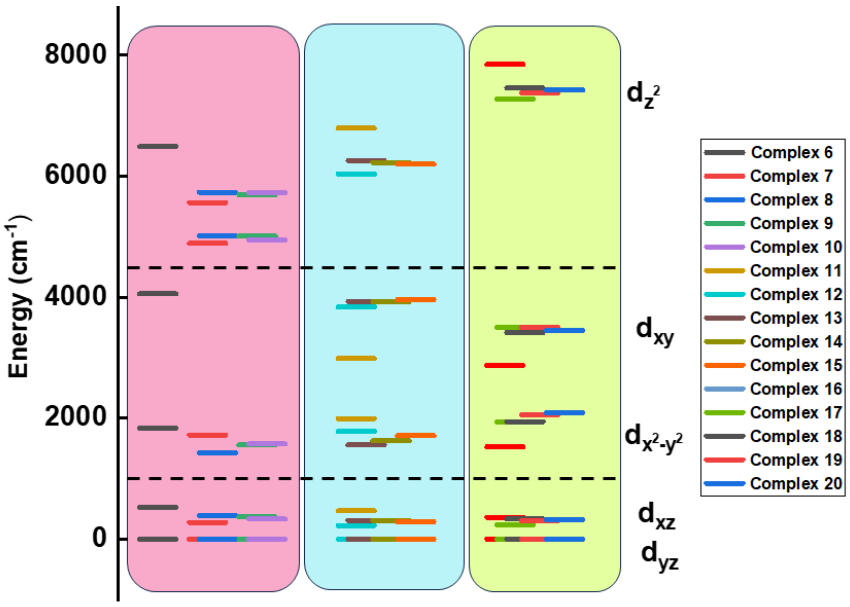

Figure 6.7. NEVPT2 computed ligand field d-orbitals splitting diagram of the investigated Type II, III, and IV complexes.

The overall D-value for these complexes also corresponds to the covalent character of the Mn-X bond (X=Cl, Br, I). The increase in covalent character was further validated by QTAIM analysis, as illustrated in Figure 6.8. This analysis justifies that electron density decreases with increasing covalency in the sequence of Cl < Br < I [Figure 6.8(a)]. Consequently, there is a decrease in $[\nabla^2_{\rho(bcp)}]$ at the corresponding bond critical point (bcp) as we progress down the group [Figure 6.8(b)]. Similarly, the decrease in the kinetic energy density (G_{bcp}) at the corresponding bcp is associated with the lower electron density at that point in Figure 6.8(c). Furthermore, the Mayer bond order of the investigated Type II, Type III, and Type IV complexes decrease in the sequence Mn-Cl> Mn-Br> Mn-I, as depicted in Figure 6.8(d), indicating a stronger axial donor-acceptor bond is associated with a lower D-value. Thus, this aligns with the ligand field strength described by the general spectrochemical series.

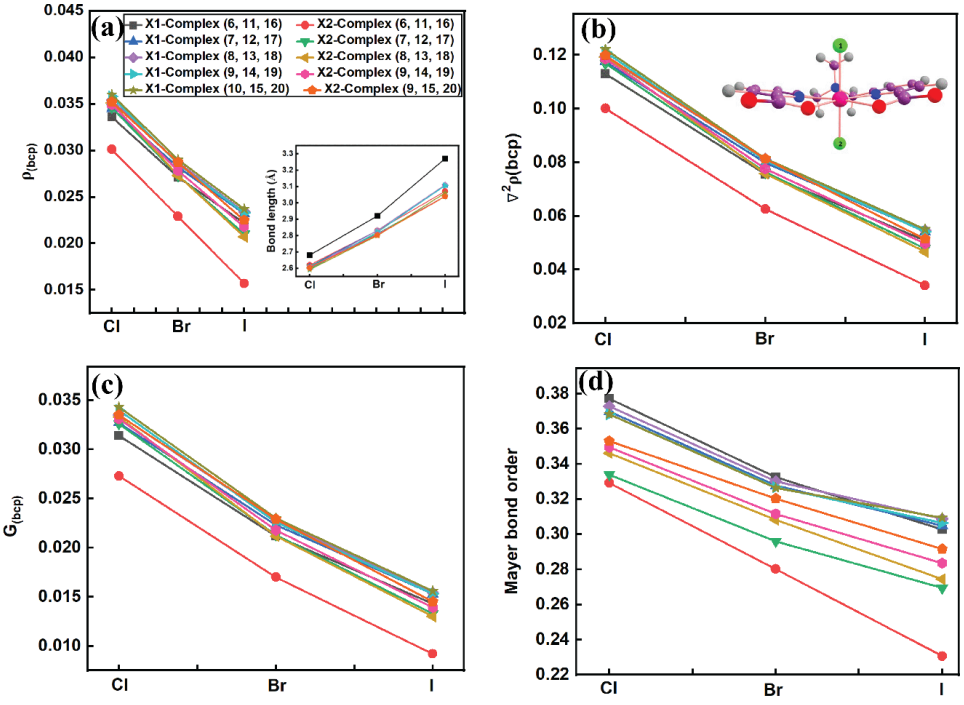

Figure 6.8. (a) Variation of Mn-X donor distance and electron density, (b) variation of $\nabla^2_{\rho(bcp)}$, (c) variation of G_{bcp}, and (d) variation of Mayer bond order for Type II, Type III, and Type IV complexes. The solid line represents a guideline to follow the trend better.

The effect of covalency was also calculated by using the Racah parameter (B) and spin-orbit coupling parameters (ζ). The percentage reduction in the B-parameter and SOC constant was calculated as $[(1-\frac{B}{B_0})\times 100]$ and $[(1-\frac{\zeta}{\zeta_0})\times 100]$, respectively, as shown in Figures 6.9 (a) and 6.9 (b). Our calculations demonstrate that the large spin-orbit coupling associated with heavier halides and the covalency of metal-ligand bonds significantly influence the ZFS parameters.

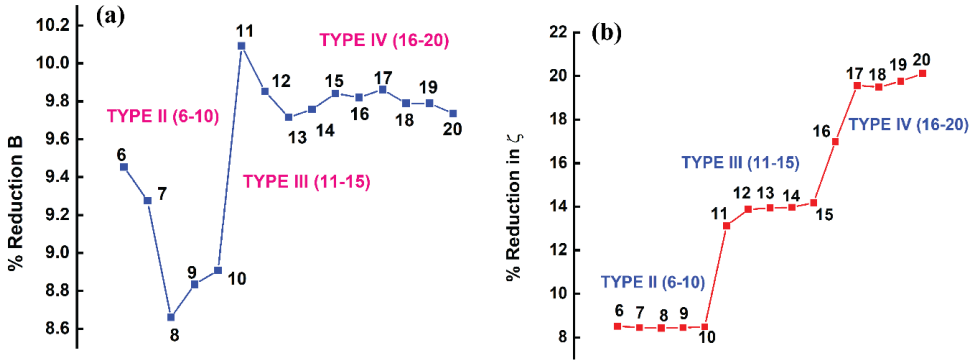

Figure 6.9. (a) Variation of nephelauxetic reduction of Racah parameter B and (b) effective spin-orbit coupling constant ζ among the Type II, Type III, and Type IV complexes.

To better understand the influence of structural parameters on D-value in seven coordinated Mn^{2+} complexes, we developed a magneto-structural correlation by varying the Mn-Cl, Mn-Br, and Mn-I bond lengths in model complexes 7, 12, and 17 from 2.6-2.0 Å, 2.7-2.2 Å, and 2.8-2.5 Å, respectively. We observed that as the bond length decreases, the D-value increases, as shown in Figure 6.10(a), Figure D13(a), and Figure D14(a) in Appendix-D. A similar d-orbital splitting pattern is observed upon compression of the Mn-X bond for all three complexes, as shown in Figure 6.10(b), Figure D13(b), and Figure D14(b) in Appendix D. The gap between the $d_{x^2-y^2}$ and d_{xy} orbitals increase upon an increase in the bond length, and the D-value decreases. Besides, the E/D ratio does not follow a regular trend, as shown in Figure 6.10(c), Figure D13(c), and Figure D14(c) in Appendix-D. The developed correlation highlights the importance of the compression of axial bond length, which is directly correlated with the sign and magnitude of the D-value of the halide derivatives. However, upon variation of bond length, the sign of D changes several times, but the overall ZFS energy ($\triangle$) value is enhanced upon axial compression, as depicted in Figure 6.10(d). These will assist experimentalists in rationally targeting ligands that can stabilize large negative D-values for designing SMMs. Thus, these ZFS parameters are highly sensitive to small changes in structural parameters. In addition, we related the D-value with the Racah parameter (B) value and observed a reduction in the D-value with an increase in B-value from Cl to I, presented in Figure D15 in Appendix-D.

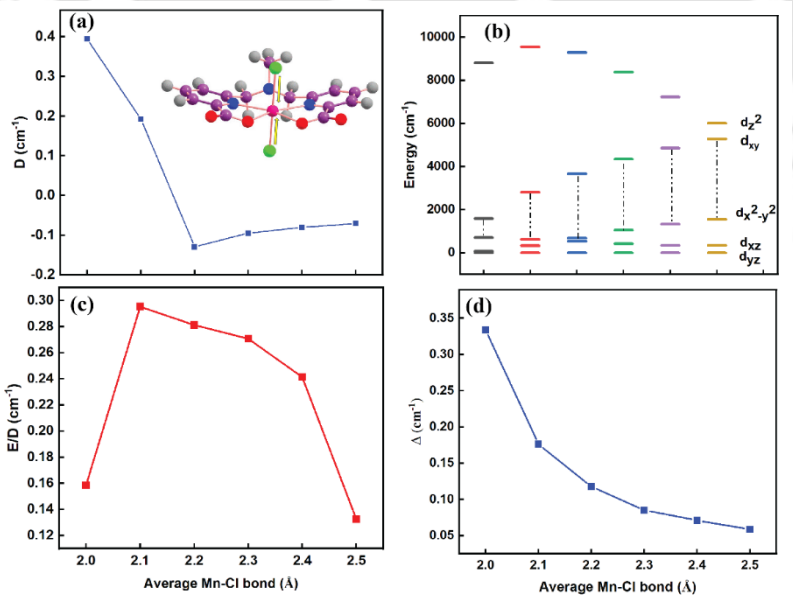

Figure 6.10. Graphical output of the *ab initio* CASSCF/NEVPT2 calculations for the model complex 7 in which bond length varies from 2.0-2.7 Å (a) d-orbital splitting, (b) variation of D-parameter, (c) variation of E/D parameter, and (d) variation of ZFS energy $\triangle$.

The O-atoms in the equatorial positions are substituted for the Type V complexes with soft Se-atoms. It is well known that the softness of the atom increases down the group. It is expected that substituting Se in place of O and halogens in place of water molecules will ultimately increase the D-value.[40,84,89] Therefore, the D-value for Type V complexes is larger than the Type I, II, and III complexes. However, when we compared the D-value for Type IV (Oxygen-based iodide derivatives) and Type V (Selenium-based iodide derivatives), the D value decreased. The D-value of Se-analogs follows the order $D(\mathrm{Cl}) < D(\mathrm{I}) < D(\mathrm{Br})$, as shown in Table D16 in Appendix-D, i.e., it does not follow the regular spectrochemical series. This discrepancy is most likely a consequence of the interplay between the Mn^{2+}-Se bond covalency and ligand field splitting Δ. The QTAIM analysis of these Type V complexes is shown in Table D31 in Appendix-D. Moreover, the Mayer bond order suggests that it increases from bromide to iodide derivatives, and hence, the D-value decreases, as shown in Table D32 in Appendix-D. This confirms the more covalent character of Se-analogs compared with O-analogs. Compared to oxygen derivatives, Se-derivatives have a weak ligand field, resulting in a smaller gap between the d-orbitals, as shown in Figure 6.7, Figure 6.11, Figure D12, and Figure D16 in Appendix-D, and D-value increases.

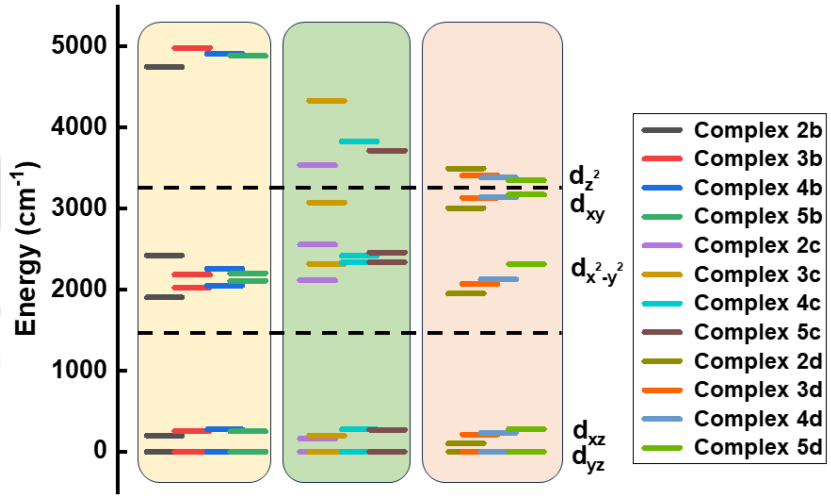

Figure 6.11. NEVPT2 computed ligand field d-orbitals splitting diagram of the investigated halogen derivatives of Type V complexes.

Additionally, the percentage reduction in the B and ζ parameters for Se-analogs is greater than the O-analogs, as shown in Figures D17 and D18 in Appendix-D, due to the increased covalent character. Hence, the combined analysis of the soft Se-donor atoms in the equatorial position and halogens in the axial position significantly changes the electronic structure of the Mn^{2+} ion.

6.4. Conclusions

This work demonstrates the aqueous phase dynamics of two experimentally synthesized and two modeled bis-hydrated Mn^{2+} complexes. The ligands' binding affinity to the metal center varies in the following order: complex 1 > complex 4 > complex 3 > complex 2 > complex 5, establishing complex 1 as the most stable of the examined Mn^{2+} complexes with a rigid piperazine unit in the ligand backbone. The complex with higher binding affinity remains relatively rigid with increasing temperature, exhibiting only minimal changes in the RDFs. In contrast, the RDFs of the complex with weaker binding affinity change more significantly with increasing temperature, thereby demonstrating a decrease in peak sharpness. This will help to predict the dynamics of solvent molecule interactions with the metal complexes, enabling the precise tuning of their structural properties and the development of stable contrast agents. A detailed quantum chemical and ligand field analysis of the physical origin of the ZFS in a series of halogen-containing seven coordinated Mn^{2+} complexes has been carried out. The ZFS parameter D of the halogen analogs under investigation demonstrates a progressive increase in the sequence of Cl < Br < I. This trend is corroborated by the highlighted covalency observed for I-derivatives, coinciding with a reduction in bond order. This reduction is ascribed to the attenuation of both σ and π antibonding interaction between the Mn^{2+} and axial halide ligand. Among the Type I complexes, the D-value is the highest for complex 2, having an electron-donating Me-group. We observed that the D-value increases for Type V complexes by substituting the equatorial O-atoms with the Se-donor atoms. The D-value for the halogen derivatives of Se increases in the order of $D(\mathrm{Cl}) < D(\mathrm{I}) < D(\mathrm{Br})$. This discrepancy results from the interplay between the Mn-Se bond covalency and ligand field strength. Furthermore, the magneto-structural correlation performed on the model complexes suggests that substantial magnetic anisotropy could be achieved by fine-tuning the axial ligands and optimizing the Mn-X bond length ratio. This will provide the chemists with a viable playground for the designing and development of SMMs. The general trend observed using DFT methods for halogens is in line with the *ab initio* results ($D(\mathrm{I}) > D(\mathrm{Br}) > D(\mathrm{Cl})$). Our calculations demonstrate that the occurrence of large SOC due to the presence of heavier halides is not the sole factor in increasing the ZFS of transition metal complexes, as metal-ligand covalency drastically affects the nature of the ZFS parameters. In summary, the interpretation of magnetic parameters utilizing the *ab initio* CASSCF/NEVPT2 method has provided insights into the influence of molecular geometry, ligand field effects, and metal-ligand covalency on the magnitude of ZFS. We believe this study on the stability and the aqueous phase dynamics of bis-hydrated Mn^{2+}

complexes, as well as the magnetic characterization of the complexes with heavy and soft donor atoms shed light on the field of MRI contrast agents and SMMs.

6.5. References

[1] G. H. Reed and W. J. Ray, *Biochemistry*, 1971, **10**, 3190-3197.

[2] B. Drahoš, I. Lukeš and É. Tóth, *Eur. J. Inorg. Chem.*, 2012, **2012**, 1975-1986.

[3] A. Smeraldo, P. A. Netti and E. Torino, *Contrast Media Mol. Imaging*, 2020, **2020**, 1-10.

[4] R. H. Elattar, S. F. El-Malla, A. H. Kamal and F. R. Mansour, *Coord. Chem. Rev.*, 2024, **501**, 215568-215589.

[5] Y. Qin, P. She, X. Huang, W. Huang and Q. Zhao, *Coord. Chem. Rev.*, 2020, **416**, 213331-213349.

[6] R. Cineus, S. M. Abozeid, G. E. Sokolow, J. A. Spernyak and J. R. Morrow, *Inorg. Chem.*, 2023, **62**, 16513-16522.

[7] C. Henoumont, M. Devreux and S. Laurent, *Molecules*, 2023, **28**, 7275-7299.

[8] A. C. Sedgwick, J. T. Brewster, P. Harvey, D. A. Iovan, G. Smith, X.-P. He, H. Tian, J. L. Sessler and T. D. James, *Chem. Soc. Rev.*, 2020, **49**, 2886-2915.

[9] D. Foster and J. Larsen, *ACS Biomater. Sci. Eng.*, 2023, **9**, 1224-1242.

[10] T. Glaser, *Chem Commun*, 2011, **47**, 116-130.

[11] M. Atanasov, P. Comba, S. Hausberg and B. Martin, *Coord. Chem. Rev.*, 2009, **253**, 2306-2314.

[12] M. A. Hay, A. Sarkar, K. E. R. Marriott, C. Wilson, G. Rajaraman and M. Murrie, *Dalton Trans.*, 2019, **48**, 15480-15486.

[13] D. Hao, T. Ai, F. Goerner, X. Hu, V. M. Runge and M. Tweedle, *J. Magn. Reson. Imaging*, 2012, **36**, 1060-1071.

[14] C. Claussen, M. Laniado, E. Kazner, W. Sch□rner and R. Felix, *Neuroradiology*, 1985, **27**, 164-171.

[15] Z. Zhou and Z. Lu, *WIREs Nanomedicine Nanobiotechnology*, 2013, **5**, 1-18.

[16] J. Uhlig, O. Al-Bourini, R. Salgado, M. Francone, R. Vliegenthart, J. Bremerich, J. Lotz and M. Gutberlet, *Radiol. Cardiothorac. Imaging*, 2020, **2**, e200102.

[17] P. Marckmann, L. Skov, K. Rossen, A. Dupont, M. B. Damholt, J. G. Heaf and H. S. Thomsen, *J. Am. Soc. Nephrol.*, 2006, **17**, 2359-2362.

[18] T. Grobner, *Nephrol. Dial. Transplant.*, 2006, **21**, 1104-1108.

[19] L. Blomqvist, G. F. Nordberg, V. M. Nurchi and J. O. Aaseth, *Biomolecules*, 2022, **12**, 742-752.

[20] N. Kostevšek, *Magnetochemistry*, 2020, **6**, 11-21.

[21] C. Comanescu, *Chemistry*, 2022, **4**, 872-930.

[22] R. B. Van Heeswijk, W. R. Bauer, F. Bönner, J. M. Janjic, W. J. M. Mulder, L. M. Schreiber, J. Schwitter and U. Flögel, *Circ. Cardiovasc. Imaging* **2023**, *16*, 014742-014754

[23] J. Chen, G. M. Lanza and S. A. Wickline, *WIREs Nanomedicine Nanobiotechnology*, 2010, **2**, 431-440.

[24] K.-A. Hansen and J. P. Blinco, *Polym. Chem.*, 2018, **9**, 1479-1516.

[25] O. U. Akakuru, M. Z. Iqbal, M. Saeed, C. Liu, T. Paunesku, G. Woloschak, N. S. Hosmane and A. Wu, *Bioconjug. Chem.*, 2019, **30**, 2264-2286.

[26] R. Zheng, J. Guo, X. Cai, L. Bin, C. Lu, A. Singh, M. Trivedi, A. Kumar and J. Liu, *Colloids Surf. B Biointerfaces*, 2022, **213**, 112432-112453.

[27] D. Pan, S. D. Caruthers, A. Senpan, A. H. Schmieder, S. A. Wickline and G. M. Lanza, *WIREs Nanomedicine Nanobiotechnology*, 2011, **3**, 162-173.

[28] M. Botta, F. Carniato, D. Esteban-Gómez, C. Platas-Iglesias and L. Tei, *Future Med. Chem.*, 2019, **11**, 1461-1483.

[29] B. Phukan, C. Mukherjee, U. Goswami, A. Sarmah, S. Mukherjee, S. K. Sahoo and S. Ch. Moi, *Inorg. Chem.*, 2018, **57**, 2631-2638.

[30] K. M. Andruska and B. A. Racette, *Curr. Epidemiol. Rep.*, 2015, **2**, 143-148.

[31] D. P. Perl and C. W. Olanow, *J. Neuropathol. Exp. Neurol.*, 2007, **66**, 675-682.

[32] J. Wahsner, E. M. Gale, A. Rodríguez-Rodríguez and P. Caravan, *Chem. Rev.*, 2019, **119**, 957-1057.

[33] P. Caravan, C. Comuzzi, W. Crooks, T. J. McMurry, G. R. Choppin and S. R. Woulfe, *Inorg. Chem.*, 2001, **40**, 2170-2176.

[34] M. Port, J.-M. Idée, C. Medina, C. Robic, M. Sabatou and C. Corot, *BioMetals*, 2008, **21**, 469-490.

[35] A. D. Sherry and Y. Wu, *Curr. Opin. Chem. Biol.*, 2013, **17**, 167-174.

[36] M. Regueiro-Figueroa and C. Platas-Iglesias, *J. Phys. Chem. A*, 2015, **119**, 6436-6445.

[37] N. Keot and M. Sarma, *RSC Adv.*, 2023, **13**, 1516-1529.

[38] C. Platas-Iglesias, D. Esteban-Gómez, L. Helm and M. Regueiro-Figueroa, *J. Phys. Chem. A*, 2016, **120**, 6467-6476.

[39] R. Uzal-Varela, L. Valencia, D. Lalli, M. Maneiro, D. Esteban-Gómez, C. Platas-Iglesias, M. Botta and A. Rodríguez-Rodríguez, *Inorg. Chem.*, 2021, **60**, 15055-15068.

[40] N. Keot and M. Sarma, *Phys. Chem. Chem. Phys.*, 2023, **25**, 31165-31177.

[41] A. M. Coffey, M. L. Truong and E. Y. Chekmenev, *J. Magn. Reson.*, 2013, **237**, 169-174.

[42] *Proc. R. Soc. Lond. Ser. Math. Phys. Sci.*, 1964, **280**, 271-288.

[43] M. Atanasov, P. Comba, S. Helmle, D. Müller and F. Neese, *Inorg. Chem.*, 2012, **51**, 12324-12335.

[44] A. K. Bar, C. Pichon and J.-P. Sutter, *Coord. Chem. Rev.*, 2016, **308**, 346-380.

[45] S. Tripathi, S. Vaidya, K. U. Ansari, N. Ahmed, E. Rivière, L. Spillecke, C. Koo, R. Klingeler, T. Mallah, G. Rajaraman and M. Shanmugam, *Inorg. Chem.*, 2019, **58**, 9085-9100.

[46] A. Sarkar, S. Dey and G. Rajaraman, *Chem. – Eur. J.*, 2020, **26**, 14036-14058.

[47] P. Comba, G. Rajaraman, A. Sarkar and G. Velmurugan, *Dalton Trans.*, 2022, **51**, 5175-5183.

[48] C. Duboc, *Chem. Soc. Rev.*, 2016, **45**, 5834-5847.

[49] A. Sarkar, S. Tewary, S. Sinkar and G. Rajaraman, *Chem. – Asian J.*, 2019, **14**, 4696-4704.

[50] K. A. Schulte, K. R. Vignesh and K. R. Dunbar, *Chem. Sci.*, 2018, **9**, 9018-9026.

[51] C. Duboc, T. Phoeung, S. Zein, J. Pécaut, M.-N. Collomb and F. Neese, *Inorg. Chem.*, 2007, **46**, 4905-4916.

[52] S. R. Chowdhury and S. Mishra, *Phys. Chem. Chem. Phys.*, 2017, **19**, 16914-16922.

[53] H. I. Karunadasa, K. D. Arquero, L. A. Berben and J. R. Long, *Inorg. Chem.*, 2010, **49**, 4738-4740.

[54] I. Solomon and N. Bloembergen, *J. Chem. Phys.*, 1956, **25**, 261-266.

[55] N. Bloembergen and L. O. Morgan, *J. Chem. Phys.*, 1961, **34**, 842-850.

[56] A. Sauza-de La Vega, R. Pandharkar, G. D. Stroscio, A. Sarkar, D. G. Truhlar and L. Gagliardi, *JACS Au*, 2022, **2**, 2029-2037.

[57] D. S. Kaliakin, J. A. Sobrinho, J. H. S. K. Monteiro, A. De Bettencourt-Dias and D. C. Cantu, *Phys. Chem. Chem. Phys.*, 2021, **23**, 4287-4299.

[58] R. D. O'Brien, T. J. Summers, D. S. Kaliakin and D. C. Cantu, *Phys. Chem. Chem. Phys.*, 2022, **24**, 10263-10271.

[59] J. Wang, R. M. Wolf, J. W. Caldwell, P. A. Kollman and D. A. Case, *J. Comput. Chem.*, 2004, **25**, 1157-1174.

[60] D. Vassetti, M. Pagliai and P. Procacci, *J. Chem. Theory Comput.*, 2019, **15**, 1983-1995.

[61] A. K. Rappe, C. J. Casewit, K. S. Colwell, W. A. Goddard and W. M. Skiff, *J. Am. Chem. Soc.*, 1992, **114**, 10024-10035.

[62] J. Martinelli, E. Callegari, Z. Baranyai, A. Fraccarollo, M. Cossi and L. Tei, *Molecules*, 2021, **26**, 5993-6011.

[63] W. L. Jorgensen, J. Chandrasekhar, J. D. Madura, R. W. Impey and M. L. Klein, *J. Chem. Phys.*, 1983, **79**, 926-935.

[64] P. Mark and L. Nilsson, *J. Phys. Chem. A*, 2001, **105**, 9954-9960.

[65] T. Lu and V. Sobtop, *1.0 (dev3. 1)*, 2022.

[66] D. Van Der Spoel, E. Lindahl, B. Hess, G. Groenhof, A. E. Mark and H. J. C. Berendsen, *J. Comput. Chem.*, 2005, **26**, 1701-1718.

[67] M. J. Abraham, T. Murtola, R. Schulz, S. Páll, J. C. Smith, B. Hess and E. Lindahl, *SoftwareX*, 2015, **1**, 19-25.

[68] A. C. Oliveira, H. A. L. Filipe, J. P. P. Ramalho, A. Salvador, C. F. G. C. Geraldes, M. J. Moreno and L. M. S. Loura, *Inorg. Chem.*, 2022, **61**, 11837-11858.

[69] M. Parrinello and A. Rahman, *J. Appl. Phys.*, 1981, **52**, 7182-7190.

[70] H. J. C. Berendsen, J. P. M. Postma, W. F. Van Gunsteren, A. DiNola and J. R. Haak, *J. Chem. Phys.*, 1984, **81**, 3684-3690.

[71] I.-C. Lin, A. P. Seitsonen, I. Tavernelli and U. Rothlisberger, *J. Chem. Theory Comput.*, 2012, **8**, 3902-3910.

[72] J. VandeVondele and J. Hutter, *J. Chem. Phys.*, 2007, **127**, 114105-114114.

[73] J. Hutter, M. Iannuzzi, F. Schiffmann and J. VandeVondele, *WIREs Comput. Mol. Sci.*, 2014, **4**, 15-25.

[74] M. Walker, A. J. A. Harvey, A. Sen and C. E. H. Dessent, *J. Phys. Chem. A*, 2013, **117**, 12590-12600.

[75] M. J. Frisch, G. W. Trucks, H. B. Schlegel, G. E. Scuseria, M. A. Robb, J. R. Cheeseman, G. Scalmani, V. Barone, G. A. Petersson, H. Nakatsuji, X. Li, M. Caricato, A. V. Marenich, J. Bloino, B. G. Janesko, R. Gomperts, B. Mennucci, H. P. Hratchian, J. V. Ortiz, A. F. Izmaylov, J. L. Sonnenberg, D. Williams-Young, F. Ding, F. Lipparini, F. Egidi, J. Goings, B. Peng, A. Petrone, T. Henderson, D. Ranasinghe, V. G. Zakrzewski, J. Gao, N. Rega, G. Zheng, W. Liang, M. Hada, M. Ehara, K. Toyota, R. Fukuda, J. Hasegawa, M. Ishida, T. Nakajima, Y. Honda, O. Kitao, H. Nakai, T. Vreven, K. Throssell, J. A. Montgomery, J. E. Peralta, F. Ogliaro, M. J. Bearpark, J. J. Heyd, E. N. Brothers, K. N. Kudin, V. N. Staroverov, T. A. Keith, R. Kobayashi, J. Normand, K. Raghavachari, A. P. Rendell, J. C. Burant, S. S. Iyengar, J. Tomasi, M. Cossi, J. M. Millam, M. Klene, C. Adamo, R. Cammi, J. W. Ochterski, R. L. Martin, K. Morokuma, O. Farkas, J. B. Foresman and D. J. Fox, Gaussian 16 Revision C.01, Gaussian Inc., Wallingford CT, 2016.

[76] J. Tomasi, B. Mennucci and R. Cammi, *Chem. Rev.*, 2005, **105**, 2999-3094.

[77] F. Neese, *WIREs Comput. Mol. Sci.*, 2012, **2**, 73-78.

[78] J. W. Park, *J. Chem. Theory Comput.*, 2019, **15**, 5417-5425.

[79] E. V. Lenthe, E. J. Baerends and J. G. Snijders, *J. Chem. Phys.*, 1993, **99**, 4597-4610.

[80] A. Rodríguez-Rodríguez, Á. Arnosa-Prieto, I. Brandariz, D. Esteban-Gómez and C. Platas-Iglesias, *J. Phys. Chem. A*, 2020, **124**, 1362-1371.

[81] C. F. Matta, *The Quantum Theory of Atoms in Molecules: From Solid State to DNA and Drug Design*, John Wiley & Sons, Incorporated, Hoboken, 1st ed., 2007.

[82] T. Lu and F. Chen, *J. Comput. Chem.*, 2012, **33**, 580-592.

[83] S. Zein, C. Duboc, W. Lubitz and F. Neese, *Inorg. Chem.*, 2008, **47**, 134-142.

[84] R. Khurana, S. Gupta and Md. E. Ali, *J. Phys. Chem. A*, 2021, **125**, 2197-2207.

[85] S. Vaidya, S. K. Singh, P. Shukla, K. Ansari, G. Rajaraman and M. Shanmugam, *Chem. – Eur. J.*, 2017, **23**, 9546-9559.

[86] S. K. Singh, M. Atanasov and F. Neese, *J. Chem. Theory Comput.*, 2018, **14**, 4662-4677.

[87] A. Forgács, R. Pujales-Paradela, M. Regueiro-Figueroa, L. Valencia, D. Esteban-Gómez, M. Botta and C. Platas-Iglesias, *Dalton Trans.*, 2017, **46**, 1546-1558.

[88] L. Llanos and D. Aravena, *Inorganics*, 2018, **6**, 24-36.

[89] S. Tripathi, S. Vaidya, N. Ahmed, E. Andreasen Klahn, H. Cao, L. Spillecke, C. Koo, S. Spachmann, R. Klingeler, G. Rajaraman, J. Overgaard and M. Shanmugam, *Cell Rep. Phys. Sci.*, 2021, **2**, 100404-100423.

Chapter 7

Summary and Conclusions

Lanthanides and TMs are important for modern technology, such as permanent magnets, electric car batteries, lasers, phosphors, medical imaging agents, etc. The aim of this thesis was to provide a deeper understanding of the geometric, electronic, and magnetic characterization of a selection of lanthanide and TMs molecular compounds, with a primary focus on Gd^{3+} and Mn^{2+} systems. Using both quantum mechanical and molecular dynamics simulations, this work aims to advance the understanding and design of new families of lanthanide and TMs-based single-molecule magnets (SMMs) and MRI contrast agents.

Chapter 3 explores the thermodynamic stability and water exchange kinetics of hexadentate and heptadentate Ln^{3+}-based complexes using DFT. Comparative studies revealed that the hexadentate ligand $cbda^{3-}$ forms a more stable complex than $dpaa^{3-}$, and among heptadentate ligands, $peada^{4-}$ shows enhanced selectivity toward Gd^{3+} due to the higher number of carboxylate groups. Structural analyses of bis- and tris-aquated complexes showed distinct hydration behaviors, with $[Gd(cbda)(H_2O)_3]\cdot 6H_2O$ exhibiting a stable tris-aquated form, while $[Gd(peada)(H_2O)_2]^-.4H_2O$ displayed a hydration equilibrium. The study revealed that k_{ex}^{298} are strongly influenced by ligand structure, Ln-O(w) bond strength, electron density, and ELF values. A dissociative mechanism was predominant, and one coordinated water in the bis-aquated complex displayed an unusually high k_{ex}^{298} value (750×10^6 S^{-1}), attributed to flexible ligand geometry and hydration equilibrium. Energy decomposition (EDA) analysis indicated that electrostatic contributions increased with ligand charge and decreased across the lanthanide series due to lanthanide contraction.

Chapter 4 examined the aqueous-phase dynamics and solution structures of $[Ln(DOTA)]^-$ and its derivatives $[Ln(HMDOTA\text{-}SS)]^-$ and $[Ln(T)]^-$ using DFT-based AIMD simulations. These simulations showed minimal changes in RDFs with increasing temperature for DOTA and its derivatives, indicating high aqueous stability. The RDF peaks became sharper and shifted leftward from La^{3+} to Lu^{3+}, reflecting lanthanide contraction. Ligand binding affinities and thermodynamic stabilities followed the order: $[Ln(HMDOTA\text{-}SS)]^- > [Ln(T)]^- > [Ln(DOTA)]^-$. The presence of bulky, hydrophilic groups in the modified DOTA derivatives facilitated faster water exchange rates in the 9th coordination site. TSAP geometries exhibited consistently

higher k_{ex}^{298} values than SAP geometries, attributed to increased steric compression and elongated Ln-O(water) bonds. These findings support the rational design of Gd^{3+}-based MRI CAs with enhanced relaxivity and stability, which reduces toxicity.

Chapter 5 is devoted to Mn^{2+}-based complexes and their magnetic anisotropy properties. Several seven-coordinate Mn^{2+} model complexes were investigated to evaluate the influence of ligand environment on ZFS parameters. The ligand $dpasam^{3-}$ exhibited the strongest binding affinity and the lowest D-value due to significant distortion from the ideal pentagonal bipyramidal geometry. A clear trend in D-values was observed across complexes: $[Mn(dpasam)(H_2O)]^-$ < $[Mn(dpaaa)(H_2O)]^-$ < $[Mn(cbda)(H_2O)]^-$ < $[Mn(pydpa)(H_2O)]$. The splitting patterns of the Kramers doublets were consistent with the computed D-values, providing further validation of the magnetic anisotropy trends observed across the complexes. Additionally, shortening the Mn-O(water) axial bond increased D-values, indicating the importance of axial ligand field strength. NEVPT2 analysis showed that low-lying excited states contributed significantly to the ZFS values, validating the use of *ab initio* methods for reliable magnetic predictions.

Chapter 6 extended the magnetic analysis to Mn^{2+} complexes bearing halogen and soft donor atoms. AIMD simulations of bis-hydrated Mn^{2+} complexes confirmed dynamic hydration behavior and stability trends, where rigid complexes showed minimal RDF changes with temperature. Ligand binding affinity analysis observed $[Mn(pmpa)(H_2O)_2]$ complex (with a piperazine unit) as the most stable complex among the series, indicating strong thermodynamic stability imparted by the ligand framework. A detailed ligand field and *ab initio* analysis of halogen-substituted complexes revealed that D-values increased in the order Cl < Br < I, due to increasing covalency and reduced antibonding interactions in Mn-X bonds. Additionally, Se-substituted analogs showed increased D-values, particularly for equatorial substitutions. Notably, the D-value trend for halogenated Se-donors (Cl < I < Br) highlighted the intricate balance between covalency and ligand field strength. The magneto-structural correlation underscored the potential of fine-tuning axial ligands and Mn-X bond lengths for maximizing magnetic anisotropy.

The studies presented in this thesis provide critical insights into the structure-property relationships governing the behavior of lanthanide and TM complexes in aqueous environments. This work not only aids in the development of next-generation MRI CAs with improved safety and performance but also advances the design principles of SMMs with

enhanced anisotropy. The insights gained will serve as a valuable guide for experimental chemists working toward the synthesis of high-performance lanthanide and TM-based functional materials. Moreover, the thorough understanding of the electronic structures and coordination environment developed in this work can be applied to fine-tune the emission properties and energy transfer pathways of lanthanide complexes, thereby supporting the design of highly efficient luminescent probes and advanced optoelectronic materials.

Since this thesis focuses on the three key relaxivity parameters, the effect of increasing the number of inner-sphere water molecules, the water exchange kinetics (k_{ex}^{298}), and the electronic relaxation of the complexes, we have deliberately limited the scope to these aspects. In the future, we plan to investigate the interactions of these metal complexes with human serum albumin (HSA) protein using classical molecular dynamics simulations. This interactions are expected to increase the rotational correlation time by restricting the rotation of the complexes. An increase in the rotational correlation time can, in turn, significantly improve the water exchange rate (k_{ex}^{298}) and other relaxivity parameters. Also, these computational frameworks can be extended to machine-learning-assisted screening of ligands that could accelerate the discovery of efficient CAs and magnetic materials by predicting stability, exchange kinetics, and anisotropy with low computational cost.

Key findings

1

Identification of ligand features that enhance thermodynamic stability and selective coordination with Ln^{3+} and Mn^{2+} ions.

2

Mechanistic understanding of water exchange kinetics and factors influencing the k_{ex}^{298} values.

3

Quantitative evolution of magnetic anisotropy in Mn^{2+} complexes, establishing a link between ligand field effect, metal-ligand covalency, and ZFS.

Appendix-A

Table A1. Binding energy values ($\triangle E_{total} = E_{complex} - E_{ligand} - E_{Gd(III)}$) and relative binding energy ($\triangle E_{rel}$) values (in kcal mol^{-1}) of the chosen complexes were calculated using TPSSh/6- 31G(d,p)/SCRECP level of theory.

Methods	Complex	$\triangle E_{total}$ (BSSE corrected)	$\triangle E_{rel}$
TPSSh/6-31G(d,p)/SCRECP	Gd(III)-peada	-197.13	0.00
	Gd(III)-tpaa	-165.73	+31.40
	Gd(III)-cbda	-166.42	0.00
	Gd(III)-dpaa	-165.06	+1.36

Table A2. Binding energy values ($\triangle E_{total} = E_{complex} - E_{ligand} - E_{Gd(III)}$) and relative binding energy ($\triangle E_{rel}$) values (in kcal mol^{-1}) of the chosen complexes using different density functionals and basis sets with LCRECP level of theory.

Methods	Complex	$\triangle E_{total}$ (BSSE corrected)	$\triangle E_{rel}$
TPSSh/6-31G(d,p)	Gd(III)-peada	-157.86	0.00
	Gd(III)-tpaa	-127.51	+30.35
	Gd(III)-cbda	-129.26	0.00
	Gd(III)-dpaa	-127.76	+1.50
TPSSh/def2-TZVP(single point energy)	Gd(III)-peada	-126.79	0.00
	Gd(III)-tpaa	-101.32	+25.47
	Gd(III)-cbda	-100.25	0.00
	Gd(III)-dpaa	-98.53	+1.72
B3LYP-D3/6-31G(d,p)	Gd(III)-peada	-162.74	0.00
	Gd(III)-tpaa	-138.78	+23.96
	Gd(III)-cbda	-140.69	0.00
	Gd(III)-dpaa	-139.29	+1.40
ωB97XD/6-31G(d,p)	Gd(III)-peada	-159.45	0.00

	Gd(III)-tpaa	-132.04	+27.41
	Gd(III)-cbda	-134.87	0.00
	Gd(III)-dpaa	-133.28	+1.59

Table A3. Thermodynamic parameters (kcal mol^{-1}) obtained with different density functionals and basis sets for [Gd(cbda)] and [Gd(dpaa)] complexes.

Methods	$\triangle G^{a}_{(g)}$	$\triangle G^{a}_{(sol)}$ [Gd(cbda)]	$\triangle G^{b}_{(sol)}$ [Gd(dpaa)]	$\triangle G^{c}_{(aq)}$ (calcd)	$\triangle G^{d}_{(aq)}$ (exp)
TPSSh/6-31G(d,p)/LCRECP	-3.72	-83.54	-85.45	-1.08	-5.48
TPSSh/6-31+G(d,p)/LCRECP	-4.60	-93.34	-94.13	-7.60	-5.48
TPSSh/6-31G(d,p)/SCRECP	-3.83	-69.72	-70.97	-1.88	-5.48
B3LYP-D3/6-31G(d,p)/LCRECP	-3.50	-85.45	-87.89	-0.43	-5.48
M06/6-31G(d,p)/LCRECP	-3.76	-88.48	-90.99	-1.25	-5.48
ωB97XD/6-31G(d,p)/LCRECP	-4.4	-90.75	-92.51	-11.47	-5.48

Table A4. Thermodynamic parameters (kcal mol^{-1}) obtained with different density functionals and basis sets for $[Gd(peada)]^{-}$ and [Gd(tpaa)] complexes.

Methods	$\triangle G^{a}_{(g)}$	$\triangle G^{a}_{(sol)}$ $[Gd(peada)]^{-}$	$\triangle G^{b}_{(sol)}$ [Gd(tpaa)]	$\triangle G^{e}_{(aq)}$ (calcd)	$\triangle G^{d}_{(aq)}$ (exp)
TPSSh/6-31G(d,p)/LCRECP	-222.29	-99.37	-76.51	-11.52	-9.24
TPSSh/6-31+G(d,p)/LCRECP	-218.44	-107.97	-85.96	-6.26	-9.24
TPSSh/6-31G(d,p)/SCRECP	-219.55	-89.19	-65.03	-10.09	-9.24
B3LYP-D3/6-31G(d,p)/LCRECP	-227.79	-100.72	-79.86	-15.95	-9.24
M06/6-31G(d,p)/LCRECP	-226.49	-102.96	-79.33	-18.49	-9.24
ωB97XD/6-31G(d,p)/LCRECP	-226.59	-104.63	-82.83	-12.84	-9.24

$\triangle G^{a}_{(g)}$= Change in Gibbs free energy value in gas phase along with BSSE correction using counterpoise method.

$\triangle G^{a}_{(sol)}$= Calculated in the solvent phase with the structure optimized in the gas phase.

$\triangle G^{c}_{(aq)} = \triangle G_{(g)} + \triangle G_{(sol)}[Gd(cbda)] + \triangle G_{(sol)}[dpaa^{3-}] - \triangle G_{(sol)}[cbda^{3-}] - \triangle G_{(sol)}[Gd(dpaa)]$

$\triangle G^{e}_{(aq)} = \triangle G_{(g)} + \triangle G_{(sol)}[Gd(peada)]^{-} + \triangle G_{(sol)}[tpaa^{3-}] - \triangle G_{(sol)}[peada^{4-}] - \triangle G_{(sol)}[Gd(tpaa)]$

$\triangle G^{d}_{(aq)}(exp)$= -RTlnK, where K is the equilibrium constant.

Table A5. Bond length values of the $[Gd(cbda)(H_2O)_3].6H_2O$, $[Gd(peada)(H_2O)_2]^{-}.4H_2O$ complex using SCRECP with 6-31G(d,p) for H, C, N, O, and TPSSh level of theory.

Complex	Gd-O36(w)	Gd-O39(w)	Gd-O47(w)	Gd-N1	Gd-N9	Gd-N15	Gd-O12	Gd-O14	Gd-O7
Gd-cbda	2.46	2.44	2.37	2.80	2.65	2.63	2.42	2.48	2.30
	Gd-O40(w)	Gd-O43(w)	Gd-N1	Gd-N2	Gd-N23	Gd-O11	Gd-O12	Gd-O17	Gd-O29
Gd-peada	2.62	2.51	2.66	2.67	2.54	2.31	2.30	2.34	2.41

Table A6. Bond length values of the complex $[Gd(cbda)(H_2O)_3].6H_2O$ and $[Ln(peada)(H_2O)_2]^{-}.4H_2O$ using LCRECP with different density functionals and basis sets.

Complex	Method	Gd-O36(w)	Gd-O39(w)	Gd-O47(w	Gd-N1	Gd-N9	Gd-N15	Gd-O12	Gd-O14	Gd-O7
Gd-cbda	TPSSh/6-31G(d,p)	2.53	2.46	2.42	2.87	2.71	2.69	2.50	2.52	2.35
	B3LYP-D3/6-31G(d,p)	2.50	2.49	2.41	2.90	2.70	2.71	2.47	2.52	2.37
	ωB97XD/6-31G(d,p)	2.51	2.49	2.42	2.87	2.69	2.69	2.47	2.52	2.36
Complex	Method	Gd-O40(w)	Gd-O43(w)	Gd-N1	Gd-N2	Gd-N23	Gd-O11	Gd-O12	Gd-O17	Gd-O29

Gd-peada	TPSSh/6-31G(d,p)	2.63	2.54	2.73	2.75	2.60	2.40	2.37	2.39	2.45
	B3LYP-D3/6-31G(d,p)	2.59	2.53	2.75	2.76	2.61	2.40	2.39	2.40	2.44
	ωB97XD/6-31G(d,p)	2.60	2.54	2.74	2.76	2.60	2.40	2.38	2.39	2.44

Table A7. Electron density (ρ_{BCP}), electron localization function (ELF), and Laplacian of electron density (∇_ρ^2) at the Ln-O(w) bond critical points calculated for the [Ln(cbda)(H_2O)$_3$]·6H_2O system (Ln = La-Lu) at the TPSSh/SCRECP/6-31G(d,p) theoretical level.

Metal	ρ_{BCP}			ELF			∇_ρ^2		
	Ln-O36(w)	Ln-O39(w)	Ln-O47(w)	Ln-O36(w)	Ln-O39(w)	Ln-O47(w)	Ln-O36(w)	Ln-O39(w)	Ln-O47(w)
La	0.0404	0.0422	0.0482	0.1228	0.1295	0.1371	0.1511	0.1563	0.1888
Gd	0.0434	0.0453	0.0521	0.1010	0.1041	0.1080	0.1948	0.2048	0.2641
Lu	0.0439	0.0457	0.0511	0.0810	0.0901	0.0956	0.2074	0.2239	0.2730

Table A8. Electron density (ρ_{BCP}), electron localization function (ELF), and Laplacian of electron density (∇_ρ^2) at the Ln-O(w) bond critical points calculated for the [Ln(peada)(H_2O)$_2$]$^-$·4H_2O system (Ln = La-Lu) at the TPSSh/SCRECP/6-31G(d,p) theoretical level.

Metal	ρ_{BCP}		ELF		∇_ρ^2	
	Ln-O40(w)	Ln-O43(w)	Ln-O40(w)	Ln-O43(w)	Ln-O40(w)	Ln-O43(w)
La	0.0302	0.0361	0.1077	0.1175	0.1071	0.1363
Gd	0.0360	0.0389	0.0960	0.0999	0.1229	0.1687
Lu	0.0271	0.0363	0.0621	0.0750	0.1153	0.1754

Table A9. Calculated Gd-O(w) bond length, electron density (ρ_{BCP}, au), electron localization function (ELF), and k_{ex}^{298} value of $[Gd(cbda)(H_2O)_3]\cdot 6H_2O$ complex using LCRECP and different density functionals and basis sets

Method	Ln-O(w) bond length	ρ_{BCP}	ELF	$k_{ex}^{298}/10^6$ (S^{-1})
TPSSh/6-31G(d,p)	Gd-O36(w)=2.53	0.0375	0.0968	43.68
	Gd-O39(w)=2.46	0.0410	0.1006	4.2
	Gd-O47(w)=2.42	0.0429	0.1003	4.6
TPSSh/6-31+G(d,p)	Gd-O36(w)=2.56	0.0342	0.0939	118.9
	Gd-O39(w)=2.49	0.0376	0.1009	6.9
	Gd-O47(w)=2.45	0.0393	0.1012	3.51
B3LYP-D3/6-31G(d,p)	Gd-O36(w)=2.50	0.0378	0.0978	17.8
	Gd-O39(w)=2.49	0.0418	0.1099	0.25
	Gd-O47(w)=2.41	0.0450	0.1094	0.08
ωB97XD/6-31G(d,p)	Gd-O36(w)=2.51	0.0357	0.0921	173.92
	Gd-O39(w)=2.49	0.0364	0.0927	133.51
	Gd-O47(w)=2.42	0.0433	0.1025	1.6

Table A10. Calculated Gd-O(w) bond length, electron density (ρ_{BCP}, au), electron localization function (ELF), and k_{ex}^{298} value of $[Gd(peada)(H_2O)_2]^{-}\cdot 4H_2O$ complex using LCRECP and different density functionals and basis sets.

Method	Ln-O(w) bond length	ρ_{BCP}	ELF	$k_{ex}^{298}/10^6$ (S^{-1})
TPSSh/6-31G(d,p)	Gd-O40(w)=2.63	0.0342	0.0940	118.9
	Gd-O43(w)=2.54	0.0364	0.0989	16.61
TPSSh/6-31+G(d,p)	Gd-O40(w)=2.71	0.0310	0.0926	522.75

	Gd-O43(w)=2.58	0.0350	0.0976	20.48
B3LYP-D3/6-31G(d,p)	Gd-O40(w)=2.59	0.0350	0.0959	56.6
	Gd-O43(w)=2.53	0.0398	0.1006	4.7
ωB97XD/6-31G(d,p)	Gd-O40(w)=2.60	0.0339	0.0976	75.5
	Gd-O43(w)=2.54	0.0411	0.0986	10.23

Table A11. Activation energy values of $[Gd(cbda)(H_2O)_3].6H_2O$ and $[Gd(peada)(H_2O)_2]^-.4H_2O$ complexes calculated using SCRECP/TPSSh/6-31G(d,p) theoretical level.

	$[Gd(cbda)(H_2O)_3].6H_2O$			$[Gd(peada)(H_2O)_2]^-.4H_2O$	
Activation Parameters	Gd-O36(w)	Gd-O39(w)	Gd-O47(w)	Gd-O40(w)	Gd-O43(w)
$\triangle E^{\ddagger}$(kcal/mol)	5.33	7.02	10.29	-0.63	5.2
$r_{Gd\text{-}O}$/Å	2.46	2.43	2.36	2.62	2.50
$r_{Gd\text{-}O}$(TS)/Å	3.42	3.34	3.50	2.98	3.54
$\triangle H^{\ddagger}$ (kcal/mol)	4.7	6.27	9.78	-0.78	4.26
$\triangle G^{\ddagger}$ (kcal/mol)	4.26	5.31	9.16	1.08	3.25
$\triangle S^{\ddagger}$ (J/mol/K)	4.19	13.51	8.78	-26.10	13.80

Table A12. Bonding behaviour of the $[Gd(cbda)(H_2O)_3].6H_2O$ and $[Gd(peada)(H_2O)_2]^-.4H_2O$ complexes from ETS analysis (in kJ/mol).

Metal	Ligand	$\triangle E_{int}$	$\triangle E_{pauli}$	$\triangle E_{oi}$	$\triangle V_{elst}$	$(a)_{\%elst}$
La	cbda+H_2O	-5202.50	811.51	-1765.70	-4248.31	70.64
	Peada+H_2O	-5954.71	732.18	-1733.36	-4953.53	74.07
Lu	cbda+H_2O	-5618.75	601.31	-1925.46	-4294.60	69.04

	Peada+H_2O	-6479.69	711.38	-2029.73	-5161.34	71.77

$(a)_{\%elst} = \triangle V_{elst}/(\triangle V_{elst} + \triangle E_{oi})$

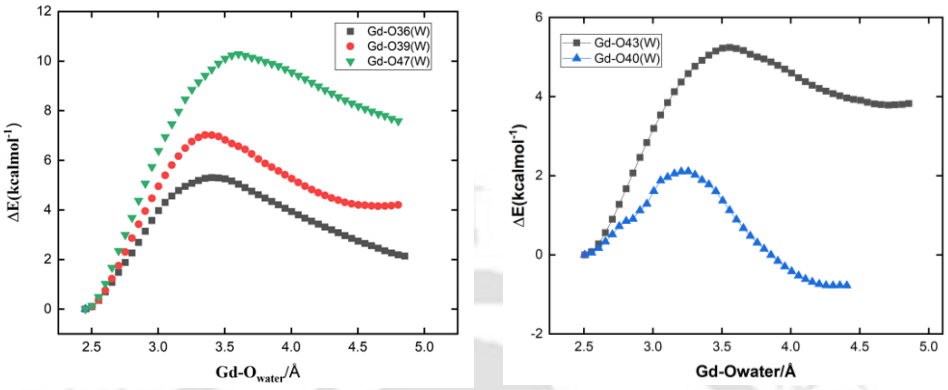

Figure A1. Relaxed potential energy surface scans of the tris-aquated $[Gd(cbda)(H_2O)_3].6H_2O$ and bis-aquated $[Gd(peada)(H_2O)_2]^-.4H_2O$ complex calculated using SCRECP/TPSSh/6-31G(d,p) method.

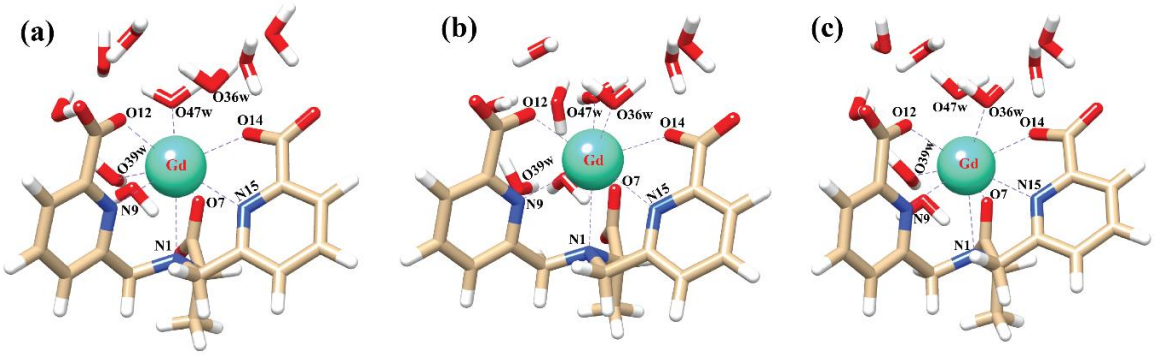

Figure A2. Structure of the transition states (TSs) for the three water molecules of [Gd(cbda)(H2O)3].6H2O using LCRECP; (a) TS of Gd-O36(w), (b)TS of Gd-O39(w), and (c) TS of Gd-O47(w).

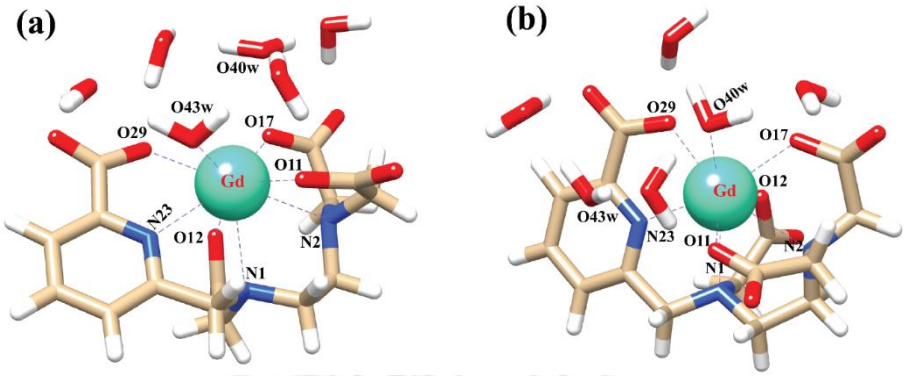

Figure A3: Structure of the transition states (TSs) for the two water molecules of $[Gd(peada)(H_2O)_2]^-.4H_2O$ complex using LCRECP; a) TS of Gd-O40(w) and b)TS of GdO43(w).

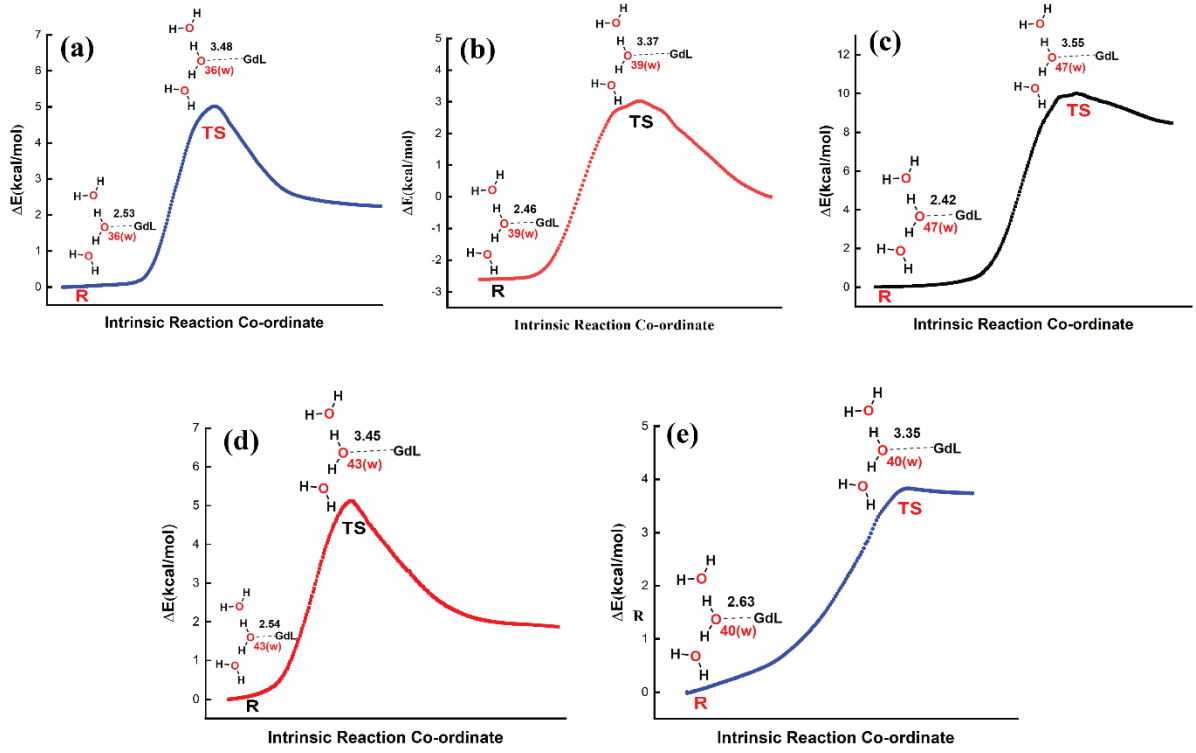

Figure A4. IRC plot for the dissociation of a) Gd-O36(w), b) Gd-O39(w), c) Gd-O47(w), bond of the $[Gd(cbda)(H_2O)_3].6H_2O$ complex (top) and d) Gd-O40(w), e) Gd-O43(w) bond for $[Gd(peada)(H_2O)_2]^-.4H_2O$ (bottom) complexes respectively using LCRECP/TPSSh/6-31G(d,p) level of theory.

Appendix-B

Table B1. Binding energy values and relative binding energy ($\triangle E_{REL}$) values (in kcal mol^{-1}) of the chosen complexes at 25°C using TPSSh/DKH2-SARC/6-311G(d,p) method.

Complexes	$\triangle E_{total}$	ΔE_{REL}
TSAP isomer		
$[La(DOTA)]^-$	-1189.39	0.77
$[La(HMDOTA\text{-}SS)]^-$	-1400.87	0.91
$[La(T)]^-$	-1550.60	1.00
$[Gd(DOTA)]^-$	-1258.05	0.78
$[Gd(HMDOTA\text{-}SS)]^-$	-1474.35	0.91
$[Gd(T)]^-$	-1622.83	1.00
$[Lu(DOTA)]^-$	-1278.13	0.78
$[Lu(HMDOTA\text{-}SS)]^-$	-1501.96	0.92
$[Lu(T)]^-$	-1644.79	1.00
SAP		
$[La(DOTA)]^-$	-1185.70	0.77
$[La(HMDOTA\text{-}SS)]^-$	-1400.24	0.91
$[La(T)]^-$	-1547.46	1.00
$[Gd(DOTA)]^-$	-1263.70	0.78
$[Gd(HMDOTA\text{-}SS)]^-$	-1473.85	0.91
$[Gd(T)]^-$	-1624.71	1.00
$[Lu(DOTA)]^-$	-1289.42	0.78
$[Lu(HMDOTA\text{-}SS)]^-$	-1495.06	0.91
$[Lu(T)]^-$	-1652.95	1.00

Table B2. Bond length values of the studied complexes optimized using TPSSh/6-LCRECP/311G(d,p) level of theory with two explicit water molecules.

Complex	Ln-O	Ln-Ow	Ln-N	Isomer	Exp(Ln-O)	Exp(Ln-Ow)	Exp(Ln-N)
$[La(DOTA)(H_2O)]^-.2H_2O$	2.528	2.610	2.795	TSAP	2.492	2.537	2.769
$[La(DOTA)(H_2O)]^-.2H_2O$	2.512	2.601	2.792	SAP			
$[Gd(DOTA)(H_2O)]^-.2H_2O$	2.407	2.521	2.730	TSAP			
$[Gd(DOTA)(H_2O)]^-.2H_2O$	2.397	2.492	2.708	SAP	2.365	2.456	2.655
$[Lu(DOTA)(H_2O)]^-.2H_2O$	2.317	2.477	2.672	TSAP			
$[Lu(DOTA)(H_2O)]^-.2H_2O$	2.301	2.455	2.656	SAP	2.279	2.417	2.614
$[La(HMDOTA\text{-}SS)(H_2O)]^-.2H_2O$	2.513	2.634	2.795	TSAP			
$[La(HMDOTA\text{-}SS)(H_2O)]^-.2H_2O$	2.510	2.630	2.789	SAP			
$[Gd(HMDOTA\text{-}SS)(H_2O)]^-.2H_2O$	2.391	2.547	2.720	TSAP			

[Gd(HMDOTA-SS)(H_2O)]$^-$.2H_2O	2.379	2.542	2.705	SAP			
[Lu(HMDOTA-SS)(H_2O)]$^-$.2H_2O	2.302	2.502	2.688	TSAP			
[Lu(HMDOTA-SS)(H_2O)]$^-$.2H_2O	2.294	2.450	2.671	SAP			
[La(T)(H_2O)]$^-$.2H_2O	2.503	2.641	2.825	TSAP			
[La(T)(H_2O)]$^-$.2H_2O	2.511	2.623	2.805	SAP			
[Gd(T)(H_2O)]$^-$.2H_2O	2.386	2.551	2.746	TSAP			
[Gd(T)(H_2O)]$^-$.2H_2O	2.381	2.510	2.718	SAP			
[Lu(T)(H_2O)]$^-$.2H_2O	2.294	2.522	2.705	TSAP			
[Lu(T)(H_2O)]$^-$.2H_2O	2.292	2.491	2.684	SAP			

Table B3. Thermodynamic parameters (kcal mol^{-1}, Scheme 4.1) obtained with different density functionals and basis sets for TSAP and SAP isomers of [Gd(DOTA)]$^-$ and [Gd(HMDOTA-SS)]$^-$ complexes.

Methods	$\triangle G^{a}_{(g)}$	$\triangle G^{a}_{(sol)}$ **[Gd(HMDOTA-SS)]$^-$**	$\triangle G^{b}_{(sol)}$ **[Gd(DOTA)]$^-$**	$\triangle G^{c(calculated))}_{(aq)}$
TSAP				
TPSSh/6-311G(d,p)	-4.17	-119.19	-118.02	-10.42
ωB97XD/def2-TZVPP	-2.34	-118.54	-117.48	-7.11
SAP				
TPSSh/6-311G(d,p)	-1.73	-121.11	-119.24	-8.68
ωB97XD/def2-TZVPP	-3.85	-119.79	-116.08	-11.97

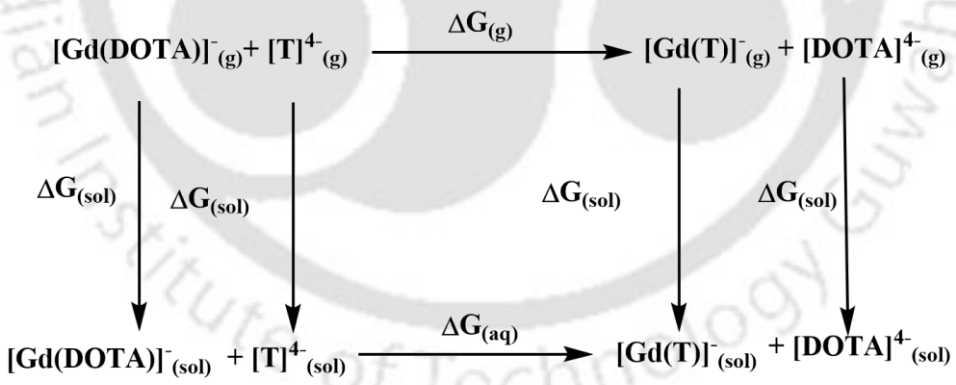

Scheme B1. Thermodynamic cycle for explaining the relative stabilities of [Gd(T)]$^-$ and [Gd(DOTA)]$^-$ complexes.

Table B4. Thermodynamic parameters (kcal mol^{-1}, Scheme B1) obtained with different density functionals and basis sets, TSAP and SAP isomers of [Gd(DOTA)]$^-$ and [Gd(T)]$^-$ complexes.

Methods	$\triangle G^{a}_{(g)}$	$\triangle G^{a}_{(sol)}$ **[Gd(T)]$^-$**	$\triangle G^{b}_{(sol)}$ **[Gd(DOTA)]$^-$**	$\triangle G^{d(calculated))}_{(aq)}$	$\triangle G^{e(exp)}_{(aq)}$
TSAP					
TPSSh/6-311G(d,p)	-3.93	-123.57	-118.02	-9.86	
ωB97XD/def2-TZVPP	-5.05	-119.07	-117.48	-5.58	
SAP					
TPSSh/6-311G(d,p)	-4.27	-121.07	-119.24	-6.47	-6.02
ωB97XD/def2-TZVPP	-3.52	-118.87	-116.08	-5.24	-6.02

$\triangle G^{a}_{(g)}$= Change in Gibbs free energy value in gas phase along with BSSE correction using counterpoise method.

$\triangle G^{a}_{(sol)}$= Calculated in the solvent phase with the structure optimized in the gas phase.

$\triangle G^{c(calculated))}_{(aq)} = \triangle G_{(g)} + \triangle G_{(sol)}[Gd(HMDOTA\text{-}SS)]^- + \triangle G_{(sol)}[(DOTA^{4-})] - \triangle G_{(sol)}[Gd(DOTA)]^- - \triangle G_{(sol)}[(HMDOTA\text{-}SS^{4-})]$

$\triangle G^{d(calculated))}_{(aq)} = \triangle G_{(g)} + \triangle G_{(sol)}[Gd(T)]^- + \triangle G_{(sol)}[(DOTA^{4-})] - \triangle G_{(sol)}[Gd(DOTA)]^- - \triangle G_{(sol)}[(T^{4-})]$

$\triangle G^{e(exp)}_{(aq)}$=-RTlnK, where K is the equilibrium constant. The values of the stability constant ($\log K_{GdL}$) were mentioned in earlier literature.[1]

Table B5. Activation parameters values for [Gd(DOTA)(H_2O)]$^-$.2H_2O, [Gd(HMDOTA-SS)(H_2O)]$^-$. 2H_2O, and [Gd(T)(H_2O)]$^-$.2H_2O complexes using TPSSh/LCRECP/6-311G(d,p) level of theory.

Complexes	$r_{Gd\text{-}O(w)}$/Å	△H‡ (kcalmol^{-1})	△G‡ (kcalmol^{-1})	△E‡ (kcalmol^{-1})	△S‡ (kcalmol^{-1})	A_0/ħ
[Gd(DOTA)(H_2O)]$^-$.2H_2O	3.44	4.37	4.34	4.99	0.33	4.09
[Gd(HMDOTA-SS)(H_2O)]$^-$. 2H_2O	3.42	3.46	2.25	4.21	17.01	3.82
[Gd(T)(H_2O)]$^-$.2H_2O	3.46	3.12	2.87	3.94	3.37	3.71
[Gd(DOTA)(H_2O)]$^-$.2H_2O	3.33	5.54	4.72	6.18	11.58	5.40
[Gd(HMDOTA-SS)(H_2O)]$^-$. 2H_2O	3.41	3.77	2.83	4.55	13.24	4.34
[Gd(T)(H_2O)]$^-$.2H_2O	3.42	4.51	4.12	5.36	5.49	4.61

Table B6. ZFS Parameters of Gd^{3+} complexes calculated using DFT and *ab initio* multireference methods, along with their available experimental values,[2,3] in brackets.

Complex	Isomer	Method	D (cm^{-1})	E/D	$\triangle$ (cm^{-1})	$\triangle^2(S^{-2})/10^{19}$
$[Gd(DOTA)(H_2O)]^{-}.2H_2O$	TSAP	CASSCF/ NEVPT2	0.014	0.331	0.013	0.563
		TPSSh	-0.199	0.025	0.163	94.301
$[Gd(DOTA)(H_2O)]^{-}.2H_2O$	SAP	CASSCF/ NEVPT2	0.039 (Exp= -0.019)	0.254	0.033	3.855
		TPSSh	-0.212	0.045	0.174	106.985
$[Gd(HMDOTA\text{-}SS)(H_2O)]^{-}.2H_2O$	TSAP	CASSCF/ NEVPT2	-0.011	0.297	0.010	0.358
		TPSSh	-0.235	0.052	0.192	131.052
$[Gd(HMDOTA\text{-}SS)(H_2O)]^{-}.2H_2O$	SAP	CASSCF/N EVPT2	0.038	0.255	0.034	3.956
		TPSSh	-0.252	0.024	0.206	150.617
$[Gd(T)(H_2O)]^{-}.2H_2O$	TSAP	CASSCF/N EVPT2	-0.010	0.152	0.009	0.287
		TPSSh	-0.243	0.004	0.199	140.050
$[Gd(T)(H_2O)]^{-}.2H_2O$	SAP	CASSCF/N EVPT2	0.029	0.091	0.024	2.029
		TPSSh	-0.223	0.048	0.182	117.824

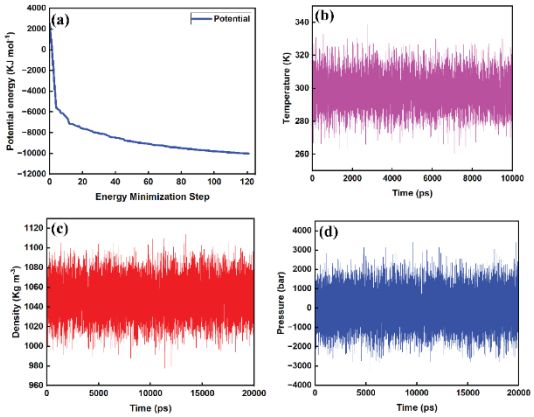

Figure B1. Classical MD simulation results for the TSAP isomer of $[Gd(DOTA)]^{-1}$ showing: (a) energy minimization, (b) temperature evolution, (c) density evolution, and (d) pressure evolution over time.

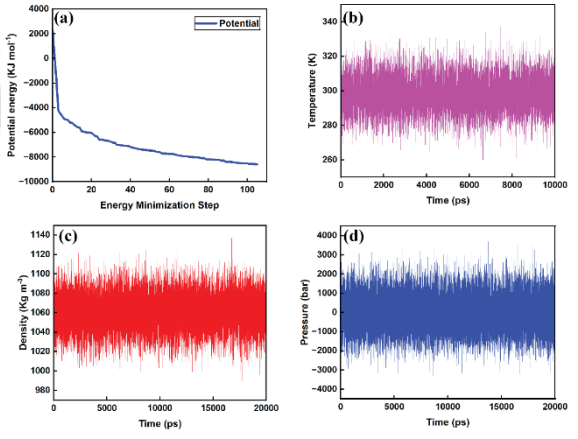

Figure B2. Classical MD simulation results for the TSAP isomer of $[Gd(HMDOTA\text{-}SS)]^{-1}$ showing: (a) energy minimization, (b) temperature evolution, (c) density evolution, and (d) pressure evolution over time.

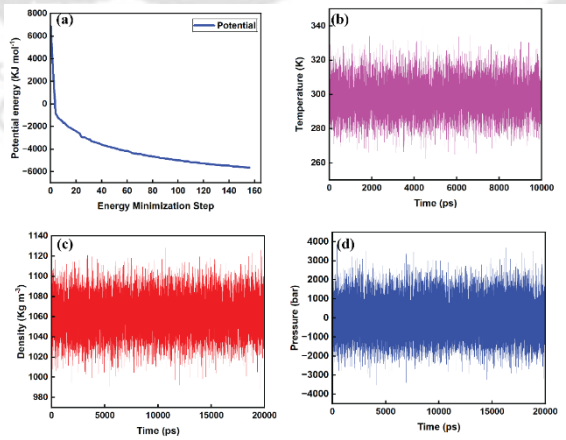

Figure B3. Classical MD simulation results for the TSAP isomer of $[Gd(T)]^{-1}$ showing: (a) energy minimization, (b) temperature evolution, (c) density evolution, and (d) pressure evolution over time.

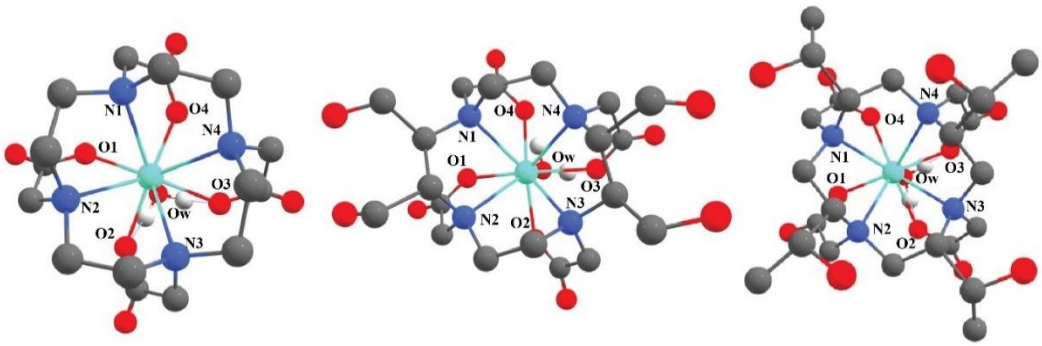

Figure B4. The optimized structures of the SAP geometry of the (a) $[Gd(DOTA)(H_2O)]^-$, (b) $[Gd(HMDOTA\text{-}SS)(H_2O)]^-$, and (c) $[Gd(T)(H_2O)]^-$ complexes using PBE/DZVP method with GTH pseudopotentials.

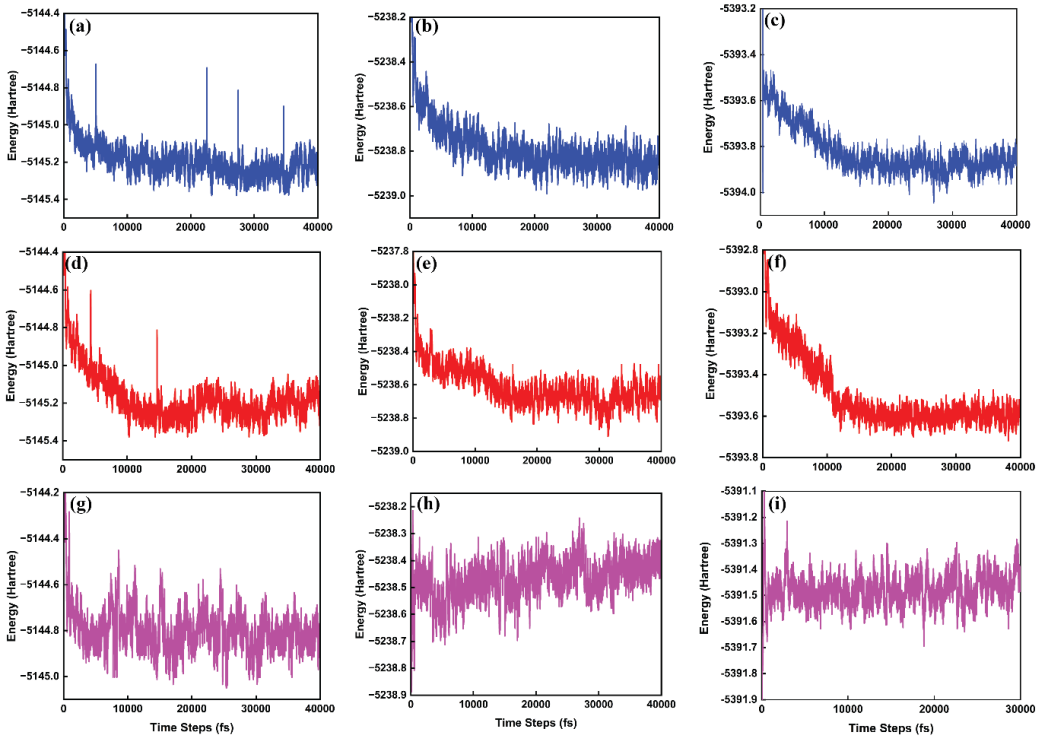

Figure B5. Potential energy plot of $[Ln(DOTA)]^-$ complexes at 25˚C (a, b, c), 45˚C (d, e, f), and 65˚C (g, h, i) for TSAP geometry. From La^{3+} (a, d, g), Gd^{3+} (b, e, h), and Lu^{3+} (c, f, i) complexes from left to right.

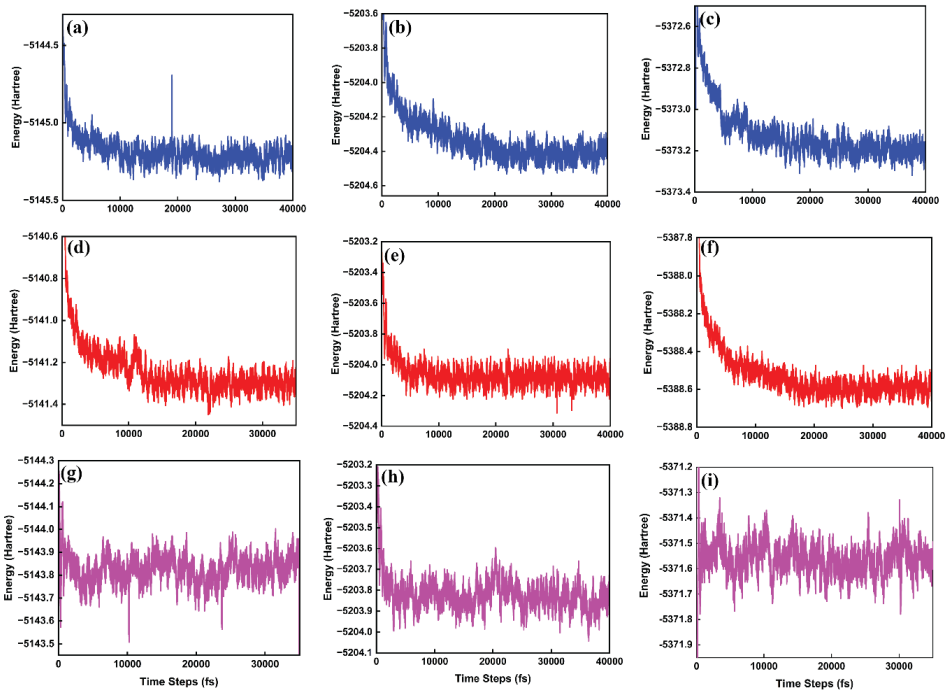

Figure B6. Potential energy plot of $[Ln(DOTA)]^-$ complexes at 25˚C (a, b, c), 45˚C (d, e, f), and 65˚C (g, h, i) for SAP geometry. From La^{3+} (a, d, g), Gd^{3+} (b, e, h), and Lu^{3+} (c, f, i) complexes from left to right.

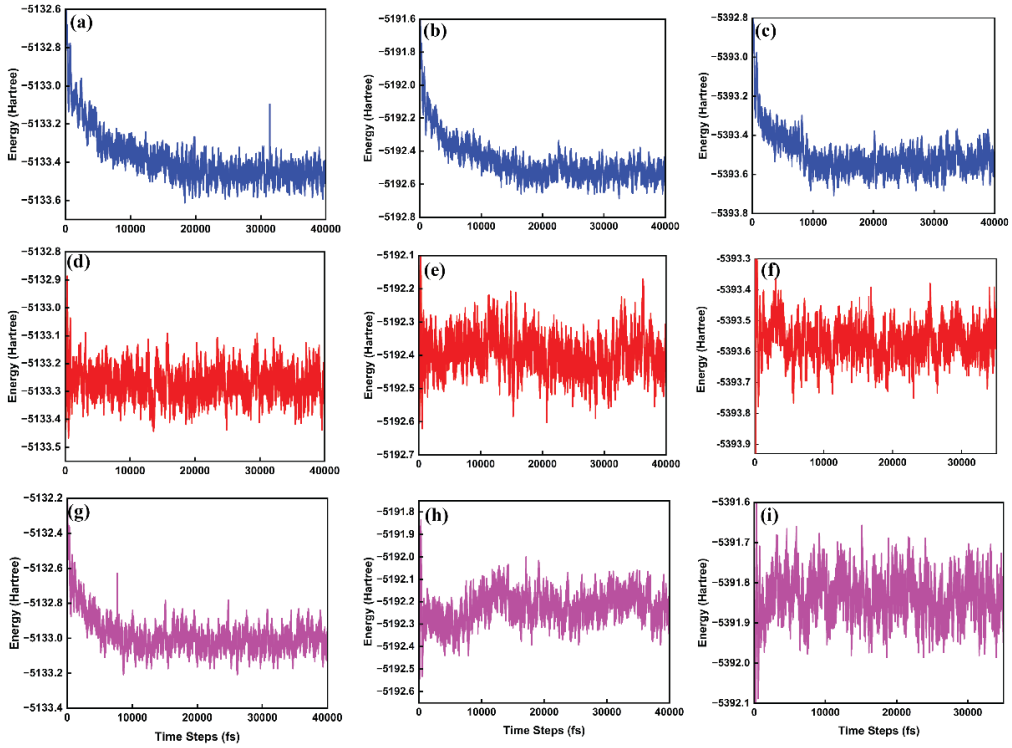

Figure B7. Potential energy plot of $[Ln(HMDOTA-SS)]^-$ complexes at 25˚C (a, b, c), 45˚C (d, e, f), and 65˚C (g, h, i) for TSAP geometry. From La^{3+} (a, d, g), Gd^{3+} (b, e, h), and Lu^{3+} (c, f, i) complexes from left to right.

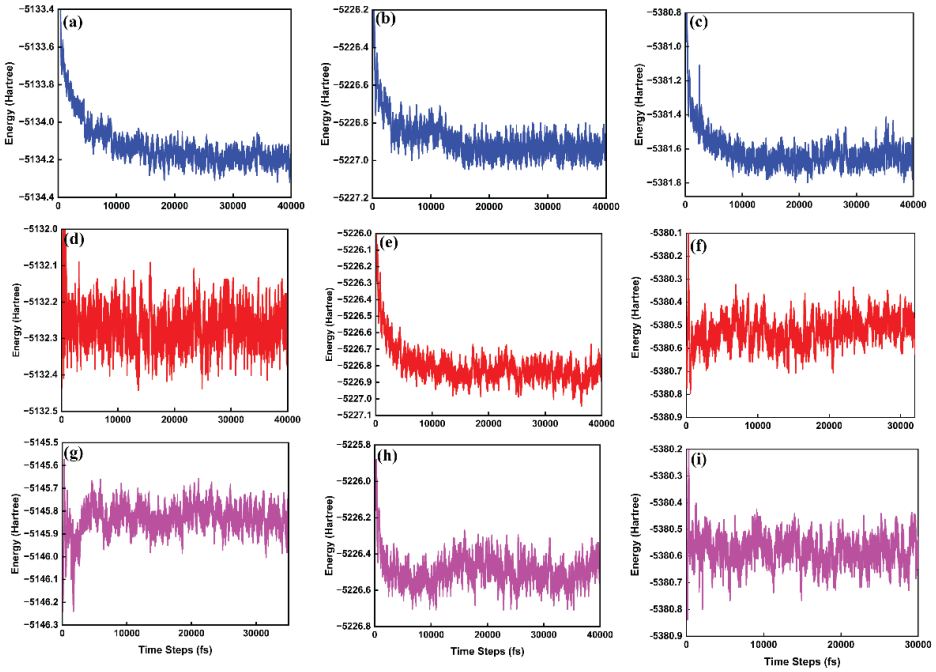

Figure B8. Potential energy plot of $[Ln(HMDOTA\text{-}SS)]^-$ complexes at 25˚C (a, b, c), 45˚C (d, e, f), and 65˚C (g, h, i) for SAP geometry. From La^{3+} (a, d, g), Gd^{3+} (b, e, h), and Lu^{3+} (c, f, i) complexes from left to right.

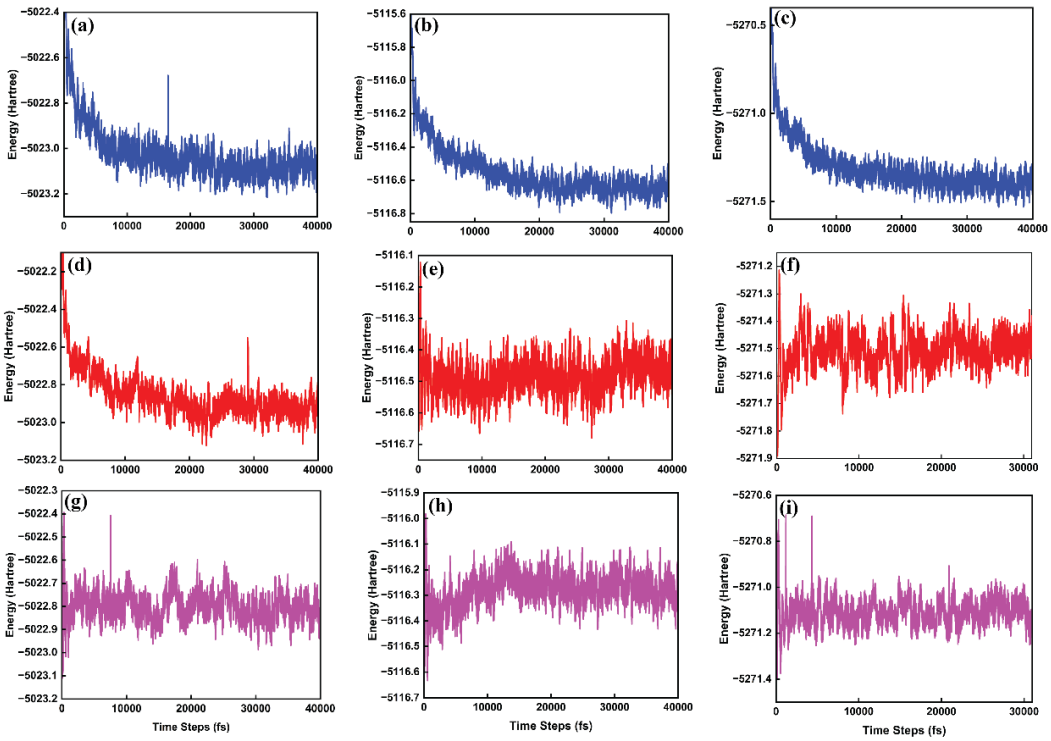

Figure B9. Potential energy plot of $[Ln(T)]^-$ complexes at 25˚C (a, b, c), 45˚C (d, e, f), and 65˚C (g, h, i) for TSAP geometry. From La^{3+} (a, d, g), Gd^{3+} (b, e, h), and Lu^{3+} (c, f, i) complexes from left to right.

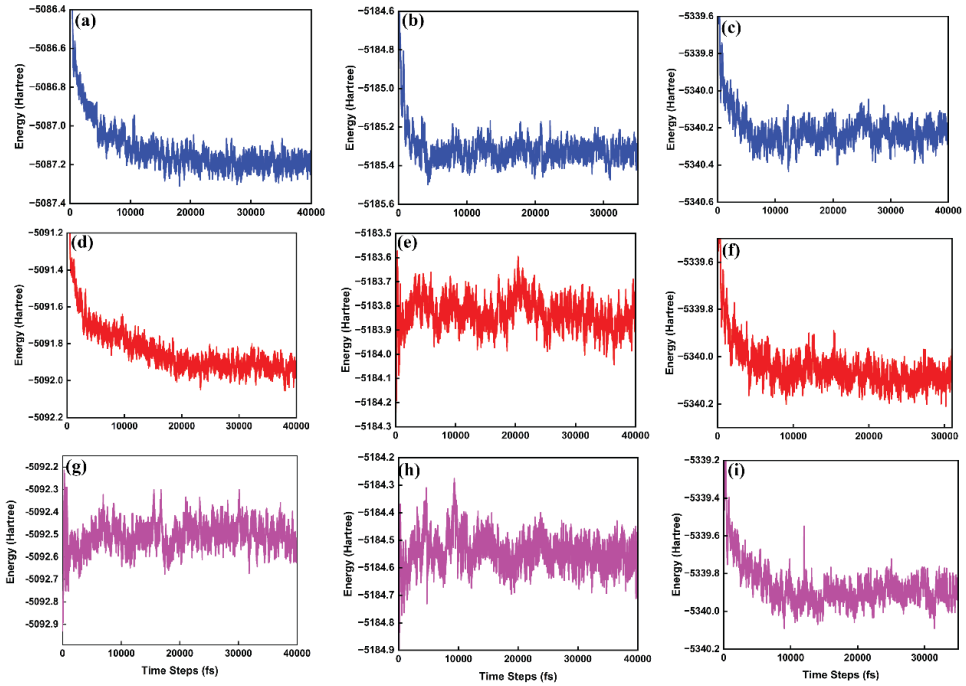

Figure B10. Potential energy plot of $[Ln(T)]^-$ complexes at 25˚C (a, b, c), 45˚C (d, e, f), and 65˚C (g, h, i) for SAP geometry. From La (a, d, g), Gd (b, e, h) and Lu (c, f, i) complexes from left to right.

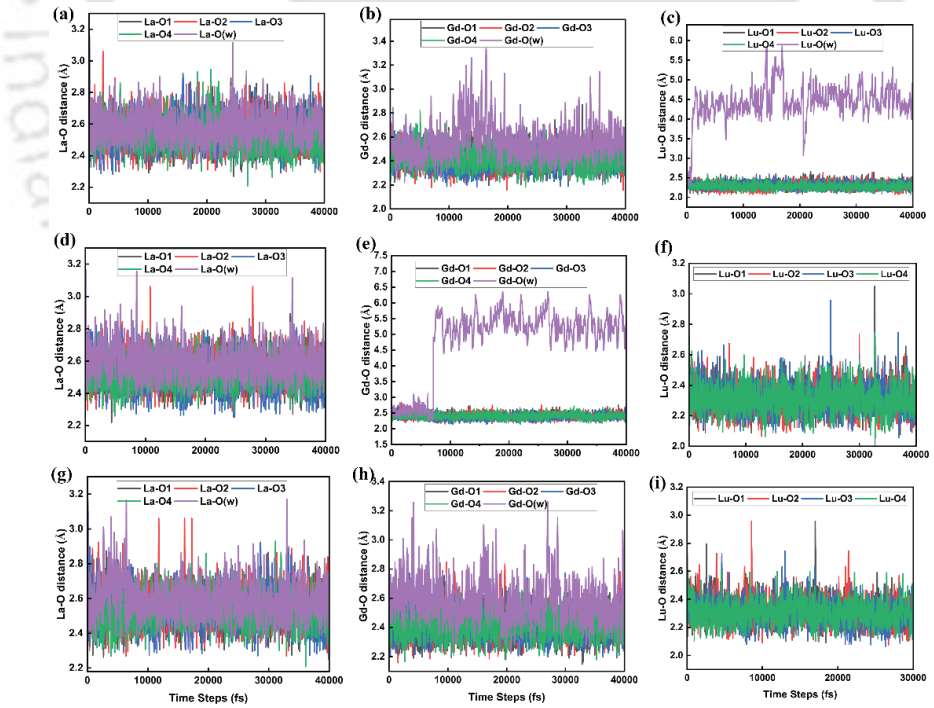

Figure B11. Ln-O bond distances during the AIMD trajectories of $[Ln(DOTA)]^-$ complex at 25˚C (a, b, c), 45˚C (d, e, f), and 65˚C (g, h, i) for TSAP isomer. Black, blue, purple, red, and green curves represent the Ln-O distances for individual oxygen atoms along the AIMD trajectory.

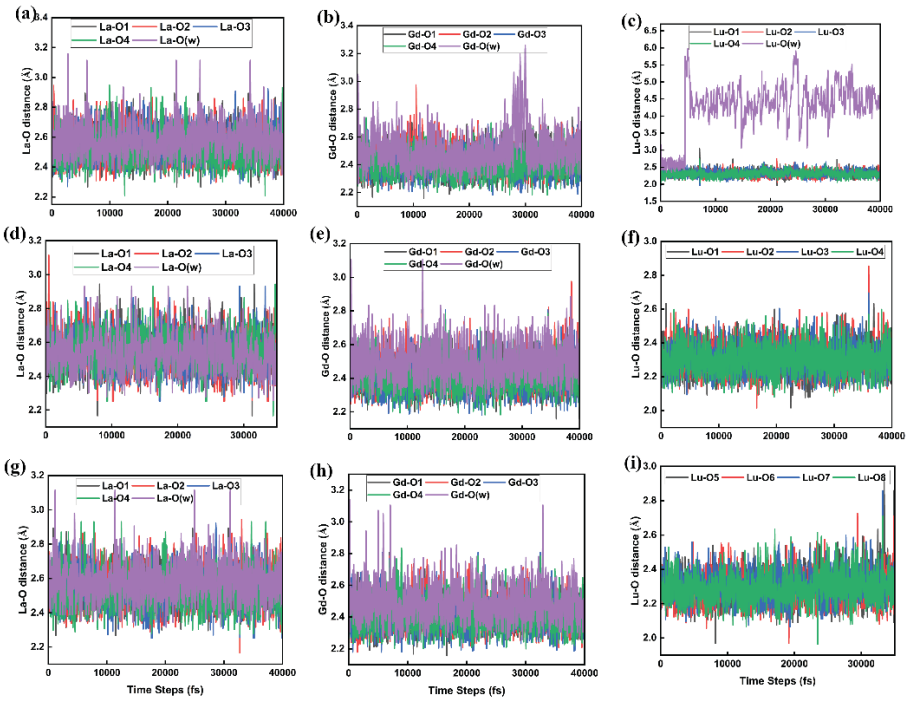

Figure B12. Ln-O bond distances during the AIMD trajectories of $[Ln(DOTA)]^-$ complex at 25˚C (a, b, c), 45˚C (d, e, f), and 65˚C (g, h, i) for SAP isomer. Black, blue, purple, red, and green curves represent the Ln-O distances for individual oxygen atoms along the AIMD trajectory.

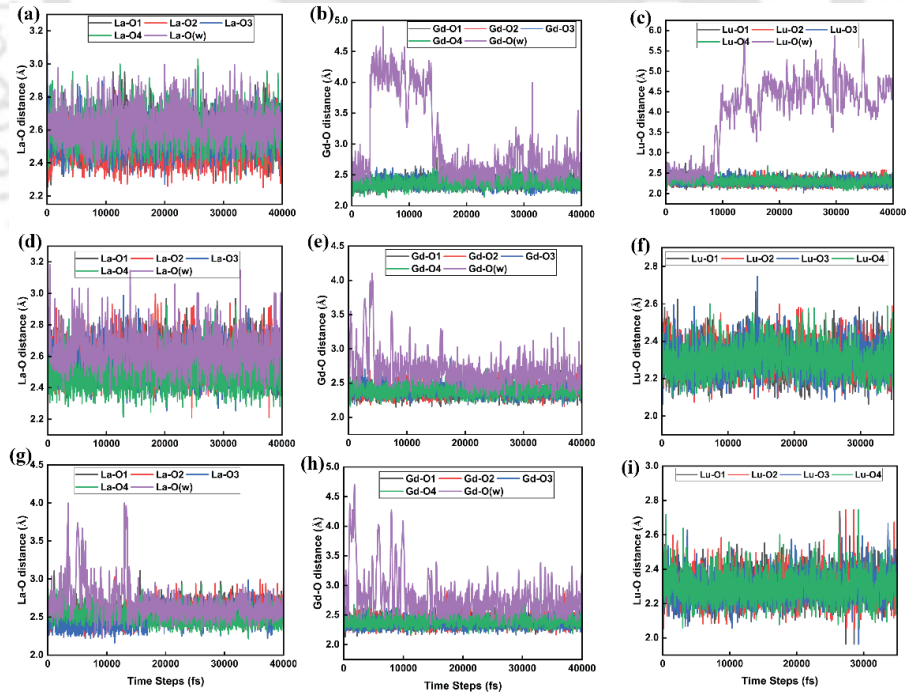

Figure B13. Ln-O bond distances during the AIMD trajectories of $[Ln(HMDOTA\text{-}SS)]^-$ complex at 25˚C (a, b, c), 45˚C (d, e, f), and 65˚C (g, h, i) for TSAP isomer. Black, blue, purple, red, and green curves represent the Ln-O distances for individual oxygen atoms along the AIMD trajectory.

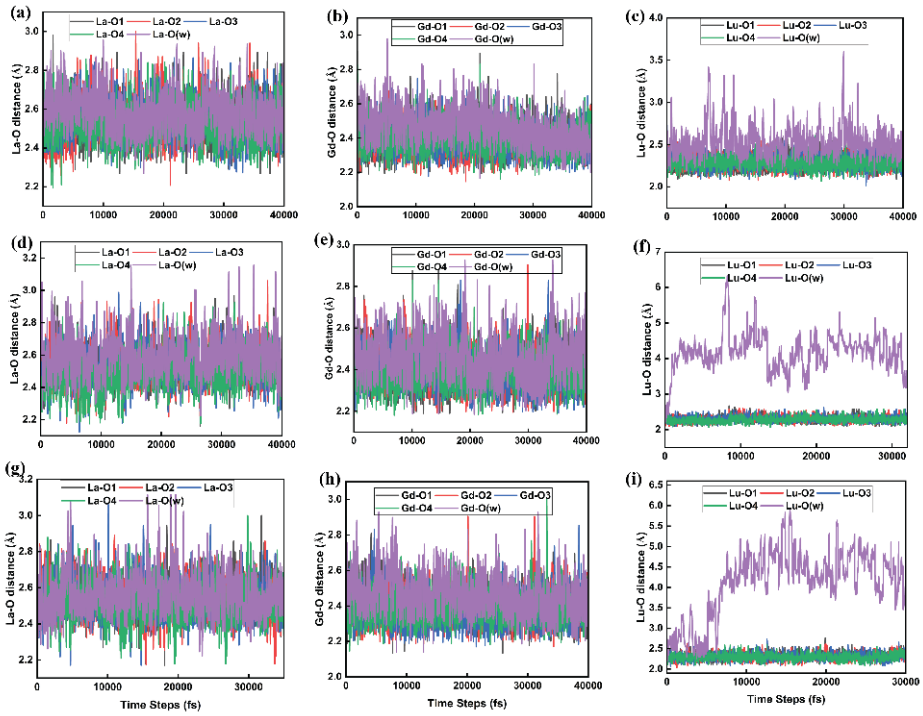

Figure B14. Ln-O bond distances during the AIMD trajectories of $[Ln(HMDOTA\text{-}SS)]^-$ complex at 25˚C (a, b, c), 45˚C (d, e, f), and 65˚C (g, h, i) for SAP isomer. Black, blue, purple, red, and green curves represent the Ln-O distances for individual oxygen atoms along the AIMD trajectory.

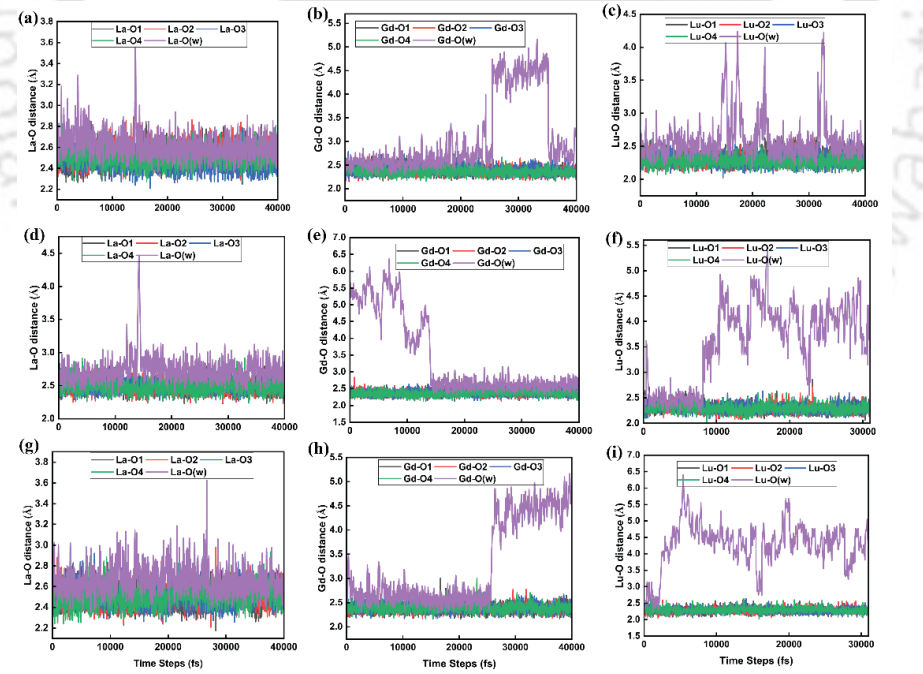

Figure B15. Ln-O bond distances during the AIMD trajectories of $[Ln(T)]^-$ complex at 25˚C (a, b, c), 45˚C (d, e, f), and 65˚C (g, h, i) for TSAP isomer. Black, blue, purple, red, and green curves represent the Ln-O distances for individual oxygen atoms along the AIMD trajectory.

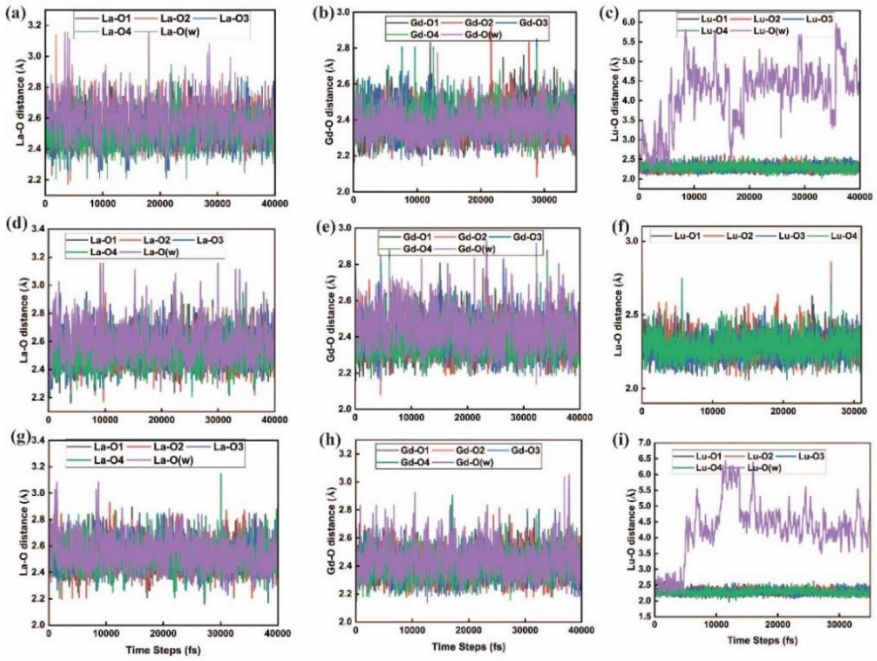

Figure B16. Ln-O bond distances during the AIMD trajectories of $[Ln(T)]^-$ complex at 25˚C (a, b, c), 45˚C (d, e, f), and 65˚C (g, h, i) for SAP isomer. Black, blue, purple, red, and green curves represent the Ln-O distances for individual oxygen atoms along the AIMD trajectory.

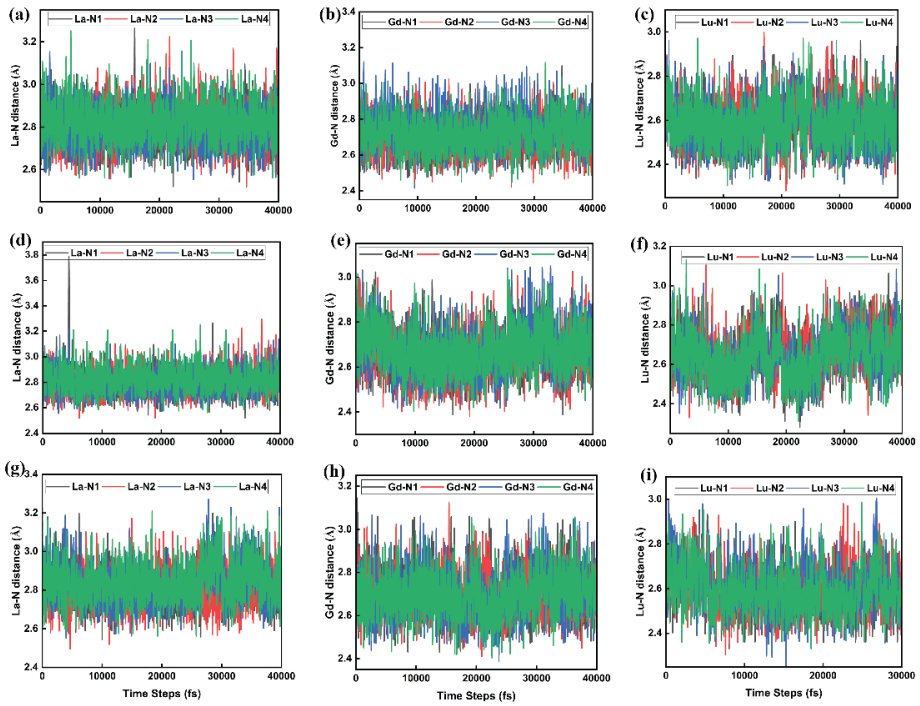

Figure B17. Ln-N bond distances during the AIMD trajectories of $[Ln(DOTA)]^-$ complex at 25˚C (a, b, c), 45˚C (d, e, f), and 65˚C (g, h, i) for TSAP isomer. Black, red, blue, and green curves represent the Ln-N distances for individual nitrogen atoms along the AIMD trajectory.

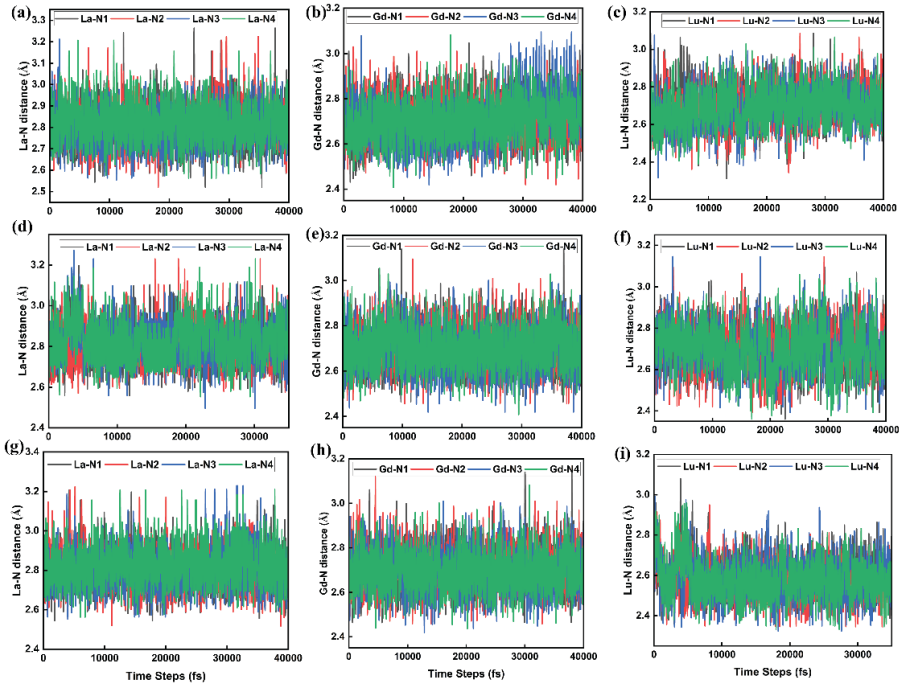

Figure B18. Ln-N bond distances during the AIMD trajectories of $[Ln(DOTA)]^-$ complex at 25˚C (a, b, c), 45˚C (d, e, f), and 65˚C (g, h, i) for SAP isomer. Black, red, blue, and green curves represent the Ln-N distances for individual nitrogen atoms along the AIMD trajectory.

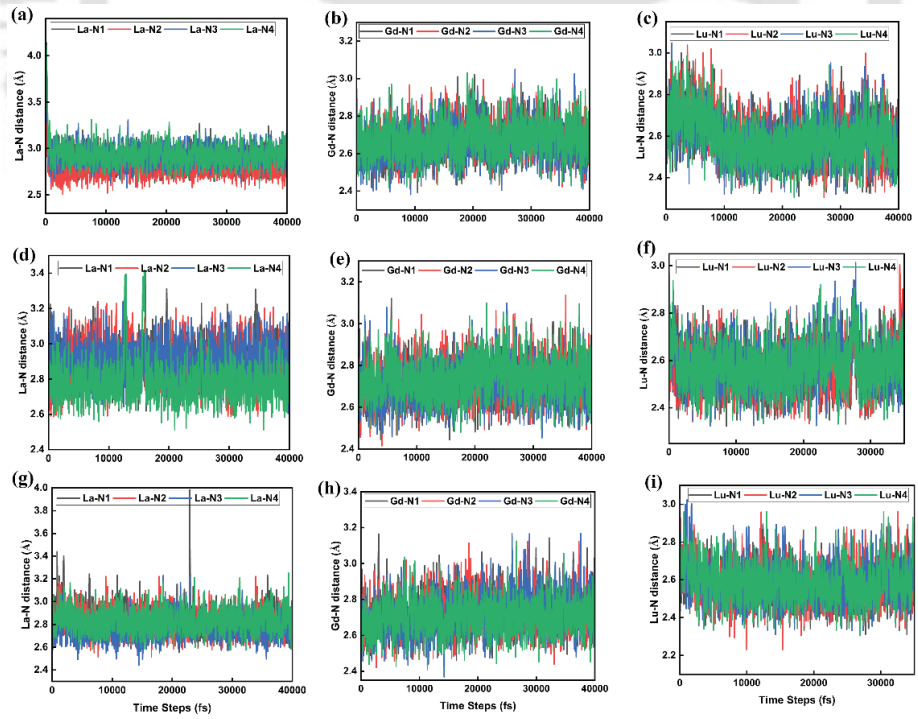

Figure B19. Ln-N bond distances during the AIMD trajectories of $[Ln(HMDOTA\text{-}SS)]^-$ complex at 25˚C (a, b, c), 45˚C (d, e, f), and 65˚C (g, h, i) for TSAP isomer.

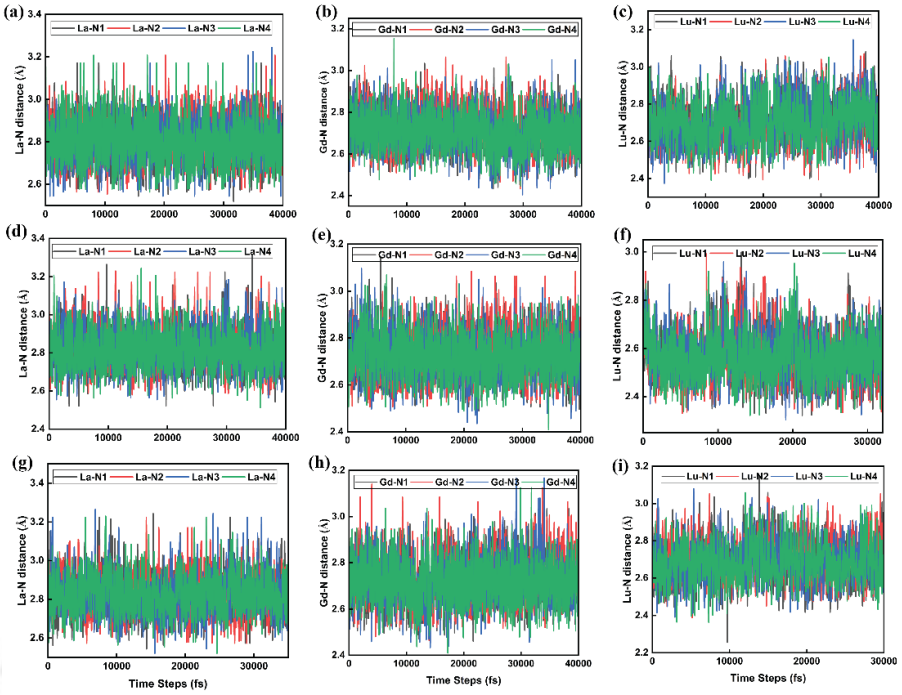

Figure B20. Ln-N bond distances during the AIMD trajectories of $[Ln(HMDOTA\text{-}SS)]^-$ complex at 25˚C (a, b, c), 45˚C (d, e, f), and 65˚C (g, h, i) for SAP isomer.

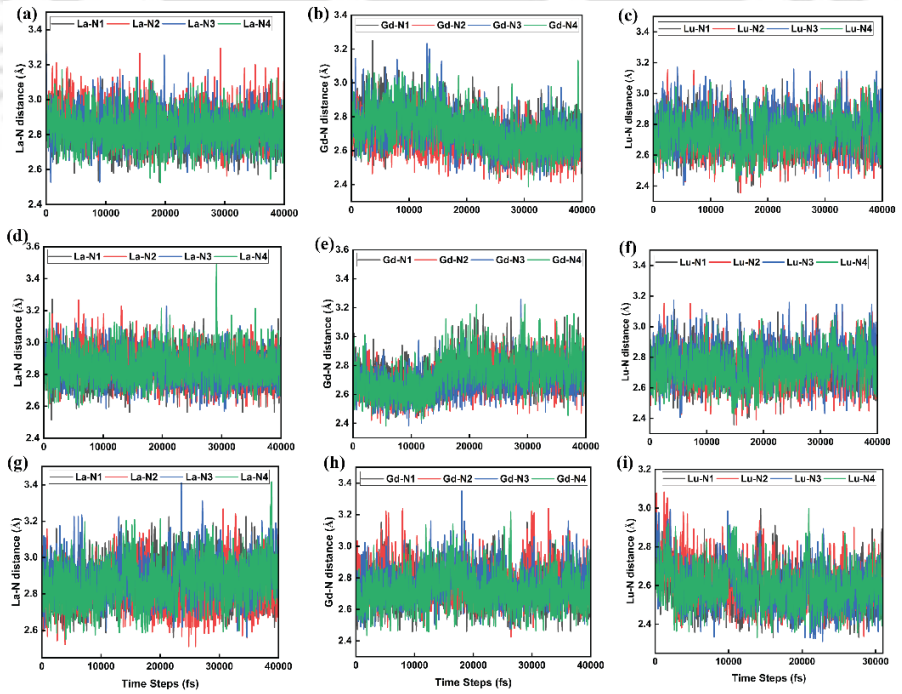

Figure B21. Plots of Ln-N bond distances during the AIMD trajectories of $[Ln(T)]^-$ complex at 25˚C (a, b, c), 45˚C (d, e, f), and 65˚C (g, h, i) for TSAP isomer.

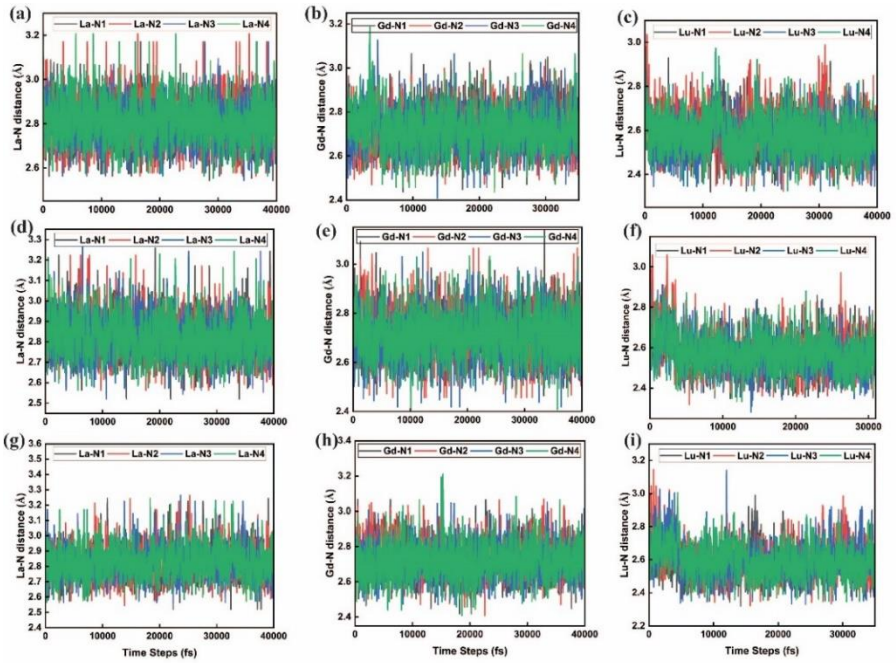

Figure B22. Ln-N bond distances during the AIMD trajectories of $[Ln(T)]^-$ complex at 25˚C (a, b, c), 45˚C (d, e, f), and 65˚C (g, h, i) for SAP isomer.

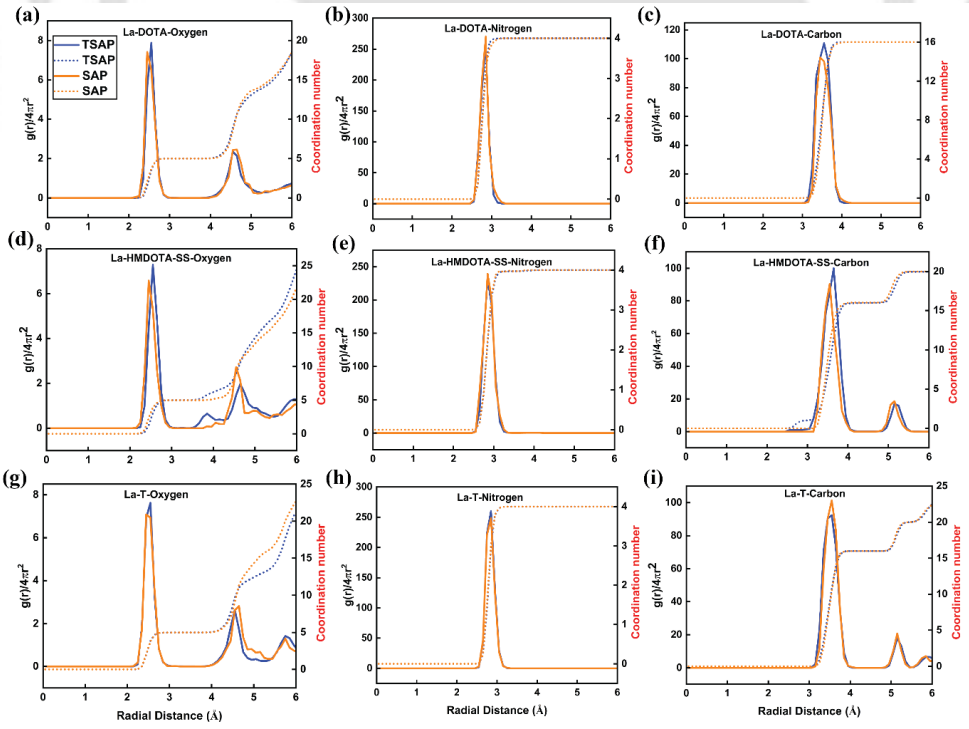

Figure B23. Radial distribution functions for the $[La(DOTA)]^-$, $[La(HMDOTA-SS)]^-$, and $[La(T)]^-$ complexes at 25˚C for both TSAP (blue) and SAP (orange) geometry. The left, center, and right panels illustrate La-O, La-N, and La-C pair distribution functions, respectively.

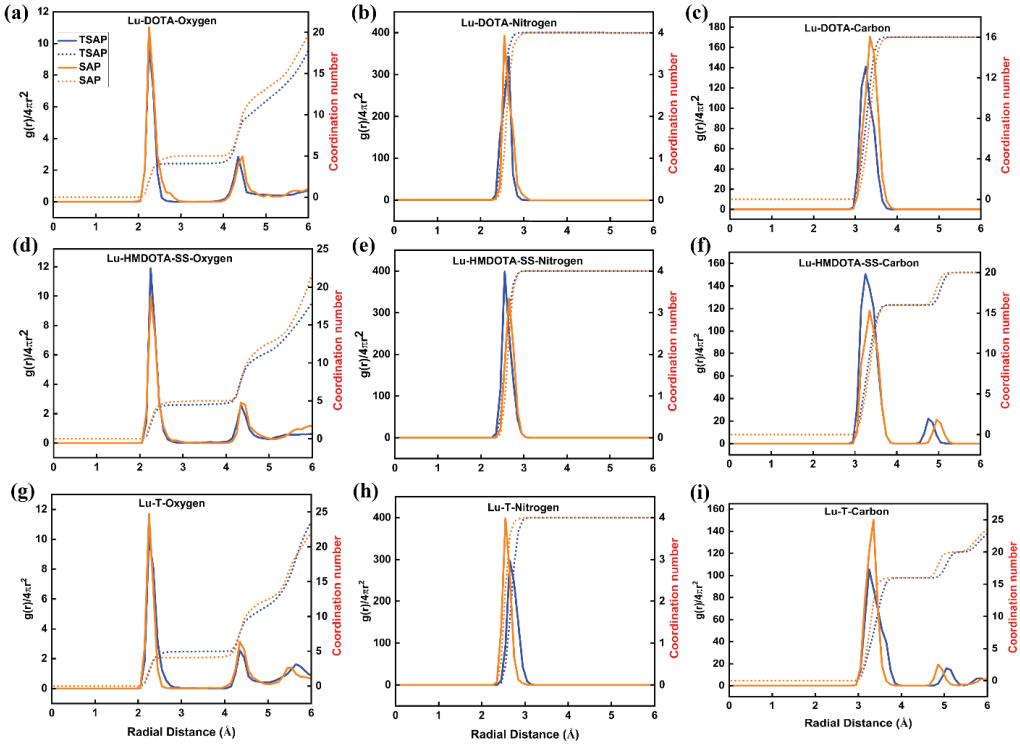

Figure B24. Radial distribution functions for the $[Lu(DOTA)]^-$, $[Lu(HMDOTA\text{-}SS)]^-$, and $[Lu(T)]^-$ complexes at 25˚C for both TSAP (blue) and SAP (orange) geometry. The left, center, and right panels illustrate Lu-O, Lu-N, and Lu-C pair distribution functions, respectively.

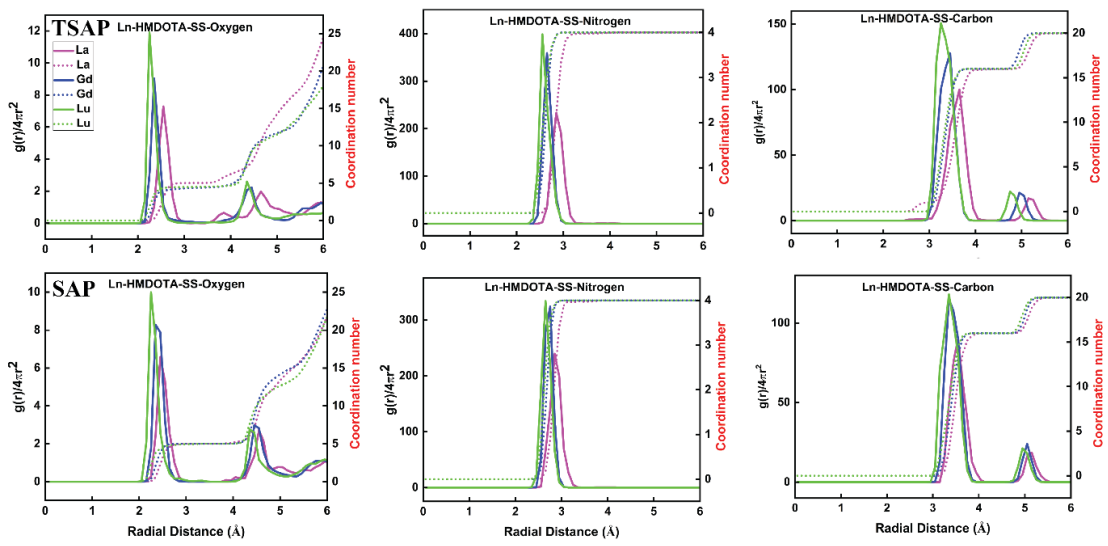

Figure B25. Radial distribution functions of the $[Ln(HMDOTA\text{-}SS)]^-$, complexes along the Ln^{3+}-series (Ln^{3+}=La^{3+}, Gd^{3+}, and Lu^{3+}) at 25˚C in the TSAP (top) and SAP (bottom) geometries. The left, center, and right panels represent Ln-O, Ln-N, and Ln-C pair distribution functions, respectively.

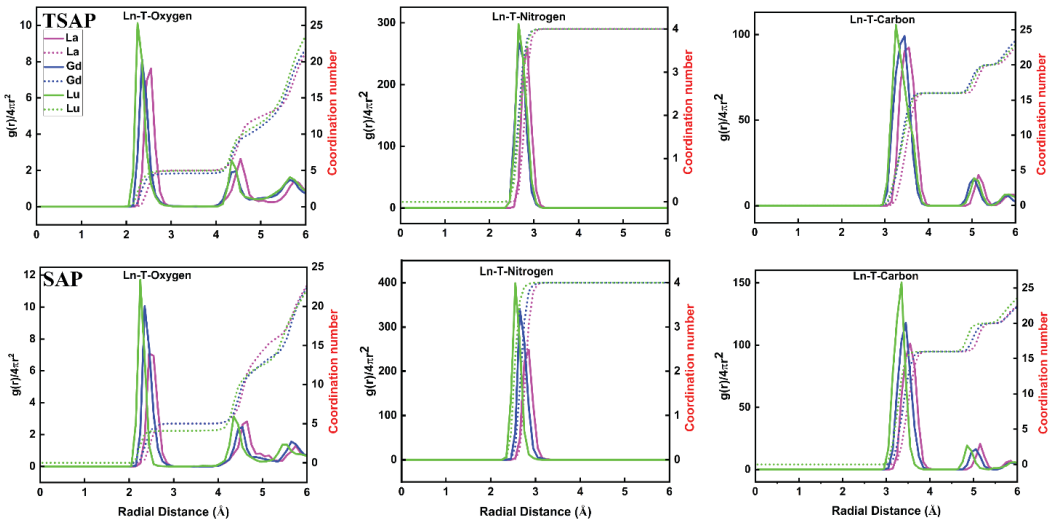

Figure B26. Radial distribution functions of the $[Ln(T)]^-$, complexes along the Ln^{3+}-series (Ln^{3+}=La^{3+}, Gd^{3+}, and Lu^{3+}), at 25˚C in the TSAP (top) and SAP (bottom) geometries. The left, center, and right panels represent Ln-O, Ln-N, and Ln-C pair distribution functions, respectively.

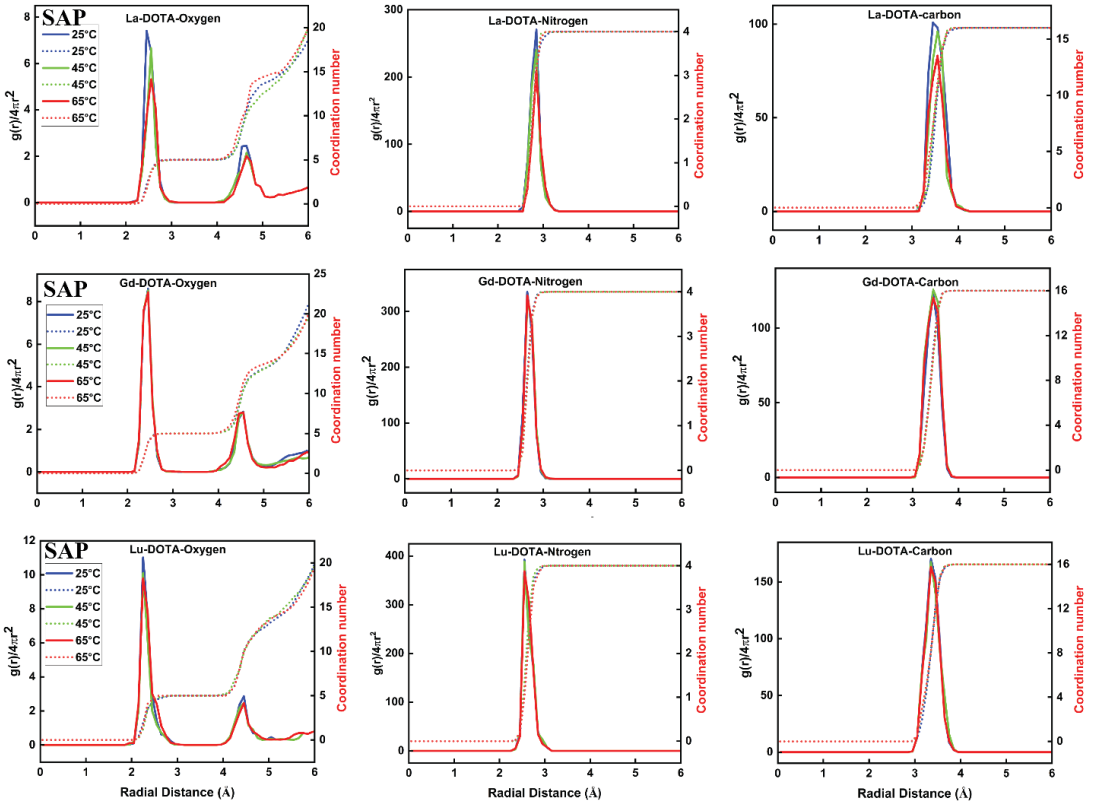

Figure B27. Radial distribution functions of the $[Ln(DOTA)]^-$, complexes, shown in three different temperatures (25˚C, 45˚C, and 65˚C). The left, center, and right panels represent Ln-O, Ln-N, and Ln-C pair distribution functions, respectively.

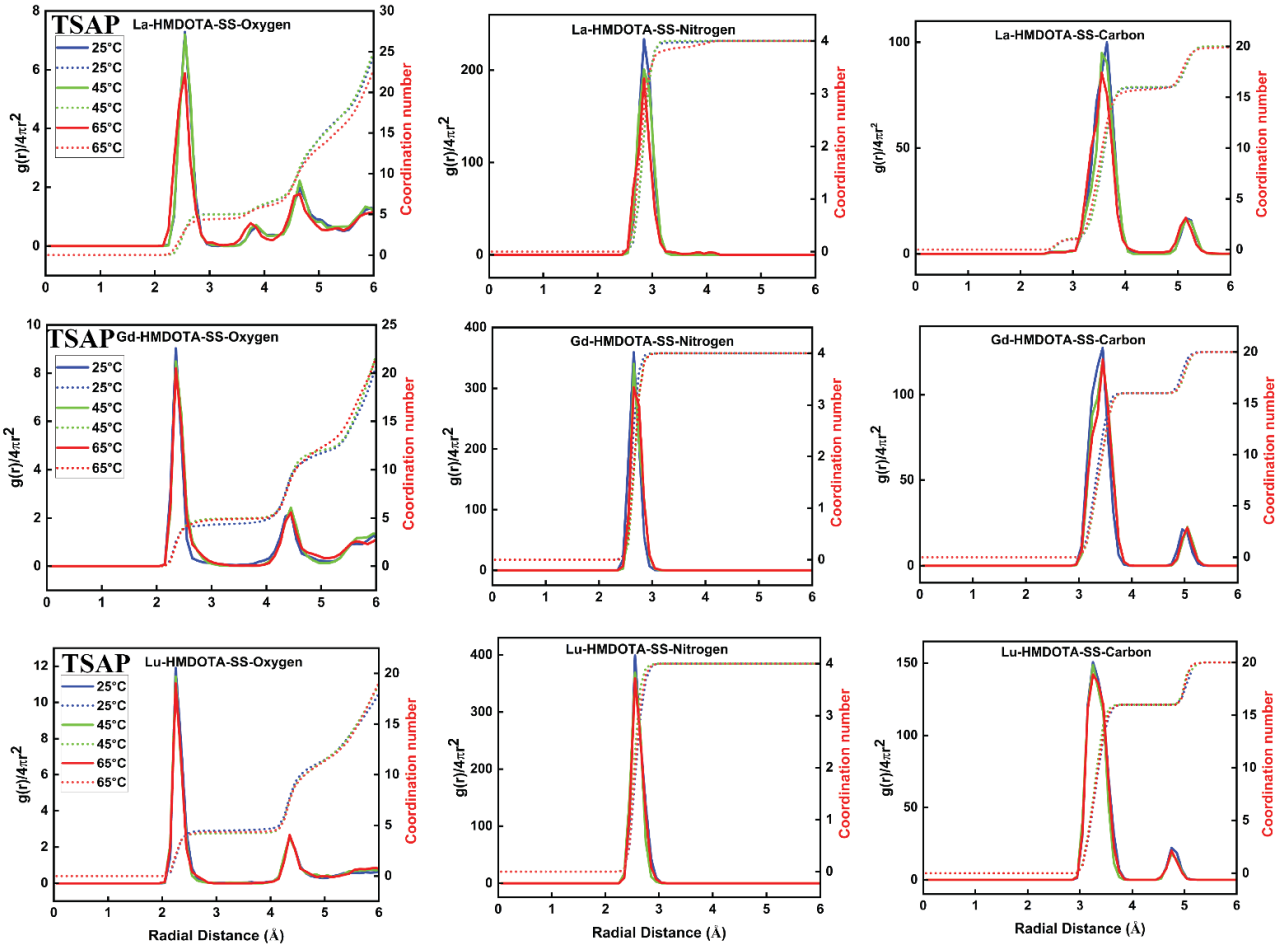

Figure B28. Radial distribution functions of the $[Ln(HMDOTA\text{-}SS)]^-$, complexes, shown in three different temperatures (25˚C, 45˚C, and 65˚C). The left, center, and right panels represent Ln-O, Ln-N, and Ln-C pair distribution functions, respectively.

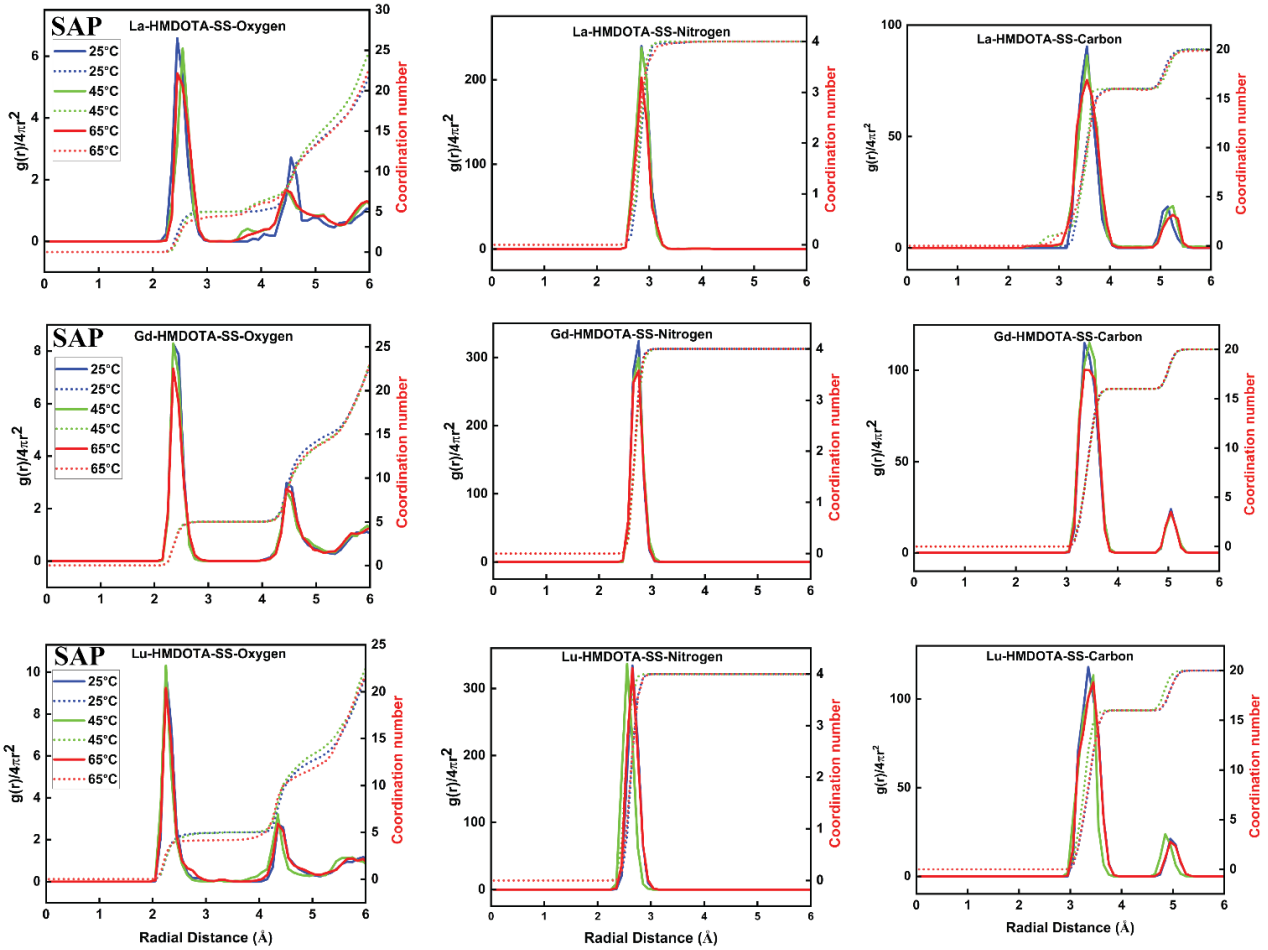

Figure B29. Radial distribution functions of the $[Ln(HMDOTA\text{-}SS)]^-$, complexes, shown in three different temperatures (25˚C, 45˚C, and 65˚C). The left, center, and right panels represent Ln-O, Ln-N, and Ln-C pair distribution functions, respectively.

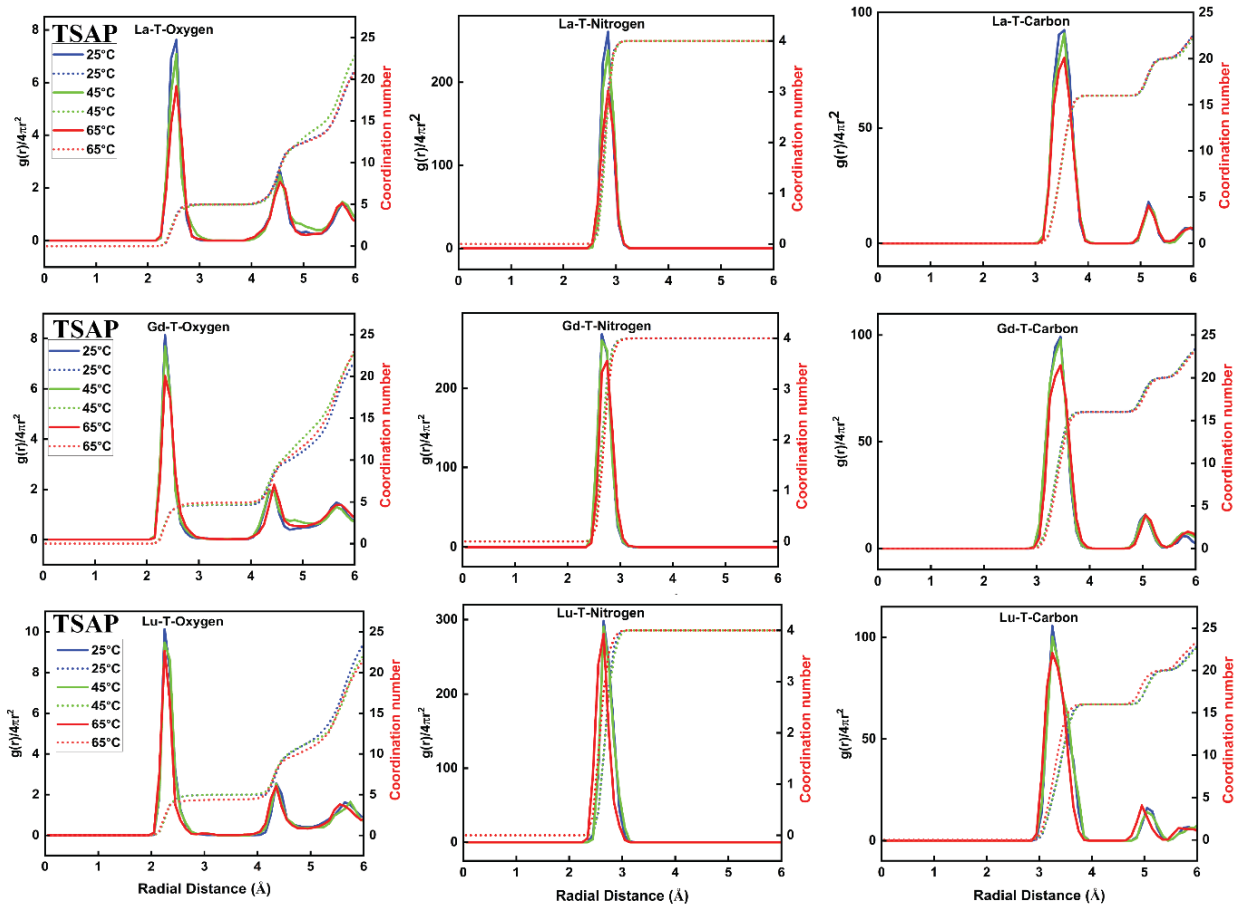

Figure B30. Radial distribution functions of the $[Ln(T)]^-$, complexes, shown in three different temperatures (25˚C and 45˚C and 65˚C). The left, center, and right panels represent Ln-O, Ln-N, and Ln-C pair distribution functions, respectively.

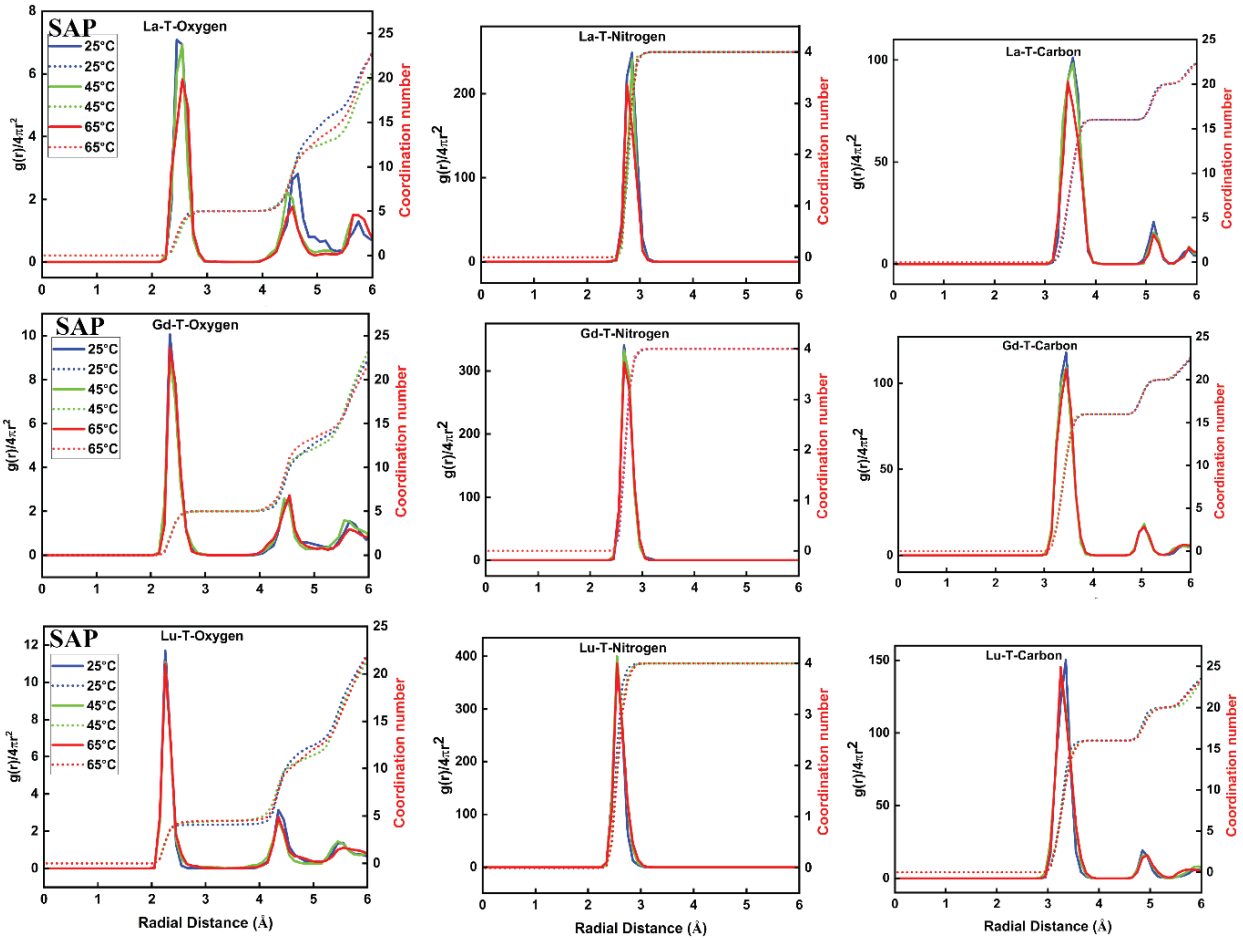

Figure B31. Radial distribution functions of the $[Ln(T)]^-$, complexes, shown in three different temperatures (25˚C, 45˚C, and 65˚C). The left, center, and right panels represent Ln-O, Ln-N, and Ln-C pair distribution functions, respectively.

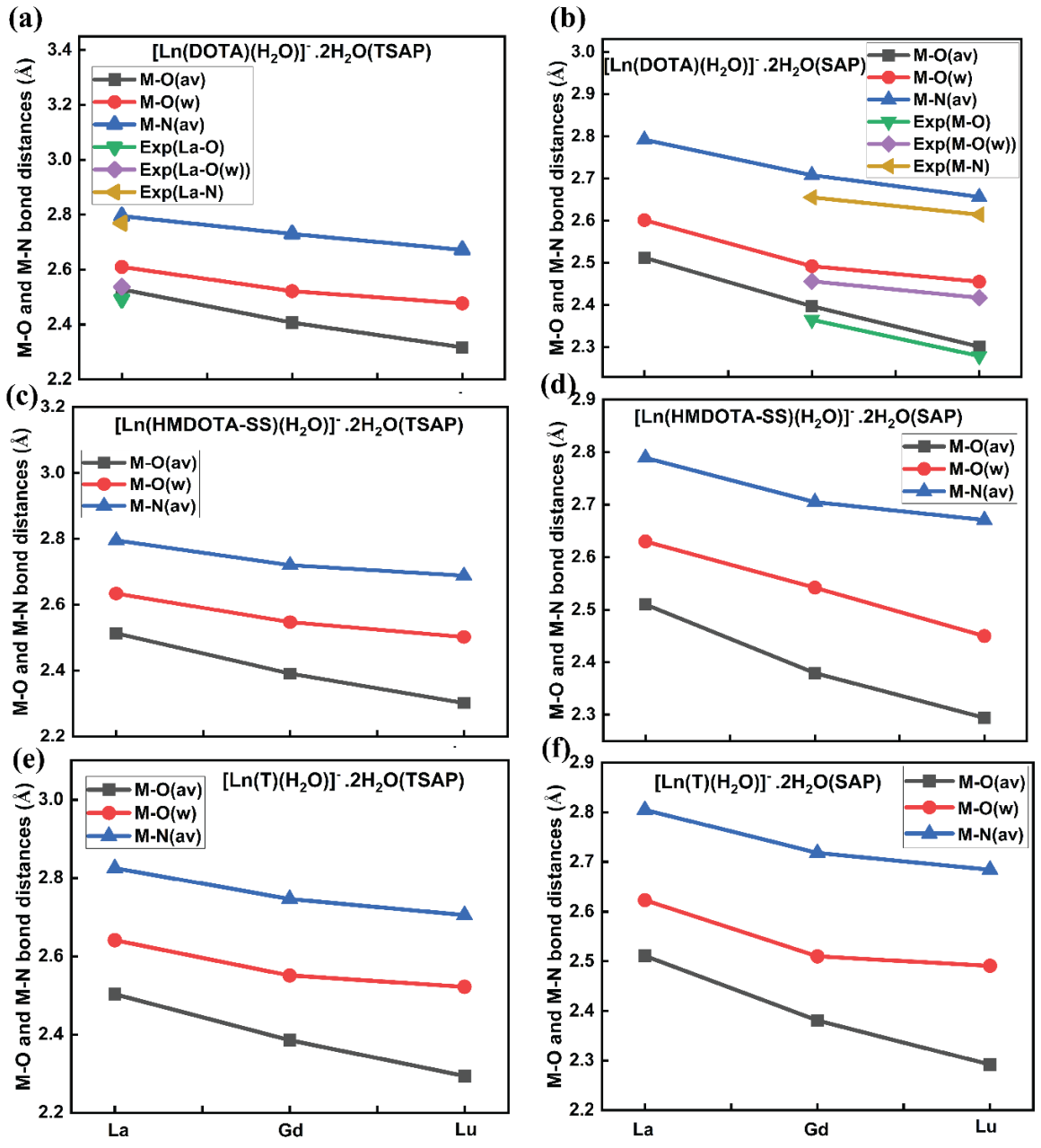

Figure B32. Variation of metal-ligand bond length along the Ln-series for $[Ln(DOTA)(H_2O)]^-.2H_2O$ (a, b), $[Ln(HMDOTA\text{-}SS))(H_2O)]^-.2H_2O$ (c, d), and $[Ln(T))(H_2O)]^-.2H_2O$ (e, f) complexes for both TSAP and SAP isomers with outer sphere water at the TPSSh/6-311G(d,p)/LCRECP level of theory.

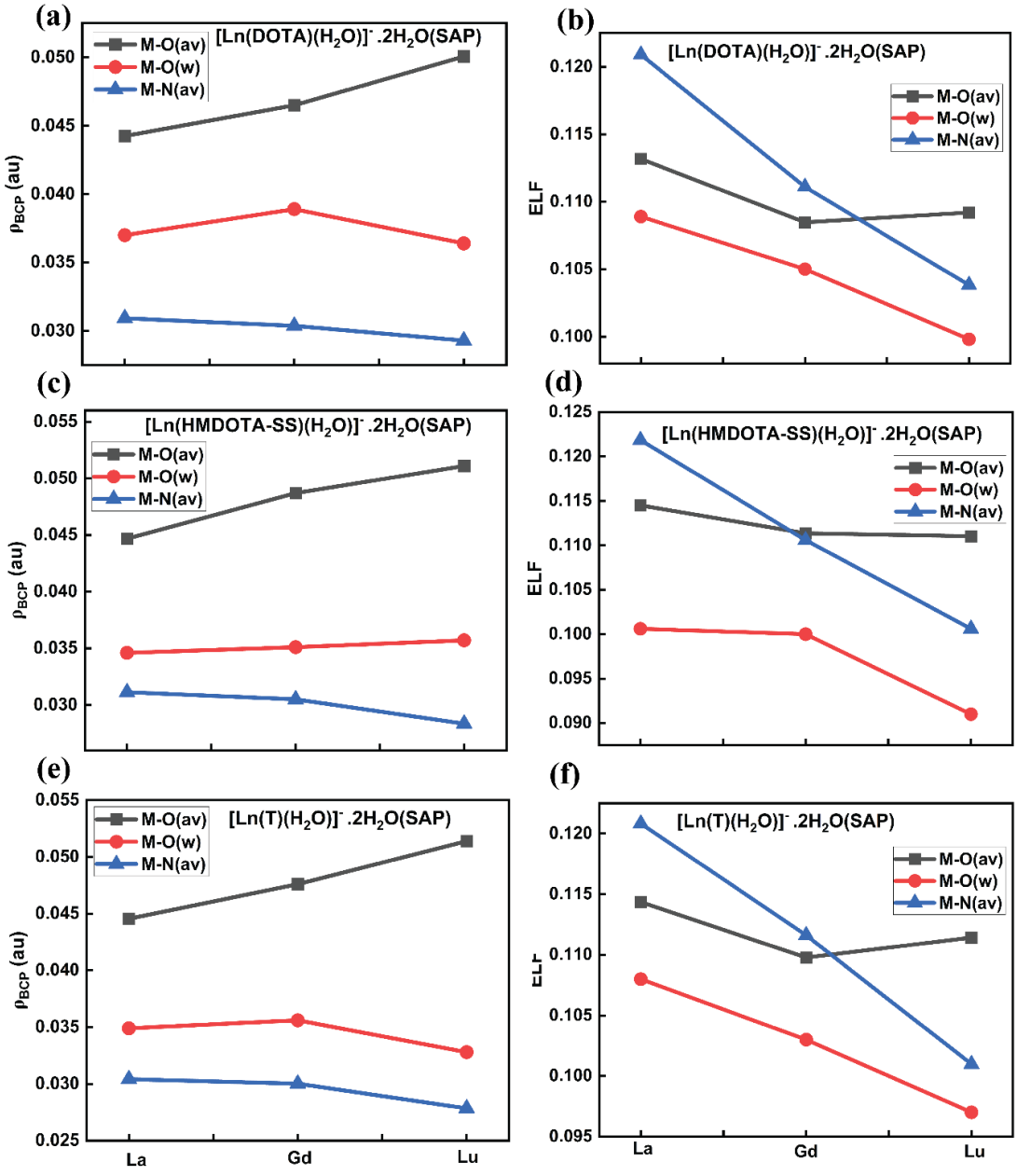

Figure B33. Electron density ($\rho_{(BCP)}$) and electron localization function (ELF) values along the lanthanide series for [Ln(DOTA))$(H_2O)]^-.2H_2O$ (a, b), [Ln(HMDOTA-SS))$(H_2O)]^-.2H_2O$ (c, d), and [Ln(T))$(H_2O)]^-.2H_2O$ (e, f) complexes for SAP isomer.

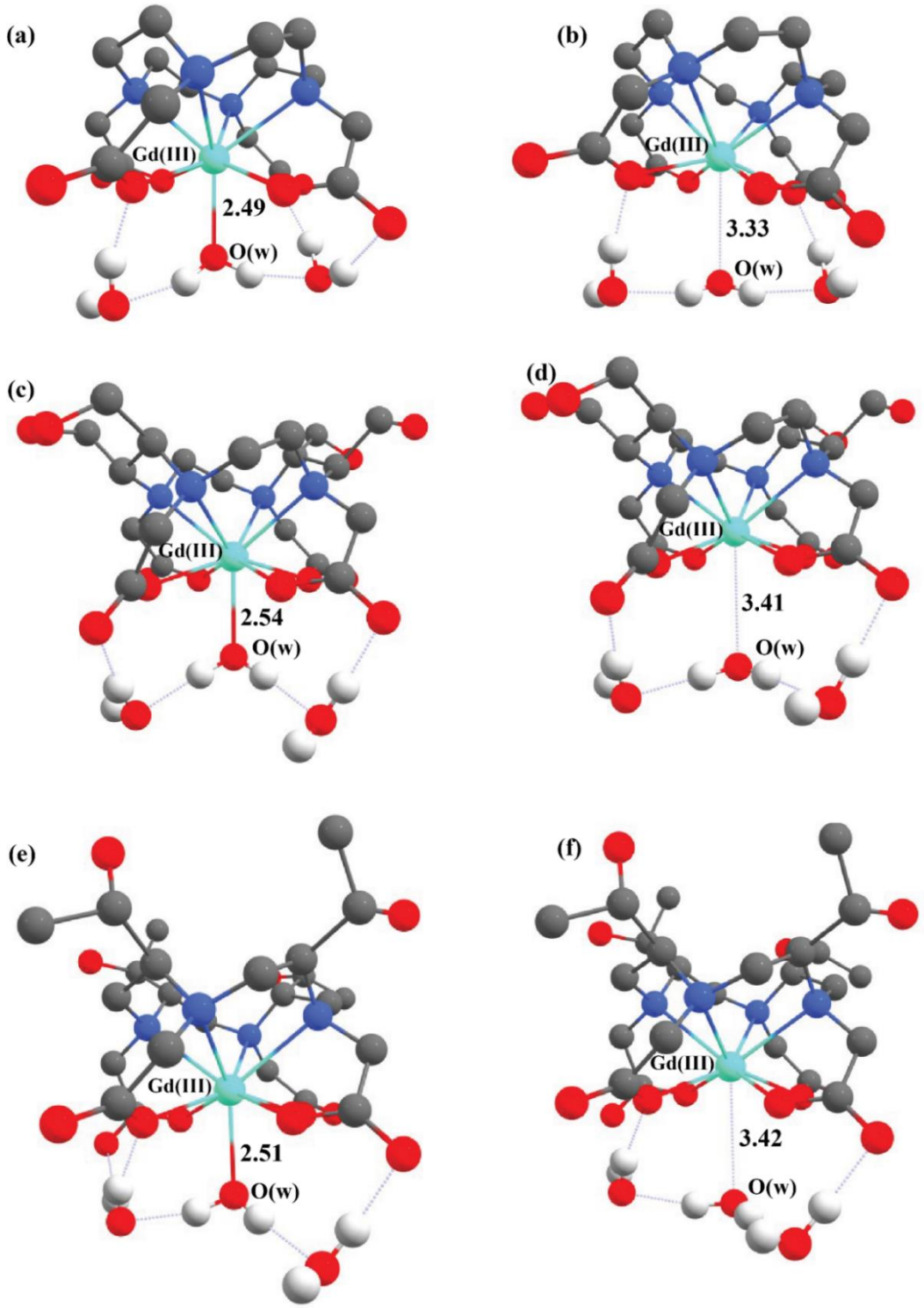

Figure B34. Optimized structures of the ground states (left panel) and transition states (right panel) obtained from DFT calculations for the $[Gd(DOTA)(H_2O)]^{-}.2H_2O$ (a and b), $[Gd(HMDOTA\text{-}SS)(H_2O)]^{-}.2H_2O$ (c and d) and $[Gd(T)(H_2O)]^{-}.2H_2O$ (e and f) systems for SAP isomer.

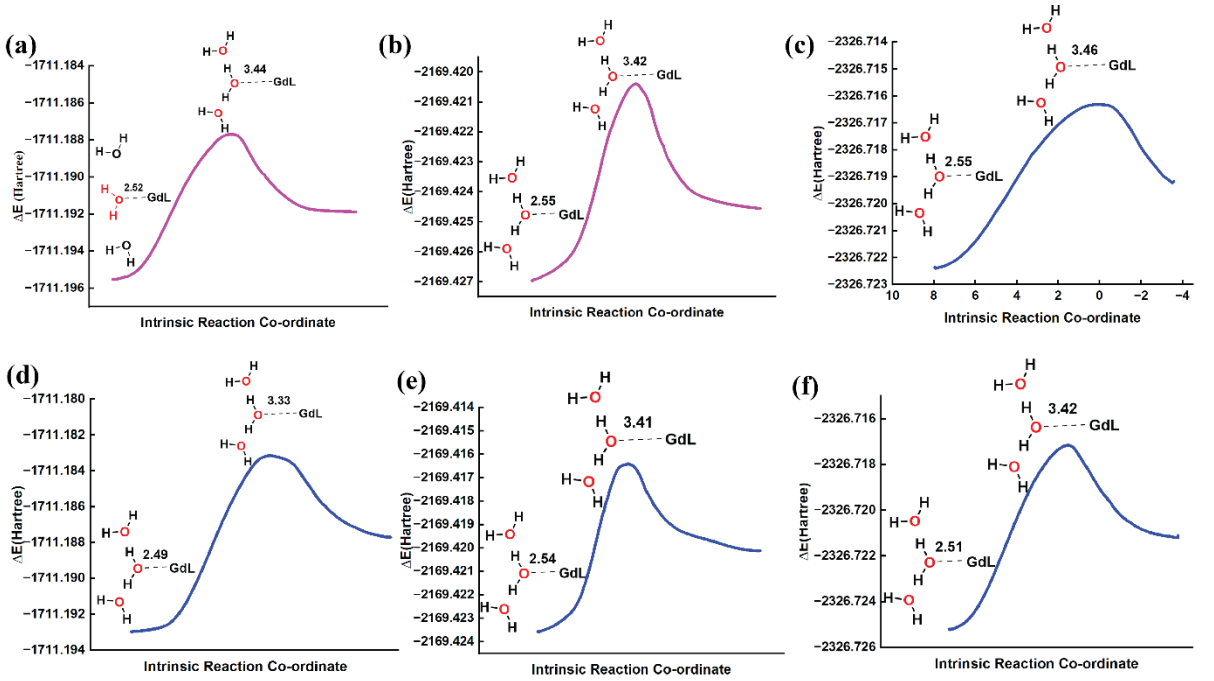

Figure B35. IRC plots for the dissociation of the Gd-O(w) bond, of the $[Gd(DOTA)(H_2O)]^-.2H_2O$ (a, d), $[Gd(HMDOTA\text{-}SS)(H_2O)]^-.2H_2O$ (b, e), and $[Gd(T)(H_2O)]^-.2H_2O$ (c, f) complexes for TSAP (top) and SAP (bottom) isomer using TPSSh/6-311G(d,p)/LCRECP level of theory.

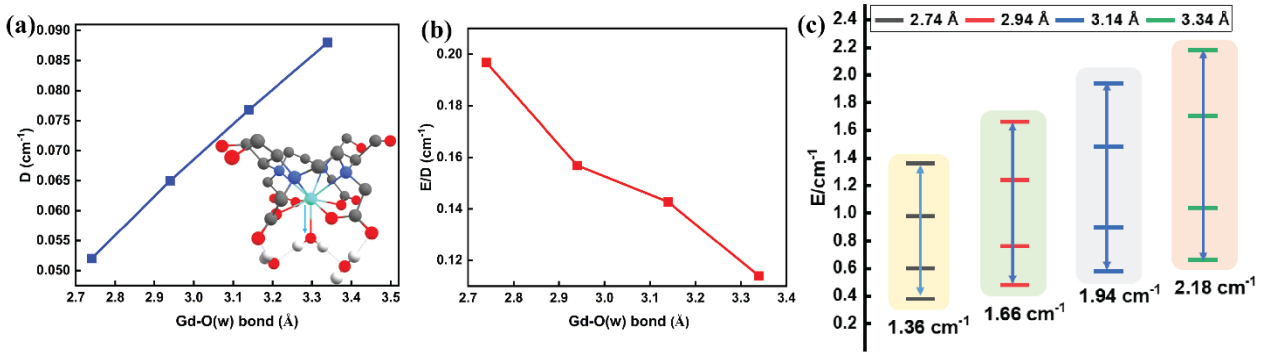

Figure B36. Graphical representation of *ab initio* CASSCF/NEVPT2 results for the SAP isomer of $[Gd(HMDOTA\text{-}SS)(H_2O)]^-.2H_2O$ complex with the variation of Gd-O(w) bond length from 2.74-3.34 Å (a) variation in D-parameter, (b) variation in E/D ratio, (c) corresponding variation of Kramers doublet energy levels with bond length.

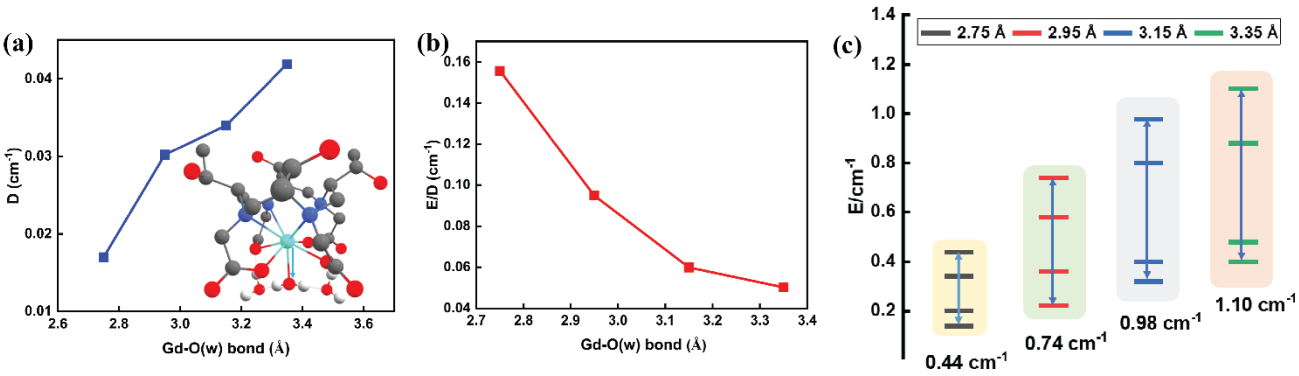

Figure B37. Graphical representation of *ab initio* CASSCF/NEVPT2 results for the TSAP isomer of $[Gd(T)(H_2O)]^{-}$. $2H_2O$ complex with the variation of Gd-O(w) bond length from 2.75-3.35 Å (a) variation in D-parameter, (b) variation in E/D ratio, (c) corresponding variation of Kramers doublet energy levels with bond length.

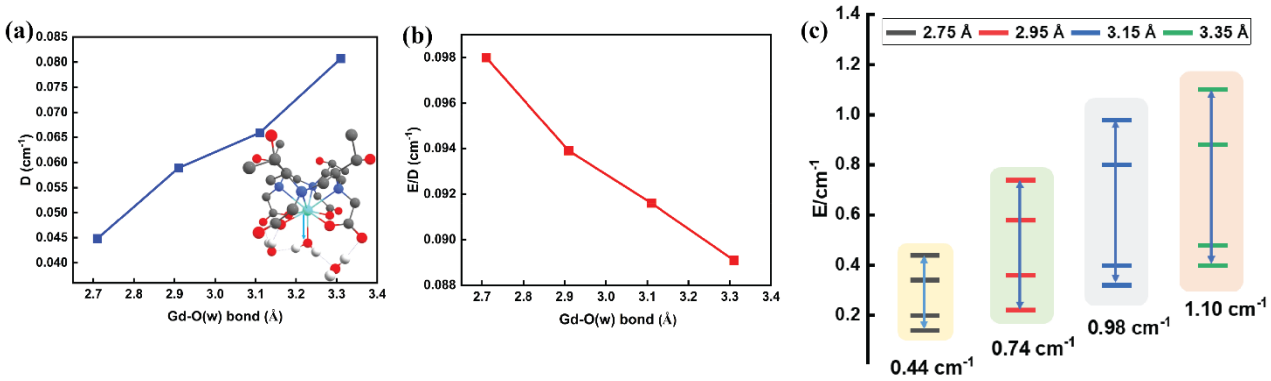

Figure B38. Graphical representation of *ab initio* CASSCF/NEVPT2 results for the SAP isomer of $[Gd(T)(H_2O)]^{-}$. $2H_2O$ complex with the variation of Gd-O(w) bond length from 2.71-3.31 Å (a) variation in D-parameter, (b) variation in E/D ratio, (c) corresponding variation of Kramers doublet energy levels with bond length.

Reference

1. J. Zhang, L. Dai, L. He, A. Bhattarai, C.-M. Chan, W. C.-S. Tai, V. Vardhanabhuti and G.-L. Law, *Commun. Chem.*, 2023, **6**, 251-260.

2. S. Khan, A. Kubica-Misztal, D. Kruk, J. Kowalewski and M. Odelius, *J. Chem. Phys.*, 2015, **142**, 034304-034314.

3. M. Benmelouka, J. Van Tol, A. Borel, M. Port, L. Helm, L. C. Brunel, and A. E. Merbach, *J. Am. Chem. Soc.*, 2006, **128**, 7807-7816.

Appendix-C

Table C1. RMSD value of the structures was calculated at 2 ps intervals against the Crystal structure using discovery studio and Pymol (at 25°C).

25^{0}C	**Complex 1**	**Complex 2**	**Complex 3**	**Complex 4**
Poses	RMSD	RMSD	RMSD	RMSD
14ps	0.328	0.394	0.322	0.277
16ps	0.324	0.420	0.311	0.275
18ps	0.310	0.301	0.540	0.397
20ps	0.418	0.531	0.430	0.435
22ps	0.496	0.396	0.530	0.317
24ps	0.518	0.418	0.590	0.426
26ps	0.310	0.353	0.499	0.437
28ps	0.505	0.368	0.411	0.527
30ps	0.300	0.314	0.548	0.518
32ps	0.499	0.399	0.239	0.533
34ps	0.327	0.315	0.346	0.421
36ps	0.410	0.355	0.540	0.321
38ps	0.433	0.433	0.344	0.324
40ps	0.460	0.401	0.344	0.513

Table C2. Bond length and bond angles of the Mn^{2+} complexes (temperature annealing+geometry optimization) with their crystallographic structure.

AIMD simulated structure	**AIMD simulated bond length**	**X-ray Crystallographic bond length**
[Mn(dpasam)(H_2O)]$^-$ (Complex 1)	Mn-O(w)=2.41	2.35
	Mn-O1=2.18	2.26
	Mn-O2=2.28	2.22
	Mn-N1=2.35	2.26
	Mn-N2=2.62	2.27

	Mn-N3=2.29	2.52
	Mn-N4=2.17	2.20
[Mn(dpaaa)(H₂O)]⁻ (Complex 2)	Mn-O(w)=2.30	2.27
	Mn-O1=2.17	2.21
	Mn-O2=2.08	2.17
	Mn-O3=2.02	2.20
	Mn-N1=2.31	2.25
	Mn-N2=2.35	2.25
	Mn-N3=2.78	2.46
[Mn(cbda)(H₂O)]⁻ (Complex 3)	Mn-O(w)=2.29	2.24
	Mn-O1=2.43	2.28
	Mn-O2=2.07	2.21
	Mn-O47=2.08	2.14
	Mn-N4=2.24	2.22
	Mn-N5=2.55	2.45
	Mn-N9=2.24	2.24
[Mn(pydpa)(H₂O)] (Complex 4)	Mn-O(w)=2.28	2.21
	Mn-O1=2.28	2.23
	Mn-O2=2.28	2.26
	Mn-N1=2.23	2.29
	Mn-N2=2.21	2.28
	Mn-N3=2.46	2.31
	Mn-N4=2.21	--

Table C3. Binding energy values and relative binding energy (ΔE_{REL}) values (in kcal mol^{-1}) of the chosen complexes at 25°C.

	Complex	**ΔE_{total}**	**$\Delta E_{relative}$**
M06-2X/def2-TZVP	[Mn(dpasam)(H₂O)]⁻	-152.009	0.000
	[Mn(dpaaaa)(H₂O)]⁻	-150.942	+1.066
	[Mn(cbda)(H₂O)]⁻	-146.047	+5.962
	[Mn(pydpa)(H₂O)]	-130.799	+21.210
M06/def2-TZVP	[Mn(dpasam)(H₂O)]⁻	-139.980	0.000
	[Mn(dpaaaa)(H₂O)]⁻	-138.410	+1.570
	[Mn(cbda)(H₂O)]⁻	-131.760	+8.220
	[Mn(pydpa)(H₂O)]	-117.141	+22.840

Table C4. Spin-orbit coupling (SOC) and spin-spin (SS) contributions to the D values (cm^{-1}) calculated using TPSS/def2-TZVP level of theory.

Complexes	D_{SOC}	D_{SS}	$\alpha \rightarrow \alpha$	$\beta \rightarrow \beta$	$\alpha \rightarrow \beta$	$\beta \rightarrow \alpha$
Complex 1	-0.0890	-0.0096	-0.0595	-0.0479	-0.0437	0.0620
Complex 2	-0.0214	-0.0127	-0.0664	-0.0753	0.0813	0.0389
Complex 3	-0.0183	-0.0127	-0.0660	-0.0735	0.0837	0.0376
Complex 4	-0.0375	-0.0127	-0.0433	-0.0605	0.0386	0.0277
Complex 5	-0.0400	-0.0141	-0.0624	-0.0732	0.0577	0.0379
Complex 6	-0.0409	-0.0120	-0.0591	-0.0714	0.0518	0.0378
Complex 7	-0.0407	-0.0113	-0.0639	-0.0759	0.0583	0.0409
Complex 8	-0.0628	-0.0132	-0.0421	-0.0612	0.0129	0.0275
Complex 9	0.0878	0.0216	0.0174	0.0057	0.1235	-0.0588
Complex 10	-0.0961	-0.0072	0.0362	0.0121	-0.1664	0.0219
Complex 11	-0.0956	-0.0072	0.0316	0.0103	-0.1611	0.0236
Complex 12	-0.1359	-0.0002	0.0118	-0.0365	-0.1577	0.0464
Complex 13	-0.0222	-0.0181	-0.0906	-0.0941	0.1148	0.0478
Complex 14	-0.0409	-0.0120	-0.0591	-0.0714	0.0518	0.0378
Complex 15	0.0305	-0.0012	0.0372	0.0448	-0.0281	-0.2334
Complex 16	-0.0263	-0.0139	-0.0349	-0.0534	0.0362	0.0258
Complex 17	-0.0252	-0.0196	-0.0977	-0.0994	0.1212	0.0507
Complex 18	-0.0213	-0.0132	-0.0669	-0.0754	0.0820	0.0389
Complex 19	-0.0196	-0.01291	-0.0653	-0.0721	0.0808	0.0369
Complex 20	-0.0445	-0.01159	-0.0387	-0.0565	0.0239	0.0266

Table C5. Spin-orbit coupling (SOC) and spin-spin (SS) contributions to the D values (cm^{-1}) calculated using M06-2X/def2-TZVP level of theory.

Complexes	D_{SOC}	D_{SS}	$\alpha \rightarrow \alpha$	$\beta \rightarrow \beta$	$\alpha \rightarrow \beta$	$\beta \rightarrow \alpha$
Complex 1	-0.0898	0.0097	-0.0679	-0.0879	0.0320	0.0339
Complex 2	-0.0461	-0.0073	-0.0619	-0.0669	0.0444	0.0383
Complex 3	-0.0361	-0.0072	-0.0611	-0.0657	0.0532	0.0374
Complex 4	0.0555	-0.0055	0.0183	0.0228	0.0264	-0.0119
Complex 5	-0.0570	-0.0028	-0.0472	-0.0523	0.0085	0.0339
Complex 6	-0.0651	-0.0018	-0.0426	-0.0479	-0.0077	0.0331
Complex 7	-0.0664	-0.0010	-0.0458	-0.0515	-0.0045	0.0355
Complex 8	-0.0464	-0.0047	-0.0325	-0.0379	0.0054	0.0186
Complex 9	0.8223	0.0077	-0.0729	-0.0480	1.0024	-0.0593
Complex 10	0.2615	0.0045	-0.1431	-0.1122	0.4968	0.0199
Complex 11	0.5533	0.0032	0.0119	0.0513	0.4908	-0.0007
Complex 12	0.4354	-0.0091	0.0757	0.1077	0.3164	-0.0644

Complex 13	0.0360	-0.0064	0.0005	0.0019	0.0394	-0.0059
Complex 14	-0.0651	-0.0018	-0.0426	-0.0479	-0.0077	0.0331
Complex 15	0.0833	-0.0016	0.0555	0.0579	-0.0031	-0.0271
Complex 16	0.0431	-0.0072	0.0207	0.0234	0.0139	-0.0149
Complex 17	-1.4536	-0.2574	-0.5460	-0.0822	-0.8623	0.0369
Complex 18	-0.0415	-0.0068	-0.0570	-0.0623	0.0404	0.0375
Complex 19	-0.0399	-0.0068	-0.0615	-0.0666	0.0494	0.0388
Complex 20	0.0555	-0.0055	0.0183	0.0228	0.0264	-0.0119

Table C6. ZFS parameter of all the complexes using M06-2X/def2-TZVP.

Complexes	D **(cm^{-1})**	E/D	$\triangle$ **(cm^{-1})**	$\triangle^2$ **(10^{20} s^{-2})**
Complex 1	-0.0995	0.1044	0.0826	2.4209
Complex 2	-0.0537	0.1017	0.0445	0.7039
Complex 3	-0.0429	0.1839	0.0369	0.4822
Complex 4	0.0499	0.1550	0.0422	0.6323
Complex 5	-0.0597	0.0358	0.0530	0.9980
Complex 6	-0.0667	0.2053	0.0578	1.1850
Complex 7	-0.0672	0.2171	0.0586	1.2198
Complex 8	-0.0509	0.2497	0.0454	0.7299
Complex 9	0.8299	0.0357	0.6789	163.7102
Complex 10	0.2659	0.2334	0.2342	19.4848
Complex 11	0.5564	0.0702	0.4577	74.3959
Complex 12	0.4263	0.0973	0.3529	44.2548
Complex 13	0.0297	0.2796	0.0269	0.2575
Complex 14	-0.0666	0.2053	0.0577	1.1831
Complex 15	0.0815	0.0924	0.0674	1.6132
Complex 16	0.0356	0.2536	0.0317	0.3572
Complex 17	-0.0561	0.2400	0.0496	0.8739
Complex 18	-0.0479	0.2491	0.0426	0.6437
Complex 19	-0.0464	0.0195	0.0379	0.5096
Complex 20	0.0473	0.1374	0.0397	0.5602

Table C7. Transition energies and corresponding D value contributions for Complex 1, computed via NEVPT2, include up to 17 quartets and 13 doublets.

Complex 1	**NEVPT2 Transition energies**	D **(cm^{-1})**	**Major CASSCF electronic Wave function $d_{yz}d_{xz}d_{x^2-y^2}d_{xy}d_{z^2}$**	E **(cm^{-1})**
^{6}S	0.000	0.000	**1 1 1 1 1**	0.000
^{4}G	22576.1	0.454	**0 2 1 1 1 (37%)**	0.044
	23065.7	-0.164	**0 1 2 1 1 (38%)**	0.166

	25126.9	-0.130		-0.131
	26544.1	-0.012		-0.009
	26776.7	-0.000		-0.002
	27226.1	-0.001		-0.000
	27606.8	-0.000		0.000
	27710.5	-0.000		-0.000
	27811.4	-0.000		0.000
^{4}P	31139.5	-0.448	**1 1 1 0 2 (52%)**	-0.388
	31848.8	-0.053		0.055
	32085.3	0.142		-0.008
^{4}D	32346.2	-0.009		-0.009
	33360.6	-0.192		0.153
	33865.5	0.215		0.034
	34441.3	-0.236		0.104
	35316.5	0.464	**2 0 1 1 1 (22%)**	-0.004
^{2}I	32691.3	0.000		0.000
	34545.6	0.000		0.000
	34772.2	0.000		0.000
	35815.8	0.000		0.000
	36542.4	0.000		0.000
	36976.9	0.000		0.000
	37114.0	0.000		0.000
	37829.1	0.000		0.000
	38836.8	0.000		0.000
	39297.3	0.000		0.000
	39548.1	0.000		0.000
	39596.8	0.000		0.000
	39954.5	0.000		0.000

Table C8. Transition energies and corresponding *D* value contributions for Complex 2, computed via NEVPT2, include up to 17 quartets.

Complex 2	**NEVPT2 Transition energies**	***D* (cm^{-1})**	**Major CASSCF electronic Wave function $d_{xz}d_{yz}d_{x^2-y^2}d_{xy}d_{z^2}$**	***E* (cm^{-1})**
^{6}S	0.000	0.000	**1 1 1 1 1**	0.000
^{4}G	22142.4	0.643	**2 1 1 1 0 (66%)**	-0.012
	23110.8	-0.274	**1 2 1 1 0 (53%)**	0.269
	25199.9	-0.164		-0.173
	26560.3	-.0003		-0.007

	26755.4	-0.002		0.001
	27212.2	-0.000		0.000
	27774.2	-0.000		0.000
	27828.2	-0.000		0.000
	27861.6	-0.000		0.000
^{4}P	31144.1	-0.043	**1 1 0 2 1 (55%)**	0.019
	31919	-0.432		-0.422
	32373.5	0.053		-0.080
^{4}D	32389.9	-0.003		0.003
	33588.6	-0.223		0.222
	33744.3	-0.017		-0.056
	34495.7	-0.265		0.262
	36036.1	0.760	**0 1 1 1 2 (42%)**	-0.025
	39919.3	0.000		0.000

Table C9. Transition energies and corresponding *D* value contributions for Complex 3, computed via NEVPT2, include up to 17 quartets.

Complex 3	**NEVPT2 Transition energies**	***D* (cm^{-1})**	**Major CASSCF electronic Wave function $d_{xz}d_{yz}d_{x^2-y^2}d_{xy}d_{z^2}$**	***E* (cm^{-1})**
^{6}S	0.000	0.000	**1 1 1 1 1**	0.000
^{4}G	22165.4	0.636	**1 0 1 1 2 (53%)**	0.012
	23122.3	-0.275	**1 0 1 2 1 (49%)**	-0.227
	24978.8	-0.174		0.155
	26568.3	-0.001		0.003
	26773.4	-0.001		-0.000
	27154.5	-0.000		-0.000
	27783.6	-0.000		-0.000
	27836.9	-0.000		-0.000
	27871.0	-0.026		-0.000
^{4}P	31219.2	-0.333	**1 1 0 2 1 (40%)**	0.256
	32289.3	-0.039		0.138
	32382.3	-0.003		-0.001

^{4}D	33595.1	-0.239		-0176
	33798.0	-0.020		-0.066
	34467.3	-0.245		-0.226
	35998.1	0.750	**1 1 2 1 0 (42%)**	-0.012
	44952.6	-0.001		0.005

Table C10. Transition energies and corresponding *D* value contributions for Complex 4, computed via NEVPT2, include up to 17 quartets.

Complex 4	**NEVPT2 Transition energies**	***D* (cm^{-1})**	**Major CASSCF electronic Wave function $d_{yz}d_{xz}d_{x^2-y^2}d_{xy}d_{z^2}$**	***E* (cm^{-1})**
^{6}S	0.000	0.000	**1 1 1 1 1**	0.000
^{4}G	21692.4	0.716	**0 1 1 2 1 (50%)**	-0.000
	22430.0	-0.303	**0 2 1 1 1 (47%)**	0.292
	25387.1	-0.109		-0.107
	26092.9	-0.032		-0.032
	26288.6	-0.029		-0.019
	27335.0	-0.000		-0.000
	27689.7	-0.000		-0.000
	27743.1	-0.000		-0.000
	27819.4	-0.000		0.000
^{4}P	30374.4	-0.056		0.046
	31101.0	-0.076		-0.150
	32169.3	-0.382	**1 1 2 1 0 (42%)**	-0.404
^{4}D	32636.6	0.000		0.000
	33397.6	-0.002		0.002
	33589.8	-0.050		-0.045
	35274.4	-0.444		0.422
	36445.4	0.803	**2 1 1 0 1 (31%)**	-0.002

Table C11. Transition energies and corresponding *D* value contributions for Complex 5, computed via NEVPT2, include up to 17 quartets.

Complex 5	**NEVPT2 Transition energies**	***D* (cm^{-1})**	**Major CASSCF electronic Wave function $d_{yz}d_{xz}d_{x^2-y^2}d_{xy}d_{z^2}$**	***E* (cm^{-1})**
^{6}S	0.000	0.000	**1 1 1 1 1**	0.000

^{4}G	23139.6	-0.261	**2 1 1 0 1 (82%)**	-0.100
	23571.7	-0.248	**1 2 1 0 1 (43%)**	0.081
	26792.8	0.034		0.000
	26989.8	0.000		-0.000
	27277.8	-0.000		0.000
	27373.7	0.000		0.000
	27407.6	0.018		0.000
	27533.2	0.000		0.000
	27599.0	0.000		-0.000
^{4}P	30518.6	1.452	**1 2 0 1 1 (24%)**	0.018
	31775.8	-0.013		0.018
	32178.5	-0.151		-0.147
^{4}D	32940.7	-0.110		0.136
	32954.1	-0.100		-0.025
	33236.4	-0.279	**1 0 2 1 1 (43%)**	0.278
	33240.5	-0.127		-0.059
	34000.9	-0.237		-0.204

Table C12. Transition energies and corresponding D value contributions for Complex 6, computed via NEVPT2, include up to 17 quartets and 13 doublets.

Complex 6	**NEVPT2 Transition energies**	***D* (cm^{-1})**	**Major CASSCF electronic Wave function $d_{xz}d_{yz}d_{x^2-y^2}d_{xy}d_{z^2}$**	***E* (cm^{-1})**
^{6}S	0.000	0.000	**1 1 1 1 1**	0.000
^{4}G	22704.6	-0.268	**2 1 1 1 0 (55%)**	0.210
	23025.4	-0.280	**1 2 1 1 0 (46%)**	-0.206
	26650.5	0.055		0.000
	26952.1	0.000		0.000
	27158.9	0.004		0.000
	27316.7	0.003		0.000
	27354.6	0.022		0.000
	27522.5	-0.000		-0.000
	27666.9	0.000		-0.000
^{4}P	30705.2	1.418	**1 1 0 2 1 (55%)**	0.020
	31735.5	-0.004		-0.007
	31871.5	-0.039		-0.015
^{4}D	32368.9	-0.001		-0.000
	32920.5	-0.095		-0.069
	33159.0	-0.138		-0.132
	34185.9	-0.431	**0 1 1 1 2 (46%)**	0.457

	34601.5	-0.268		-0.263

Table C13. Transition energies and corresponding *D* value contributions for Complex 7, computed via NEVPT2, include up to 17 quartets and 13 doublets.

Complex 7	**NEVPT2 Transition energies**	***D* (cm^{-1})**	**Major CASSCF electronic Wave function** $d_{yz}d_{xz}d_{x^2-y^2}d_{xy}d_{z^2}$	***E* (cm^{-1})**
^{6}S	0.000	0.000	**1 1 1 1 1**	0.000
^{4}G	22679.5	-0.269	**0 1 1 2 1 (55%)**	-0.281
	22996.0	-0.280	**1 1 0 2 1 (72%)**	-0.275
	26717.0	0.047		0.000
	26960.2	0.000		0.000
	27126.1	0.007		0.000
	27308.7	0.005		0.000
	27336.0	0.021		0.000
	27524.3	-0.000		-0.000
	27660.9	0.000		-0.000
4p	30701.2	1.421	**0 2 1 1 1 (59%)**	0.022
	31794.6	-0.002		-0.006
	31873.0	-0.023		-0.019
^{4}D	32312.9	-0.002		-0.003
	32978.1	-0.133		-0.127
	33047.5	-0.116		-0.093
	34197.9	-0.438	**1 2 0 1 1 (30%)**	0.472
	34600.6	-0.263	**2 1 0 1 1 (53%)**	-0.258

Table C14. Transition energies and corresponding *D* value contributions for Complex 8, computed via NEVPT2, include up to 17 quartets.

Complex 8	NEVPT2 Transition energies	*D* (cm^{-1})	Major CASSCF electronic Wave function $d_{xz}d_{yz}d_{x^2-y^2}d_{xy}d_{z^2}$	*E* (cm^{-1})
^6S	0.000	0.000	**1 1 1 1 1**	0.000
^4G	22082.1	-0.279	**1 2 1 0 1 (69%)**	-0.144
	22189.5	-0.240	**2 1 1 0 1 (63%)**	0.138
	26425.4	0.010		0.000
	26511.1	-0.000		-0.000
	27249.8	0.000		0.000
	27338.6	0.000		-0.000
	27426.1	0.015		0.000
	27542.7	0.000		0.000
	27620.1	0.001		-0.000
^4P	30386.6	1.333	**0 2 1 1 1 (42%)**	0.000
	30945.1	-0.033		0.011
	31159.4	-0.045		-0.016
^4D	32567.5	0.002		0.000
	32725.9	0.009		-0.001
	33132.4	-0.017		0.005
	35171.4	-0.394	**2 1 0 1 1 (50%)**	0.394
	35405.4	-0.391	**0 1 1 1 2 (26%)**	-0.390

Table C15. Transition energies and corresponding *D* value contributions for Complex 9, computed via NEVPT2, include up to 17 quartets and 13 doublets.

Complex 9	NEVPT2 Transition energies	*D* (cm^{-1})	Major CASSCF electronic Wave function $d_{yz}d_{xz}d_{x^2-y^2}d_{xy}d_{z^2}$	*E* (cm^{-1})
^6S	0.000	0.000	**1 1 1 1 1**	0.000
^4G	23318.6	-0.236	**2 1 1 1 0 (45%)**	-0.097
	23977.3	-0.222	**1 2 1 1 0 (56%)**	0.110
	27172.0	0.013		-0.000
	27253.8	0.000		0.000
	27391.0	0.002		0.000
	27410.3	0.001		0.000
	27636.0	0.001		-0.000
	27669.7	-0.000		0.000
	27708.8	1.340	**1 1 0 2 1 (51%)**	-0.070

^{4}P	30430.5	-0.181		0.068
	32567.2	-0.146		0.055
	32714.8	0.015		0.005
^{4}D	32789.3	-0.028		0.019
	32852.9	-0.188		0.084
	32913.1	-0.208	**1 0 1 1 2 (21%)**	-0.222
	33152.5	-0.189		0.043
	33907.2	0.000		0.000

Table C16. Transition energies and corresponding *D* value contributions for Complex 10, computed via NEVPT2, include up to 17 quartets.

Complex 10	**NEVPT2 Transition energies**	***D* (cm^{-1})**	**Major CASSCF electronic Wave function $d_{xz}d_{yz}d_{x^2-y^2}d_{xy}d_{z^2}$**	***E* (cm^{-1})**
^{6}S	0.000	0.000	**1 1 1 1 1**	0.000
^{4}G	22947.6	-0.510	**1 2 1 1 0 (41%)**	-0.013
	23187.5	0.266	**2 1 1 1 0 (41%)**	0.264
	26915.0	0.015		-0.014
	27084.4	0.004		-0.005
	27193.9	0.002		-0.002
	27308.1	0.001		-0.001
	27461.8	0.004		-0.004
	27568.8	0.000		0.000
	27692.5	0.000		-0.000
^{4}P	30505.7	0.605	**1 1 0 2 1 (44%)**	-0.688
	32266.2	-0.029		0.002
	32331.5	-0.000		-0.010
^{4}D	32543.0	0.101		0.107
	32638.7	0.008		0.069
	33101.3	-0.050		0.173
	33934.7	-0.332	**0 1 1 1 2 (47%)**	0.019
	34088.6	-0.110		0.069

Table C17. Transition energies and corresponding *D* value contributions for Complex 11, computed via NEVPT2, include up to 17 quartets.

Complex 11	**NEVPT2 Transition energies**	***D* (cm^{-1})**	**Major CASSCF electronic Wave function $d_{xz}d_{yz}d_{x^2-y^2}d_{xy}d_{z^2}$**	***E* (cm^{-1})**
^{6}S	0.000	0.000	**1 1 1 1 1**	0.000

^{4}G	23132.0	-0.239	**1 1 0 1 2 (45%)**	-0.256
	23317.0	-0.267	**0 1 1 2 1 (48%)**	0.260
	27010.0	0.024		0.000
	27164.6	0.016		-0.000
	27282.4	0.004		0.000
	27390.4	0.001		-0.000
	27548.6	0.009		-0.000
	27649.3	-0.000		-0.000
	27769.4	0.000		0.000
^{4}P	30598.8	1.371	**0 1 2 1 1 (42%)**	-0.034
	32319.3	-0.032		-0.033
	32498.1	-0.002		-0.003
^{4}D	32528.6	-0.127		0.126
	32850.6	-0.009		-0.002
	33101.9	-0.125		0.045
	33937.1	-0.426	**1 0 2 1 1 (52%)**	-0.198
	34121.2	-0.223		0.087

Table C18. Transition energies and corresponding *D* value contributions for Complex 12, computed via NEVPT2, include up to 17 quartets.

Complex 12	**NEVPT2 Transition energies**	***D* (cm^{-1})**	**Major CASSCF electronic Wave function $d_{yz}d_{xz}d_{x^2-y^2}d_{xy}d_{z^2}$**	***E* (cm^{-1})**
^{6}S	0.000	0.000	**1 1 1 1 1**	0.000
^{4}G	23390.0	-0.089	**2 1 1 1 0 (62%)**	-0.174
	24107.6	-0.173	**1 2 1 1 0 (36%)**	0.131
	26375.4	0.064		0.004
	26813.9	0.002		-0.000
	27280.4	0.005		0.001
	27489.1	-0.000		0.001
	27543.4	0.000		0.000
	27582.2	-0.000		-0.000
	27685.4	0.001		0.000
^{4}P	30827.5	0.756	**1 1 0 2 1 (40%)**	0.049
	31772.4	-0.179	**1 2 0 1 1 (32%)**	0.159
	31879.7	-0.062		-0.064
^{4}D	33083.2	-0.209	**1 0 1 1 2 (14%)**	0.037
	33171.4	-0.111		-0.097
	33290.5	-0.040		0.040
	33342.0	-0.017		0.008

	34217.0	0.020		-0.099

Table C19. Transition energies and corresponding *D* value contributions for Complex 13, computed via NEVPT2, include up to 17 quartets.

Complex 13	NEVPT2 Transition energies	*D* (cm^{-1})	Major CASSCF electronic Wave function $d_{yz}d_{xz}d_{x^2-y^2}d_{xy}d_{z^2}$	*E* (cm^{-1})
^6S	0.000	0.000	**1 1 1 1 1**	0.000
^4G	22473.2	0.458	**2 1 1 0 1 (47%)**	0.042
	22985.3	-0.176	**2 1 1 0 1 (39%)**	0.162
	24983.7	-0.137		-0.135
	26464.7	-0.010		-0.007
	26751.5	0.001		-0.001
	27174.4	-0.001		-0.000
	27603.2	-0.000		0.000
	27702.5	-0.000		-0.000
	27800.0	-0.000		0.000
^4P	31104.0	-0.422	**2 1 0 1 1 (60%)**	-0.352
	31838.3	-0.050		0.050
	32127.9	0.126		-0.013
^4D	32284.6	-0.013		-0.009
	33365.8	-0.199		0.147
	33915.9	0.219		0.029
	34467.8	-0.247		0.100
	35357.7	0.472	**1 0 2 1 1 (26%)**	-0.006

Table C20. Transition energies and corresponding *D* value contributions for Complex 14, computed via NEVPT2, include up to 17 quartets.

Complex 14	NEVPT2 Transition energies	*D* (cm^{-1})	Major CASSCF electronic Wave function $d_{xz}d_{yz}d_{x^2-y^2}d_{xy}d_{z^2}$	*E* (cm^{-1})
^6S	0.000	0.000	**1 1 1 1 1**	0.000
^4G	22381.1	0.512	**2 1 1 1 0 (57%)**	-0.004
	23196.6	-0.262	**1 2 1 1 0 (47%)**	-0.063
	25083.4	-0.188		0.044
	26465.6	-0.006		0.002
	26750.4	-0.003		0.003
	27274.7	-0.000		0.000
	27774.8	-0.000		-0.000

	27827.3	-0.000		-0.000
	27856.9	-0.000		-0.000
^{4}P	31139.0	-0.060		-0.061
	31872.5	0.187		0.018
	32473.2	-0.434	**1 1 0 2 1 (49%)**	0.160
^{4}D	32498.7	-0.001		0.000
	33618.5	-0.209		-0.022
	33757.0	-0.070		0.051
	34406.5	-0.267		-0.127
	35832.5	0.823	**0 1 1 1 2 (39%)**	0.000

Table C21. Transition energies and corresponding D value contributions for Complex 15, computed via NEVPT2, include up to 17 quartets.

Complex 15	**NEVPT2 Transition energies**	***D* (cm^{-1})**	**Major CASSCF electronic Wave function $d_{xz}d_{yz}d_{x^2-y^2}d_{xy}d_{z^2}$**	***E* (cm^{-1})**
^{6}S	0.000	0.000	**1 1 1 1 1**	0.000
^{4}G	22163.3	0.617	**1 2 1 0 1 (80%)**	0.016
	22649.8	-0.272	**2 1 1 0 1 (76%)**	-0.259
	23412.5	-0.201		0.235
	26197.3	0.002		-0.000
	26546.7	-0.000		0.001
	26661.5	-0.001		-0.000
	27203.8	-0.000		-0.000
	27637.7	-0.000		0.000
	27882.3	-0.000		-0.000
^{4}P	31076.9	-0.003		-0.001
	31754.9	-0.257		0.250
	32075.3	0.066		0.055
^{4}D	32398.9	-0.043		0.019
	33478.3	-0.330	**0 1 1 2 1 (39%)**	-0.318
	33897.7	-0.201		-0.200
	34403.1	0.000		0.150
	35744.4	0.646	**1 1 2 1 0 (22%)**	0.063

Table C22. Transition energies and corresponding *D* value contributions for Complex 16, computed via NEVPT2, include up to 17 quartets.

Complex 16	NEVPT2 Transition energies	*D* (cm^{-1})	Major CASSCF electronic Wave function $d_{yz}d_{xz}d_{x^2-y^2}d_{xy}d_{z^2}$	*E* (cm^{-1})
^6S	0.000	0.000	**1 1 1 1 1**	0.000
^4G	22156.6	0.624	**2 1 1 0 1 (46%)**	-0.011
	22776.6	-0.276	**1 2 1 0 1 (42%)**	0.274
	25252.8	-0.086		-0.093
	26164.0	-0.017		-0.009
	26364.5	-0.039		-0.044
	27426.7	-0.000		0.000
	27644.5	-0.000		-0.000
	27666.6	-0.000		0.000
	27795.3	-0.000		0.000
^4P	30342.2	-0.079		0.072
	31203.5	0.034		-0.073
	32027.1	-0.392		-0.472
^4D	32770.0	-0.007		0.008
	33294.8	-0.080		0.082
	33559.8	0.001		-0.049
	34995.0	-0.348	**1 0 1 2 1 (19%)**	0.344
	36010.0	0.692	**0 1 1 2 1 (24%)**	-0.023

Table C23. Transition energies and corresponding *D* value contributions for Complex 17, computed via NEVPT2, include up to 17 quartets.

Complex 17	NEVPT2 Transition energies	*D* (cm^{-1})	Major CASSCF electronic Wave function $d_{yz}d_{xz}d_{x^2-y^2}d_{xy}d_{z^2}$	*E* (cm^{-1})
^6S	0.000	0.000	**1 1 1 1 1**	0.000
^4G	22550.4	0.468	**1 2 1 1 0 (48%)**	0.036
	23076.5	-0.180	**2 1 1 1 0 (49%)**	0.176
	25153.7	-0.123		-0.129
	26560.7	-0.012		-0.010
	26764.7	-0.000		-0.003
	27235.3	-0.001		-0.000
	27591.8	-0.000		0.000
	27701.6	-0.000		-0.000

	27800.9	-0.000		0.000
^{4}P	31107.1	-0.452	**1 1 0 2 1 (36%)**	-0.396
	31838.2	-0.055		0.058
	32023.9	0.148		-0.009
^{4}D	32361.2	-0.010		-0.010
	33314.0	-0.196		0.159
	33815.5	0.220		0.025
	34454.7	-0.235		0.115
	35341.1	0.458	**1 0 1 1 2 (29%)**	-0.006

Table C24. Transition energies and corresponding *D* value contributions for Complex 18, computed via NEVPT2, include up to 17 quartets.

Complex 18	**NEVPT2 Transition energies**	***D* (cm^{-1})**	**Major CASSCF electronic Wave function $d_{yz}d_{xz}d_{x^2-y^2}d_{xy}d_{z^2}$**	***E* (cm^{-1})**
^{6}S	0.000	0.000	**1 1 1 1 1**	0.000
^{4}G	22091.2	0.620	**2 1 1 1 0 (65%)**	-0.007
	23115.6	-0.273	**1 2 1 1 0 (52%)**	0.244
	25182.9	-0.170		-0.164
	26550.1	-0.002		-0.005
	26751.8	-0.002		0.001
	27196.9	-0.000		0.000
	27770.0	-0.000		0.000
	27823.5	-0.000		0.000
	27855.0	-0.000		0.000
^{4}P	31142.9	-0.033		0.030
	31906.6	-0.445	**1 1 0 2 1 (59%)**	-0.408
	32353.8	0.078		-0.067
^{4}D	32429.1	-0.004		0.003
	33593.8	-0.226		0.212
	33725.9	-0.033		-0.043
	34460.4	-0.256		0.226
	36053.0	0.777	**0 1 1 1 2 (42%)**	-0.021

Table C25. Transition energies and corresponding *D* value contributions for Complex 19, computed via NEVPT2, include up to 17 quartets.

Complex 19	NEVPT2 Transition energies	*D* (cm^{-1})	Major CASSCF electronic Wave function $d_{xz}d_{yz}d_{x^2-y^2}d_{xy}d_{z^2}$	*E* (cm^{-1})
^6S	0.000	0.000	**1 1 1 1 1**	0.000
^4G	22065.0	0.640	**1 2 1 0 1 (27%)**	-0.014
	23171.0	-0.269	**2 1 1 0 1 (29%)**	0.237
	25056.3	-0.127		-0.163
	26583.2	-0.000		-0.004
	26781.1	-0.001		0.001
	27133.9	-0.000		0.000
	27760.4	-0.000		-0.000
	27811.6	-0.000		0.000
	27839.5	-0.000		0.000
^4P	31173.3	-0.027		0.018
	31994.4	-0.423	**2 1 0 1 1 (23%)**	-0.369
	32264.9	0.056		-0.070
^4D	32434.2	-0.006		0.006
	33527.6	-0.260		0.231
	33777.8	-0.017		-0.061
	34365.8	-0.241		0.214
	36056.6	0.755	**0 1 2 1 1 (32%)**	-0.026

Table C26. Transition energies and corresponding *D* value contributions for Complex 20, computed via NEVPT2, include up to 17 quartets.

Complex 20	NEVPT2 Transition energies	*D* (cm^{-1})	Major CASSCF electronic Wave function $d_{yz}d_{xz}d_{x^2-y^2}d_{xy}d_{z^2}$	*E* (cm^{-1})
^6S	0.000	0.000	**1 1 1 1 1**	0.000
^4G	21525.4	0.667	**2 1 1 1 0 (58%)**	-0.019
	22160.4	-0.296	**1 2 1 1 0 (57%)**	0.314
	25229.0	-0.082		-0.092
	26195.1	-0.004		-0.000
	26423.1	-0.042		-0.052
	27264.1	-0.000		0.000
	27636.8	0.000		0.000

	27674.0	-0.000		0.000
	27784.1	-0.000		0.000
^{4}P	30272.9	-0.062		0.034
	31317.7	-0.396	**1 1 0 2 1 (38%)**	-0.395
	31732.6	0.065		-0.132
^{4}D	32485.5	0.000		-0.002
	33369.2	-0.071		0.073
	33628.0	-0.006		-0.055
	35438.8	-0.374		0.378
	36520.0	0.692	**0 1 1 1 2 (34%)**	-0.032

Table C27. Racah-parameters and spin-orbit coupling parameters for free Metal ion (Mn^{2+}) and complexes AILFT parameters (in cm^{-1}) from AILFT calculations.

Metal	**Metal parameters**	**Complex**	**Complex parameters**
Mn^{2+}	**B^0=952.4 ζ^0=319.6**	Complex 1	B=900.3 ζ=313.6
		Complex 2	B=903.9 ζ=314.1
		Complex 3	B=904.0 ζ=314.19
		Complex 4	B=903.7 ζ=314.0
Mn^{2+}	**B^0=952.4 ζ^0=319.6**	Complex 5	B=883.0 ζ=312.14
		Complex 6	B=886.5 ζ=312.26
		Complex 7	B=886.4 ζ=312.27
		Complex 8	B=888.9 ζ=312.39
Mn^{2+}	**B^0=952.4 ζ^0=319.6**	Complex 9	B=882.1 ζ=312.29
		Complex 10	B=886.4 ζ=310.18
		Complex 11	B=883.4 ζ =311.27
		Complex 12	B=886.1 ζ=310.56
		Complex 13	B=900.7

			ζ=313.60
Mn^{2+}	**B^0=952.4 ζ^0=319.6**	Complex 14	B=902.7 ζ=314.07
		Complex 15	B=904.7 ζ=316.1
		Complex 16	B=902.2 ζ=313.78
Mn^{2+}	**B^0=952.4 ζ^0=319.6**	Complex 17	B=899.3 ζ=313.60
		Complex 18	B=903.5 ζ=314.11
		Complex 19	B=902.3 ζ=314.07
		Complex 20	B=904.1 ζ=313.9

Table C28. Topological parameters of the complexes analyzed here; the electron density at bond critical points (ρ_{bcp}), its Laplacian ($\nabla^2_{\rho(bcp)}$), and the kinetic electron energy density (G_{bcp}). The results obtained at M06-2X/def2-TZVP level of approximation correspond to Mn-O, Mn-S, and Mn-Se bonds.

Complex	ρ_{bcp}	$\nabla^2_{\rho(bcp)}$	G_{bcp}
Complex 1	Mn-O1=0.0508 Mn-O2=0.0467	Mn-O1=0.2415 Mn-O2=0.2174	Mn-O1=0.0664 Mn-O2=0.0595
Complex 2	Mn-O1=0.0509 Mn-O2=0.0497	Mn-O1=0.2431 Mn-O2=0.2352	Mn-O1=0.0668 Mn-O2=0.0646
Complex 3	Mn-O1=0.0495 Mn-O2=0.517	Mn-O1=0.2339 Mn-O2=0.2477	Mn-O1=0.0642 Mn-O2=0.0681
Complex 4	Mn-O2=0.0492 Mn-O3=0.0511	Mn-O2=0.2295 Mn-O3=0.2412	Mn-O2=0.0632 Mn-O3=0.0665
Complex 5	Mn-S1= 0.0374 Mn-S2=0.0324	Mn-S1= 0.1001 Mn-S2=0.0869	Mn-S1= 0.0306 Mn-S2=0.0257
Complex 6	Mn-S1=0.0340 Mn-S2=0.0392	Mn-S1=0.0911 Mn-S2=0.1059	Mn-S1=0.0272 Mn-S2=0.0326
Complex 7	Mn-S1=0.0339 Mn-S2=0.0389	Mn-S1=0.0908 Mn-S2=0.1053	Mn-S1=0.0271 Mn-S2=0.0323
Complex 8	Mn-S1=0.0330 Mn-S2=0.0376	Mn-S1=0.0869 Mn-S2=0.0995	Mn-S1=0.0260 Mn-S2=0.0305
Complex 9	Mn-Se1=0.0344 Mn-Se2=0.0276	Mn-Se1=0.0798 Mn-Se2=0.0639	Mn-Se1=0.0249 Mn-Se2=0.0190
Complex 10	Mn-Se1=0.0289 Mn-Se2=0.0364	Mn-Se1=0.0666 Mn-Se2=0.0853	Mn-Se1=0.0200 Mn-Se2=0.0269
Complex 11	Mn-Se1=0.0281 Mn-Se2=0.0366	Mn-Se1=0.0649 Mn-Se2=0.0857	Mn-Se1=0.0194 Mn-Se2=0.0270
Complex 12	Mn-Se1=0.0365 Mn-Se2=0.0272	Mn-Se1=0.0833 Mn-Se2=0.0622	Mn-Se1=0.0265 Mn-Se2=0.0187

Table C29. NPA charge analysis obtained at the M06-2X/def2-TZVP level of theory.

Complex 1		**Complex 5**		**Complex 9**	
Atom	**Charge**	**Atom**	**Charge**	**Atom**	**Charge**
Mn	1.036	Mn	0.601	Mn	0.566
O1	-0.744	S1	-0.243	Se1	-0.233
O2	-0.714	S2	-0.188	Se2	-0.170
Complex 2		**Complex 6**		**Complex 10**	
Atom	**Charge**	**Atom**	**Charge**	**Atom**	**Charge**
Mn	1.132	Mn	0.694	Mn	0.660
O1	-0.723	S1	-0.214	Se1	-0.660
O2	-0.733	S2	-0.275	Se2	-0.285
Complex 3		**Complex 7**		**Complex 11**	
Atom	**charge**	**Atom**	**charge**	**Atom**	**Charge**
Mn	1.146	Mn	0.696	Mn	0.662
O1	-0.727	S1	-0.272	Se1	-0.286
O2	-0.718	S2	-0.216	Se2	-0.187
Complex 4		**Complex 8**		**Complex 12**	
Atom	**charge**	**Atom**	**Charge**	**Atom**	**charge**
Mn	1.1016	Mn	0.551	Mn	0.499
O1	-0.732	S1	-0.205	Se1	-0.225
O2	-0.736	S2	-0.240	Se2	-0.169

Table C30. Mayer bond order obtained at the M06-2X/def2-TZVP level of theory.

Complex	**Bond order**	**Complex**	**Bond order**	**Complex**	**Bond order**
Complex 1	Mn-O1=0.264 Mn-O2=0.296	**Complex 5**	Mn-S1=0.465 Mn-S2=0.384	**Complex 9**	Mn-Se1=0.452 Mn-Se2=0.397
Complex 2	Mn-O1=0.309 Mn-O2=0.289	**Complex 6**	Mn-S1=0.467 Mn-S2=0.401	**Complex 10**	Mn-Se1=0.465 Mn-Se2=0.387
Complex 3	Mn-O1=0.309 Mn-O2=0.281	**Complex 7**	Mn-S1=0.465 Mn-S2=0.400	**Complex 11**	Mn-Se1=0.456 Mn-Se2=0.378
Complex 4	Mn-O1=0.283 Mn-O2=0.278	**Complex 8**	Mn-S1=0.474 Mn-S2=0.438	**Complex 12**	Mn-Se1=0.492 Mn-Se2=0.356

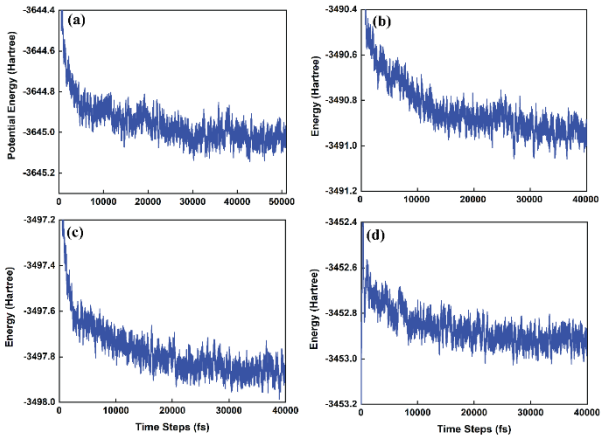

Figure C1. Potential energy (Hartree) plots at 25°C for AIMD trajectories of simulated complexes. a) $[Mn(dpasam)(H_2O)]^-$, b) $[Mn(dpaaa)(H_2O)]^-$, c) $[Mn(cbda)(H_2O)]^-$, d) $[Mn(pydpa)(H_2O)]$ complexes.

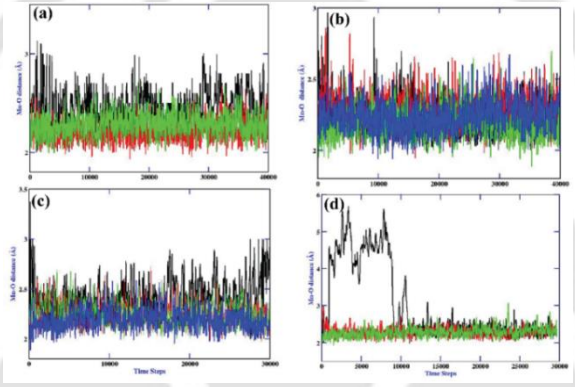

Figure C2. Mn-O bond distances, at 25°C during the AIMD trajectories of a) $[Mn(dpasam)(H_2O)]^-$, b) $[Mn(dpaaa)(H_2O)]^-$, c) $[Mn(cbda)(H_2O)]^-$, d) $[Mn(pydpa)(H_2O)]$ complexes. Black, blue, red, and green curves represent the Mn-O distances for individual oxygen atoms along the AIMD trajectory.

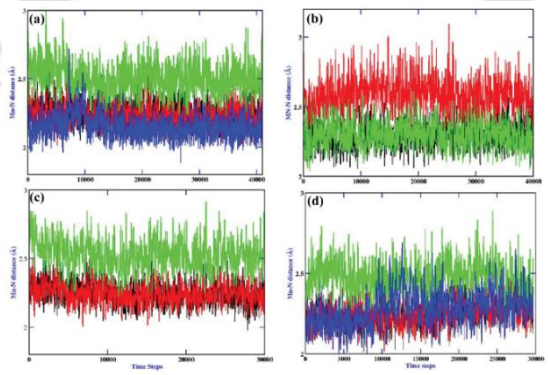

Figure C3. Mn-N bond distances, at 25°C during the AIMD trajectories of a) $[Mn(dpasam)(H_2O)]^-$, b) $[Mn(dpaaa)(H_2O)]^-$, c) $[Mn(cbda)(H_2O)]^-$, d) $[Mn(pydpa)(H_2O)]$ complexes.

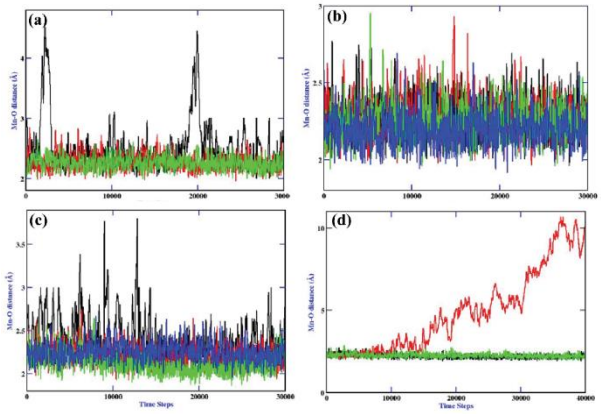

Figure C4. Mn-O bond distances, at 90°C during the AIMD trajectories of a) [Mn(dpasam)(H_2O)]$^-$, b) [Mn(dpaaa)(H_2O)]$^-$, c) [Mn(cbda)(H_2O)]$^-$, d) [Mn(pydpa)(H_2O)] complexes.

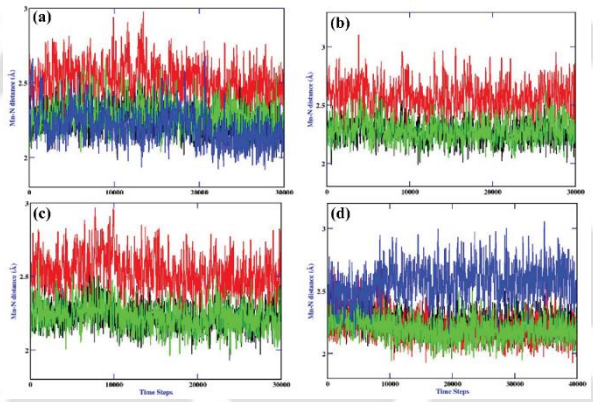

Figure C5. Mn-N bond distances, at 90°C during the AIMD trajectories of a) [Mn(dpasam)(H_2O)]$^-$, b) [Mn(dpaaa)(H_2O)]$^-$, c) [Mn(cbda)(H_2O)]$^-$, d) [Mn(pydpa)(H_2O)] complexes.

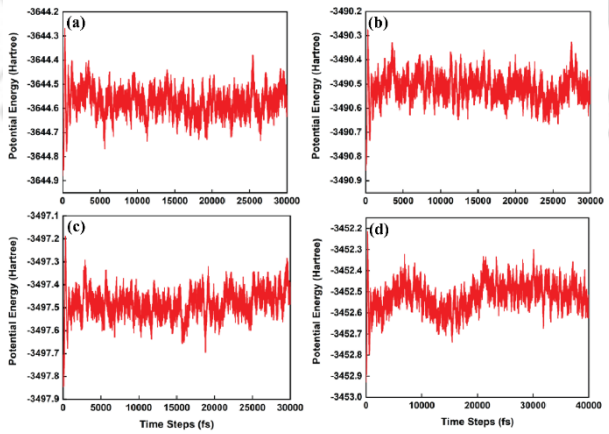

Figure C6. Potential energy (Hartree) plots at 90°C for AIMD trajectories of simulated complexes. a) [Mn(dpasam)(H_2O)]$^-$, b) [Mn(dpaaa)(H_2O)]$^-$, c) [Mn(cbda)(H_2O)]$^-$, d) [Mn(pydpa)(H_2O)] complex.

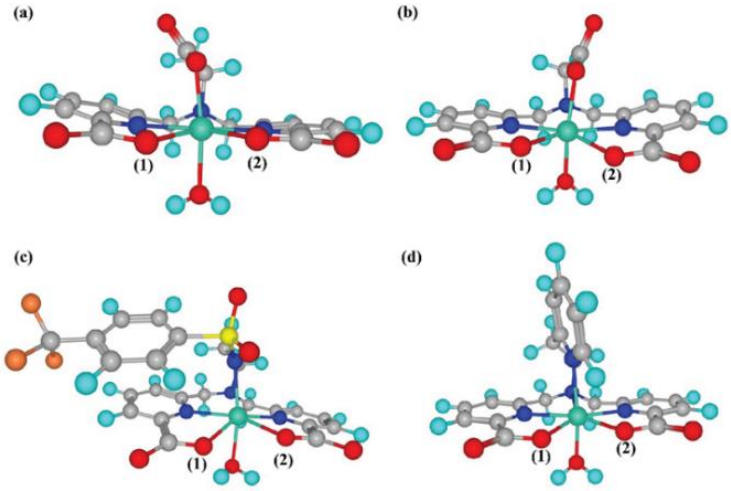

Figure C7. Optimized structure of a) $[Mn(dpasam)(H_2O)]^-$, b) $[Mn(dpaaa)(H_2O)]^-$, c) $[Mn(cbda)(H_2O)]^-$, and d) $[Mn(pydpa)(H_2O)]$ PBE/DZVP with GTH pseudopotential.

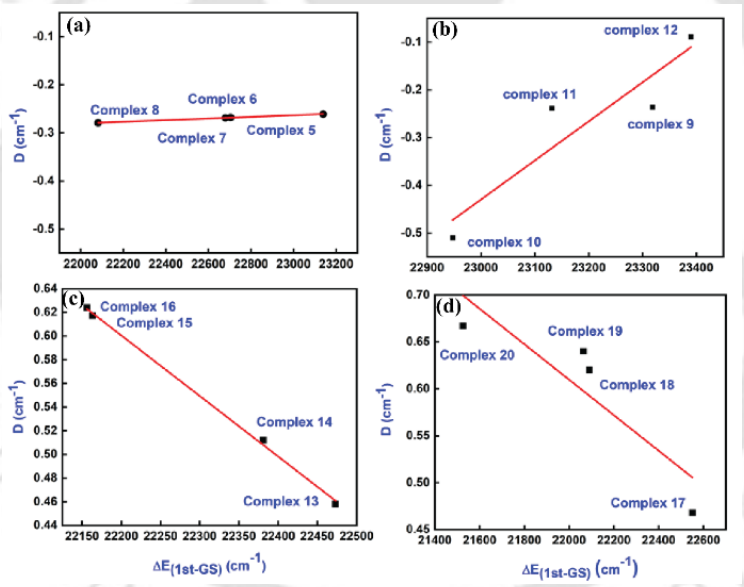

Figure C8. Variation of *D* values of Class II (a, b) and Class III (c, d) complexes with the energy difference between the ground and first excited $\triangle E_{(1st\text{-}GS)}$.

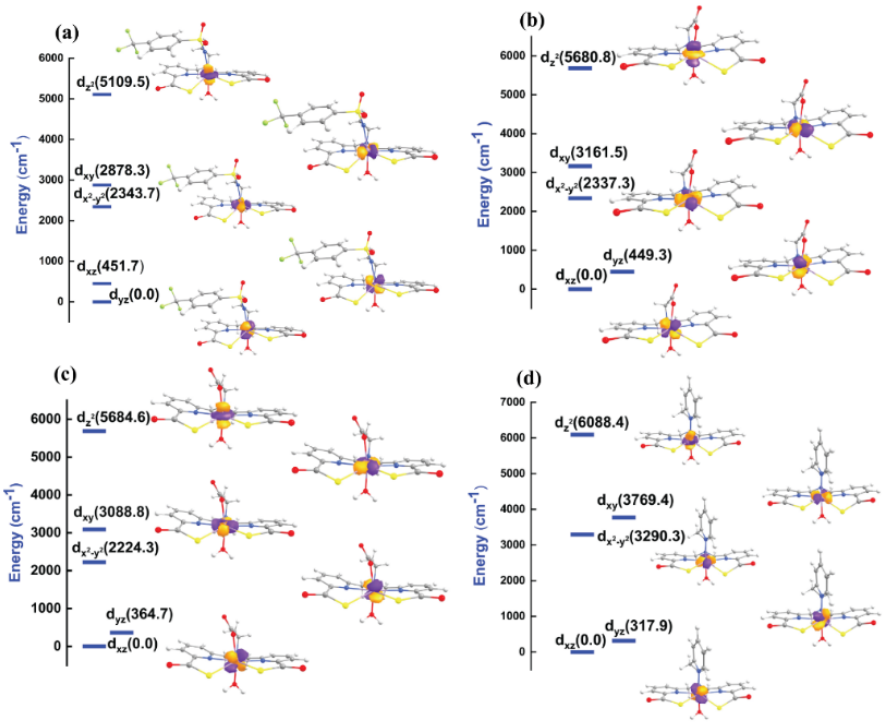

Figure C9. Splitting of metal d-orbitals obtained with AILFT calculations a) Complex 5, b) Complex 6, c) Complex 7, and d) Complex 8, respectively.

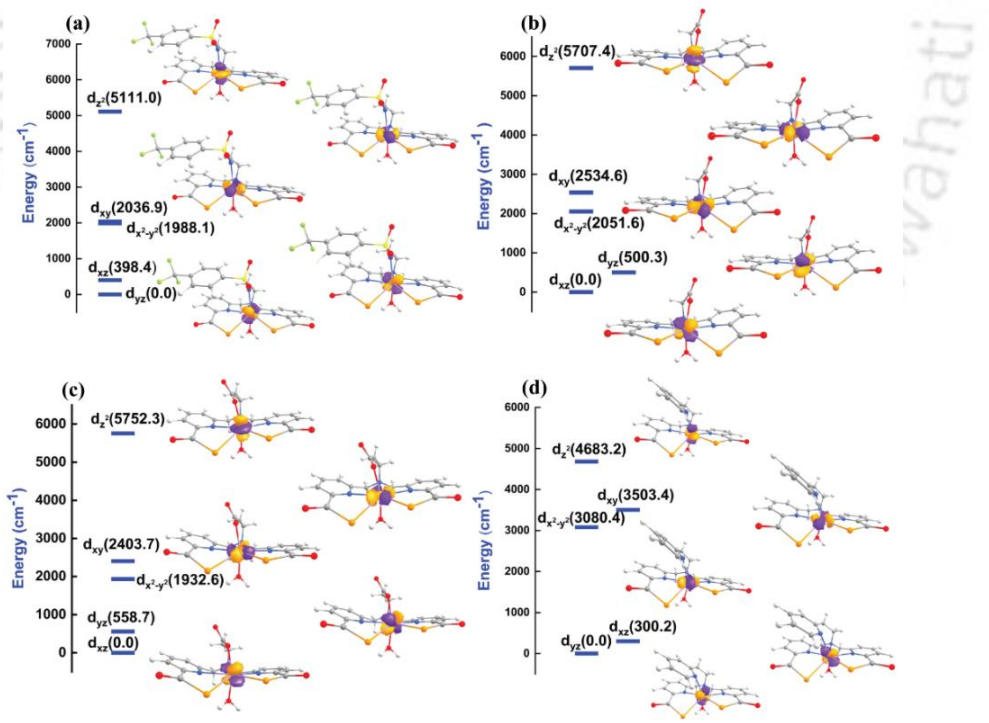

Figure C10. Splitting of metal d-orbitals obtained with AILFT calculations a) Complex 9, b) Complex 10, c) Complex 11, and d) Complex 12, respectively.

Appendix-D

Table D1. Peak distances (Å) of the RDFs from AIMD simulations of **complexes 1**, **2**, **3**, **4,** and **5** at 25˚C. The absence of peaks in RDFs is represented by the symbol "-"

	Complex 1			Complex 2			Complex 3			Complex 4			Complex 5		
	1st	2nd	3rd	1st	2nd	3rd	1st	2nd	3rd	1st	2nd	3rd	1st	2nd	3rd
Mn-O	2.25	4.35	-	2.25	4.35	-	2.25	3.15	4.35	2.25	3.15	4.35	2.25	4.25	-
Mn-N	2.35	-	-	2.25	-	-	2.25	-	-	2.35	-	-	2.25	-	-
Mn-C	3.15	4.45	4.95	3.15	4.45	5.05	3.15	4.45	4.95	3.15	4.45	5.05	3.15	4.45	5.05

Table D2. Bond length values of the studied complexes optimized using M06-2X/def2-TZVP level of theory.

Complex	**Mn-N (Å)**	**Mn-O (Å)**	**Mn-X (Å)**
Type I			
Complex 1	Mn-N1=2.279 Mn-N2=2.468 Mn-N3=2.353	Mn-O1=2.211 Mn-O2=2.165	Mn-Ow1=2.211 Mn-Ow2=2.165
Complex 2	Mn-N1=2.297 Mn-N2=2.569 Mn-N3=2.299	Mn-O1=2.188 Mn-O2=2.226	Mn-Ow1=2.301 Mn-Ow2=2.269
Complex 3	Mn-N1=2.327 Mn-N2=2.685 Mn-N3=2.338	Mn-O1=2.173 Mn-O2=2.161	Mn-Ow1=2.256 Mn-Ow2=2.276
Complex 4	Mn-N1=2.337 Mn-N2=2.644 Mn-N3=2.334	Mn-O1=2.166 Mn-O2=2.175	Mn-Ow1=2.260 Mn-Ow2=2.272
Complex 5	Mn-N1=2.341 Mn-N2=2.610 Mn-N3=2.345	Mn-O1=2.168 Mn-O2=2.159	Mn-Ow1=2.259 Mn-Ow2=2.271
Type II			
Complex 6	Mn-N1=2.296 Mn-N2=2.557 Mn-N3=2.437	Mn-O1=2.224 Mn-O2=2.168	Mn-Cl1=2.681 Mn-Cl2=2.627
Complex 7	Mn-N1=2.321 Mn-N2=2.677 Mn-N3=2.322	Mn-O1=2.229 Mn-O2=2.228	Mn-Cl1=2.612 Mn-Cl2=2.611
Complex 8	Mn-N1=2.332	Mn-O1=2.217	Mn-Cl1=2.601

	Mn-N2=2.727 Mn-N3=2.330	Mn-O2=2.225	Mn-Cl2=2.604
Complex 9	Mn-N1=2.335 Mn-N2=2.691 Mn-N3=2.334	Mn-O1=2.218 Mn-O2=2.219	Mn-Cl1=2.595 Mn-Cl2=2.606
Complex 10	Mn-N1=2.346 Mn-N2=2.644 Mn-N3=2.345	Mn-O1=2.210 Mn-O2=2.210	Mn-Cl1=2.593 Mn-Cl2=2.603
Type III			
Complex 11	Mn-N1=2.286 Mn-N2=2.547 Mn-N3=2.431	Mn-O1=2.207 Mn-O2=2.148	Mn-Br1=2.925 Mn-Br2=2.835
Complex 12	Mn-N1=2.312 Mn-N2=2.683 Mn-N3=2.312	Mn-O1=2.208 Mn-O2=2.209	Mn-Br1=2.831 Mn-Br2=2.812
Complex 13	Mn-N1=2.321 Mn-N2=2.717 Mn-N3=2.317	Mn-O1=2.194 Mn-O2=2.204	Mn-Br1=2.832 Mn-Br2=2.804
Complex 14	Mn-N1=2.324 Mn-N2=2.693 Mn-N3=2.323	Mn-O1=2.198 Mn-O2=2.198	Mn-Br1=2.822 Mn-Br2=2.807
Complex 15	Mn-N1=2.336 Mn-N2=2.637 Mn-N3=2.337	Mn-O1=2.192 Mn-O2=2.193	Mn-Br1=2.799 Mn-Br2=2.804
Type IV			
Complex 16	Mn-N1=2.277 Mn-N2=2.536 Mn-N3=2.414	Mn-O1=2.183 Mn-O2=2.135	Mn-I1=3.276 Mn-I2=3.076
Complex 17	Mn-N1=2.304 Mn-N2= 2.682 Mn-N3=2.304	Mn-O1=2.190 Mn-O2=2.191	Mn-I1=3.105 Mn-I2=3.047
Complex 18	Mn-N1=2.311 Mn-N2=2.6874 Mn-N3=2.312	Mn-O1=2.186 Mn-O2=2.179	Mn-I1=3.114 Mn-I2=3.043
Complex 19	Mn-N1=2.316 Mn-N2=2.663 Mn-N3=2.316	Mn-O1=2.183 Mn-O2=2.184	Mn-I1=3.085 Mn-I2=3.047
Complex 20	Mn-N1=2.328 Mn-N2=2.635 Mn-N3=2.330	Mn-O1=2.176 Mn-O2=2.176	Mn-I1=3.068 Mn-I2=3.038
Type V			
Complex 2a	Mn-N1=2.435 Mn-N2=2.402 Mn-N3=2.443	Mn-Se1=2.884 Mn-Se2=2.769	Mn-Ow1=2.251 Mn-Ow2=2.263
Complex 3a	Mn-N1=2.476 Mn-N2=2.467 Mn-N3=2.467	Mn-Se1=2.739 Mn-Se2=2.838	Mn-Ow1=2.222 Mn-Ow2=2.257
Complex 4a	Mn-N1=2.467 Mn-N2=2.451	Mn-Se1=2.826 Mn-Se2=2.733	Mn-Ow1=2.229 Mn-Ow2=2.262

	Mn-N3=2.474		
Complex 5a	Mn-N1=2.492 Mn-N2=2.436 Mn-N3=2.489	Mn-Se1=2.725 Mn-Se2=2.804	Mn-Ow1=2.227 Mn-Ow2=2.251
Complex 2b	Mn-N1=2.438 Mn-N2=2.474 Mn-N3=2.461	Mn-Se1=2.921 Mn-Se2=2.888	Mn-Cl1=2.561 Mn-Cl2=2.574
Complex 3b	Mn-N1=2.438 Mn-N2=2.516 Mn-N3=2.445	Mn-Se1=2.897 Mn-Se2=2.575	Mn-Cl1=2.538 Mn-Cl2=2.575
Complex 4b	Mn-N1=2.449 Mn-N2=2.497 Mn-N3=2.469	Mn-Se1=2.895 Mn-Se2=2.872	Mn-Cl1=2.542 Mn-Cl2=2.577
Complex 5b	Mn-N1=2.484 Mn-N2=2.484 Mn-N3=2.479	Mn-Se1=2.850 Mn-Se2=2.857	Mn-Cl1=2.536 Mn-Cl2=2.578
Complex 2c	Mn-N1=2.445 Mn-N2=2.476 Mn-N3=2.439	Mn-Se1=2.864 Mn-Se2=2.878	Mn-Br1=2.775 Mn-Br2=2.793
Complex 3c	Mn-N1=2.295 Mn-N2=2.433 Mn-N3=2.391	Mn-Se1=2.824 Mn-Se2=2.784	Mn-Br1=2.776 Mn-Br2=2.829
Complex 4c	Mn-N1=2.447 Mn-N2=2.495 Mn-N3=2.437	Mn-Se1=2.848 Mn-Se2=2.873	Mn-Br1=2.748 Mn-Br2=2.789
Complex 5c	Mn-N1=2.482 Mn-N2=2.476 Mn-N3=2.473	Mn-Se1=2.816 Mn-Se2=2.829	Mn-Br1=2.744 Mn-Br2=2.792
Complex 2d	Mn-N1=2.430 Mn-N2=2.477 Mn-N3=2.429	Mn-Se1=2.856 Mn-Se2=2.842	Mn-I1=3.071 Mn-I2=3.077
Complex 3d	Mn-N1=2.431 Mn-N2=2.485 Mn-N3=2.426	Mn-Se1=2.819 Mn-Se2=2.855	Mn-I1=3.055 Mn-I2=3.077
Complex 4d	Mn-N1=2.439 Mn-N2=2.481 Mn-N3=2.444	Mn-Se1=2.835 Mn-Se2=2.821	Mn-I1=3.036 Mn-I2=3.091
Complex 5d	Mn-N1=2.461 Mn-N2=2.471 Mn-N3=2.467	Mn-Se1=2.809 Mn-Se2=2.799	Mn-I1=3.021 Mn-I2=3.075

Table D3. Spin-orbit coupling (SOC) and spin-spin (SS) contributions to the D values (cm^{-1}) at the M06-2X/def2-TZVP level of theory.

Complex	D_{SOC} (cm^{-1})	D_{SSC} (cm^{-1})	α → α	β → β	α → β	β → α
Type I						
Complex 1	0.0454	0.0118	0.0246	0.0266	-0.0033	-0.0025
Complex 2	0.0251	0.0173	0.0405	0.0412	-0.0754	0.0189
Complex 3	-0.0548	-0.0025	-0.0023	0.0013	-0.0136	-0.0403
Complex 4	0.0308	-0.0003	0.0081	0.0087	0.00211	0.0119
Complex 5	0.0865	-0.0153	-0.0439	-0.0497	0.1485	0.0316
Type II						
Complex 6	0.0688	-0.0100	0.0173	0.0148	0.0413	-0.0045
Complex 7	0.1586	-0.0079	0.0230	0.0173	0.0844	0.0339
Complex 8	0.1449	-0.0063	0.0301	0.0249	0.0548	0.0351
Complex 9	0.1387	-0.0063	0.0277	0.0219	0.0528	0.0362
Complex 10	0.1744	-0.0059	0.0238	0.0178	0.0949	0.0379
Type III						
Complex 11	-0.7343	-0.0199	0.1736	0.1321	-0.5216	-0.5184
Complex 12	-2.1698	-0.0154	0.1203	0.0580	-1.9165	-0.4317
Complex 13	-2.1882	-0.0145	0.1844	0.1247	-2.0523	-0.4449
Complex 14	-0.7695	-0.0134	0.2343	0.1751	-0.6244	-0.5545
Complex 15	-2.2739	-0.0135	0.1016	0.0378	-1.9656	-0.4476
Type IV						
Complex 16	-16.5950	-0.0241	-2.7794	-3.1793	-32.1042	21.4678
Complex 17	-15.2295	-0.0204	-3.5270	-4.0385	-30.0576	22.3936
Complex 18	-15.7027	-0.0203	-3.5486	-4.0495	-30.6409	22.5362
Complex 19	-15.0334	-0.0192	-3.3836	-3.8947	-30.3792	22.6241
Complex 20	-15.0591	-0.0179	-3.4772	-3.9935	-30.3127	22.7242
Type V						
Complex 2a	1.2563	-0.0061	-0.0572	-0.0071	1.4302	-0.1097
Complex 3a	0.1438	0.0003	-0.0286	0.0244	0.1755	-0.0274
Complex 4a	0.2259	-0.0014	-0.0185	0.0268	0.2388	-0.0213
Complex 5a	0.1832	-0.0003	-0.0239	0.0243	0.2063	-0.0234
Complex 2b	-0.4311	0.0026	-0.0993	-0.0305	-0.2462	-0.0552
Complex 3b	0.6690	0.0047	-0.0987	-0.0302	0.9451	-0.1472
Complex 4b	0.7093	0.0042	-0.0894	-0.0215	0.9681	-0.1479
Complex 5b	0.9197	0.0042	-0.0686	-0.0024	1.1439	-0.1533
Complex 2c	2.3704	0.0039	-0.0949	-0.0876	2.6001	-0.0473
Complex 3c	-4.7350	-0.0149	-1.3912	-1.3584	-3.1194	1.1339
Complex 4c	2.6261	0.0043	-0.0343	-0.0282	2.7803	-0.0919
Complex 5c	-1.9626	0.0024	-0.2969	-0.2886	-1.6533	0.2762
Complex 2d	-19.799	-0.0159	-0.5962	-1.0109	-14.7574	-3.4355
Complex 3d	-22.5896	-0.0151	0.6023	0.1806	-12.4808	-10.8918
Complex 4d	-20.4048	-0.0148	-0.3678	-0.7855	-16.1048	-3.1468
Complex 5d	-22.3071	-0.0135	-0.6174	-1.0365	-17.5721	-3.0812

Table D4. Zero field splitting (ZFS) parameter of all the complexes using M06-2X/def2-TZVP level of theory.

Complex	D (cm^{-1})	E/D
Type I		
Complex 1	0.0571	0.0444
Complex 2	0.0421	0.2849
Complex 3	-0.0569	0.2425
Complex 4	0.0307	0.2789
Complex 5	0.0708	0.1992
Type II		
Complex 6	0.0587	0.2218
Complex 7	0.1508	0.1784
Complex 8	0.1385	0.0674
Complex 9	0.1323	0.0745
Complex 10	0.1663	0.1663
Type III		
Complex 11	-0.7543	0.0358
Complex 12	-2.1852	0.0433
Complex 13	-2.2026	0.0381
Complex 14	-0.7829	0.0999
Complex 15	-2.2874	0.0301
Type IV		
Complex 16	-16.6191	0.0749
Complex 17	-15.2499	0.0785
Complex 18	-15.7229	0.0826
Complex 19	-15.0526	0.0786
Complex 20	-15.0772	0.0616
Type V		
Complex 2a	1.2502	0.0471
Complex 3a	0.1438	0.2283
Complex 4a	0.2243	0.2771
Complex 5a	0.1827	0.1633
Complex 2b	-0.4286	0.1583
Complex 3b	0.6737	0.1131
Complex 4b	0.7135	0.0884
Complex 5b	0.9239	0.0436
Complex 2c	2.3742	0.0918
Complex 3c	-4.7499	0.1821
Complex 4c	2.6304	0.1455
Complex 5c	-1.9603	0.1135
Complex 2d	-19.8158	0.0509
Complex 3d	-22.6048	0.0347
Complex 4d	-20.4195	0.0744
Complex 5d	-22.3206	0.0554

Table D5. NEVPT2 transition energy and their individual contribution to the *D* values for **complex 1** (up to 17 quartets and 13 doublets are shown).

State	NEVPT2 Transition energy	*D* (cm^{-1})	*E* (cm^{-1})
^{6}S	0.000	0.000	0.000
^{4}G	18337.4	0.670	-0.000
	20224.1	-0.268	0.078
	21561.7	-0.216	-0.097
	23508.7	-0.004	0.003
	23879.7	0.010	-0.005
	25582.5	0.001	-0.000
	25885.0	-0.000	0.000
	25899.7	-0.000	0.000
	25985.7	0.001	-0.000
^{4}P	26936.5	-0.143	-0.037
	28992.6	0.026	0.056
	30564.5	-0.269	0.280
^{4}D	30803.5	0.038	-0.008
	31744.2	-0.147	-0.120
	32453.8	-0.156	-0.124
	32470.6	-0.151	-0.018
	35136.7	0.647	-0.004

Table D6. NEVPT2 transition energy and their individual contribution to the *D* values for **complex 2** (up to 17 quartets and 13 doublets are shown).

State	NEVPT2 Transition energy	*D* (cm^{-1})	*E* (cm^{-1})
^{6}S	0.000	0.000	0.000
^{4}G	18293.2	0.660	-0.017
	19413.6	-0.255	0.204
	23009.0	-0.142	-0.106
	23309.7	-0.000	-0.000
	23889.1	-0.012	0.005
	25934.6	-0.000	0.000
	26034.5	-0.001	-0.000
	26123.4	-0.000	0.000
	26247.8	0.000	0.000
^{4}P	28081.9	-0.344	-0.325
	28416.7	-0.152	0.140
	29917.9	0.099	-0.063
^{4}D	31200.0	-0.091	0.045
	31532.4	-0.003	0.000

	31861.8	0.165	-0.024
	34317.1	-0.282	0.167
	35359.2	0.427	-0.009

Table D7. NEVPT2 transition energy and their individual contribution to the *D* values for **complex 3** (up to 17 quartets and 13 doublets are shown).

State	NEVPT2 Transition energy	*D* (cm^{-1})	*E* (cm^{-1})
^{6}S	0.000	0.000	0.000
^{4}G	18438.7	0.661	-0.015
	19471.2	-0.269	0.244
	21081.2	-0.201	-0.188
	23265.4	-0.001	0.000
	24647.5	-0.007	0.000
	25684.5	-0.000	0.000
	26043.0	-0.002	-0.000
	26119.1	-0.000	0.000
	26242.1	0.000	0.000
^{4}P	27842.9	-0.111	-0.083
	29699.2	-0.002	0.046
	30811.0	-0.154	-0.046
^{4}D	31583.8	-0.157	-0.006
	31737.3	-0.035	-0.002
	32414.6	0.006	-0.128
	33430.2	-0.111	0.151
	35237.7	0.432	0.031

Table D8. NEVPT2 transition energy and their individual contribution to the *D* values for **complex 4** (up to 17 quartets and 13 doublets are shown).

State	NEVPT2 Transition energy	*D* (cm^{-1})	*E* (cm^{-1})
^{6}S	0.000	0.000	0.000
^{4}G	18417.2	0.672	-0.010
	19417.9	-0.264	0.267
	21491.8	-0.206	-0.218
	23275.8	-0.001	-0.000
	24494.7	-0.008	0.006
	25805.3	-0.000	0.000
	26079.8	-0.002	0.001
	26142.8	-0.000	0.000
	26270.5	0.000	0.000
^{4}P	27879.9	-0.129	-0.042

	29649.8	-0.022	-0.037
	30861.8	-0.156	-0.184
^{4}D	31465.6	-0.143	0.092
	31735.3	-0.025	0.015
	32373.1	0.076	-0.101
	33558.2	-0.181	0.228
	35274.6	0.441	-0.003

Table D9. NEVPT2 transition energy and their individual contribution to the *D* values for **complex 5** (up to 17 quartets are shown).

State	NEVPT2 Transition energy	*D* (cm^{-1})	*E* (cm^{-1})
^{6}S	0.000	0.000	0.000
^{4}G	18624.4	0.665	-0.009
	19494.1	-0.262	0.268
	21447.8	-0.210	-0.228
	23258.7	-0.001	-0.000
	24469.9	-0.009	0.008
	25889.1	-0.000	0.000
	26111.6	-0.001	0.001
	26131.5	-0.000	-0.000
	26298.2	0.000	0.000
^{4}P	27871.7	-0.123	0.006
	29580.3	-0.004	-0.061
	30930.9	-0.175	-0.222
^{4}D	31602.6	-0.141	0.098
	31730.1	-0.030	0.020
	32317.4	0.073	-0.098
	33501.1	-0.184	0.240
	35227.4	0.448	-0.009

Table D10. NEVPT2 transition energy and their individual contribution to the *D* values for **complex 6** (up to 17 quartets and 13 doublets are shown).

State	NEVPT2 Transition energy	*D* (cm^{-1})	*E* (cm^{-1})
^{6}S	0.000	0.000	0.000
^{4}G	18366.8	-0.269	0.273
	20492.0	0.457	-0.018
	20905.3	-0.167	-0.171
	23656.5	0.001	-0.000
	24795.3	-0.001	-0.000

	25571.7	-0.003	-0.000
	25576.4	-0.000	0.000
	25703.6	-0.000	0.000
	25864.0	-0.000	-0.000
^{4}P	29476.7	-0.196	-0.194
	30149.7	-0.198	0.195
	30502.8	0.462	-0.021
^{4}D	30737.8	-0.090	-0.077
	31068.1	-0.092	-0.198
	31863.5	-0.007	-0.006
	32187.7	0.412	0.005
	33193.2	-0.224	0.237

Table D11. NEVPT2 transition energy and their individual contribution to the *D* values for **complex 7** (up to 17 quartets and 13 doublets are shown).

State	NEVPT2 Transition energy	*D* (cm^{-1})	*E* (cm^{-1})
^{6}S	0.000	0.000	0.000
^{4}G	18059.0	-0.289	0.263
	19529.3	0.433	0.005
	22618.4	-0.196	-0.175
	23766.1	-0.001	0.000
	24587.3	0.000	0.000
	25449.6	0.007	0.000
	25778.8	0.000	-0.000
	26047.3	-0.000	-0.000
	26096.1	0.000	-0.000
^{4}P	28835.0	-0.295	0.104
	30491.6	0.360	0.013
	30727.7	-0.365	-0.313
^{4}D	31233.6	0.376	0.003
	31593.1	0.051	0.001
	31829.5	0.239	0.002
	31884.0	-0.152	-0.117
	33417.7	-0.201	0.203

Table D12. NEVPT2 transition energy and their individual contribution to the *D* values for **complex 8** (up to 17 quartets and 13 doublets are shown).

State	NEVPT2 Transition energy	*D* (cm^{-1})	*E* (cm^{-1})
^{6}S	0.000	0.000	0.000
^{4}G	18061.0	-0.297	0.303

	19414.3	-0.230	-0.229
	21728.3	0.448	0.003
	23763.3	0.000	0.000
	24676.1	-0.000	-0.000
	25235.3	-0.002	-0.002
	25788.6	-0.000	-0.000
	26055.3	0.000	0.000
	26112.9	-0.000	-0.000
^{4}P	28883.3	0.026	0.172
	29903.6	-0.164	-0.156
	31064.0	0.515	0.047
^{4}D	31420.0	-0.222	0.218
	31567.5	-0.009	-0.009
	32097.2	-0.136	-0.133
	32432.0	0.223	0.063
	33342.1	-0.102	0.172

Table D13. NEVPT2 transition energy and their individual contribution to the *D* values for **complex 9** (up to 17 quartets and 13 doublets are shown).

State	**NEVPT2 Transition energy**	***D* (cm^{-1})**	***E* (cm^{-1})**
^{6}S	0.000	0.000	0.000
^{4}G	18087.9	-0.286	0.297
	19441.3	-0.230	-0.228
	21969.2	0.422	0.005
	23779.0	0.000	0.000
	24663.9	-0.000	-0.000
	25297.5	-0.002	-0.002
	25793.5	-0.000	-0.000
	26055.2	0.000	0.000
	26134.4	-0.000	-0.000
^{4}P	28874.7	0.042	0.177
	30012.0	-0.170	-0.159
	30974.3	0.541	0.045
^{4}D	31419.6	-0.217	-0.215
	31670.4	-0.009	-0.009
	32058.2	-0.136	-0.133
	32262.3	0.249	0.043
	33380.5	-0.156	0.191

Table D14. NEVPT2 transition energy and their individual contribution to the *D* values for **complex 10** (up to 17 quartets and 13 doublets are shown).

State	NEVPT2 Transition energy	*D* (cm^{-1})	*E* (cm^{-1})
^{6}S	0.000	0.000	0.000
^{4}G	18145.2	-0.285	0.291
	19427.2	-0.231	-0.225
	21968.2	0.427	0.004
	23753.7	0.000	0.000
	24631.9	-0.000	-0.000
	25303.9	-0.002	-0.002
	25775.2	-0.000	-0.000
	26042.7	0.000	0.000
	26149.2	-0.000	-0.000
^{4}P	28957.7	-0.048	0.172
	30003.8	-0.171	-0.143
	30911.2	0.632	0.028
^{4}D	31401.1	-0.218	-0.212
	31706.7	-0.005	-0.005
	32010.1	-0.132	-0.127
	32209.8	0.254	0.039
	32209.8	-0.168	0.194

Table D15. NEVPT2 transition energy and their individual contribution to the *D* values for **complex 11** (up to 17 quartets and 13 doublets are shown).

State	NEVPT2 Transition energy	*D* (cm^{-1})	*E* (cm^{-1})
^{6}S	0.000	0.000	0.000
^{4}G	18610.6	0.534	-0.007
	20465.3	-0.198	0.185
	21573.5	-0.093	-0.101
	23851.9	-0.011	-0.011
	24644.0	-0.006	-0.006
	24662.4	-0.003	0.002
	25374.6	-0.000	-0.000
	25662.5	-0.008	0.002
	25786.2	-0.000	-0.000
^{4}P	29693.7	-0.283	-0.294
	30136.4	-0.233	0.231
	30518.9	0.252	-0.004
^{4}D	30576.1	0.126	-0.012
	31188.5	-0.049	-0.081
	31308.2	0.176	-0.023

	31614.7	0.406	-0.000
	32117.1	-0.169	0.127

Table D16. NEVPT2 transition energy and their individual contribution to the *D* values for **complex 12** (up to 17 quartets and 13 doublets are shown).

State	NEVPT2 Transition energy	*D* (cm^{-1})	*E* (cm^{-1})
^{6}S	0.000	0.000	0.000
^{4}G	18545.6	-0.208	-0.210
	19726.1	-0.141	0.147
	22126.5	0.434	0.001
	23241.6	0.000	-0.000
	24340.9	-0.000	0.000
	25713.2	-0.008	0.008
	25724.4	-0.000	0.000
	25920.3	-0.000	0.000
	25994.7	-0.208	-0.233
^{4}P	29357.2	-0.251	0.251
	30664.6	0.815	-0.007
	30676.9	-0.034	0.034
^{4}D	31214.8	-0.154	0.157
	31266.6	0.339	-0.006
	31437.8	-0.017	0.017
	31488.6	-0.115	-0.138
	32475.8	-0.000	0.000

Table D17. NEVPT2 transition energy and their individual contribution to the *D* values for **complex 13** (up to 17 quartets and 13 doublets are shown).

State	NEVPT2 Transition energy	*D* (cm^{-1})	*E* (cm^{-1})
^{6}S	0.000	0.000	0.000
^{4}G	18571.8	-0.210	-0.199
	19549.7	0.504	-0.000
	21314.3	-0.155	0.142
	23210.9	-0.000	-0.001
	24435.4	-0.000	0.000
	25619.2	0.000	0.000
	25726.9	-0.006	0.006
	25918.7	-0.000	0.000
	25977.4	-0.000	0.000
^{4}P	29621.1	-0.209	-0.230

	30457.5	-0.241	0.240
	30703.2	0.617	-0.006
^{4}D	31370.3	-0.062	0.063
	31419.3	-0.126	0.126
	31483.7	0.428	-0.010
	31835.1	0.021	0.020
	32445.9	-0.079	-0.130

Table D18. NEVPT2 transition energy and their individual contribution to the *D* values for **complex 14** (up to 17 quartets and 13 doublets are shown).

State	NEVPT2 Transition energy	*D* (cm^{-1})	*E* (cm^{-1})
^{6}S	0.000	0.000	0.000
^{4}G	18595.1	-0.207	-0.210
	20167.9	0.072	0.100
	20921.7	0.287	0.047
	23239.1	-0.000	-0.001
	24416.0	-0.000	0.000
	25657.8	0.000	0.000
	25730.8	-0.006	0.006
	25927.9	-0.000	0.000
	26006.7	-0.000	0.000
^{4}P	29613.9	-0.206	-0.229
	30551.8	-0.240	0.239
	30617.4	0.660	-0.007
^{4}D	31404.0	-0.060	0.060
	31440.3	-0.130	0.130
	31452.1	0.444	-0.013
	31861.3	-0.022	0.025
	32448.8	-0.089	-0.133

Table D19. NEVPT2 transition energy and their individual contribution to the *D* values for **complex 15** (up to 17 quartets and 13 doublets are shown).

State	NEVPT2 Transition energy	*D* (cm^{-1})	*E* (cm^{-1})
^{6}S	0.000	0.000	0.000
^{4}G	18586.0	-0.209	-0.209
	19576.5	-0.150	0.154
	21616.3	0.477	0.001
	23249.4	-0.000	-0.001
	24381.2	-0.000	0.000

	25634.8	-0.000	0.000
	25724.5	-0.005	0.005
	25894.6	-0.000	0.000
	26040.0	-0.000	0.000
^{4}**P**	29607.1	-0.204	-0.225
	30662.2	-0.234	0.235
	30688.3	0.689	-0.006
^{4}**D**	31323.3	-0.064	0.064
	31378.3	-0.111	0.113
	31380.9	0.432	-0.011
	31820.4	-0.033	0.034
	32443.3	-0.102	-0.137

Table D20. NEVPT2 transition energy and their individual contribution to the *D* values for **complex 16 (**up to 17 quartets and 13 doublets are shown).

State	**NEVPT2 Transition energy**	***D* (cm^{-1})**	***E* (cm^{-1})**
^{6}**S**	0.000	0.000	0.000
^{4}**G**	17940.8	0.590	0.005
	19605.2	-0.159	-0.159
	21123.9	-0.059	0.071
	23724.5	-0.000	0.000
	23883.2	-0.016	0.003
	23977.0	-0.002	0.002
	25107.5	-0.001	-0.001
	25320.7	-0.018	0.009
	25459.0	-0.003	0.003
^{4}**P**	27478.1	-0.275	0.254
	28608.7	-0.213	-0.193
	29170.2	0.019	-0.003
^{4}**D**	30287.2	0.192	0.010
	30582.0	0.122	0.020
	31650.0	0.349	0.100
	31729.0	0.239	0.037
	31913.5	-0.147	-0.144

Table D21. NEVPT2 transition energy and their individual contribution to the *D* values for **complex 17** (up to 17 quartets and 13 doublets are shown).

State	**NEVPT2 Transition energy**	***D* (cm^{-1})**	***E* (cm^{-1})**
^{6}**S**	0.000	0.000	0.000

^{4}G	18912.6	0.310	-0.044
	19735.1	-0.107	0.088
	20428.6	0.076	-0.074
	21887.2	-0.012	-0.013
	24179.8	0.001	-0.000
	24925.9	-0.000	0.000
	25449.5	-0.002	0.002
	25541.8	-0.011	0.011
	25857.1	-0.000	0.000
^{4}P	27845.9	-0.180	-0.193
	29706.2	-0.221	0.219
	30282.1	0.341	-0.002
^{4}D	30514.1	-0.000	0.000
	30807.1	0.852	-0.005
	31119.9	-0.023	0.023
	31419.5	-0.135	0.135
	32113.0	-0.094	-0.017

Table D22. NEVPT2 transition energy and their individual contribution to the *D* values for **complex 18** (up to 17 quartets and 13 doublets are shown).

State	NEVPT2 Transition energy	*D* (cm^{-1})	*E* (cm^{-1})
^{6}S	0.000	0.000	0.000
^{4}G	18683.5	0.523	0.002
	18878.3	-0.135	-0.097
	20687.4	-0.105	0.061
	22425.3	-0.009	-0.011
	24248.6	-0.002	-0.002
	24592.2	-0.000	0.000
	25481.5	-0.001	0.001
	25619.8	-0.010	0.010
	25892.1	-0.000	0.000
^{4}P	28117.6	-0.183	-0.191
	29871.9	-0.214	0.213
	30128.9	0.229	-0.001
^{4}D	30485.9	-0.002	0.002
	30774.3	0.918	-0.006
	31184.1	-0.047	0.048
	32091.6	-0.111	0.111
	32117.4	-0.086	-0.106

Table D23. NEVPT2 transition energy and their individual contribution to the *D* values for **complex 19** (up to 17 quartets and 13 doublets are shown)

State	NEVPT2 Transition energy	*D* (cm^{-1})	*E* (cm^{-1})
^{6}S	0.000	0.000	0.000
^{4}G	19000.3	0.195	-0.070
	19735.6	0.195	-0.065
	19893.8	-0.087	0.106
	22082.3	-0.011	-0.012
	24259.7	0.000	-0.000
	24946.4	-0.000	0.000
	25491.0	-0.011	0.011
	25548.9	-0.002	0.002
	25902.2	-0.000	0.000
^{4}P	28103.2	-0.179	-0.189
	29915.7	-0.211	0.210
	30285.3	0.297	-0.001
^{4}D	30549.8	-0.001	0.001
	30836.7	0.881	-0.005
	31190.0	-0.041	0.041
	31912.8	-0.115	0.114
	32133.0	-0.090	-0.107

Table D24. NEVPT2 transition energy and their individual contribution to the *D* values for **complex 20** (up to 17 quartets and 13 doublets are shown).

State	NEVPT2 Transition energy	*D* (cm^{-1})	*E* (cm^{-1})
^{6}S	0.000	0.000	0.000
^{4}G	18884.0	0.305	-0.052
	19505.7	0.118	-0.086
	19982.7	-0.110	0.111
	22135.0	-0.011	-0.012
	23987.4	-0.000	-0.000
	24958.9	-0.000	0.000
	25490.2	-0.011	0.012
	25780.7	-0.000	-0.000
	25889.3	-0.000	0.000
^{4}P	28250.2	-0.011	0.012
	30012.1	-0.000	0.000
	30212.2	-0.000	0.000
^{4}D	30575.2	-0.174	-0.184
	30801.3	-0.205	0.204

	31151.2	0.241	-0.001
	32094.2	-0.002	0.002
	32169.5	0.920	-0.006

Table D25. Zero field splitting (ZFS) parameters using CAS (5,10) for **Type I, Type II, Type III,** and **Type IV** complexes using CASSCF/NEVPT2 method

Complex	D	E/D
Complex 1	-0.0346	0.3137
Complex 2	0.0632	0.1758
Complex 3	0.0470	0.1788
Complex 4	0.0486	0.1886
Complex 5	0.0405	0.2144
Complex 6	0.0444	0.2889
Complex 7	0.0498	0.2351
Complex 8	0.0504	0.1801
Complex 9	-0.0367	0.2936
Complex 10	0.0623	0.1421
Complex 11	0.4235	0.0157
Complex 12	0.4382	0.0269
Complex 13	0.4728	0.0363
Complex 14	0.4758	0.0258
Complex 15	0.4727	0.0242
Complex 16	0.5873	0.0220
Complex 17	0.7428	0.0528
Complex 18	0.7226	0.0489

Complex 19	0.7667	0.0257
Complex 20	0.7801	0.0432

Table D26. Zero field splitting (ZFS) parameters (cm^{-1}) and single point energy (SPE) (Hartree) obtained with different *nroots* of particular multiplicity for **complex 6** using CAS (9,7).

nroots (multiplicilty)	**SA-CASSCF (D)**	**SA-CASSCF (E/D)**	**SA-NEVPT2 (D)**	**SA-NEVPT2 (E/D)**	**SA-NEVPT2 (SPE)**
10, 4, 16 (6,4,2)	0.155	0.327	0.156	0.325	-3068.6741
3, 4 (6,4)	-0.008	0.002	-0.008	0.002	-3069.2041
3,4,16 (6,4,2)	0.157	0.322	0.158	0.319	-3068.7058
3,4,2 (6,4,2)	0.157	0.321	0.158	0.319	-3068.7102
3, 10 (6,4)	-0.002	0.003	-0.002	0.003	-3070.7316
3,10,2 (6,4,2)	0.252	0.221	0.249	0.203	-3068.7085
4 (4)	-1.447	0.007	-1.441	0.009	-3068.7642
10 (6)	-0.021	0.134	-0.021	0.134	-3068.6439
3,24,2 (6,4,2)	0.069	0.324	0.069	0.329	-3068.6987
4,24,2 (6,4,2)	0.066	0.316	0.071	0.304	-3068.6824
10,24,2 (6,4,2)	0.078	0.315	0.078	0.305	-3068.6669

Table D27. Zero field splitting (ZFS) parameters (cm^{-1}) and single point energy (SPE) (Hartree) obtained with different *nroots* of particular multiplicity for **complex 11** using CAS (9,7).

nroots (multiplicilty)	**SA-CASSCF (D)**	**SA-CASSCF (E/D)**	**SA-NEVPT2 (D)**	**SA-NEVPT2 (E/D)**	**SA-NEVPT2 (SPE)**
10, 4, 16 (6,4,2)	-0.224	0.288	-0.227	0.284	-7411.7340
3,24,2 (6,4,2)	0.315	0.131	0.321	0.127	-7411.7387
4,24,2 (6,4,2)	0.328	0.088	0.334	0.084	-7411.7289
10,24,2 (6,4,2)	0.342	0.086	0.346	0.087	-7411.7256

Table D28. Zero field splitting (ZFS) parameters (cm^{-1}) and single point energy (SPE) (Hartree) obtained with different *nroots* of particular multiplicity for **complex 16** using CAS (9,7).

nroots (multiplicilty)	SA-CASSCF (D)	SA-CASSCF (E/D)	SA-NEVPT2 (D)	SA-NEVPT2 (E/D)	SA-NEVPT2 (SPE)
10, 4, 16 (6,4,2)	-0.576	0.321	-0.581	0.319	-16674.7642
3,24,2 (6,4,2)	0.531	0.137	0.539	0.132	-16588.7062
4,24,2 (6,4,2)	0.623	0.066	0.629	0.064	-16588.7035
10,24,2 (6,4,2)	0.716	0.204	0.722	0.204	-16588.6968

Table D29. Zero field splitting (ZFS) parameters of **Type I** complexes with explicit water molecules using *ab initio* CASSCF/NEVPT2 method.

Complex	D (cm^{-1})	E/D
Complex 1	0.097	0.183
Complex 2	0.115	0.319
Complex 3	0.097	0.251
Complex 4	-0.125	0.234
Complex 5	0.106	0.274

Table D30. Zero field splitting (ZFS) parameters of **Type V** complexes using different *ab initio* CASSCF and CASSCF/NEVPT2 methods.

Complex	Method	D (cm^{-1})	E/D	Δ (cm^{-1})	Δ^2 ($10^{20}S^{-2}$)
Complex 2a	CAS(5,5)	-0.088	0.169	0.075	1.975
	NEVPT2(5,5)	-0.085	0.178	0.073	1.855
Complex 3a	CAS(5,5)	0.127	0.225	0.111	4.354
	NEVPT2(5,5)	0.126	0.226	0.111	4.326
Complex 4a	CAS(5,5)	0.118	0.281	0.107	4.042
	NEVPT2(5,5)	0.117	0.281	0.106	3.999
Complex 5a	CAS(5,5)	0.123	0.292	0.112	4.458
	NEVPT2(5,5)	0.122	0.292	0.112	4.408
Complex 2b	CAS(5,5)	0.159	0.177	0.136	6.587
	NEVPT2(5,5)	0.159	0.177	0.136	6.508
Complex 3b	CAS(5,5)	0.149	0.121	0.125	5.488
	NEVPT2(5,5)	0.149	0.119	0.124	5.442
Complex 4b	CAS(5,5)	0.158	0.111	0.132	6.123
	NEVPT2(5,5)	0.157	0.111	0.131	6.069
Complex 5b	CAS(5,5)	0.153	0.082	0.126	5.612
	NEVPT2(5,5)	0.152	0.081	0.125	5.564
Complex 2c	CAS(5,5)	0.568	0.023	0.464	76.429
	NEVPT2(5,5)	0.567	0.024	0.464	76.296

Complex 3c	CAS(5,5)	0.522	0.006	0.426	64.502
	NEVPT2(5,5)	0.524	0.006	0.428	64.957
Complex 4c	CAS(5,5)	0.577	0.021	0.472	78.902
	NEVPT2(5,5)	0.577	0.022	0.471	78.775
Complex 5c	CAS(5,5)	0.572	0.019	0.467	77.400
	NEVPT2(5,5)	0.571	0.019	0.467	77.231
Complex 2d	CAS(5,5)	0.754	0.008	0.616	134.506
	NEVPT2(5,5)	0.757	0.008	0.618	135.623
Complex 3d	CAS(5,5)	0.753	0.005	0.615	134.336
	NEVPT2(5,5)	0.756	0.005	0.618	135.337
Complex 4d	CAS(5,5)	0.780	0.009	0.637	144.137
	NEVPT2(5,5)	0.783	0.010	0.639	145.136
Complex 5d	CAS(5,5)	0.789	0.006	0.645	147.499
	NEVPT2(5,5)	0.792	0.005	0.647	148.408

Table D31. Topological parameters of the complexes analyzed here; the electron density at bond critical points (ρ_{bcp}), its Laplacian [$\nabla^2_{\rho(bcp)}$], and the kinetic electron energy density (G_{bcp}). The results obtained at the M06-2X/def2-TZVP level of approximation correspond to Mn-O, Mn-S, and Mn-Se bonds.

Complex	**ρ_{bcp}**	**$\nabla^2_{\rho(bcp)}$**	**G_{bcp}**
Complex 2a	Mn-O1w=0.0434 Mn-O2w=0.0429 Mn-Se1=0.0351 Mn-Se2=0.0282	Mn-O1w=0.2091 Mn-O2w=0.2019 Mn-Se1=0.0805 Mn-Se2=0.0635	Mn-O1w=0.0558 Mn-O2w=0.0543 Mn-Se1=0.0253 Mn-Se2=0.0191
Complex 3a	Mn-O1w=0.0476 Mn-O2w=0.0433 Mn-Se1=0.0369 Mn-Se2=0.0307	Mn-O1w=0.2255 Mn-O2w=0.2052 Mn-Se1=0.0846 Mn-Se2=0.0692	Mn-O1w=0.0614 Mn-O2w=0.0551 Mn-Se1=0.0269 Mn-Se2=0.0212
Complex 4a	Mn-O1w=0.0429 Mn-O2w=0.0467 Mn-Se1=0.0313 Mn-Se2=0.0374	Mn-O1w=0.2028 Mn-O2w=0.2215 Mn-Se1=0.0707 Mn-Se2=0.0860	Mn-O1w=0.0544 Mn-O2w=0.0601 Mn-Se1=0.0218 Mn-Se2=0.0274
Complex 5a	Mn-O1w=0.0439 Mn-O2w=0.0463 Mn-Se1=0.0380 Mn-Se2=0.0327	Mn-O1w=0.2089 Mn-O2w=0.2234 Mn-Se1=0.0871 Mn-Se2=0.0738	Mn-O1w=0.0562 Mn-O2w=0.0601 Mn-Se1=0.0279 Mn-Se2=0.0230
Complex 2b	Mn-Cl1=0.0376 Mn-Cl2=0.0389 Mn-Se1=0.0256 Mn-Se2=0.0273	Mn-Cl1=0.1265 Mn-Cl2=0.1303 Mn-Se1=0.0589 Mn-Se2=0.0633	Mn-Cl1=0.0359 Mn-Cl2=0.0373 Mn-Se1=0.0172 Mn-Se2=0.0187
Complex 3b	Mn-Cl1=0.0407 Mn-Cl2=0.0376 Mn-Se1=0.0268 Mn-Se2=0.0267	Mn-Cl1=0.1366 Mn-Cl2=0.1263 Mn-Se1=0.0616 Mn-Se2=0.0614	Mn-Cl1=0.0395 Mn-Cl2=0.0359 Mn-Se1=0.0181 Mn-Se2=0.0181
Complex 4b	Mn-Cl1= 0.0375 Mn-Cl2=0.0404 Mn-Se1=0.0269 Mn-Se2=0.0282	Mn-Cl1=0.1257 Mn-Cl2=0.1356 Mn-Se1=0.0619 Mn-Se2=0.0651	Mn-Cl1=0.0357 Mn-Cl2=0.0391 Mn-Se1=0.0182 Mn-Se2=0.0194

Complex 5b	Mn-Cl1= 0.0374 Mn-Cl2=0.0408 Mn-Se1=0.0294 Mn-Se2=0.0290	Mn-Cl1=0.1254 Mn-Cl2=0.1375 Mn-Se1=0.0678 Mn-Se2=0.0669	Mn-Cl1=0.0356 Mn-Cl2=0.0397 Mn-Se1=0.0203 Mn-Se2=0.0200
Complex 2c	Mn-Br1=0.0296 Mn-Br2=0.0308 Mn-Se1=0.0280 Mn-Se2=0.0288	Mn-Br1=0.0822 Mn-Br2=0.0850 Mn-Se1=0.0639 Mn-Se2=0.0659	Mn-Br1=0.0234 Mn-Br2=0.0244 Mn-Se1=0.0190 Mn-Se2=0.0198
Complex 3c	Mn-Br1=0.0279 Mn-Br2=0.0310 Mn-Se1=0.0293 Mn-Se2=0.0339	Mn-Br1=0.0755 Mn-Br2=0.0837 Mn-Se1=0.0537 Mn-Se2=0.0704	Mn-Br1=0.0214 Mn-Br2=0.0243 Mn-Se1=0.0168 Mn-Se2=0.0225
Complex 4c	Mn-Br1=0.0299 Mn-Br2=0.0324 Mn-Se1=0.0296 Mn-Se2=0.0282	Mn-Br1=0.0828 Mn-Br2=0.0897 Mn-Se1=0.0675 Mn-Se2=0.0642	Mn-Br1=0.0236 Mn-Br2=0.0261 Mn-Se1=0.0204 Mn-Se2=0.0192
Complex 5c	Mn-Br1=0.0298 Mn-Br2=0.0327 Mn-Se1=0.0316 Mn-Se2=0.0307	Mn-Br1=0.0824 Mn-Br2=0.0906 Mn-Se1=0.0723 Mn-Se2=0.0702	Mn-Br1=0.0235 Mn-Br2=0.0263 Mn-Se1=0.0221 Mn-Se2=0.0214
Complex 2d	Mn-I1=0.0225 Mn-I2=0.0228 Mn-Se1=0.0294 Mn-Se2=0.0302	Mn-I1=0.0502 Mn-I2=0.0506 Mn-Se1=0.0661 Mn-Se2=0.0680	Mn-I1=0.0142 Mn-I2=0.0144 Mn-Se1=0.0200 Mn-Se2=0.0207
Complex 3d	Mn-I1=0.0225 Mn-I2=0.0235 Mn-Se1=0.0316 Mn-Se2=0.0294	Mn-I1=0.0502 Mn-I2=0.0518 Mn-Se1=0.0709 Mn-Se2=0.0659	Mn-I1=0.0142 Mn-I2=0.0149 Mn-Se1=0.0218 Mn-Se2=0.0200
Complex 4d	Mn-I1=0.0220 Mn-I2=0.0243 Mn-Se1=0.0306 Mn-Se2=0.0315	Mn-I1=0.0489 Mn-I2=0.0538 Mn-Se1=0.0688 Mn-Se2=0.0708	Mn-I1=0.0138 Mn-I2=0.0156 Mn-Se1=0.0210 Mn-Se2=0.0218
Complex 5d	Mn-I1=0.0226 Mn-I2=0.0250 Mn-Se1=0.0321 Mn-Se2=0.0328	Mn-I1=0.0505 Mn-I2=0.0555 Mn-Se1=0.0722 Mn-Se2=0.0737	Mn-I1=0.0143 Mn-I2=0.0161 Mn-Se1=0.0223 Mn-Se2=0.0229

Table D32. Mayer bond order obtained from the *ab initio* CASSCF wave function.

Complex	**Bond order**
Type I	
Complex 1	Mn-O1w=0.262 Mn-O2w=0.248 Mn-O1=0.308 Mn-O2=0.304
Complex 2	Mn-O1w=0.228 Mn-O2w=0.269 Mn-O1=0.333

	Mn-O2=0.314
Complex 3	Mn-O1w=0.236 Mn-O2w=0.258 Mn-O1=0.345 Mn-O2=0.343
Complex 4	Mn-O1w=0.233 Mn-O2w=0.259 Mn-O1=0.339 Mn-O2=0.342
Complex 5	Mn-O1w=0.221 Mn-O2w=0.259 Mn-O1=0.347 Mn-O2=0.345
Type II	
Complex 6	Mn-Cl1=0.366 Mn-Cl2=0.329 Mn-O1=0.280 Mn-O2=0.303
Complex 7	Mn-Cl1=0.352 Mn-Cl2=0.361 Mn-O1=0.287 Mn-O2=0.288
Complex 8	Mn-Cl1=0.358 Mn-Cl2=0.369 Mn-O1=0.293 Mn-O2=0.291
Complex 9	Mn-Cl1=0.369 Mn-Cl2=0.363 Mn-O1=0.292 Mn-O2=0.292
Complex 10	Mn-Cl1=0.365 Mn-Cl2=0.369 Mn-O1=0.297 Mn-O2=0.297
Type III	
Complex 11	Mn-Br1=0.293 Mn-Br2=0.261 Mn-O1=0.279 Mn-O2=0.307
Complex 12	Mn-Br1=0.286 Mn-Br2=0.289 Mn-O1=0.286 Mn-O2=0.286
Complex 13	Mn-Br1=0.296 Mn-Br2=0.287 Mn-O1=0.291 Mn-O2=0.287
Complex 14	Mn-br1=0.294 Mn-br2=0.295

	Mn-O1=0.289 Mn-O2=0.887
Complex 15	Mn-Br1=0.307 Mn-Br2=0.298 Mn-O1=0.293 Mn-O2=0.294
Type IV	
Complex 16	Mn-I2=0.191 Mn-I1=0.266 Mn-O1=0.334 Mn-O2=0.348
Complex 17	Mn-I1=0.259 Mn-I2=0.281 Mn-O1=0.331 Mn-O2=0.332
Complex 18	Mn-I1=0.285 Mn-I2=0.263 Mn-O1=0.334 Mn-O2=0.336
Complex 19	Mn-I1=0.283 Mn-I2=0.273 Mn-O1=0.334 Mn-O2=0.332
Complex 20	Mn-I1=0.278 Mn-I2=0.286 Mn-O1=0.336 Mn-O2=0.335
Type V	
Complex 2a	Mn-O1w=0.239 Mn-O2w=0.289 Mn-Se1=0.324 Mn-Se2=0.424
Complex 3a	Mn-O1w=0.279 Mn-O2w=0.283 Mn-Se1=0.441 Mn-Se2=0.355
Complex 4a	Mn-O1w=0.272 Mn-O2w=0.281 Mn-Se1=0.369 Mn-Se2=0.457
Complex 5a	Mn-O1w=0.259 Mn-O2w=0.278 Mn-Se1=0.461 Mn-Se2=0.386
Complex 2b	Mn-Cl1=0.373 Mn-Cl2=0.368 Mn-Se1=0.294 Mn-Se2=0.267
Complex 3b	Mn-Cl1=0.394

	Mn-Cl2=0.373 Mn-Se1=0.282 Mn-Se2=0.286
Complex 4b	Mn-Cl1=0.368 Mn-Cl2=0.391 Mn-Se1=0.290 Mn-Se2=0.311
Complex 5b	Mn-Cl1=0.392 Mn-Cl2=0.363 Mn-Se1=0.321 Mn-Se2=0.318
Complex 2c	Mn-Br1=0.329 Mn-Br2=0.303 Mn-Se1=0.253 Mn-Se2=0.263
Complex 3c	Mn-Br1=0.268 Mn-Br2=0.315 Mn-Se1=0.252 Mn-Se2=0.253
Complex 4c	Mn-Br1=0.347 Mn-Br2=0.306 Mn-Se1=0.279 Mn-Se2=0.264
Complex 5c	Mn-Br1=0.346 Mn-Br2=0.299 Mn-Se1=0.301 Mn-Se2=0.290
Complex 2d	Mn-I1=0.310 Mn-I2=0.305 Mn-Se1=0.392 Mn-Se2=0.385
Complex 3d	Mn-I1=0.304 Mn-I2=0.319 Mn-Se1=0.411 Mn-Se2=0.387
Complex 4d	Mn-I1=0.299 Mn-I2=0.328 Mn-Se1=0.400 Mn-Se2=0.409
Complex 5d	Mn-I1=0.332 Mn-I2=0.301 Mn-Se1=0.413 Mn-Se2=0.419

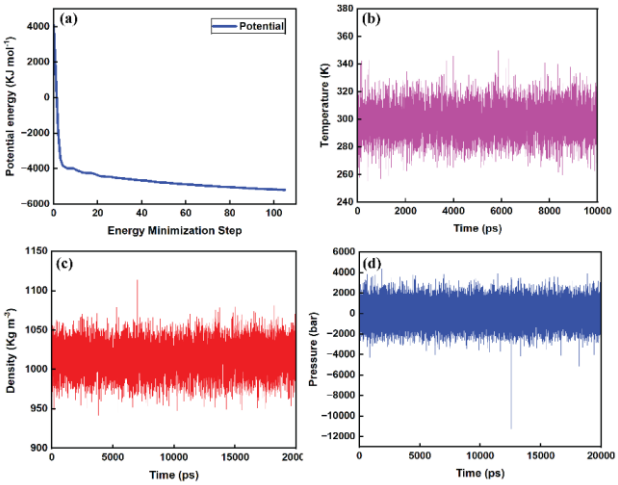

Figure D1. Classical MD simulation results for complex 1 showing: (a) energy minimization, (b) temperature evolution, (c) density evolution, and (d) pressure evolution over time.

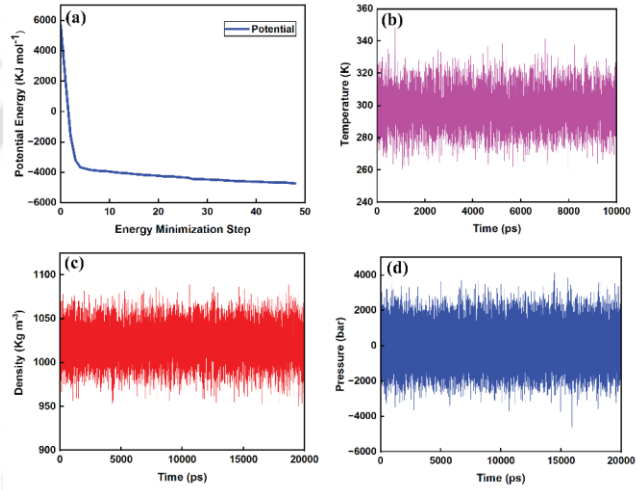

Figure D2. Classical MD simulation results for complex 2 showing: (a) energy minimization, (b) temperature evolution, (c) density evolution, and (d) pressure evolution over time.

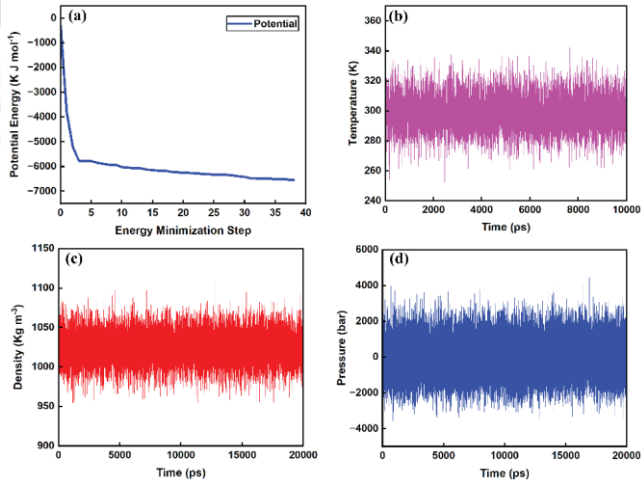

Figure D3. Classical MD simulation results for complex 3 showing: (a) energy minimization, (b) temperature evolution, (c) density evolution, and (d) pressure evolution over time.

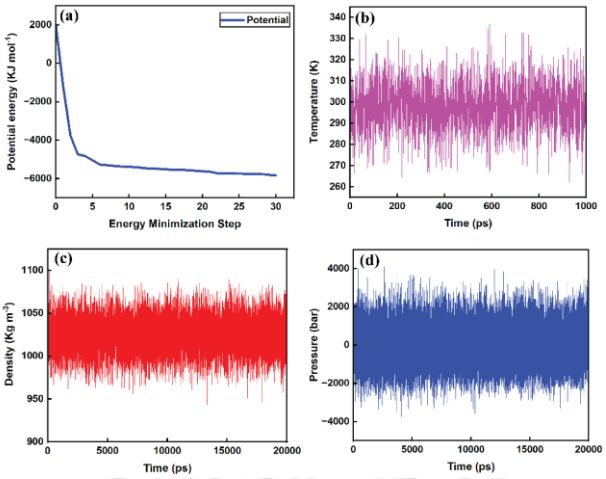

Figure D4. Classical MD simulation results for complex 4 showing: (a) energy minimization, (b) temperature evolution, (c) density evolution, and (d) pressure evolution over time.

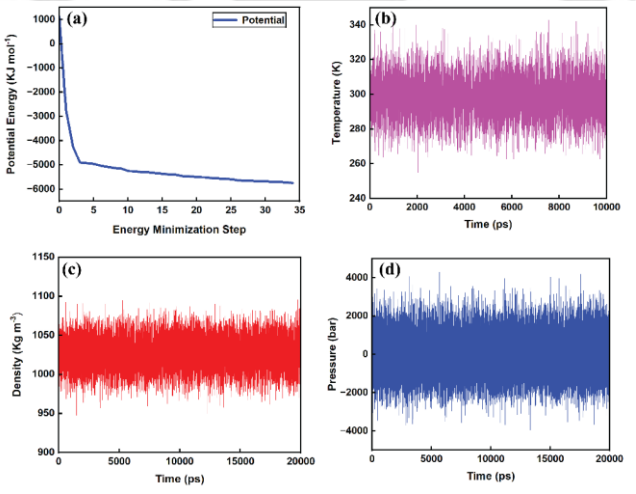

Figure D5. Classical MD simulation results for complex 5 showing: (a) energy minimization, (b) temperature evolution, (c) density evolution, and (d) pressure evolution over time.

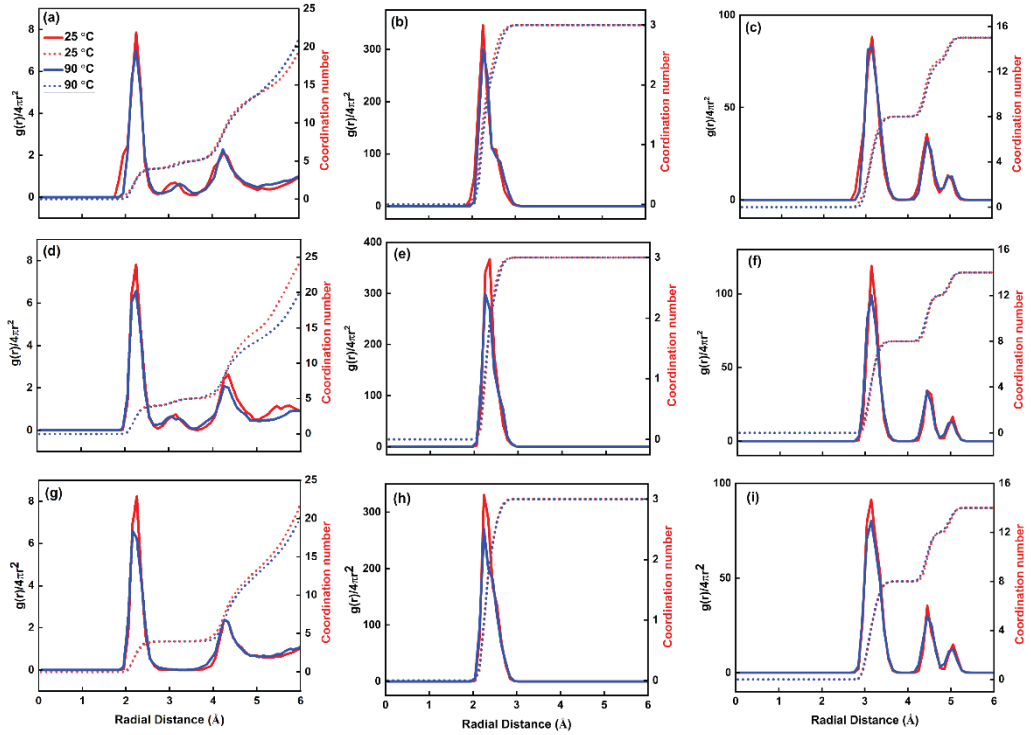

Figure D6. RDFs and CNs for complex 3 (top), complex 4 (middle), and complex 5 (bottom) at 25˚C and 90˚C from AIMD trajectories: (a, d, g) Mn-O, (b, e, h) Mn-N, and (c, f, i) Mn-C atoms.

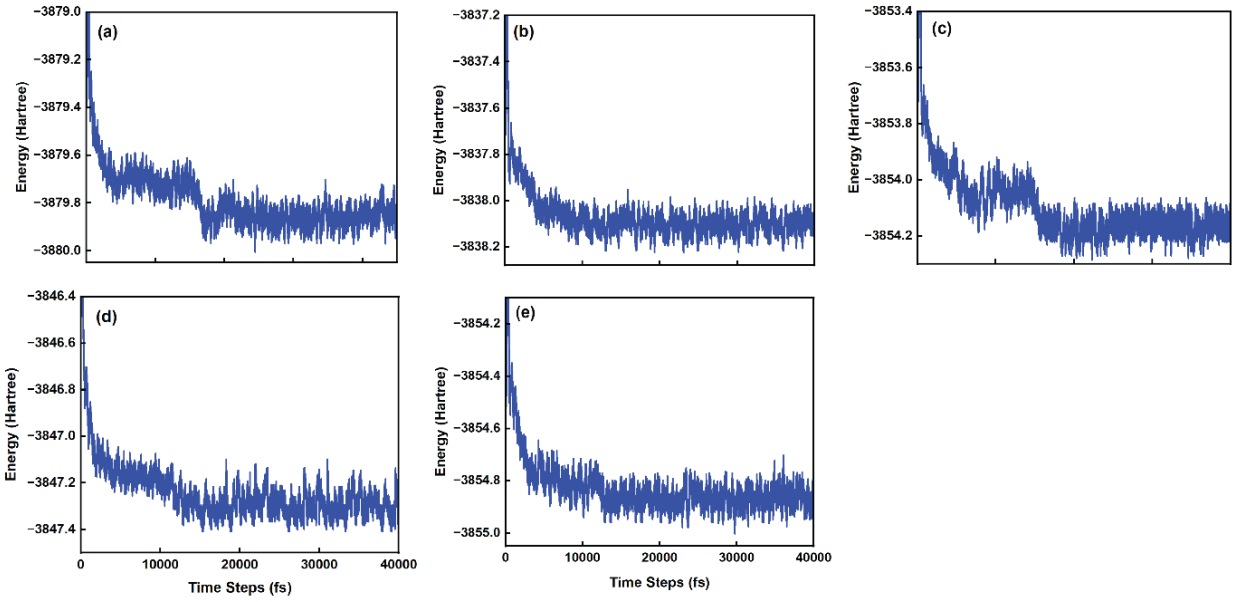

Figure D7. Potential energy (Hartree) plots for AIMD trajectories of simulated complexes at 25˚C for (a) **complex 1**, (b) **complex 2**, (c) **complex 3**, (d) **complex 4**, and (e) **complex 5**.

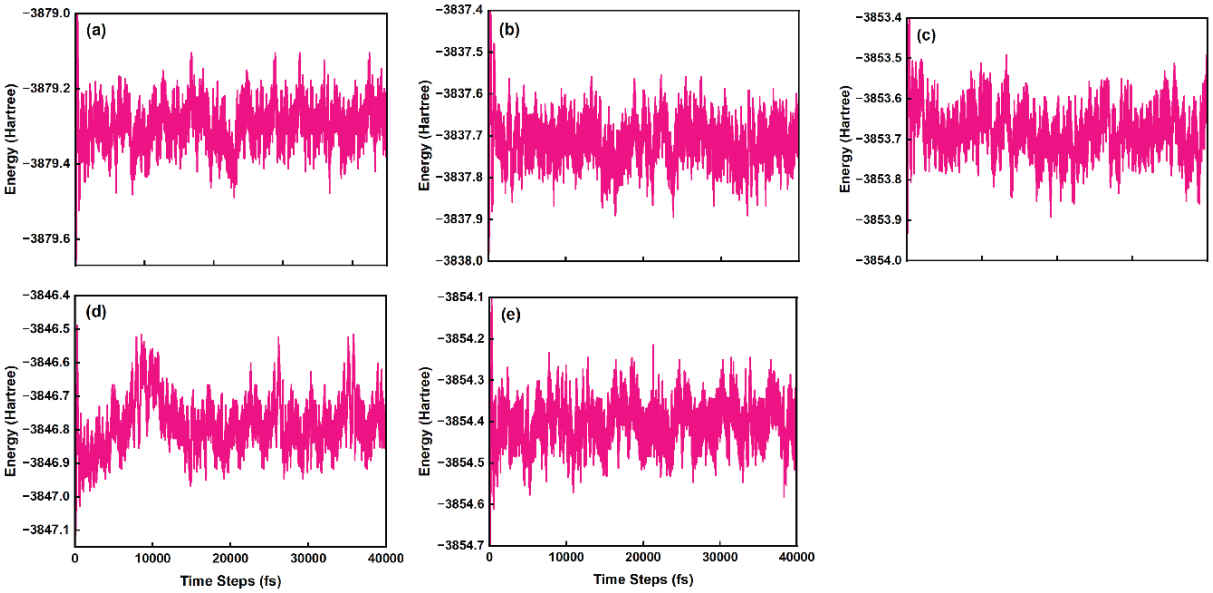

Figure D8. Potential energy (Hartree) plots for AIMD trajectories of simulated complexes at 90˚C for (a) **complex 1**, (b) **complex 2**, (c) **complex 3**, (d) **complex 4**, and (e) **complex 5**.

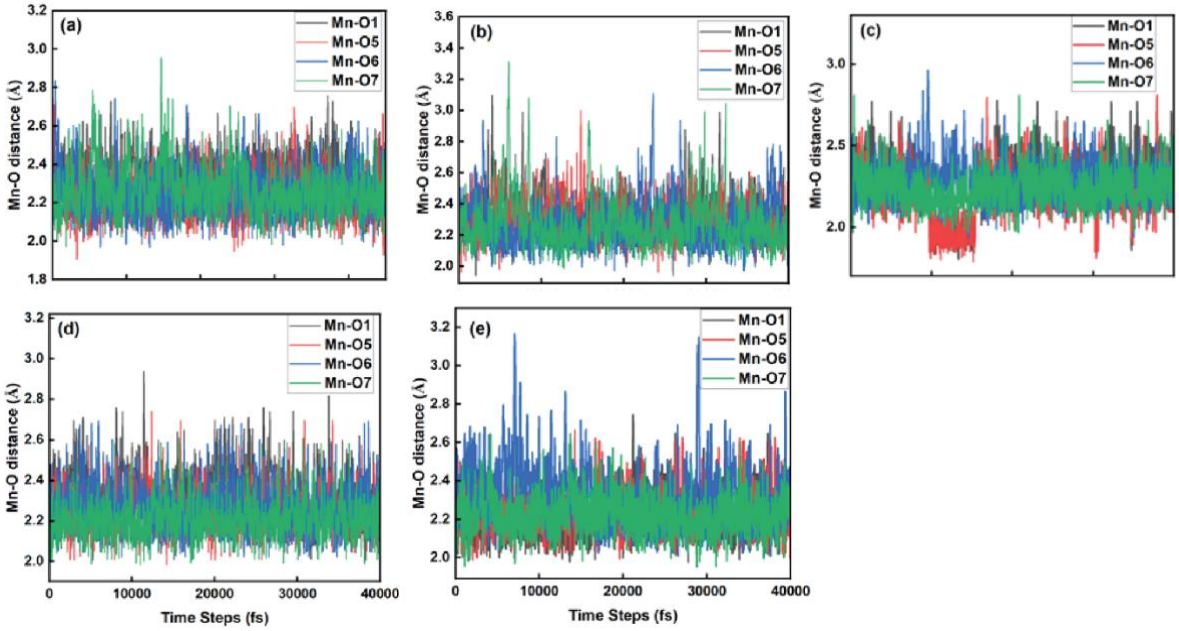

Figure D9. Mn-O bond distances during the AIMD trajectories of (a) **complex 1**, (b) **complex 2**, (c) **complex 3**, (d) **complex 4**, and (e) **complex 5** at 25˚C. The black, red, blue, and green curves represent the Mn-O distances for individual oxygen atoms along the AIMD trajectories.

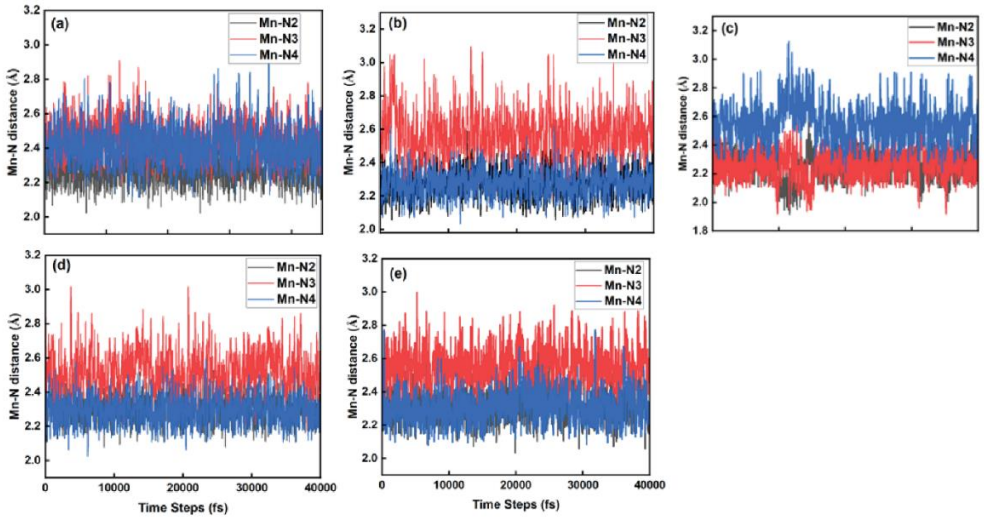

Figure D10. Mn-N bond distances during the AIMD trajectories of (a) **complex 1**, (b) **complex 2**, (c) **complex 3**, (d) **complex 4**, and (e) **complex 5** at 25˚C. The black, red, and blue curves represent the Mn-N distances for individual nitrogen atoms along the AIMD trajectories.

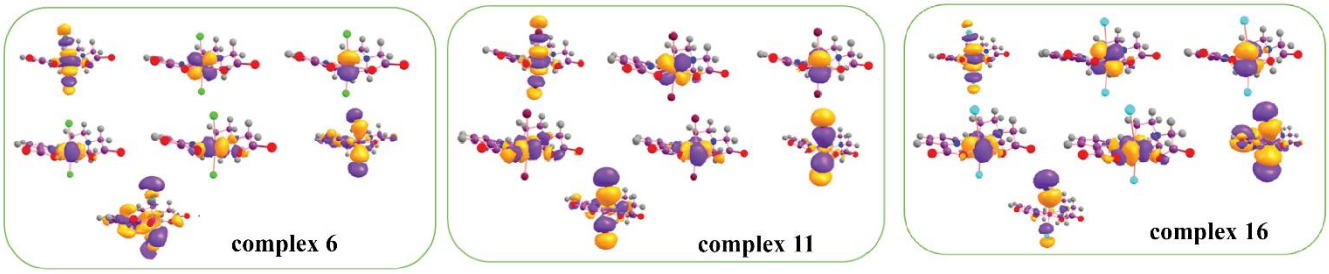

Figure D11. The CAS orbitals obtained after SA-CASSCF calculation with CAS (9,7) active space for **complex 6, complex 11, and complex 16.**

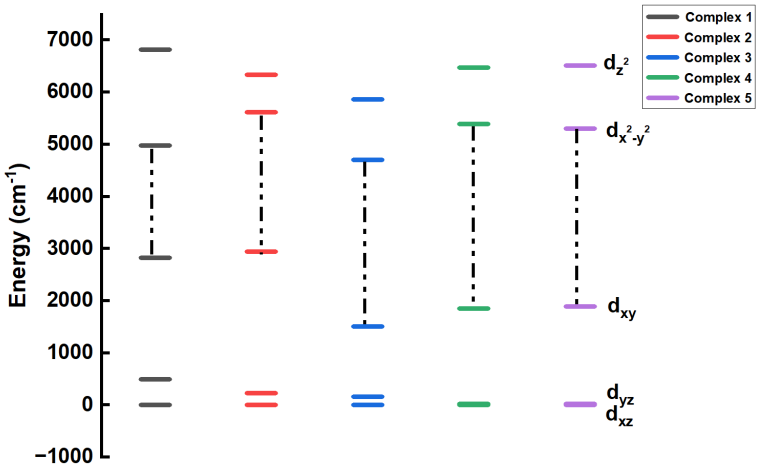

Figure D12. NEVPT2 computed ligand field d-orbital splitting diagram of the investigated **Type I** complexes.

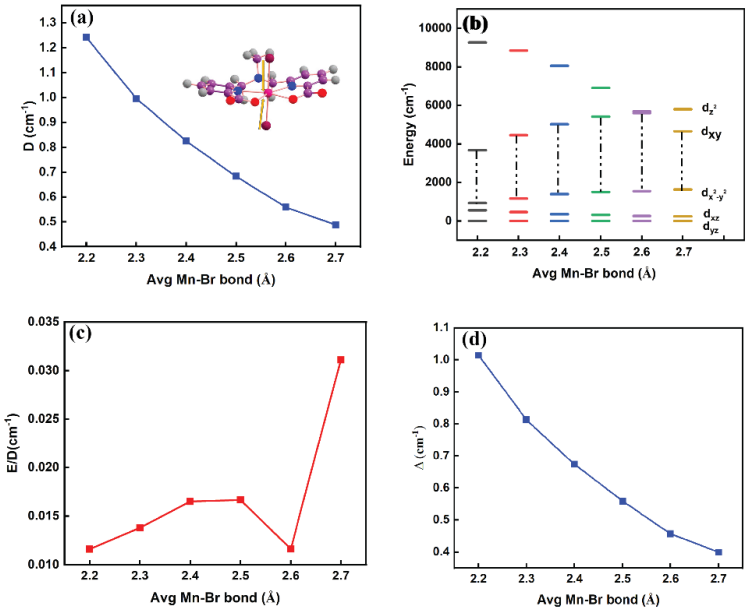

Figure D13. Graphical output of the *ab initio* CASSCF/NEVPT2 calculations for the model **complex 12** in which bond length varies from 2.7-2.2 Å, (a) variation of D-parameter, (b) the d-orbital splitting, (c) variation of E/D parameter, and (d) variation of ZFS energy (Δ).

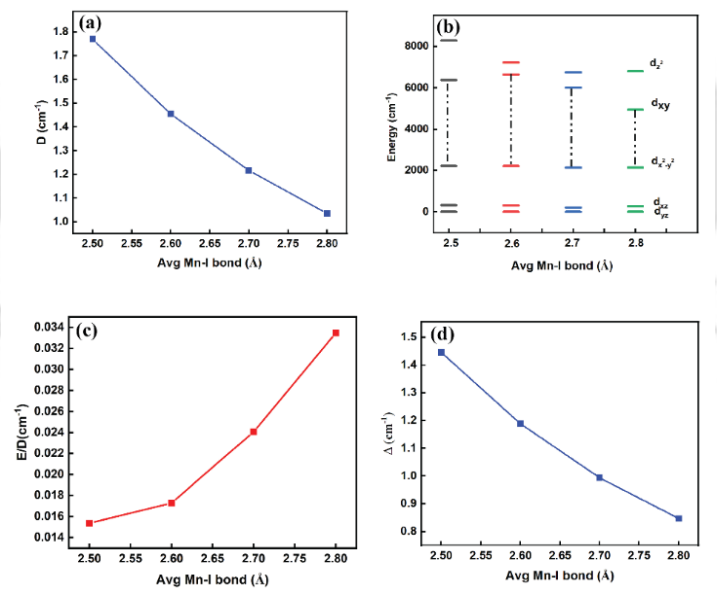

Figure D14. Graphical output of the *ab initio* CASSCF/NEVPT2 calculations for the model **complex 17** in which bond length varies from 2.8-2.5 Å, (a) variation of D-parameter, (b) the d-orbital splitting, (c) variation of E/D parameter, and (d) variation of ZFS energy (Δ).

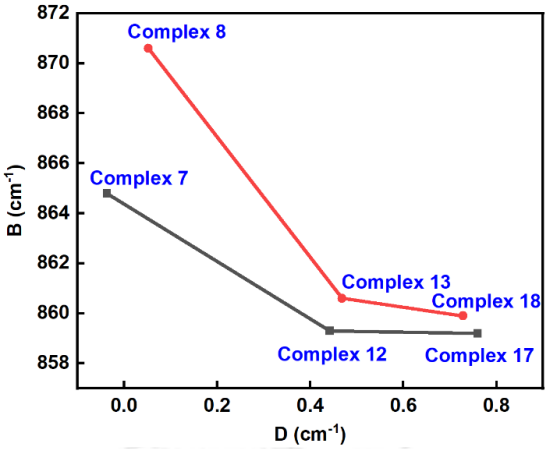

Figure D15. Variation of D with Racah parameter B for **complex 7**, **complex 12**, and **complex 17** (black) and **complex 8**, **complex 13**, and **complex 18** (red).

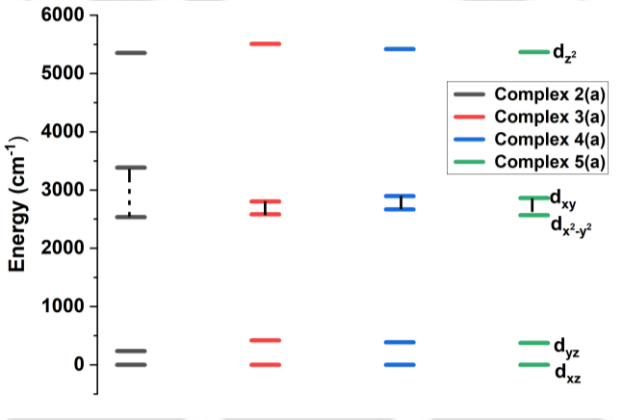

Figure D16. NEVPT2 computed ligand field d-orbitals splitting diagram of the investigated **complexes 2(a)**, **3(a)**, **4(a)**, and **5(a)**.

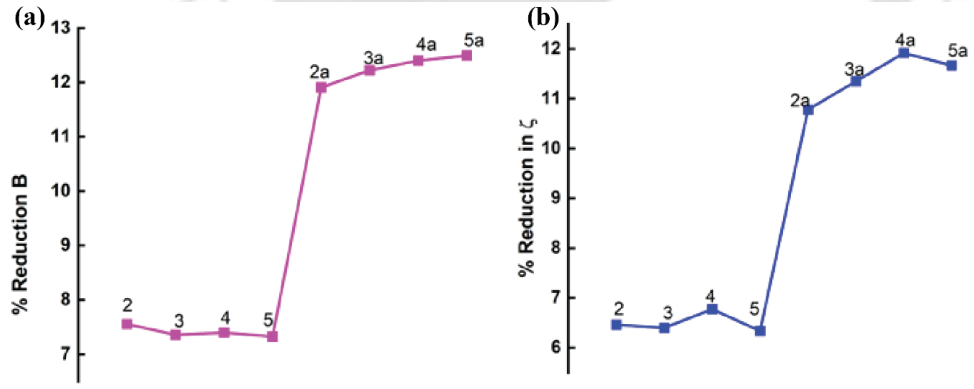

Figure D17. (a) Variation of nephelauxetic reduction of Racha parameter B and (b) effective spin-orbit coupling constant ζ of **complex 2**, **complex 3**, **complex 4**, **complex 5**, and its selenium derivatives (**complex 2a**, **complex 3a**, **complex 4a**, and **complex 5a**).

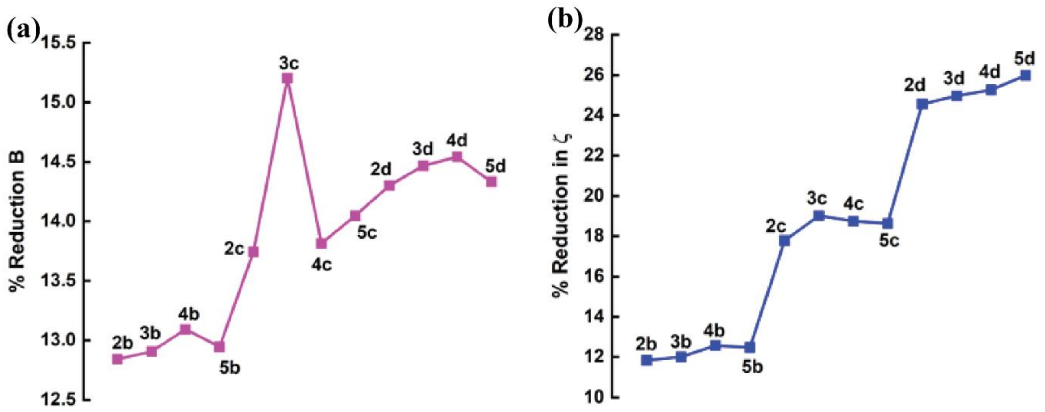

Figure D18. (a) Variation of nephelauxetic reduction of Racha parameter B and (b) effective spin-orbit coupling constant ζ among halogen derivatives of Se-derivatives.